The Impact of Giant Stellar Outflows on Molecular Clouds

A thesis presented

by

Héctor G. Arce Nazario

to

The Department of Astronomy

in partial fulfillment of the requirements

for the degree of

Doctor of Philosophy

in the subject of

Astronomy

Harvard University

Cambridge, Massachusetts

October, 2001

ABSTRACT

Thesis Advisor: Alyssa A. Goodman Thesis by: Héctor G. Arce Nazario

We use new millimeter wavelength observations to reveal the important effects that giant (parsec-scale) outflows from young stars have on their surroundings. We find that giant outflows have the potential to disrupt their host cloud, and/or drive turbulence there. In addition, our study confirms that episodicity and a time-varying ejection axis are common characteristics of giant outflows.

We carried out our study by mapping, in great detail, the surrounding molecular gas and parent cloud of two giant Herbig-Haro (HH) flows; HH 300 and HH 315. Our study shows that these giant HH flows have been able to entrain large amounts of molecular gas, as the molecular outflows they have produced have masses of 4 to 7 $M_\odot$ —which is approximately 5 to 10% of the total quiescent gas mass in their parent clouds. These outflows have injected substantial amounts of momentum and kinetic energy on their parent cloud, in the order of 10 $M_\odot$ km s^{-1} and 10^{44} erg, respectively. We find that both molecular outflows have energies comparable to their parent clouds' turbulent and gravitationally binding energies. In addition, these outflows have been able to redistribute large amounts of their surrounding medium-density ($n \sim 10^3$ cm^{-3}) gas, thereby sculpting their parent cloud and affecting its density and velocity distribution at distances as large as 1 to 1.5 pc from the outflow source.

Our study, in combination with other outflow studies, indicate that a single giant molecular outflow in a molecular cloud of less than about 80 $M_\odot$ has the potential to seriously disrupt its parent cloud. We, therefore, conclude that the cumulative action of many giant outflows will certainly have a profound effect on their cloud's evolution and fate.

Our detail study of the outflow morphology, velocity structure, and momentum distribution —among other properties of both outflows— lead us to suggest that they are predominantly formed by bow-shock prompt entrainment, from an episodic wind with a time-varying axis. Close to the outflow source of HH 315, though, the coexistence of a jet-like wind *and* a wide-angle wind explains better the observed outflow properties.

Contents

List of Figures

List of Tables

Acknowledgments

I've been a graduate student in the Astronomy Department at Harvard University for the last six years. This is not a negligible amount of time, as it is slightly more than one-fifth (21.4% to be precise) of my current life. But, the quantity is not important compared to the quality of these past six years. Not only did my hair and beard grow (you should see a "before-and-after" set of pictures), but also did my experience in research and knowledge of astronomy. I also grew personally; I came in as a happy bachelor and leave as an even happier married man. And, I also matured politically, but that is not a topic which I should discuss here.

I would like to thank Alyssa Goodman for being a great advisor and collaborator, always enthusiastic about science and our research work. I have always felt I made the right choice by choosing Alyssa as my advisor. I learned a lot from her: from dust to outflows; from science writing to graphic design. I hope she will ever forgive me for the "house heater incident".

I will also like to thank the members of my TAC and defense committee (Charlie Lada, Phil Myers, Dimitar Sasselov, and Ramesh Narayan) for helping me stay on track and their good advice throughout the time I worked on the thesis. I will also like to thank John Bally, the outside faculty in the defense committee, for taking the time to come to Cambridge for the defense, and for his careful reading of the thesis.

My friends at the CfA also made this past six years a great experience. My friend Lucas Macri has always been there since the day we both started here at Harvard six years ago. He always offered his unconditional help and knowledge, from computer programming to photometry, from "mate" to how to cook a real BBQ. I thank him for his great friendship and for those afternoon squash and tennis games.

During my first three years at the CfA, I enjoyed the company of the older students. I still communicate with them, and I hope our friendship will last many more years. Among these friends, I would like to specially thank Rohan for his

company, his “grrrreeeaaattt” friendship, and the good quality rum. I thank my friends John K. and Ann E. for their company, and for giving me such a good deal on the car. Martin K. and Diego Mardones also shared their friendship, their knowledge and their skills in squash with me while we coincided here in Harvard. I cannot forget João Alves, his good humor, camaraderie, and the great time we had in Crete. I also enjoyed very much having lunch across the street with Rafa, Pepe, Guillermo, Antonio, and Frederico.

I thank Quizhou for his friendship, his help, for coming back to the CfA after leaving for Arizona (that way I could bug him more on questions about outflows), and also for that tasty duck in Hat Creek.

The CfA is a huge place and there is always people coming and going. Out of those who came and went, I would like to specially thank Javier and Paola for being such good “cuates”, and introducing me to the wonders of “el mole poblano”. Also, I thank Javier for being a great observing partner (even though he is a theorist), and though he could sometimes be a pain (and he knows what I mean...), he is a great friend I can always count on.

I also enjoyed sharing my “160 Concord” life with Tyler, Maite, Maru, James M., Cesar B., James D., Mario T., Lincoln, Pedro E., Ted, Lori, and Tom Megeath. I thank Nuria for keeping me awake throughout the afternoons with her perfectly brewed coffee, as well as for also being helpful in answering my general questions of star formation, and her exceptionally meticulous helpful comments for improving science talks. I thank Lee for his helpful scientific discussions and for believing in the power of outflows.

I also like to thank others who made my life in the Greater Boston Metropolitan Area very enjoyable. I thank the various people who have inhabited “La 5 Mossland” throughout the years: Javier, Luiso, Consti, and Maite. Out of these, I specially thank Maite for being, not only a great roommate and friend, but also for being the best officemate I’ve had at the CfA. It’s incredible how she put up with me at the office *and* at home! I also thank my friends and comrades from LFSC and Agit•Arte: Sergio, Susana, Gilberto, Andrés, Herb, Dan, Ty, Rosa, Jorge, and Jill.

I thank my father and my mother for their eternal unconditional support and encouragement, and for always believing in me. I will also like to thank my grandfather Rafael Arce Blanco, the first astronomer I ever knew. Although he died before I started my graduate studies in astronomy, he has always been an inspiring figure to me. His knowledge about the sky and his home-built telescopes were the first contacts I had with astronomy.

And last, but not least, I will like to extend my deepest gratitude to my wife Noelia. We started our relationship just after I took the first set of observations used in this thesis, and we got married just before I finished this thesis. All this time she has provided me with joy, love, and support, all essential ingredients for me to be able to finish the work presented here.

Muchas gracias a todos,

Héctor G. Arce Nazario

This work is dedicated to the memory of my grandfather,

to my parents for their full support and encouragement,

and to Noelia, my wife, for her love.

Chapter 1

Introduction

1.1 A brief introduction to star formation

Stars are the celestial bodies that have been studied the most in history. These small speckles of light that adorn our night sky have had an important place in all major cultures. Throughout history stars have been useful tools for navigation and agriculture. In the physical sciences stars also have an important place, as they are the fundamental units of astronomy. Understanding their formation not only gives us insight into how the Sun (and the Earth) formed, but also helps us better understand the early universe and the formation of galaxies.

Stars form in objects called "molecular clouds". These are the most massive and coldest objects known in our Galaxy, reaching masses up to more than 10^6 $M_\odot$ and temperatures of about 10 to 50 K. Molecular clouds get their name from the fact that they are made mainly from molecular hydrogen (H_2). But, although molecular hydrogen is the main constituent in molecular clouds, they are detected and mapped using the second most abundant molecule in these clouds, carbon monoxide (CO). This is mainly because the lowest energy of the rotational transitions of the H_2 molecule is too high to be collisionally excited at the typical temperatures of molecular clouds (about 10 K). On the other hand, the characteristic temperature (energy/k, where k is Boltzmann's constant) of the first rotational level ($J = 1$) of the CO molecule is only 5.5 K. Thus, most large-scale

molecular cloud maps are made with the $J = 1 - 0$ rotational transition line of the CO molecule, with a wavelength of 2.6 millimeters[1].

"Clouds" are typically identified in molecular line observations, appearing as a coherent region in position-position-velocity space (e.g., Blitz & Thaddeus 1980). Like many objects in nature, molecular clouds have different shapes, structures, sizes, and masses. The large clouds, with masses on the order of 10^4 $M_\odot$ (or more), and sizes of about 50 pc (or more) are generally called giant molecular clouds. Small clouds (sometimes referred to as dark clouds by optical astronomers, e.g., Barnard 1919), with masses on the order of 10 to 10^3 $M_\odot$ and sizes of 1 to 5 pc, are usually found grouped together in molecular cloud complexes (see Figure 1.1).

The density distribution inside molecular cloud complexes and giant molecular clouds is highly nonuniform, or "clumpy" (e.g., Blitz & Shu 1980), with a hierarchical structure in which the densest regions have the smallest size scales (e.g., Blitz & Williams 1999). The mean density of the gas in a molecular cloud depends on the size scale of the region over which the average is taken. For example, the mean density of a molecular cloud complex or giant molecular cloud over a size of about 10 to 20 pc, is ~ 100 cm^{-2} (Dame et al. 1986). At smaller sizes scales of about 1 to 2 pc, the average density is about 10^3 cm^{-3}. At these higher densities the CO(1–0) is mostly optically thick, and so these regions are better mapped with the ^{13}CO(1–0) line (e.g., Bally et al. 1987; Mizuno et al. 1995), which is mostly optically thin at these densities (see Figure 1.1). At even smaller size scales of about 0.1 to 0.3 pc, the average density is about $\sim 10^4$ cm^{-3}. These high-density regions (or condensations) inside clouds, called dense cores, are better traced by the N_2H^+(1-0) and NH_3 lines (e.g., Benson, Caselli, & Myers 1998; Jijina, Myers, & Adams 1999) than by the ^{12}CO and ^{13}CO lines.

It is inside dense cores that stars form. The star-formation process begins with the collapse of a slowing-rotating core, once it can no longer sustain itself against gravity. The collapsing material quickly forms a condensation (i.e., the young

[1]Molecular rotational transition lines will hereafter be identified by the name of the molecule, followed (in parenthesis) by the two levels of the transition, that is the $J = 1 - 0$ rotational transition line of the CO molecule will be written CO(1–0).

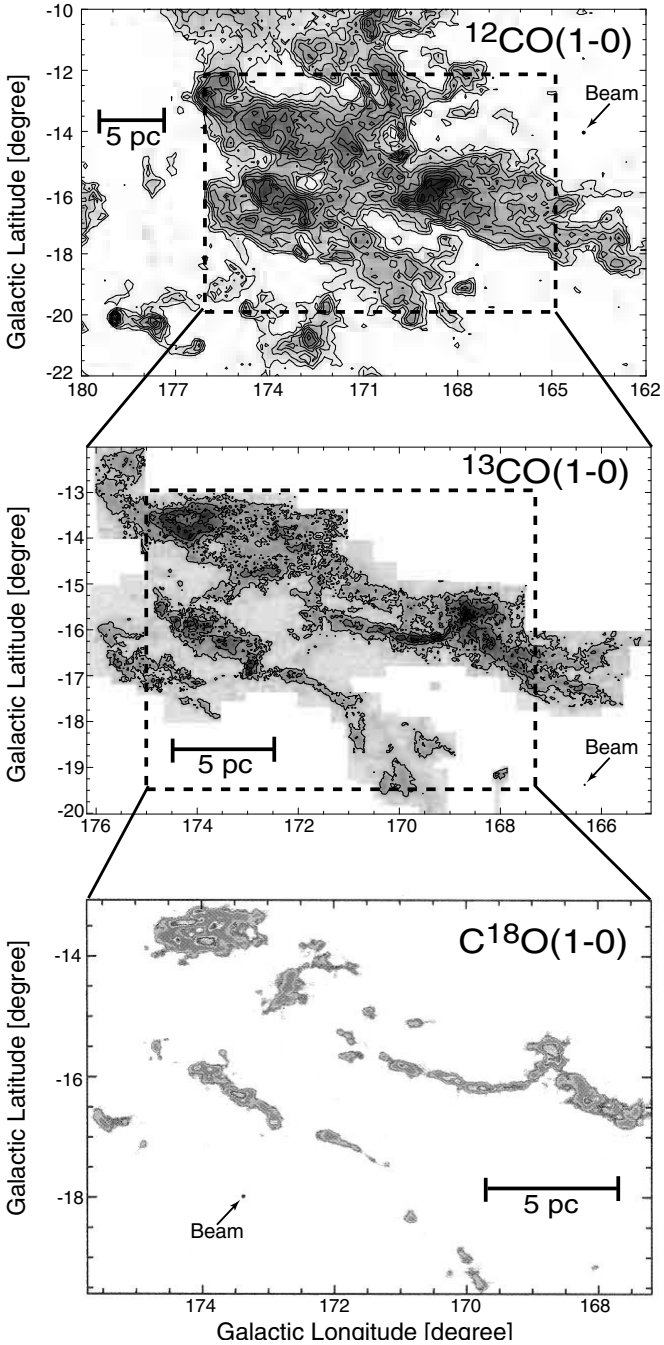

Fig. 1.1.— The Taurus molecular cloud complex observed at three different molecular spectral lines. The top panel is a ^{12}CO(1–0) map from Megeath, Dame, & Thaddeus (2001). The middle panel is a ^{13}CO(1–0) map from Mizuno et al. (1995). The lower panel is a C^{18}O(1–0) map from Onishi et al. (1996). Each of these molecular lines probes a different density regime. Among the three lines shown here, ^{12}CO(1–0) probes the lowest, while C^{18}O(1–0) probes the highest density regimes. The ^{12}CO(1–0) map was observed with a beam width of $\sim 8'$, and the ^{13}CO(1–0) and C^{18}O(1–0) maps were observed with a beam width of $\sim 3'$. A linear scale is shown for each map, assuming a distance to Taurus of 140 pc.

stellar object) in the center (Shu, Adams, & Lizano. 1987). The densest part of the star-forming core which surrounds the protostar is usually referred to as the circumstellar envelope (see a schematic picture in Figure 1.2). The vast majority of the infalling material from the circumstellar envelope will not accumulate in the central young stellar object (YSO) due to excess angular momentum, rather it will form a disk-like structure around the nascent star (e.g., Cassen & Moosman 1981; Terebey, Shu, & Cassen 1984; Yorke, Bodenheimer, & Laughlin 1993). The matter in the circumstellar disk will move inward, as angular momentum is moved outward. This inward-moving matter will eventually reach the edge of the circumstellar disk, and accrete on the protostar, thereby feeding its growth.

At the same time that stars gather matter from the circumstellar disk, they energetically spurt out mass in a bipolar flow (see Figure 1.2). This process of mass outflow was never imagined by star-formation theorists before it was actually discovered through optical (and later millimeter wavelength) observations. It apparently never occurred to anyone that a process that was supposed to be dominated by gravitational infall of gas onto a forming star would also be accompanied by powerful mass outflows. Even though there is no consensus on the exact mechanism that launches and collimates the outflow from a young stellar object, it is now clear that most (if not all) young stars undergo periods of energetic mass loss and that it is an important part of the star formation process (Richer et al. 2000).

The mass outflow phase is important to the star-formation process for two principle reasons. First, outflows serve as a way to get rid of the excess angular momentum transferred from the circumstellar disk onto the forming star, which would otherwise break the protostar apart (Hartmann & MacGregor 1982). Secondly, mass outflows can terminate the YSO accretion phase by clearing the surroundings of the forming star, so that there is no material left to infall onto the star-disk system (e.g., Velusamy & Langer 1998).

It is this mass outflow stage, of the star-formation process, which is the focus of this thesis. In particular, we study the effects giant (parsec-scale) outflows have

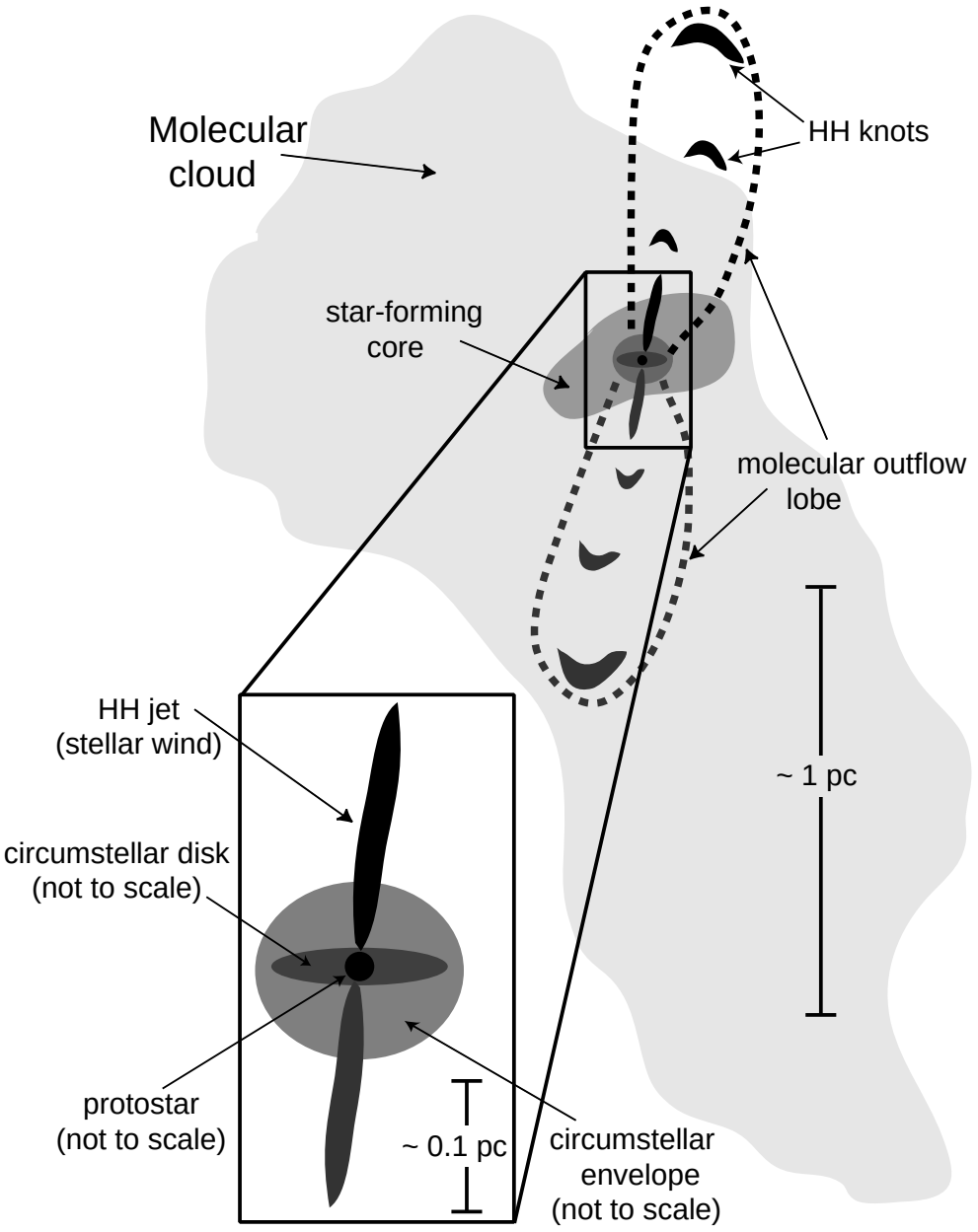

Fig. 1.2.— Schematic picture of a star-forming region. The different components of the region are identified. The protostar and the circumstellar disk and envelope are *not to scale*.

on their surroundings.

1.2 The outflow stage

The mass outflow from a young star may reveal itself in different ways. Herbig-Haro (HH) objects, and molecular (CO) outflows are among the most important manifestations of a nascent star's mass loss process. An "HH object" is a nebulous knot, seen mainly at optical wavelengths, which delineates the shock arising from the interaction of a high-velocity flow of gas ejected by a young stellar object and the ambient medium. A chain of these HH objects (or knots) is usually referred to as an "HH flow". One or more shocks associated with an HH flow can accelerate entrained gas to velocities greater than those of the quiescent cloud, transferring momentum and energy into the host molecular cloud, thereby producing a molecular outflow.

1.2.1 Herbig-Haro flows

The study of collimated bipolar mass outflows from young stellar objects started in the 1950's with the discovery by Herbig (1951) and Haro (1952) of two nebulous objects with emission line spectra. Although the nature of these nebulous objects —which were later named "Herbig-Haro objects" by Ambartsumian (1954)— was not known for a couple of decades after their discovery, it was clear from the start that they were associated with the process of star formation. Several years after their discovery, Herbig suggested that HH objects could be associated in some way with winds from young stars (Herbig 1958). A detailed study of the spectra of several HH objects by Schwartz (1975) led him to suggest that HH objects are shocks due to highly supersonics wind interacting with the ambient medium.

At the time that Schwartz's idea was put forward it was thought that the winds from young stars were spherically symmetric, but as more observations were taken it was realized that HH objects do not delineate a spherical outflow. Proper

motion studies of several HH objects [i.e., HH 28 and HH 29 (Cudworth & Herbig 1979); HH 1 and HH 2 (Herbig & Jones 1981)] showed that they move at highly supersonic velocities ($\sim$ 200 km s^{-1} or more) away from an embedded young star (the presumed powering source of the wind). In the case of the HH 1–HH 2 system, Herbig & Jones (1981) showed that each of these two HH objects were moving away, each in a different direction, from a deeply embedded infrared source. None of these early observations showed that HH objects had a spherical distribution around their pressured powering source, thus the increasing observational evidence pointed towards HH objects as being the high surface brightness knots of collimated outflows. Theorists then started to suggests different mechanisms which could produce such collimated bipolar winds (e.g., Königl 1982; Cantó et al. 1988).

The deep CCD imaging surveys of YSO and previously known HH objects by Mundt & Fried (1983) and Mundt et al. (1984) showed that HH objects are very common around young stars and that some of the previously known HH objects were really the knots with the highest surface brightness of a highly collimated chain of knots emanating from a young star. These HH flows, which are observed to have a very collimated and apparent continuous morphology are normally referred to as "HH jets". HH jets (see, Figure 1.3) are always found to originate very close to their power source (less than 10^2 to 10^3 AU from their source), and they usually extend less than 0.2 pc in length. These jets are composed of many tightly packed knots, which have velocities from about 100 km s^{-1} up to 600 km s^{-1}.

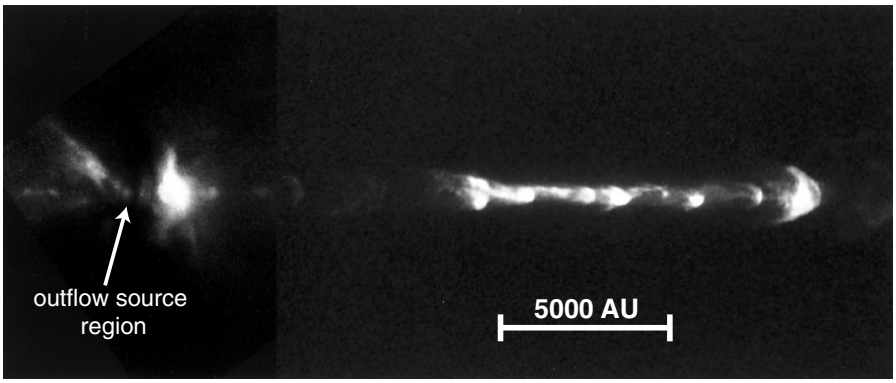

Fig. 1.3.— Mosaic image of the inner region of the HH 111 jet, from space-based near-infrared (left) and optical (right) images (from Reipurth et al. 1999). The outflow source is on the left. This is an excellent example of an HH jet with inner shock structures, and a leading (wider) bow shock at the head. The linear scale is shown, assuming a distance of 470 pc to the source.

The knotty appearance of HH jets and the spatially discrete appearance of some HH flows led some to believe that HH flows are not a continuous phenomenon, as it was originally thought. A continuous jet, with variable outflow velocity can produce the multiple emission knots observed in HH jets (e.g., Raga et al. 1990), like the inner section of HH 111 shown in Figure 1.3. But, HH flows with an intermittent appearance, in which there is no HH-like emission between contiguous knots are harder to explain with variable-velocity models. In particular, when two contiguous HH objects have a clear bow shock-like appearance it is very probable that each is produced by the interaction of a mass outflow episode (a sudden increase in the stellar wind's mass loss) and the ambient medium (e.g., Reipurth 1989; Hartmann, Kenyon, & Hartigan 1993), rather than just velocity variations in the wind. In this "discontinuous" picture, the first HH object in the chain (that is, the HH object furthest away from the source) is produced by the first mass ejection episode.

Recent optical and near-infrared surveys with wide-field CCD cameras (Eislöffel & Mundt 1997; Devine et al. 1997; Reipurth, Bally, & Devine 1997; Mader et al. 1999; Eislöffel 2000; Stanke, McCaughrean, & Zinnecker 2000) have shown that parsec-scale HH flows from young stars are a common phenomenon. In many cases these wide-field CCD observations have revealed that HH flows that were thought to extend less than about 0.5 pc, really extend 2 to 3 pc (or even more) on the sky. Most giant HH flows have sizes about an order of magnitude larger than the cloud cores from which they originate, and many are found to extend to distances well outside their parent cloud (e.g., Reipurth et al. 1997c). These parsec-scale HH flows do not have a continuous bright emission appearance (like HH jets), instead they are made of long chains of HH objects that presumably have a common origin. The distance between different HH knots of a giant HH flow might range from 0.1 pc to 2 pc. Therefore, the discovery of these giant HH flows has added more evidence to the general belief that outflows are intermittent or episodic.

1.2.2 Molecular Outflows

While optical astronomers and theorists were trying to understand the nature of HH objects in the mid 1970's, radio astronomers began making discoveries that turned out to be very important in the study of young stellar mass outflows. With the help of mm-wavelength telescopes, broad lines of CO emission were discovered towards different star-forming regions inside molecular clouds. The CO lines showed widths of 6-8 km s^{-1}, when the typical molecular cloud CO linewidth is 1-3 km s^{-1}. Originally the excess in the CO linewidth was interpreted to be the result of gravitational collapse of the cloud around forming-stars (e.g., Lada, Dickinson, & Penfield 1974; Goldreich & Kwan 1974). Later, the high-sensitivity observations of a region of known active star formation in Orion (the Kleimann-Low nebula) yielded CO gas with velocities of up to $\sim 60 - 70$ km s^{-1} away from the ambient cloud velocity (Kwan & Scoville 1976; Zuckerman, Kuiper, & Kuiper 1976). These extremely high velocities are too fast to be due to gravitational collapse or to any gravitationally bound motion, and so it was immediately realized that such extremely high velocities are due to an energetic outflow in the region.

With the first spectral line *maps* of the high-velocity CO around several young stars (of different masses), such as L1551-IRS5 (Snell, Loren, & Plambeck 1980), and Ceph A (Rodríguez, Ho, & Moran 1980), astronomers realized that molecular (CO) outflows around young stars could have a bipolar (anisotropic) spatial structure. In particular the study of L1551-IRS5 (Snell et al. 1980) showed that the axis of the blueshifted CO outflow lobe approximately coincides with the direction of the proper motions of HH 28 and HH 29, which also have blueshifted radial velocities with respect to the cloud's velocity (see Figure 1.4). Tracing the motion of these two HH knots backward, Snell et al. observed that the HH objects and the CO outflow most probably had a common origin. Thus, it was established that HH objects and CO outflows have some kind of relationship. Soon thereafter, studies of the gas around YSOs found that bipolar CO outflows are a common phenomenon amongst young stars (e.g., Edwards & Snell 1982; Bally & Lada 1983; Levreault 1988).

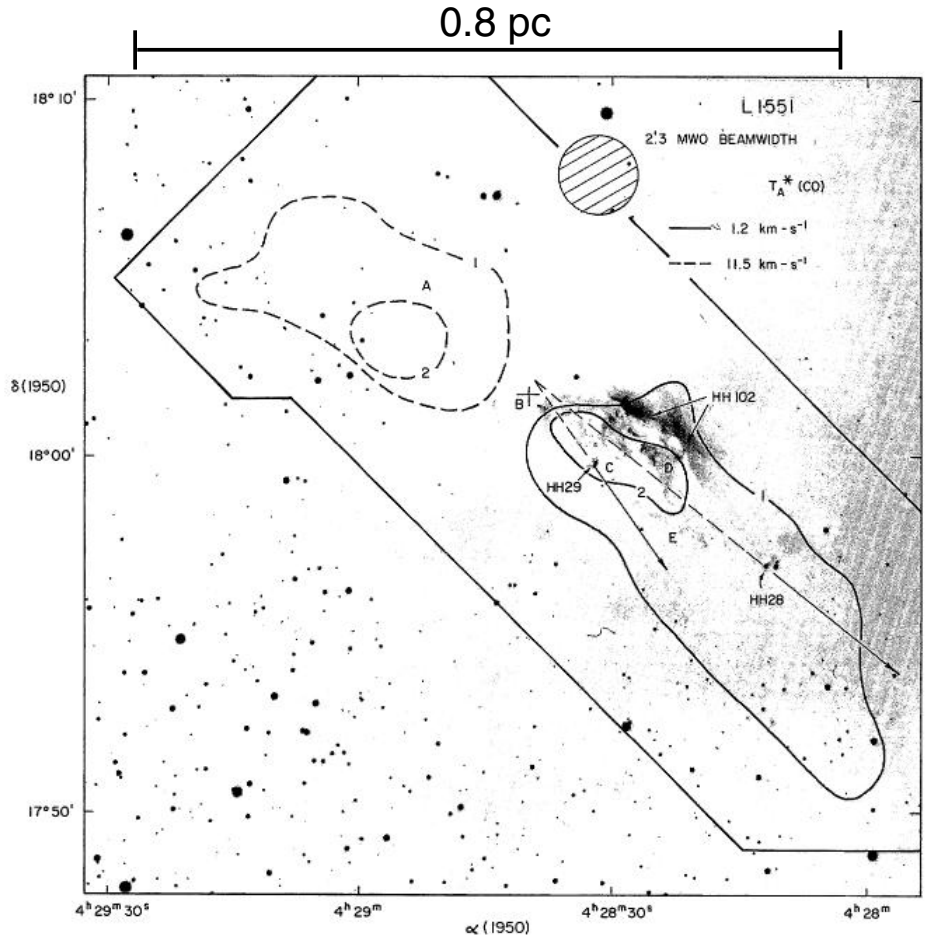

Fig. 1.4.— Image showing the L1551-IRS5 molecular outflow (from Snell et al. 1980), the first molecular outflow to be mapped. The dashed contours show the ^{12}CO(1–0) redshifted integrated intensity emission, and the solid contours show the ^{12}CO(1–0) blueshifted integrated intensity emission of the outflowing gas. The cross between the two lobes indicates position of the presumed outflow source, IRS5. The direction of the proper motions of HH 28 and HH 29 are shown, and they both trace their motion backward to a region close to IRS5, suggesting a common origin among the HH knots and the molecular outflow (Snell et al. 1980). The beam size of the telescope used is shown. Also shown is the linear scale assuming a distance to the L1551 cloud of 140 pc.

1.3 Outflow-Cloud interaction

Early on in the study of young stellar winds, it was realized that outflows have the potential to have major effects on the dynamics and structure of their parent cloud (e.g., Norman & Silk 1980). The large-scale (unbiased) molecular outflow surveys of Margulis & Lada (1985), Fukui et al. (1986), and Armstrong & Winnewisser (1989) were important in estimating the molecular outflow energy in whole clouds, and acknowledging that outflows have a significant impact on the dynamical state of their host cloud. These studies concentrated on comparing the total outflow energy with the energy needed to sustain the turbulence in the cloud, and support it against gravitational collapse. Back then it was thought that molecular clouds lived (in a state of quasi-equilibrium) for about 30 Myr (Blitz & Shu 1980), about an order of magnitude larger than the free-fall collapse timescale of the cloud. If the timescale of turbulent energy dissipation in a molecular cloud is less that the cloud's supposed lifetime, then an approximately constant source of energy is needed to maintain turbulence in the cloud, in order to support it against gravitational collapse. Outflows make a very attractive source of energy for feeding the turbulence inside clouds. Therefore, most of the early work on the effects of outflows on their parent cloud concentrated on the potential role of outflows as the leading mechanism for cloud support.

There is currently increasing evidence which suggest that molecular clouds only live for 5 to 10 Myr (e.g., Ballesteros-Paredes, Hartmann, & Vázquez-Samadeni 1999; Elmegreen 2000; Hartmann, Ballesteros-Paredes, & Bergin 2001). But, although it seems that molecular clouds can be formed in short ($\lesssim$ 3 Myr) timescales (Ballesteros-Paredes et al. 1999), it is not yet clear how they might quickly disperse. Is easy to understand the rapid dispersal of molecular gas in regions containing high-mass (O type) stars, which destroy clouds rapidly due to photoionization and strong stellar winds. But, the dispersal of clouds or cloud complexes containing only low- and/or intermediate- mass stars is much more difficult to understand. In such cases, giant outflows from young stars are suspected to be the leading disruptive agent which could hinder the life of a molecular

cloud. Although there is strong evidence for the disruptive effects of outflows on "star-forming core scales" ($\sim$ 0.1-0.5 pc), as we will discuss below, there has not been much work on the outflow-cloud interaction at "molecular cloud scales" ($\sim$ 1 pc or more).

1.3.1 Outflow-cloud interaction in the immediate vicinity of the outflow source

Outflows from young stars have a major effect on the outflow source's immediate surroundings. Several studies of young low- and high-mass stars have found kinematical evidence for acceleration of dense core gas by an outflow. These include studies of L1228 (Tafalla & Myers 1997), IRAS 12553 (Olmi, Felli, & Cesaroni 1997), Mon R2 (Tafalla et al. 1997), IRAS 3282 (Tafalla et al. 1993), L1221 (Umemoto et al. 1991), IRAS 16293 (Mizuno et al. 1990), L1251 (Sato & Fukui 1989), Cepheus A (Torrelles et al. 1987), L1551-IRS5 (Moriarty-Schieven et al. 1987a). In particular, the in-depth study of Tafalla & Myers (1997) concludes —from the large velocity shifts observed in the dense gas (see Figure 1.5) and a comparison of the outflow and core energetics— that the L1228 outflow has the potential to disperse the core gas once the outflow phase is over.

Outflows also have dramatic effects on the environment just outside their host core. Optical and/or near-infrared observations often reveal the presence of reflection nebulae coincident with one (or both) molecular outflow lobes (e.g., Figure 1.6). The nebular emission is the result of the scattering of photons, from the young star which powers the outflow, off of cavity walls created by the outflow. Most cavities are seen (in the optical or infrared) to extend less than 0.3 pc from the outflow source, and only a few extend more than 0.5 pc (and are only from high-mass sources), even though the outflow that produced the cavity has a linear extent (in CO) on the sky, much larger than the cavity. Low and high-mass sources which have outflows that have created cavities revealed by reflection nebulae include B5-IRS1 (Yu, Billawala, & Bally 1999, and references therein), B335 (Hodapp 1998), G192.16 (Shepherd et al. 1998), BHR 71 (Bourke et al. 1997) L483

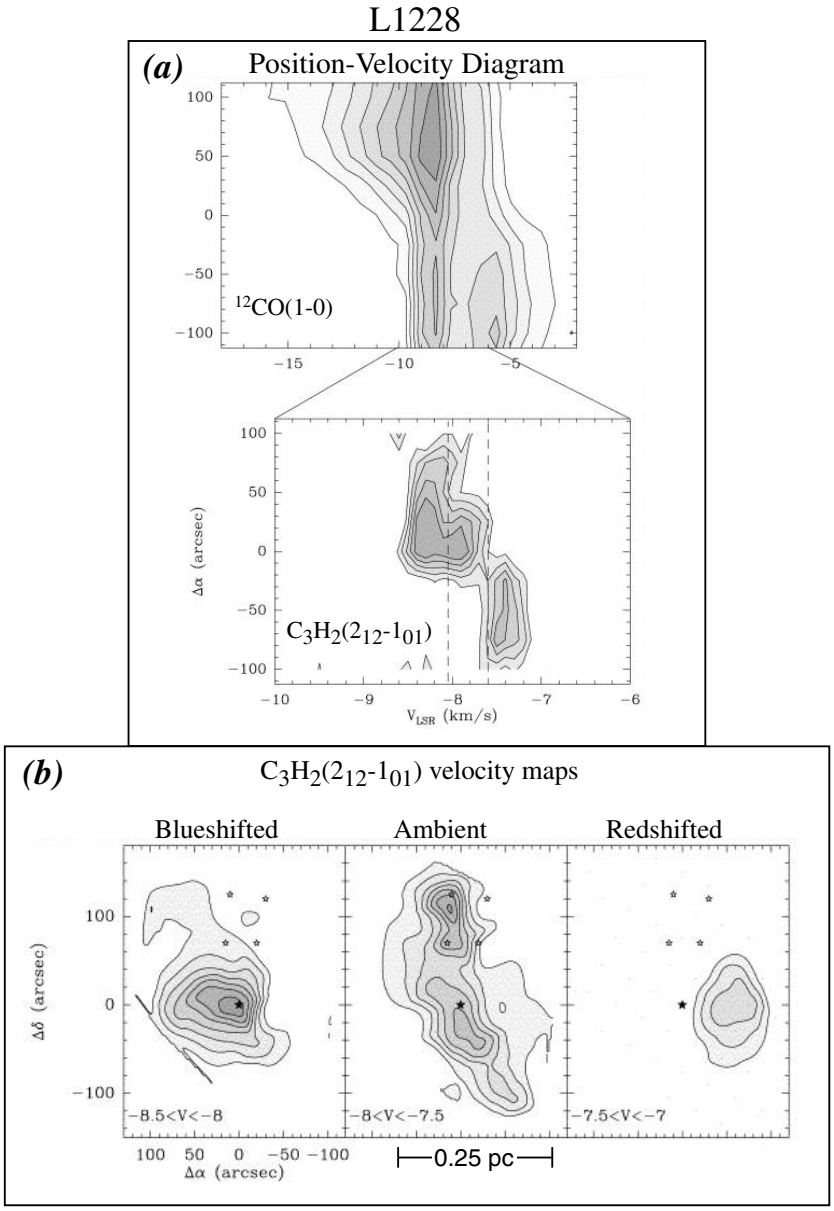

Fig. 1.5.— L1228: example of core disruption by an outflow through kinematical evidence. (*a*) Position-Velocity of the ^{12}CO(1–0) (top) and $C_3H_2(2_{12}–1_{10})$ (bottom) emission in the L1228 molecular outflow region from Tafalla & Myers (1997). Notice how the dense core gas, traced by the $C_3H_2(2_{12}–1_{10})$ emission, shows shift in the line center in the same sense as the ^{12}CO(1–0) outflow. The vertical dashed lines in the C_3H_2 panel represent the blueshifted, ambient, and redshifted velocity regimes. (*b*) $C_3H_2(2_{12}–1_{10})$ velocity maps of the L1228 outflow region from Tafalla & Myers (1997). The three panels represent the blueshifted, ambient, and redshifted velocity regimes. The velocity range of integration is shown on the bottom right corner of each panel. The dense core gas traced by the $C_3H_2(2_{12}–1_{10})$ emission shows a bipolar distribution in the same sense as the ^{12}CO(1–0) outflow. The black star symbol at (0,0) represents the position of the outflow source.

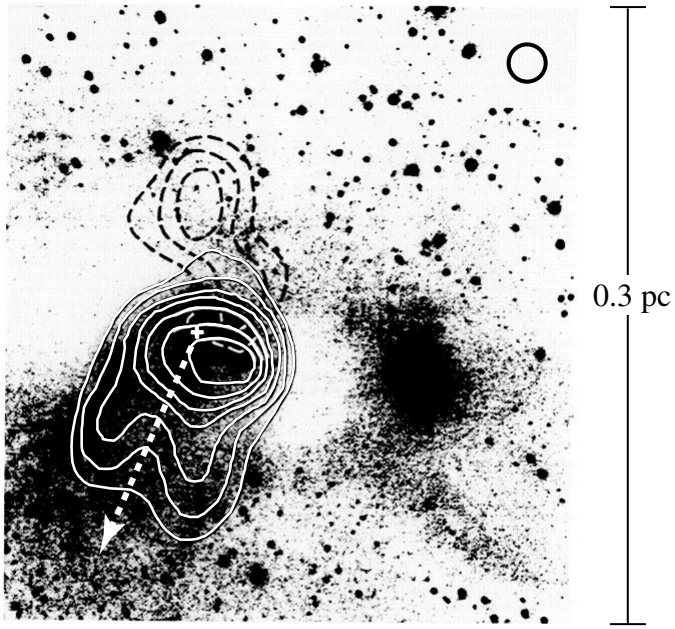

Fig. 1.6.— L43: example of an outflow-created core cavity revealed by the presence of a reflection nebula. ^{12}CO(1–0) integrated intensity contours of the L43 molecular outflow are superimposed on a CCD I band image of the L43 cloud surrounding the outflow source (RNO 91), from Mathieu et al. (1988). The solid line contours represent the blueshifted gas, and the dashed line contours represent the redshifted gas. Notice how the blueshifted lobe coincides with the nebulosity. We show a dashed white line (and arrow) to guide the eye.

(Fuller et al. 1995), L43 (Mathieu et al. 1988), L1551 (Moriarty-Schieven 1987), and GL 490 (Campbell et al. 1986).

Cavities in dark clouds may also be seen as regions of lower extinction (where background stars are seen clearly) outlined by the heavy extinction of the cavity walls. When outflow gas is found in such cavities, it is then presumed that they were formed by the clearing of gas and dust by the outflow. The HH 56/57 region (Reipurth et al. 1997a) is a good example of this (Figure 1.7). In addition, outflow-created cavities can also be detected through molecular line observations of optically thin, medium- and high-density, tracers (Figure 1.8). Examples of outflows that coincide with cavities revealed through molecular line observations include L1551-IRS5 (Moriarty-Schieven & Snell 1988), V366 Cas (i.e., LkHα 192) (Hajjar & Bastien 2000), Mon R2 (Tafalla et al. 1997), HH 34 (Anglada et al. 1995), HH 83 (Bally, Castets, & Duvert 1994), HH 81 (Nakano et al. 1994), SS88-B (White & Fridlund 1992), NGC 1333 (Warin et al. 1996; Langer, Castets, & Lefloch 1996), L1221 (Umemoto et al. 1991) HH1/2 (Martín-Pintado & Cernicharo 1987). Moreover, outflow-created cavities may also be detected through millimeter dust continuum emission observations (see Figure 1.9), like the ones detected in NGC 1333 (Sandell & Knee 2001; Lefloch et al. 1998), and Serpens (Davis et al. 1999).

The recent study of Harvey et al. (2001) shows yet another way of observing the effects of outflows on their environment. Harvey et al. use the near-infrared color excess of reddened background stars (Lada et al. 1994) to investigate the dust distribution of the B335 dense core, which harbors a young stellar object powering a molecular outflow. They find that there is less dust column density (background stars are, on average, less reddened) towards lines-of-sight through the position of the molecular outflow. They conclude that the decrease in extinction towards these lines-of-sights is best described by a hollowed-out cone, which has been cleared out of gas and dust by the outflow.

The interaction of outflows from young stellar objects and the ambient cloud just outside the high-density core does not reveal itself only through cavities. The kinematics of the medium-density ($\sim 10^3$ cm^{-3}) gas, traced by the ^{13}CO emission,

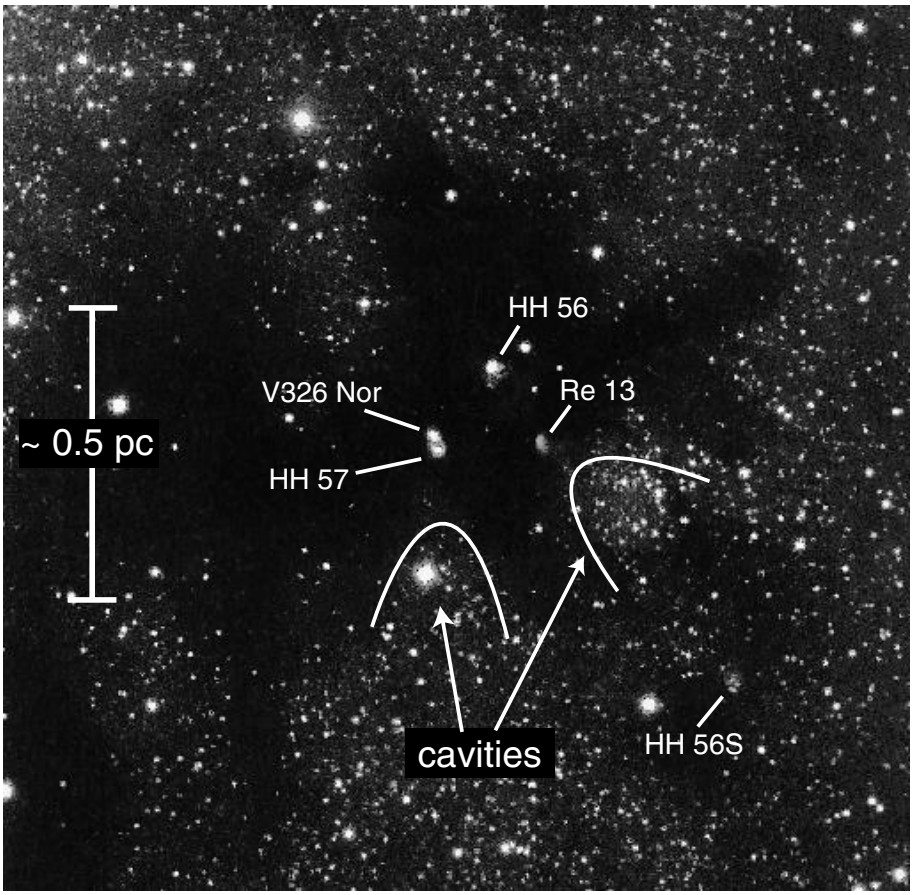

Fig. 1.7.— HH 56/57 region: example of a core cavity created by an outflow, revealed as a region of lower extinction in a dark cloud. The CCD image is from Reipurth et al. (1997a). White (parabolic) lines delineate the two cavities in this region. Each cavity coincides with a molecular outflow. The outflow sources, V326 Nor and Re 13 are identified. The HH knots HH 56 and HH 56S are associated with the outflow from Re 13, and HH 57 is associated with V326 Nor.

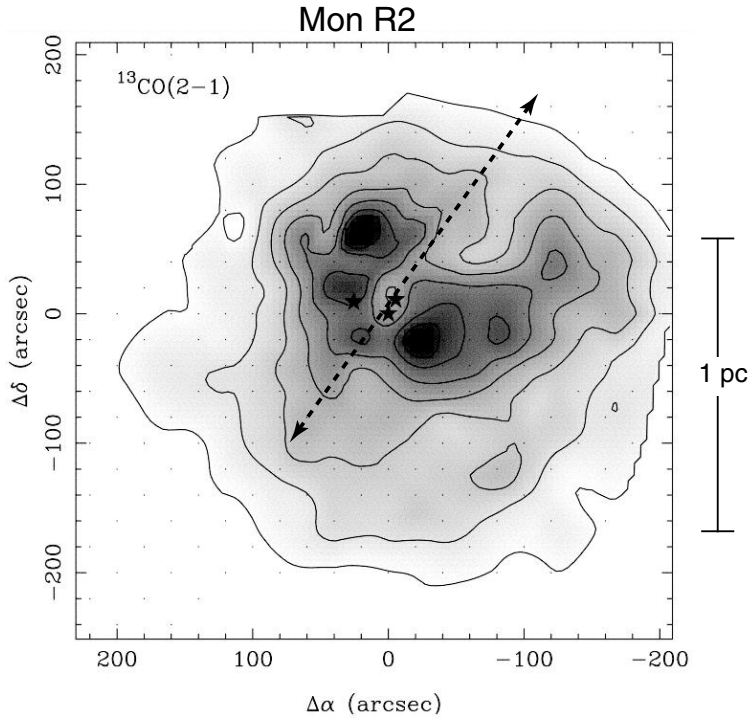

Fig. 1.8.— Mon R2: example of an outflow-created cavity revealed through molecular line observations. Here we show a grey-scale map of the ^{13}CO(2–1) integrated intensity emission from Tafalla et al. (1997). The dashed line indicates the direction of the outflow. The valley in ^{13}CO emission is coincident with the path of the outflow. The outflow has cleared the dense gas near the source, resulting in a decrease in the ^{13}CO(2–1) intensity in the region.

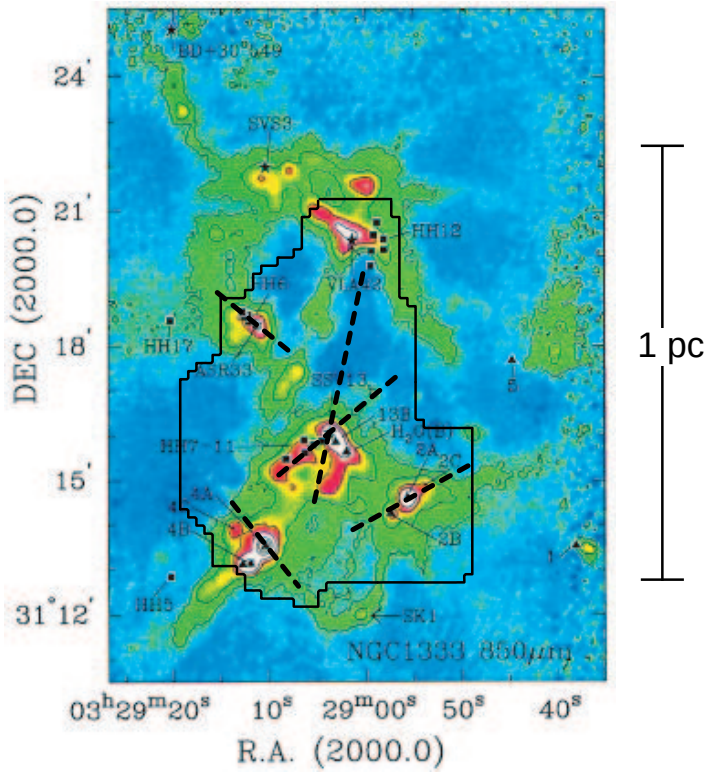

Fig. 1.9.— NGC 1333: example of a region where outflow-created cavities are observed in millimeter continuum emission. The map shown is a 850 μm image from Sandell & Knee (2001). The solid black line delineates the region mapped in ^{12}CO(3–2) by Knee & Sandell (2000). The direction of the outflows (Knee & Sandell 2000) which could be producing the different cavities observed are shown by the dashed lines. The spatial coincidence of outflows and cavities, and the energy of the outflows are consistent with the cavities being formed by the outflows.

may also reveal important aspects of the outflow-cloud interaction. For example, observations of ^{13}CO gas in the region of the L1228 (Tafalla & Myers 1997) and the HH 1-2 (Moro-Martín et al. 1999) outflows shows that in both cases the ^{13}CO has a bipolar distribution with respect to their respective outflow sources, in the same sense as the ^{12}CO outflow (e.g., Figure 1.10). In both cases each ^{13}CO "outflow lobe" extends about 0.3 pc from the source. This indicates that the outflow has been able to accelerate medium-density gas at distances of up to 0.3 pc away from the source.

Statistical studies also show outflows' influence on their host cores. Using a sample of 12 low-mass star cores with outflows Myers et al. (1988) show that there is a high degree of correlation between the outflow momentum and the "core momentum" (the mass of the core times the velocity dispersion of the core gas). This correlation suggests that the outflow might be a critical source of energy feeding the non-thermal core motions of the cores in their samples. In addition, Myers et al. (1988) compare a sample of 12 cores with CO outflows with a sample of 31 cores without CO outflows and find that the velocity dispersion in the cores with CO outflows is significantly (a factor of two) greater than for cores without outflows. The millimeter studies of Anglada, Sepúlveda, & Gómez (1997) —of 15 sources with a range of masses— and Fuente et al. (1998) —of 14 medium-mass sources— suggest that young stars (both low-mass and intermediate-mass) progressively disperse the dense gas around them. For low-mass stars, outflows are the primary candidate responsible for core gas dispersal (Myers et al. 1988). On the other hand, is possible that intermediate-mass stars disperse their surroundings with the help of both outflows and UV photons from the young stars (e.g., Fuente et al. 2001).

Thus, it is abundantly clear that outflows strongly interact with the immediate surroundings of their powering source. It is seen that the outflow-ambient gas interaction may change the space and velocity distribution of the star-forming core and its close environs. By accelerating and moving the gas surrounding the forming stars, outflows could gravitationally unbind the gas in the dense core, stop the stellar mass accretion phase, and help the embedded young star become a naked

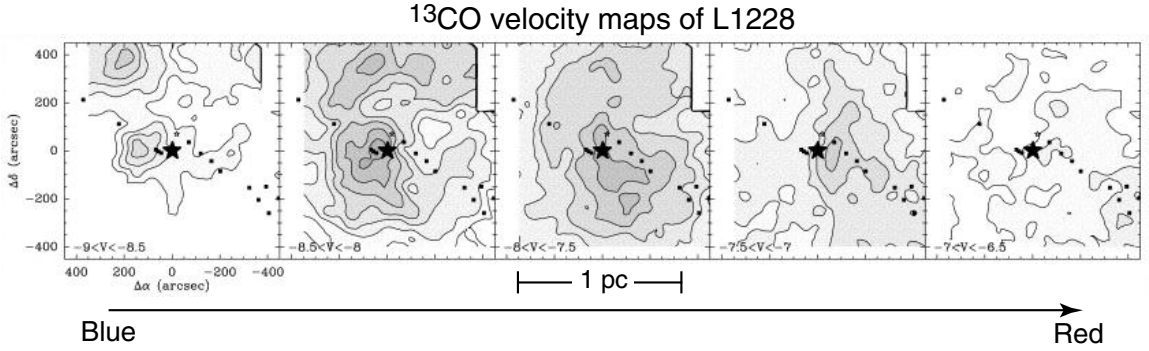

Fig. 1.10.— L1228: example of a ^{13}CO bipolar outflow. Each panel shows a 0.5 km s^{-1}-wide ^{13}CO integrated-intensity map (from Tafalla & Myers 1997). The velocity range of integration of the leftmost panel is $-9 < v < -8.5$ km s^{-1} and that of the rightmost panel is $-7 < v < 6.5$ km s^{-1}. Notice the nice bipolar structure of the ^{13}CO emission. The outflow has been able to accelerate medium-density gas, traced by the ^{13}CO emission, at distances 0.3 to 0.5 pc from the source. The star symbol represents the outflow source and the squares represent the HH knots.

main-sequence star.

1.3.2 Outflow-cloud interaction at parsec scales

The facts that: 1) outflows disrupt their parent core; 2) extend an order of magnitude in scale beyond the core from where they originate; and 3) are very common, make outflows from young stellar objects excellent candidates for being the leading disruptive agent shortening life span of molecular clouds. Yet, even though outflows have the potential to greatly affect their surrounding environment, there is a lack in the study of outflow-cloud interactions at parsec (molecular cloud) scales.

As stated above, the large-scale (unbiased) outflow surveys of Margulis & Lada (1986) and Fukui et al. (1986), were crucial in estimating, for the first time, the kinetic energy input by outflows on whole clouds. Also, they presented the first observational evidence that outflows potentially have an impact on the dynamical state of their host cloud. But, they did not focus their study on the possible disruptive effects of the outflows on the cloud. In addition, the low spatial resolution of the observations (2-3′) could have hampered the possible detection of any outflow-induced change in the cloud structure (i.e., shells and cavities).

Among the first studies of a giant molecular outflow with high-resolution observations is the study of RNO 43 by Bence, Richer & Padman (1996). They studied in great detail the morphology, and kinematics of the outflow, as well as the effects this 5 pc outflow cloud have on its parent cloud. Even though the RNO 43 molecular outflow is highly collimated, the fact that its ejection axis changes over time (presumably due to precession) enables it to affect a large fraction of its parent cloud's volume. Bence et al. conclude that by accelerating and moving gas over such great volume, the RNO 43 flow will surely help disperse its host cloud.

Another interesting outflow-cloud study is that of Fuente et al. (1998b). Their observations of the atomic and molecular gas surrounding the B3 star HD 200775 reveal that the star is located in a biconical cavity of about 1.5 by 0.8 pc. Although

there is no evidence of high-velocity molecular gas in the cavity, the shape of the cavity and the distribution of the molecular gas suggests that it was excavated by a bipolar outflow. Thus, the observations of Fuente et al. (1998b) reveal fossil evidence for the disruptive effects an outflow may have even at parsec-scale distances from its source.

Other high-resolution studies of giant molecular outflows exist (e.g., Cernicharo & Reipurth 1996; Lada & Fich 1996; Yu et al. 1999), but they mainly concentrate on studying the molecular outflow morphology and kinematics, and scarcely deal with the large-scale effects on the cloud.

The lack of large-scale outflow-cloud interaction studies with moderate resolution (less than $50''$) is mostly due to the time-consuming observations needed to conduct a thorough outflow-cloud interaction investigation, which includes mapping not only the outflow, but also a large area surrounding the outflow. The study should also be conducted in more than one molecular line, and good signal to noise ratio. Technological advances in the last 10 years have change this, and now it is possible to map large areas of the sky, with a relatively high spatial resolution, in a reasonable amount of time.

With this thesis we plan to provide a significant contribution in understanding the effects of giant HH flows on their surroundings. One of our central goals is to quantify just how well outflows can contribute to the turbulent energy of their host clouds and/or contribute to cloud disruption.

1.4 What drives molecular outflows?

Soon after the discovery of CO outflows it was established that they must be produced by the entrainment of the ambient cloud gas by an underlying stellar wind. Many molecular outflows have masses larger than their powering young star, by a factor of a few up to an order of magnitude (e.g., Wu, Huang, & He 1996). Thus, it is highly unlikely that the mass in CO outflows comes directly from the forming star and/or the circumstellar disk. Moreover, in monopolar molecular

outflows (and bipolar outflows with a lobe much weaker than the other) it is usually possible to trace the lack or weakness of a lobe on one side of the source due to the deficit of ambient molecular material on that side (e.g., Bally et al. 1994; Chernin & Masson 1995a). Hence, there is little doubt that molecular outflows consist of swept-up material, rather than stellar ejecta.

There are several models which try to explain how a wind emanating from a forming star sweeps-up the ambient gas to form a molecular outflow. The first observations of molecular outflows were limited by poor spatial resolution, and so these early observations suggested that molecular outflows had small length-to-width ratios (i.e., were very poorly collimated). Therefore, the first models that were proposed to explain the nature of molecular outflows used a wide-angle protostellar wind as the driving mechanism (e.g., Barral & Cantó 1981; Königl 1982; Boss 1987; Shu et al. 1991).

Among the different wide-angle wind models, that of Shu et al. (1991) stands out for its simplicity and the fact that it naturally explains the velocity distribution of certain molecular outflows. In this model, the outflow is produced when a momentum-conserving wide-angle wind from a YSO interacts with the ambient gas (see Figure 1.11). The wind power is dependent on polar angle, has a constant velocity and blows into a core with a prescribed radial/angular density profile. The ambient medium is swept up into a shell by a shock in the wind bubble-ambient cloud interface. The molecular outflow is then identified as the molecular gas in the entrained shell.

Masson & Chernin (1992) cast doubts on the Shu et al. (1991) model. They argued that, for "non-extreme" choices of the angular dependence of both the wind power and the core mass distribution, the wide-angle wind model of Shu et al. (1991) would produce too much mass at high velocities, and CO spectra inconsistent with those observed. Masson & Chernin (1992) found that in order for the wide-angle wind model to match observations, the stellar winds needed to be very poorly collimated and the cores needed to be highly flattened with nearly evacuated polar regions, contrary to usual expectations (as shown, e.g., by the

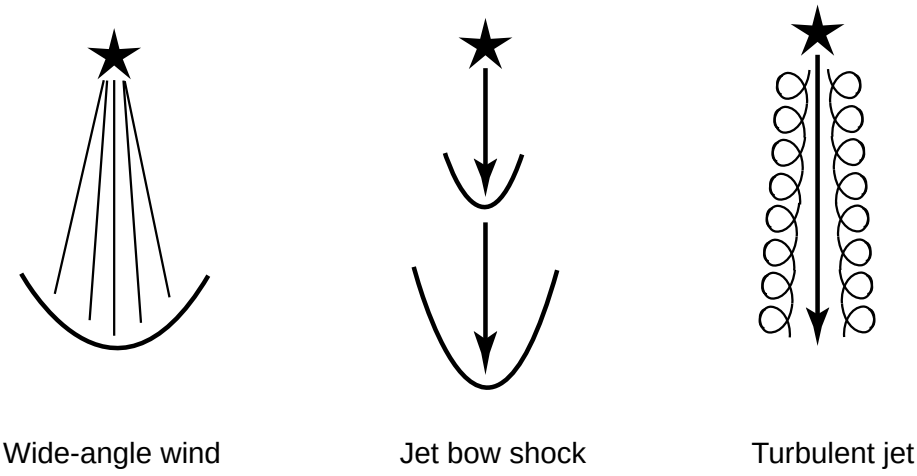

Fig. 1.11.— Schematic illustration of the three most popular entrainment models: wide-angle wind, jet bow shock, and turbulent jet.

study of core shapes by Myers et al. 1991). Also around this time, new models of outflows created by collimated jets (see below) were being proposed, and so astronomers started to pay less attention to the wide-angle wind models. Thus, for some time, the wide-angle wind model became less widely accepted than before.

Later, Shu & Li (1996) found that what Masson & Chernin (1992) had considered "extreme" was naturally encountered in models of magenotocentrifugally-driven stellar winds interacting with a self-similar magnetized cores. Shu & Li (1996) show that indeed the expected molecular outflow cavity shape, the expected mass-velocity and position-velocity relations, and the expected line profile from the wide-angle wind model are consistent with observations. Furthermore, Matzner & McKee (1999) showed that magnetohydrodynamic (MHD) protostellar winds will sweep ambient cloud material into momentum-conserving shells with features commonly observed in molecular outflows, independent of ambient density.

Thanks to recent theoretical and numerical simulation studies (Matzner & McKee 1999; Lee et al. 2000; 2001), the wide-angle wind model has regained its popularity as a possible explanation for the formation of molecular outflows. Wide-angle winds produce wider molecular outflow lobes than bow shock models, and thus can help explain the poor collimation observed in some molecular outflows. The position-velocity distribution predicted for wide-angle wind-driven molecular outflows follows a "Hubble law" —where the outflow velocity is proportional to the distance from the outflow source— which is observed in a number of molecular outflows. And, wide-angle wind models reproduce the outflow mass-velocity relation observed in many molecular outflows (see Chapter 3).

During the 1980's and 1990's, optical and millimeter observations of the environment surrounding YSOs revealed that HH objects and HH jets are, in many cases, coincident with molecular outflows. The positional coincidence of CO outflows and HH flows virtually forced astronomers to consider collimated HH jets as the driving agent of molecular outflows. In principle, a jet could entrain and accelerate ambient gas through a turbulent mixing layer along the edges of the jet (e.g., Cantó & Raga 1991; Stahler 1994; Lizano & Giovanardi 1995), or through

the leading bow shock (e.g., Raga & Cabrit 1993; Stone & Norman 1993a; Masson & Chernin 1993; Stone & Norman 1994; Suttner et al. 1997; Zhang & Zheng 1997; Smith, Suttner, & Yorke 1997; Downes & Ray 1999; Lee et al. 2001) and/or internal bow shocks (e.g., Raga et al. 1993; Stone & Norman 1993b; Suttner et al. 1997; Downes & Ray 1999; Lee et al. 2001).

Turbulent entrainment (see Figure 1.11) is produced by Kelvin-Helmholtz instabilities along the jet-environment boundary which lead to the formation of a turbulent mixing layer that grows into the surrounding ambient gas and into the jet (Cabrit,Raga, & Gueth 1997). The turbulent entrainment models (e.g., Cantó & Raga 1991; Stahler 1994; Lizano & Giovanardi 1995) have not gained popularity as they fail to reproduce important characteristics of many observed outflows. Specifically, turbulent entrainment produces outflows that are highly collimated (length-to-width ratio of more than 10). And, the velocity and momentum distribution of molecular outflows formed through turbulent entrainment is drastically different from what is usually observed. But, even though turbulent entrainment does not seem to be a good model to explain most molecular outflows, it might still be an attractive model for certain peculiar highly collimated CO outflows (e.g., HH 211, Gueth & Guilloteau 1999; NGC 2024, Richer, Hills, & Padman 1992).

In the bow shock model (see Figure 1.11) a highly-supersonic collimated wind or jet propagates into the ambient medium, forming a bow shock surface at the head of the jet. The jet will carve its way into the cloud, and the bow shock will move away from the star, interacting with the ambient gas, thereby producing a molecular outflow around the jet. Velocity variations in the jet produce bow shocks along the body of the jet, also referred to as "internal working surfaces" (e.g., Raga et al. 1990; Raga & Kofman 1992; Cantó, Raga, & D'Alessio 2000), which can also help entrain ambient gas.

Observational findings have made the bow shock (a.k.a. "prompt") entrainment model a very attractive one. In many cases bow-shaped HH knots are observed *along* the axis of the molecular outflow (e.g., Bence et al. 1996; Davis et al. 1997;

Yu et al. 1999; Davis et al. 2000). In such cases, the CO shows a local acceleration at the position of the HH knots (see Figure 1.12) which suggests that this is where the entrainment is taking place. Also, in some cases the morphology of the CO outflow and that of shock-enhanced molecules, like SiO, resembles that of a bow-shock (see Figure 1.13; Gueth, Guilloteau, & Bachiller 1998). Moreover, bow shock entrainment models can easily reproduce the mass-velocity relation and the velocity distribution observed in many molecular outflows (e.g., Lee et al. 2001).

Recent high spatial resolution studies of molecular outflows (e.g., Richer, Hills, & Padman 1992; Bence, Richer, & Padman 1996; Cernicharo & Reipurth 1996; Lada & Fich 1996; Davis, Smith, & Moriarty-Schieven 1998; Shepherd et al. 1998; Gueth & Guilloteau 1999; Yu et al. 1999; Davis et al. 2000; Lee et al. 2000) have made it possible to start testing the different models with the observations. In addition, they have provided significant constrains on the physical parameters of outflows and the entrainment mechanism. Yet, there is still no consensus on which entrainment mechanism best describes all molecular outflows or even if a single mechanism *can or should* explain all outflows.

There exist the possibility that a stellar wind could interact with the ambient cloud through more than one entrainment mechanism during the young star's mass outflow stage. The efficiency with which one or another mechanism can entrain the ambient gas may depend on the ratio of the wind density to the ambient density (e.g., De Young 1986). It has been suggested that the interaction between a stellar wind and the ambient medium might change over time, so the entrainment mechanism might depend on the evolutionary stage of the outflow (e.g., Bachiller 1996; Richer et al. 2000). Or, more than one mechanism might be working at the same time. For example, Shang et al. (1998) demonstrate that the density enhancement in the axis of magnetohydrodynamic (MHD) wide-angle winds (in the X-wind model of Shu et al. 1995) may be interpreted as a "jet". Thus, it could be that both a wide-angle wind and a jet coexist, and that they both contribute to the entrainment process. If multiple mechanisms operate, then the detection of different mechanisms depends on the nature of the observations, and the entrainment efficiency of one mechanism over the others.

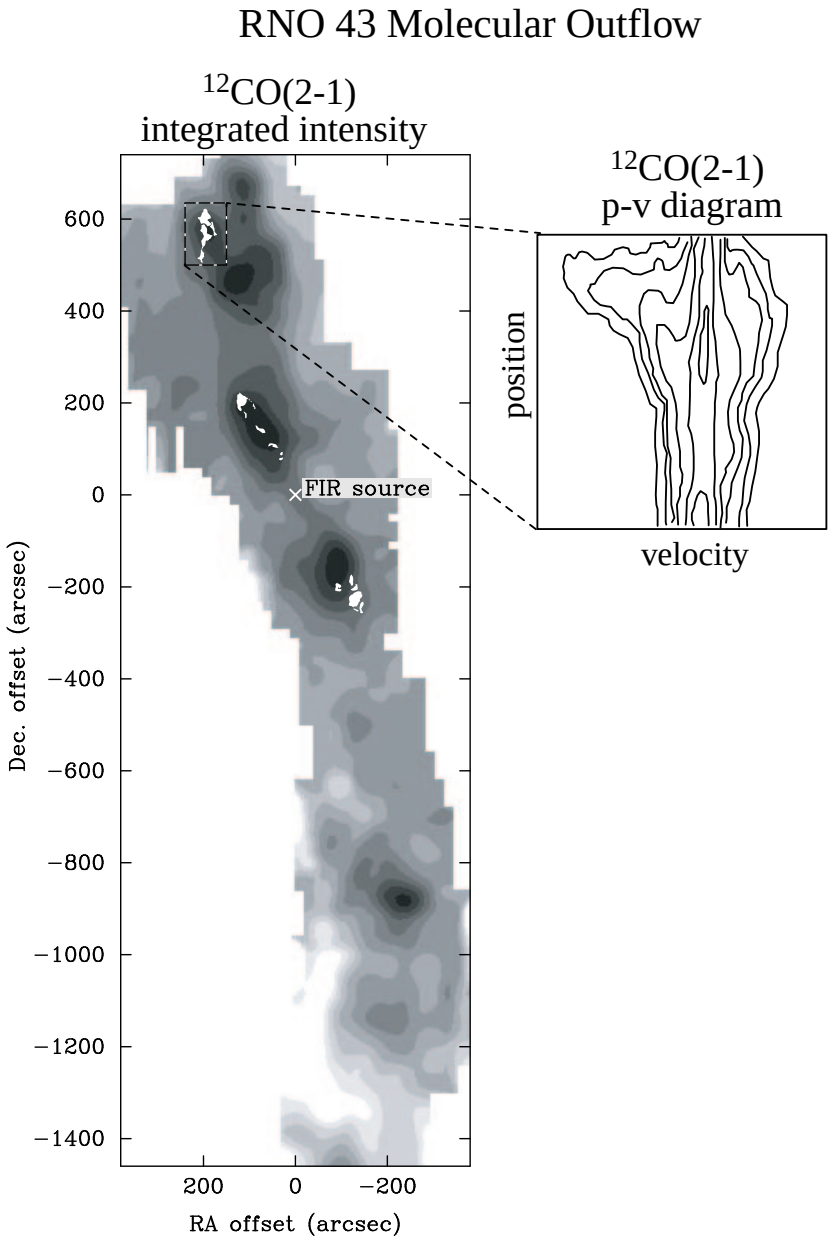

Fig. 1.12.— RNO 43: Example of a bow-shock entrained molecular outflow, inferred from the outflow kinematics and morphology. *Left.* Grey-scale map showing the ^{12}CO(2–1) integrated intensity, with solid white patches representing the Hα knots. The outflow source is also shown. *Right.* ^{12}CO(2–1) position-velocity diagram of the marked region surrounding the northernmost Hα knot. Notice the "Hubble-like" wedge (or spur) in the $p-v$ diagram, with the peak in velocity coincident with the head of the Hα knot. Figures and data from Bence et al. (1996), and Richer et al. (2000).

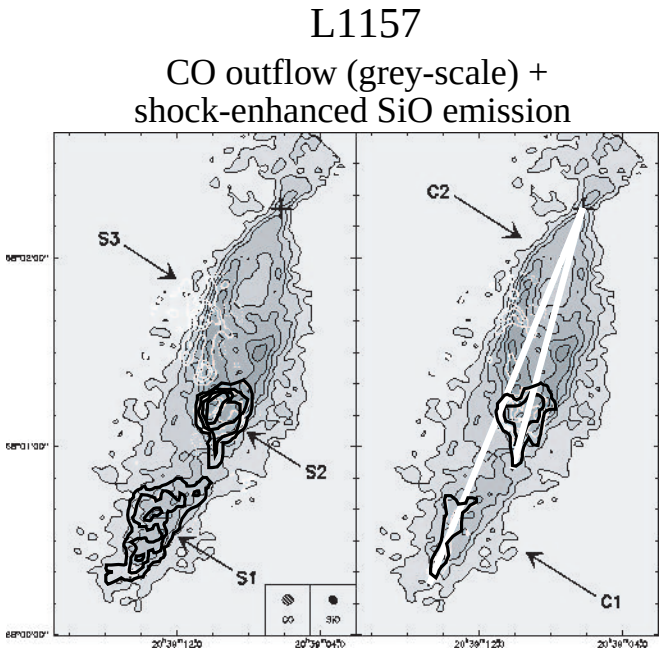

Fig. 1.13.— L1157: Example of a bow-shock entrained molecular outflow, inferred from the outflow chemistry. In both panels the grey-scale maps represent the ^{12}CO(1–0) outflow integrated intensity. *Left.* We highlight, in thick black lines, selected contours of the SiO integrated emission. Here the SiO is integrated over all velocities. *Right.* Blueshifted SiO emission in thick black contours. The thick straight white lines trace the trajectory of two mass ejection episodes which produced the two bow shocks. Figure based on data from Gueth et al. (1998).

Clearly, high-resolution studies of more molecular outflows are needed in order to better understand the entrainment mechanism(s), and further constrain the theoretical and numerical models!

1.5 Brief discussion of shocks

As described above, molecular outflows are mainly driven by shocks formed by the interaction of a highly supersonic stellar wind and the surrounding ambient molecular cloud. Thus, it is worthwhile to include a brief discussion of shocks here. For a more thorough and in depth discussion of interstellar shocks see McKee & Hollenbach (1980), Shull & Draine (1987), Draine & McKee (1993).

1.5.1 Properties of shocks

A shock wave in the interstellar medium is formed when a violent event produces a local increase in the pressure large enough to generate a supersonic compressive motion (McKee & Hollenbach 1980). Such a disturbance in the interstellar medium could be caused by, for example, a fast stellar wind or a supernova explosion. The supersonic disturbance travels at a velocity larger than the signal velocity of the medium (i.e., the sound speed) and so the region in front of a shock does not know of the existence of the shock until the shock arrives. Upon the arrival of the supersonic disturbance, the affected region will be compressed, accelerated and heated.

Following we discuss the basic physical properties of shocks. For purpose of simplicity we assume a plane-parallel "stationary" shock (where stationary means that we can choose a frame of reference in which the shock is stationary). Further, we assume that the shock is purely hydrodynamic (i.e., no magnetic fields present).

The physics of the flow in and out of a shock (see Figure 1.14) are governed by conservation principles. The equations relating the upstream and downstream flow variables are given by the integrated time-independent mass, momentum and

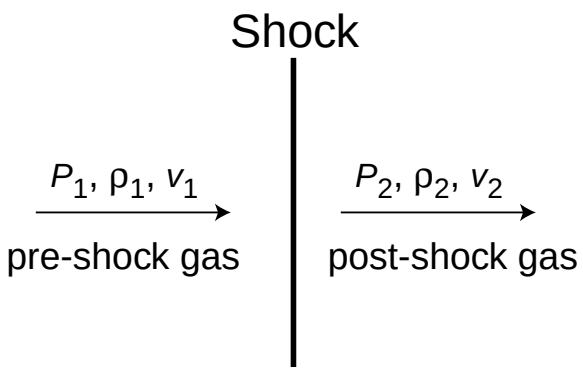

Fig. 1.14.— Variables on either side of a plane-parallel shock in a reference frame where the shock is stationary.

energy conservation equations (also known as the "jump" conditions):

$$\rho_1 v_1 = \rho_2 v_2 \text{ (mass flux conservation)} \tag{1.1}$$

$$P_1 + \rho_1 v_1^2 = P_2 + \rho_2 v_2^2 \text{ (momentum flux conservation)} \tag{1.2}$$

$$\frac{1}{2}v_1^2 + \frac{\gamma}{\gamma-1}\frac{P_1}{\rho_1} = \frac{1}{2}v_2^2 + \frac{\gamma}{\gamma-1}\frac{P_2}{\rho_2} \text{ (conservation of specific total energy)} \tag{1.3}$$

Here v, ρ, P, and γ are the velocity, density, pressure and ratio of specific heats of the gas. Variables with a subscript of 1 are for gas ahead of the shock front, and those with a subscript of 2 are for gas behind the shock front (see Figure 1.14). In Equation 1.3 we assume that the internal energy of the gas (u) is related to the gas pressure by $u = P/(\gamma - 1)$.

Solving the jump condition equations (see Dyson & Williams 1997 for a simple step-by-step example) shows that shocks are compressive (see Figure 1.15). That is, the gas just behind the shock front (the post-shock gas) has a higher pressure, density, and temperature, than the gas in front of the shock (the pre-shock gas). This sudden change in density, temperature and pressure (see Figure 1.15) is refereed to as a "J-shock" (jump shock). Another general result is that the post-shock gas compression increases with Mach number (M), where $M = v_1/c_{s_1}$ (and c_{s_1} is the pre-shock gas sound speed). In the special case of a strong shock wave, where $M >> 1$, then:

$$\frac{\rho_2}{\rho_1} = \frac{v_1}{v_2} = \frac{\gamma+1}{\gamma-1} \tag{1.4}$$

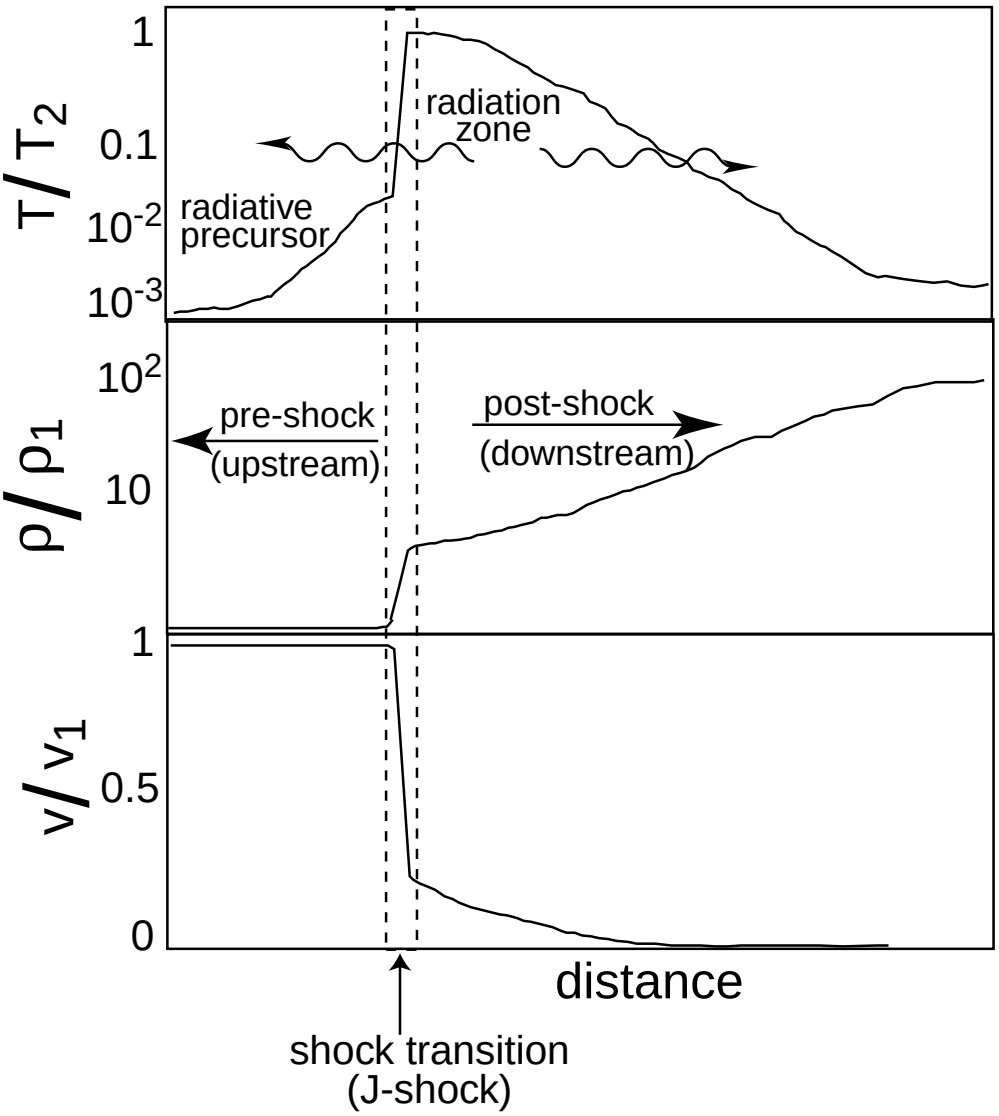

Fig. 1.15.— Plots showing the schematic behavior of the temperature, density and velocity of gas influenced by a strong shock wave. T_2 is the temperature just behind the shock wave, ρ_1 is the density of the pre-shock gas, and v_1 is the pre-shock gas velocity (in the rest frame of the shock). This figure is based on Figure 1 of Draine & McKee (1993).

$$P_2 = \frac{2\rho_1 v_1^2}{\gamma + 1} \tag{1.5}$$

And, assuming we are dealing with an ideal gas, where $P = \rho kT/\mu_s$, then:

$$kT_2 = \frac{2(\gamma - 1)}{(\gamma + 1)^2}\mu_s v_1^2 \tag{1.6}$$

where k and μ_s are Boltzmann's constant and the mean mass per particle just behind the shock front, respectively. In the (typical) case of gas with $\gamma = 5/3$, then Equations 1.4, 1.5, and 1.6 result in 4, $3\rho_1 v_1^2/4$, and $3\mu_s v_1^2/16$, respectively.

In the case where the shock is produced by the interaction of a young stellar wind and the ambient medium it is usually more convenient to consider a frame of reference where the star is stationary and the shock is moving. To obtain the desired quantities in the rest frame of the star one only has to make the proper simple transformations:

$$v_1 = v_{o,1} - V_s \tag{1.7}$$

$$v_2 = v_{o,2} - V_s \tag{1.8}$$

where $v_{o,1}$, $v_{o,2}$ are the pre-shock and post-shock gas velocities in the rest frame of the star, and V_s is the shock velocity. Usually, $v_{o,1} \sim 0$, or $V_s >> v_{o,1}$. So, from equation 1.4 (and using $\gamma = 5/3$), then $v_{o,2} \approx (3/4)V_s$. Hence, it can be seen that (if $V_s >> v_{o,1}$) the post-shock gas will move in the same direction as the shock and will be accelerated to 0.75 times the shock velocity.

In a strong shock, most of the kinetic energy of the gas is converted to heat. The heated gas will radiate, and thus it will eventually cool. As the gas cools behind the shock, its density will increase further (see Figure 1.15). If the post-shock gas cools by radiation emission on a short timescale compared to cooling by adiabatic expansion, the shock is said to be a "radiative shock". Shocks formed by the interaction of a collimated stellar wind from a young star (i.e., the shocks that produce Herbig-Haro objects) fall under the category of radiative shocks.

From Equations 1.6 and 1.7, and the fact that $V_s >> v_{o,1}$, we can see that the temperature of the post-shock gas depends mainly on the shock velocity. The temperature of the post-shock gas will determine the radiation process

which will dominate downstream of the shock front. For example, a shock with $V_s \sim 100$ km s^{-1} will be more than enough to heat the gas to temperatures high enough to ionize hydrogen (i.e., $3kT_2/2 > 13.6$ eV). And so the post-shock gas, as it cools will radiate hydrogen recombination lines. Similarly, a strong shock ($V_s \gtrsim 100$ km s^{-1}) could, for example, double-ionize oxygen atoms. In such case, as the post-shock gas cools and becomes denser, different oxygen ion species will lie in "well-defined cooling zones" (Hartigan et al. 2000), that is: OIII lines will be found right behind the shock, followed by OII lines, which will be followed by OI lines. Even though sound waves will not alert the pre-shock gas of the incoming shock, the radiation from the post-shock gas will. This radiation (also called a radiative precursor) will excite, and could even ionize some of the pre-shock gas, depending on the shock velocity.

1.5.2 Shocks with Magnetic Fields

If we now add a magnetic field to the shocked medium, our previous simple picture is slightly modified. In the interstellar medium, magnetic fields are coupled (or "frozen") to the gas. So, when interstellar gas is compressed by a shock wave, the magnetic field is also compressed. This disturbance in the magnetic filed will create magnetic waves which may propagate ahead of the shock (i.e., magnetic precursor) and excite ions present in the pre-shock gas. The ions will then collide with the neutral components of the gas, and so the pre-shock gas could be heated even before the shock front arrives. If the shock is strong enough, then the magnetic precursor could eliminate the sudden ("discontinuous") jump in temperature and density (the J-shock) and instead could produce a smooth increase in density and temperature (also known as a C-shock). In addition, if magnetic fields are present then some of the energy that would otherwise have gone solely to increase the temperature of the post-shock gas will be used to compress the magnetic field. Thus, for a given shock velocity, when magnetic fields are present the post-shock gas temperature will be lower than for purely hydrodynamic shocks.

1.5.3 Bow shocks in collimated winds from young stellar objects

The region where a collimated wind from a YSO interacts with the ambient medium (also known as a working surface) has two shocks (see Figure 1.16). One is the jet shock (also known as the Mach disk), where the fast jet material is decelerated as it impacts the slower shocked material. The other shock is the ambient shock, where the shocked material impacts, and accelerates, the quiescent gas. The shocked gas will flow (or squirt) towards the sides of the jet shock and some of the energy released will be transformed into thermal energy (Masson & Chernin 1993). The exact amount of thermal energy will depend on the cooling efficiency of the post-shock gas (e.g., Chernin et al. 1994). The "squirted" shocked gas will push the ambient material, forming a low-density cocoon (see Figure 1.16). The cocoon walls will then form a bow-like shell around the jet head made up of swept-up ambient material.

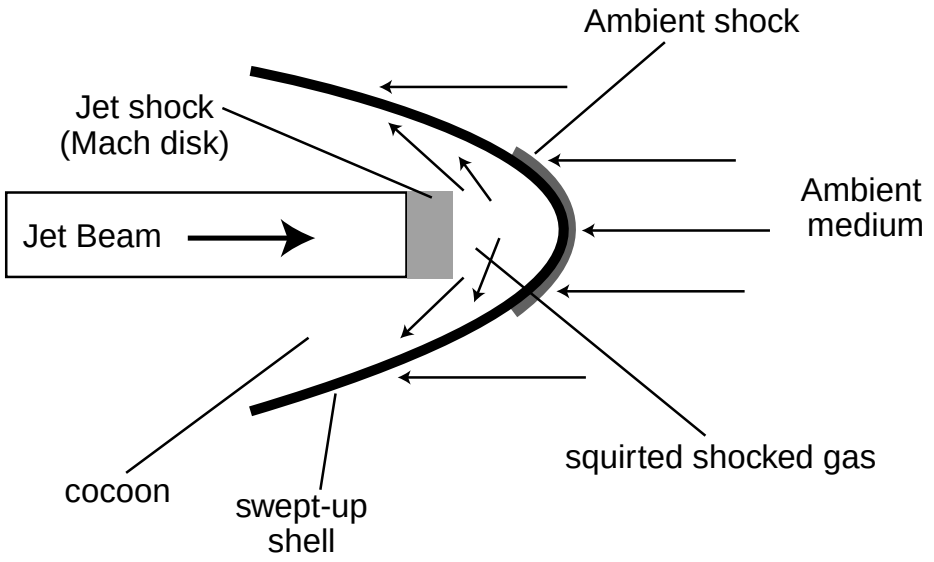

Fig. 1.16.— Schematic illustration a bow shock formed by the interaction of a jet from a young stellar object and the ambient medium.

1.6 Why this Thesis?

It has become clear that giant (parsec-scale) HH flows are common amongst young stars of all different masses. As explained above, the prevalence and properties of the flows give young stars the potential to inject energy into their parent molecular clouds *even at parsec-scale distances* and/or to disrupt clouds on large scales. The specific effects that giant HH flows have on their clouds need further, more detailed, investigation. The goal of this thesis is to study the giant outflow-cloud interaction in order to better understand the effects that these giant HH flows have on their parent clouds.

Most of the outflow momentum from young stellar flows is deposited in molecular outflows. Thus, the best way to investigate the effects of giant HH flows on their cloud is through millimeter observations of the molecular gas surrounding the HH flow. Molecular line observations do not suffer from extinction, like optical and near-infrared observations, and so even very deeply embedded objects may be studied. In addition, molecular line observations come with velocity information, which is essential for studying the kinematics of the gas.

In order to study the effects an outflow has on its environment's kinematic and density structure, it is imperative to observe a large area of the cloud gas surrounding the outflow, in addition to the outflow itself. The observations should preferably be of more than one molecular line transition, probing a range of densities, and at least one of the lines should be relatively optically thin, in order to take line opacity into account. The observations should be of relatively high spatial resolution, in order to detect possible peculiar structures in the cloud caused by the outflow. High spatial resolution observations may also be used to study the entrainment mechanism that produced the molecular outflow. Also, if one is to avoid source confusion, one should study regions with a very low density of young stellar objects.

Recent advances in the technology of millimeter wave observation techniques have made it possible to image large areas on the sky in a relatively short time,

with moderate spatial resolution (less than $1'$). These key new techniques include on-the-fly (OTF) mapping, and observing with a focal plain array receiver. A telescope in OTF mode moves across the source at a constant speed while taking data at a constant rate (see Figure 1.17). In OTF mode the telescope does not need to point to an OFF (or reference) position every time data at the source (or ON position) are taken, like conventional position-switching observing mode. Instead, when observing in OTF mode, the observer may choose how often an OFF is observed, for example every other row of the OTF map.

Another recent technological advancement that has helped radio astronomers is the installment of focal plane array receivers on mm-wave telescopes. A focal plane array allows the observer to obtain several spectra (one for each receiver in the array) each time the telescope points and integrates at a given position.[2] Both OTF-mode mapping and receiver arrays have made possible to observe large outflows and their parent clouds in more than one molecular line, in a timely and efficient manner, which is essential to the study of the outflow-cloud interaction. For example, a Nyquist (half-beam) sampled $5'.5$ by $5'.5$ map, with a telescope beam of $\sim 46''$, obtained using conventional (single-receiver) position-switching mode would require at least a factor of 4 more time than if it were done using a single receiver in OTF mode, and a factor of 16 more time if done in position-switching mode with a 16-receiver array. In addition, improvement in the telescope's backends has made possible high spectral resolution observations, with a broad spectral bandwidth at the same time.[3]

[2]The first millimeter-wave 15-element focal plane array, QUARRY, became available at the Five College Radio Astronomy Observatory (FCRAO) in 1991 (Erickson et al. 1992), and its far superior successor (with a factor of four improvement in receiver noise), the 16-element array named SEQUOIA (used in this thesis), came on line in 1998 (Heyer et al. 2000). SEQUOIA is currently advertised as "the world's fastest 3 mm imaging array".

[3]Radio telescopes are now equipped with fast autocorrelators, which can be set to a variety of bandwidths and resolutions. For example, the Focal Plane Array Autocorrelator Spectrometer (FAAS) installed in the FCRAO 14 m telescope has the option of observing at a spectral resolution of 24 kHz, with a bandwith of 20 MHz, which at the frequency of the ^{13}CO(1–0) line equates to a velocity resolution of 0.06 km s^{-1} and a velocity range of 55 km s^{-1}.

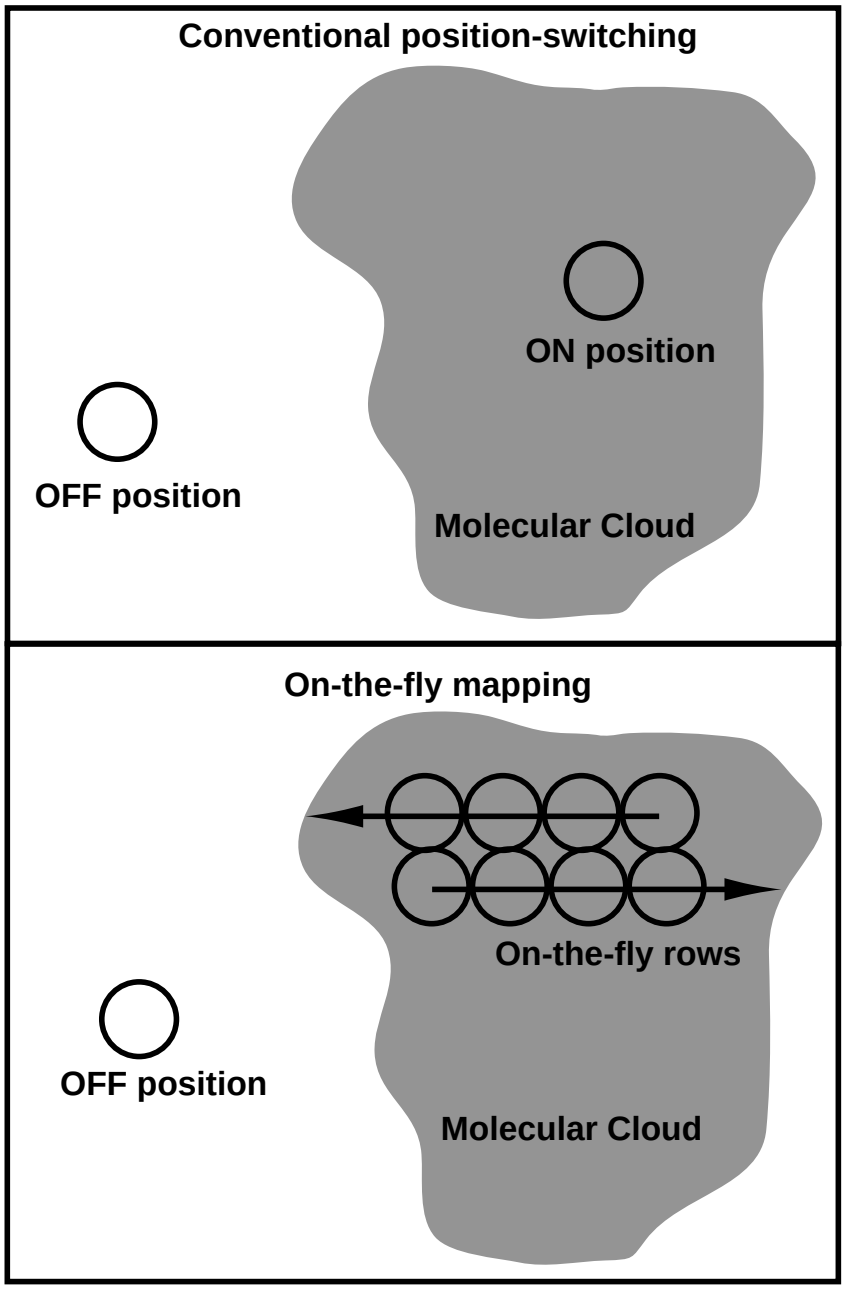

Fig. 1.17.— Cartoon figure of the on-the-fly (OTF) mapping technique. The upper panel show the conventional position switching observing mode. Here every time an ON is observed, a reference (OFF) position needs to be observed. The lower panel shows how the OTF mapping technique works. A telescope in OTF mode moves across the source at a constant speed while taking data at a constant rate. An OFF position may be observed, for example, every other row. Still, the time between consecutive OFFs should be relatively short in order to minimize atmospheric variations between OFFs.

Table 1.1. Molecular Outflows and Parent Cloud Observations in Thesis

Molecular Line	Telescope	Resolution[a] [″]	Sources Studied	Mapped Region
^{12}CO(2–1)	NRAO 12 m	27	HH 300, HH 315	Outflow
^{12}CO(1–0)	FCRAO 14 m	45	HH 300, HH 315	Outflow/Cloud
^{13}CO(1–0)	FCRAO 14 m	47	HH 300, HH 315	Outflow/Cloud
^{12}CO(2–1)	IRAM 30 m	11	HH 315	HH knots
^{12}CO(1–0)	IRAM 30 m	21	HH 315	HH knots
^{13}CO(1–0)	IRAM 30 m	22	HH 315	HH knots

[a]Telescope's half power beam size for the given spectral line.

1.7 Thesis Plan

Using the techniques described above we mapped a large extent of the molecular gas surrounding two giant HH flows at moderate angular resolution (see Table 1.1, and Figure 1.18). We also performed higher spatial and velocity resolution observations of the gas immediately surrounding the HH knots of one of the outflows.

The two giant HH flows mapped were HH 300, from the young star IRAS 04239+2436, and HH 315, from the young star PV Ceph. These HH flows were chosen because: 1) of their parsec-scale sizes; 2) they were both discovered in the same giant HH flow study by Reipurth et al. (1997c); and 3) spectra of some of the HH knots in both flows exist (Reipurth et al. 1997c; Devine 1997).

The ^{12}CO(2–1) observations (see Table 1.1, and Figure 1.18) were aimed at studying the morphology and kinematics of the molecular outflow. The goal of the large scale ^{12}CO(1–0) and ^{13}CO(1–0) observations (see Table 1.1, and Figure 1.18) were to study the outflow in context with their parent molecular cloud, and their surroundings. With these observations we studied the effects the outflows have on the structure and kinematics of the ambient cloud, on large scales. In addition, we were able to use the $J = 1 - 0$ lines to correct for the ^{12}CO velocity-dependent

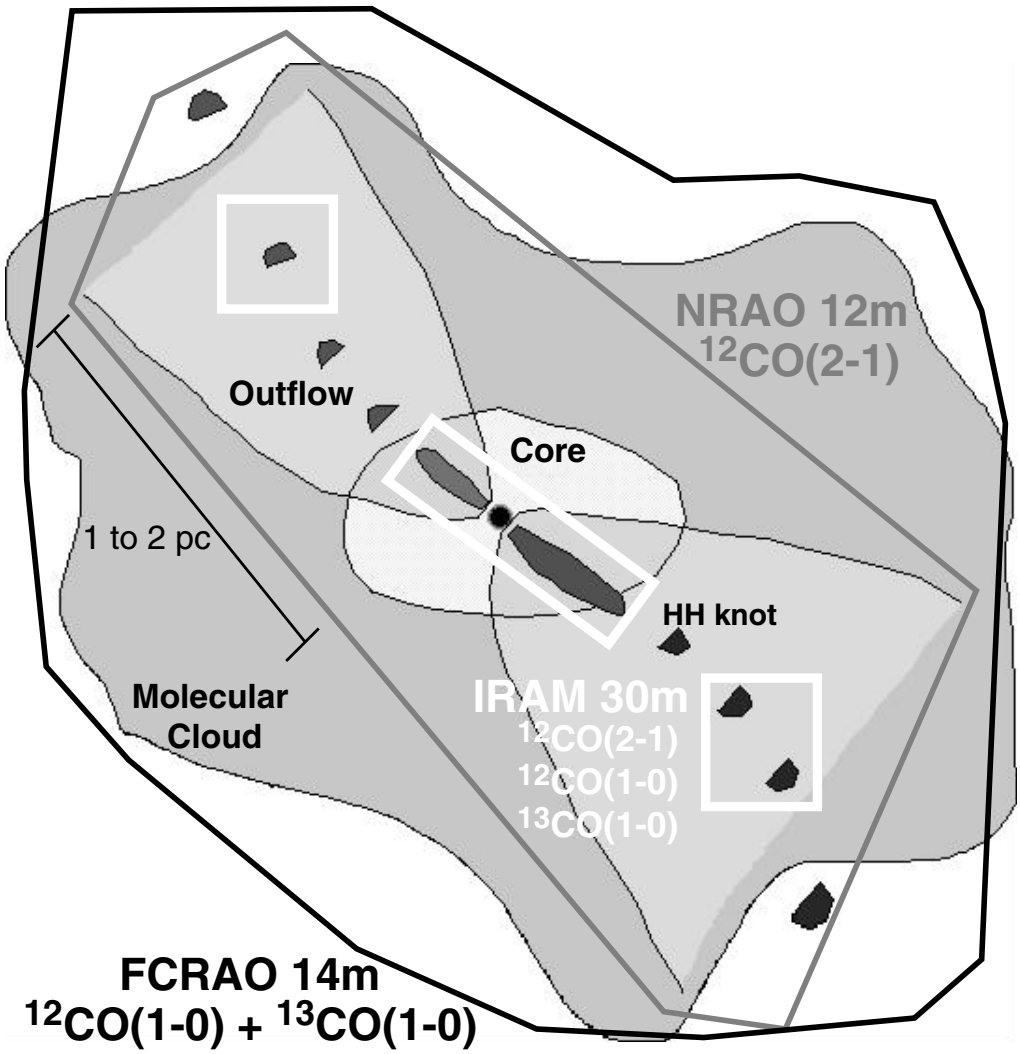

Fig. 1.18.— Schematic representation of thesis observations. The figure shows an HH flow, which forms a molecular outflow, inside a cloud. Each color indicates the different regions mapped using different telescopes, and different molecular lines (see Table 1.1).

opacity, which is extremely important for obtaining accurate estimates of the outflow physical parameters. By observing the molecular gas close to some of the HH knots of HH 315 (see Table 1.1, and Figure 1.18) at relatively high spatial resolution we were able to study the morphology and structure of the outflow in detail, and to investigate the entrainment mechanism that produced the molecular outflow.

In the next chapter (Chapter 2), we present our detailed study of the molecular outflow produced by the HH 300 flow and its effect on its surroundings. In Chapter 3, inspired by our results from the HH 300 study, we discuss the effects of outflow episodicity on the mass-velocity and position-velocity relations in molecular outflows. Chapter 4 is dedicated to the study of the effects of the HH 315 flow on its parent cloud. In the subsequent chapter (Chapter 5), we present our high-resolution study of the entrainment mechanisms at work in the HH 315 flow. In Chapter 6 we use our results and those of previous studies to draw general conclusions about: 1) the effects of giant outflows on their cloud; 2) the entrainment mechanism; 3) outflow episodicity; and 4) time-varying ejection angles in outflows. Chapter 7 offers a summary of our results and conclusions, and a list of possible future work.

Chapter 2

The Episodic, Precessing Giant Molecular Outflow from IRAS 04239+2436 (HH 300)

ABSTRACT

We present the first set of detailed molecular line maps of the region associated with the giant Herbig-Haro flow HH 300, from the young star IRAS 04239+2436. Our results indicate that the red lobe of the HH 300 flow is depositing a fair amount of momentum (3.2 $(\sin i)^{-1}$ $M_\odot$ km s^{-1}) and kinetic energy (2.6 $(\sin i)^{-2} \times 10^{43}$ erg) over a notable volume ($\sim 11\%$) of its host dark cloud. This makes HH 300 a key player in the evolution and fate of its parent cloud. The redshifted molecular outflow lobe of HH 300 is 1.1 pc long and 0.3 pc wide, and has a very clumpy structure. The density, velocity, and momentum distributions in the outflow indicate that the observed clumps arise from the prompt entrainment of ambient gas. Bow shock-shaped structures are associated with the clumps, and we hypothesize that the shocks are produced by different mass ejection episodes. Lines drawn from IRAS 04239+2436 to each of these clumps have different orientations on the plane of the sky, and we conclude that HH 300 is a precessing and episodic outflow.

Published in: *The Astrophysical Journal*, 554, 132–151, 2001 by H. G. Arce & A. A. Goodman

The observations include a map of the red lobe in the ^{12}CO(2–1) line, with a beam size of 27″, and more extended maps of the outflow region in the ^{12}CO(1–0) and ^{13}CO lines, with 45″ and 47″ beam sizes, respectively. Due to "contamination" by emission from another molecular cloud along the same line-of-sight, we are not able to study the blueshifted lobe of HH 300. The combined ^{12}CO(1–0) and ^{13}CO line observations enable us to estimate the outflow mass accounting for the velocity-dependent opacity of the ^{12}CO(1–0) line. This method is much more precise than using ^{12}CO data alone. We obtain a steep power-law mass spectrum for HH 300, which we believe is best explained by the evolution of the outflow mass kinematics. In addition, our ^{13}CO observations show that the HH 300 flow has been able to redistribute (in space and velocity) considerable amounts of its surrounding medium-density ($\sim 10^3$ cm^{-3}) gas.

2.1 Introduction

A Herbig-Haro (HH) object is a nebulous knot which delineates the shock arising from the interaction of a high-velocity flow of gas ejected by a young stellar object (YSO) and the ambient medium. A chain of these HH objects (or knots) is usually referred as an HH flow. Recently, it has been found that very long —parsec-scale— HH flows exist, and that they are quite common (Reipurth, Bally, & Devine 1997, hereafter RBD). This has sparked major interest on the impact of these energetic mass flows on their environment, in particular the relation between optical jets and molecular outflows and the physics of the entrainment mechanism. Giant HH flows have sizes about an order of magnitude larger than the cloud cores from which they originate, and many are found to extend to distances well outside the boundary of their parent dark cloud (RBD). One or more shocks associated with the same flow can accelerate the entrained gas to velocities greater than those of the quiescent cloud, transferring momentum and energy into the molecular cloud, and thus producing a molecular outflow. The colossal size of a giant HH flow enables it to entrain molecular material at parsec-scale distances from the source, and thus it may affect the kinematics and density of a substantial volume of its

parent molecular cloud.

Although several models try to explain the entrainment mechanism that forms molecular outflows (e.g., Shu et al. 1991; Masson & Chernin 1993) and other numerous theoretical works investigate the effects YSO outflows have on their environment (e.g., Norman & Silk 1980; Raga, Cantó, & Steffen 1996; Matzner & McKee 2000), there has yet to be a consensus reached on these issues. On the observational front, recent high-resolution studies of molecular outflows (e.g., Bence, Richer, & Padman 1996; Cernicharo & Reipurth 1996; Lada & Fich 1996; Davis et al. 1997; Yu, Billawala, & Bally 1999, Lee et al. 2000) have provided significant new constraints on the physical parameters of outflows and the entrainment mechanism.

In order to study the effects an outflow has on its environment's kinetic and density structure, it is imperative to observe a large area of the cloud gas surrounding the outflow, in addition to the outflow itself. The observations should preferably be of more than one molecular line transition, probing a range of densities, and at least one of the lines should be relatively optically thin, in order to take line opacity into account. In this paper, we present new ^{12}CO(2–1), ^{12}CO(1–0), and ^{13}CO observations of the HH 300 outflow, its surroundings and a large fraction of its parent dark cloud.

The HH 300 flow was discovered, in the optical, by RBD. HH 300 is located in the westernmost region of the B18 molecular cloud (usually called B18w) in the Taurus cloud complex. The B18w region, also called IRAS core Tau G1 by Wood, Myers, & Daugherty (1994), looks like a 1.7 by 0.7 pc filamentary protuberance from the main cloud (B18), see Figure 2.1. The source of the HH 300 flow was established to be IRAS 04239+2436[1] (RBD), which lies at the northern end of B18w, just west of the "bridge" between B18 and B18w. Near- and mid-infrared photometry (Myers et al. 1987), and its infrared spectrum (Greene & Lada 1996) indicate that this is a 1.3 $L_\odot$ Class I young stellar object. The HH 300 flow was

[1] Although this paper is the first one to present a map of the HH 300 molecular outflow, Moriarty-Schieven et al. (1992) observed high-velocity wings in the ^{12}CO(3–2) line at the source position, which led them to conclude that IRAS 04239+2436 is a molecular outflow source.

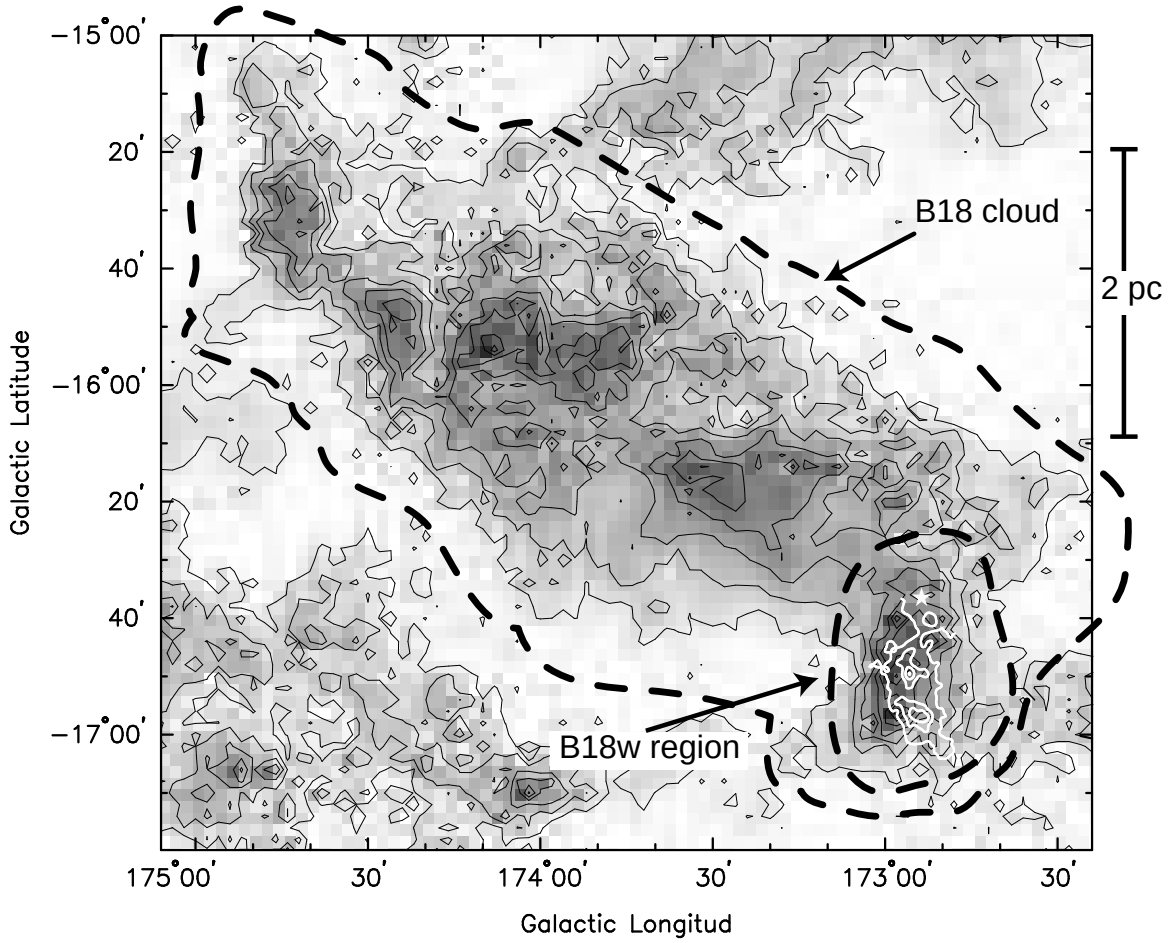

Fig. 2.1.— ^{13}CO(1–0) integrated intensity map of the B18 cloud in Taurus for the velocity range $2.9 < v < 8.9$ km s^{-1}. The map is part of the large scale ^{13}CO map of the Taurus molecular cloud complex from Mizuno et al. (1995). The source of the HH 300 flow, IRAS 04239+2436, is shown with a white star symbol. The integrated intensity map of the HH 300 molecular outflow's red lobe is shown in white contours. The B18 and B18w regions are identified.

originally discovered to consist of three redshifted HH objects (HH 300A, B, and C), each with a bow-shock-like morphology, close together at a distance of about 1.1 pc southwest of the outflow source, and a small blueshifted knot (HH 300D) about 0.02 pc northeast from the source, assuming a distance to Taurus of 140 pc (Kenyon, Dobrzycka, & Hartmann 1994). Recent space-based images at 1.644 and 2.122μm, with a spatial resolution of $\sim 0.13''$, of the HH 300 source region by Reipurth et al. (2000) reveal: a cometary nebula surrounding the source; a jet on the blueshifted side of the HH flow (northeast of the source) along the symmetry axis of the nebula; and that IRAS 04239+2436 is a binary.

2.2 Observations

2.2.1 ^{12}CO(2–1) Data

The ^{12}CO(2–1) line data were obtained using the on-the-fly mapping technique at the National Radio Astronomy Observatory (NRAO) 12 m telescope on Kitt Peak, Arizona, in December 1998. At the observed frequency of 230 GHz, the telescope's half-power beam width, main beam efficiency, and aperture efficiency are $27''$, 0.32 and 0.44, respectively. The spectrometer used was a filter bank with 250 kHz resolution, with two independent sections of 128 channels each. The filter bank was put in parallel configuration, in which each of the two sections received independent signals with a different polarization. The parallel configuration was chosen so that ultimately the two polarizations could be averaged to produce spectra with a better signal-to-noise ratio (S/N). At a frequency of 230 GHz, the resultant velocity resolution for this setup is 0.65 km s^{-1}.

The on-the-fly (OTF) mapping technique was used to observe an $11'$ by $37.5'$ area, along a position angle of 49°, surrounding the axis of the HH 300 flow's redshifted lobe. The OTF technique allowed the extended area to be mapped in a more efficient way than the conventional point-by-point mapping. The telescope in OTF mode moved across the source at a constant speed of $30''$ s^{-1}, while data were

taken a rate of 10 samples s^{-1}. In order to map the desired area more efficiently, the total area mapped consists of overlapping regions of different sizes: one large sized map of $8'\times$ by $33'$, one medium sized map of $8' \times 20'$ and two small sized maps of $3' \times 6'$ and $8' \times 5'$. All the regions were scanned along the direction perpendicular to the HH flow's axis, which has a P.A.$= 49°$. The separation, in the direction perpendicular to the scanning direction, between subsequent rows was $6''$. The telescope was pointed to an OFF position, located at R.A. $4^h21^m40^s$, decl. $24°05'00''$(B1950), after every other row, where it would observe the OFF position for 10 sec and then calibrate for 5 sec. The OFF position was later observed to have emission in the velocity range between 2.4 and 6.3 km s^{-1}, with $0.1 \lesssim T_A^* \lesssim 0.5$ K, and no emission greater than 0.1 K at other velocities. The emission from the red lobe of the HH 300 outflow is at velocities greater than 6.7 km s^{-1}. Therefore, the small amount of emission at velocities between 2.4 and 6.3 km s^{-1} at the OFF position does not affect our outflow data (see Figure 2.2). The different regions were observed several times to improve the S/N in the spectra. The system temperature was measured to be in the range between 400 and 900 K. In order to keep a constant noise level through the whole map, the regions that were mapped with a higher system temperature were observed more than the regions with lower system temperature.

The raw OTF data were reduced using the various Astronomical Image Processing System (AIPS) OTF tasks. A first-order baseline was fitted and subtracted to each spectrum, and the two polarizations were averaged. The different mapped regions were combined and averaged. The map was then convolved onto a grid with $14''$ pixels. The resultant RMS noise in each 0.65 km s^{-1} channel was 0.12 K, for most (non border) spectra. The intensity scale of the spectral data presented in this chapter is in units of T_A^* (Kutner & Ulich 1981) unless it is stated otherwise.

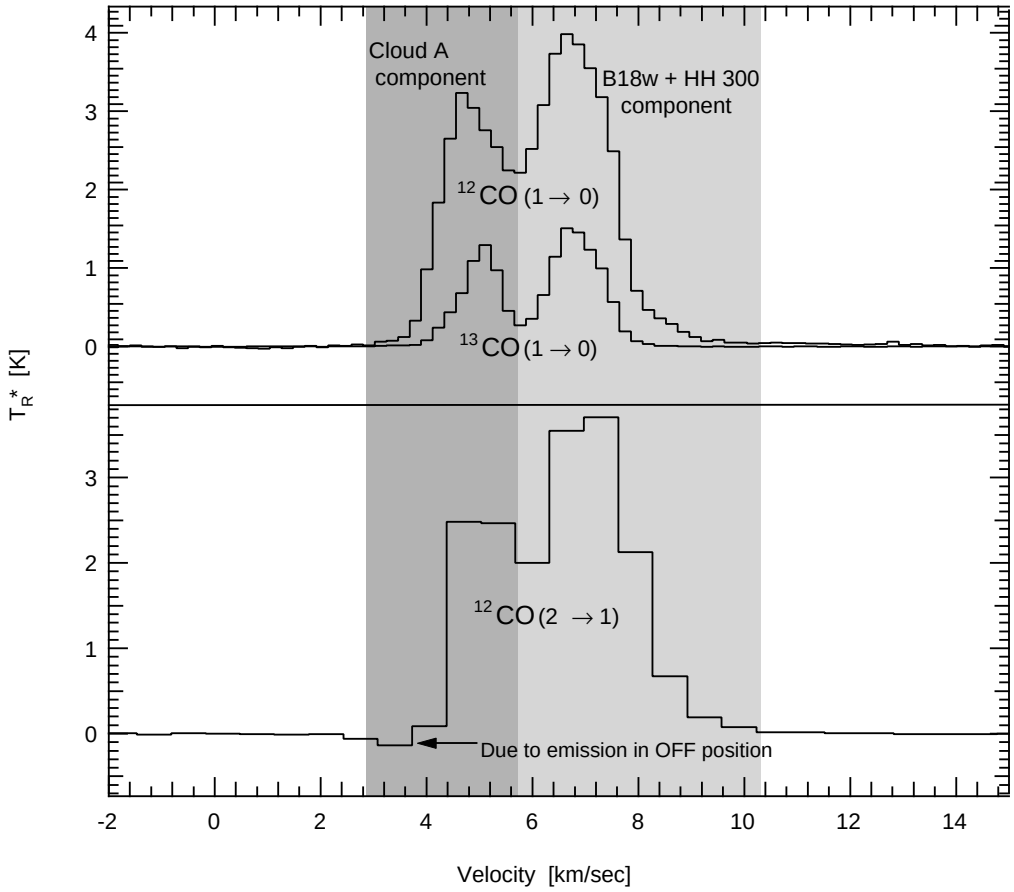

Fig. 2.2.— (*Top*) Average ^{12}CO(1–0) and ^{13}CO spectra of the area mapped in ^{12}CO(2–1), which includes most of the HH 300 outflow red lobe and some cloud regions unaffected by the outflow. (*Bottom*) Average ^{12}CO(2–1) spectrum over the same area as the spectra above [the area covered by the ^{12}CO(2–1) map].

2.2.2 ^{12}CO(1–0), ^{13}CO(1–0), and C^{18}O(1–0) Data

In order to study the effect of the HH 300 outflow on a larger scale and to attain a better estimate of the outflow mass, we observed the ^{12}CO(1–0) and ^{13}CO lines in a region 17.5′ by 59′ along a position angle of 49°, surrounding the HH 300 outflow source (IRAS 04239+2436). The data were obtained using the SEQUOIA 16 element focal plane array receiver of the Five College Radio Astronomy Observatory (FCRAO) 14 m telescope. The observations were done over the course of three different observing rounds, which took place in April 1999, December 1999, and February 2000. Both lines were observed in frequency-switched mode and the backend used was the Focal Plane Array Autocorrelator Spectrometer (FAAS), with a channel spacing of 78 kHz (0.21 km s^{-1}) for ^{12}CO(1–0), at a frequency of 115 GHz, and 20 kHz (0.05 km s^{-1}) for ^{13}CO(1–0), at a frequency of 110 GHz. The telescope half-power beam width for the ^{12}CO(1–0) and ^{13}CO lines are 45″ and 47″, and the main beam efficiencies are 0.45 and 0.54, respectively. The ^{12}CO(1–0) spectra were taken with a spacing of 44″ (beam sampled) and with an integration time of 150 sec for each position. The ^{13}CO spectra were taken with a spacing of 22″ (Nyquist sampled), and with an integration time of 100 sec for each position. The system temperature of our observations ranged between 700 and 1000 K for ^{12}CO(1–0), and between 300 and 500 K for ^{13}CO(1–0).

Observations of the C^{18}O(1–0) emission were also made using the same telescope and backend configuration as the ^{13}CO(1–0) observations. We made three Nyquist sampled FCRAO-SEQUOIA footprints. The 5.5′ × 5.5′ footprints were centered at offsets (0, 0), (-3.1′, -3.1′), and (-6.9′, -9.4′) with respect to the outflow source position at $(\alpha,\delta)_{1950}$ = ($4^h23^m54^s.5$, 24°36′54″). The telescope half-power beam width and main beam efficiency for C^{18}O(1–0), at a frequency of 109 GHz, are 47″and 0.54, respectively. Each position was observed for 200 to 300 sec, with a system temperature ranging from 170 to 350 K.

The ^{12}CO(1–0) and ^{13}CO(1–0) data were reduced with the CLASS and MIRIAD packages. The original spectra from both lines were smoothed and resampled to a channel spacing of 0.22 km s^{-1}. The spectra were spatially linearly

interpolated and a data cube of 11.5″ pixels was produced for each line. The data cube was then smoothed by convolving it with a Gaussian with a FWHM of 46″, using the task *smooth* in MIRIAD. The resultant RMS noise of the spectra in the ^{12}CO(1–0) and ^{13}CO(1–0) smoothed maps was 0.17 K and 0.07 K for each 0.22 km s^{-1} channel, respectively. Interpolating the ^{12}CO(1–0) and the ^{13}CO(1–0) data to this common position-velocity grid allowed us to use them in concert when calculating the mass estimates presented in §2.3.3.

2.3 Results

Figure 2.2 shows spectra of ^{12}CO(2–1), ^{12}CO(1–0), and ^{13}CO(1–0) averaged over the area mapped in ^{12}CO(2–1). The most notable property of the spectra in Figure 2.2 is that they are composed of two main (Gaussian-like) components. One component is centered at a velocity close to 6.7 km s^{-1} and the other component is centered at a velocity close to 5 km s^{-1}. The $v = 6.7$ km s^{-1} component is produced by the molecular emission of the HH 300 outflow host cloud (B18w), while the other component, at $v = 5$ km s^{-1}, is produced by another cloud in Taurus (hereafter cloud A), along the same line-of sight. Unlike many other average outflow spectra (e.g., HH 111, Cernicharo & Reipurth 1996; NGC 2264G, Lada & Fich 1996; RNO 43, Bence et al. 1996), the red wing of the ^{12}CO(2–1) and ^{12}CO(1–0) average spectra is not very prominent. The wing only extends from about 8 to about 10 km s^{-1}. In addition to the small red wing, the line core component of the B18w cloud, seems to have a slight asymmetry, with more emission towards red velocities. This suggests that the HH 300 outflow is composed mainly of gas with slow radial velocities, and the gas emission of its slowest velocities might be hidden under the ambient cloud emission.

The cloud A component is visible not only in the area surrounding the red lobe of HH 300, but through most of the area we mapped in ^{12}CO(1–0) and ^{13}CO(1–0). This area includes the region where the blue lobe of HH 300 should be, assuming that it lies northeast of IRAS 04239+2436, opposite to the red lobe, at the same

position angle. There is evidence in the optical (RBD) and near-infrared (Reipurth et al. 2000) for blueshifted outflowing material only very close to the source. But, even if the HH 300 flow's blue lobe were interacting with the surrounding gas (close to and/or far from the source), we would not be able to study it. The "contamination" from cloud A on the blue side of the B18w component is such that we would not be able to observe the high-velocity blue wings that presumably would have been present in the ^{12}CO spectra. Therefore we concentrate our study on the interaction between the redshifted lobe of the HH 300 flow and its surroundings.

2.3.1 ^{13}CO(1–0) Maps

Figure 2.3 shows five ^{13}CO(1–0) velocity maps, integrated over five different velocity ranges. The first map is integrated over the velocity in which the emission from cloud A is present, $3.79 < v < 5.77$ km s^{-1}. The other three maps are made over velocity ranges in which there is emission from the B18w cloud (and HH 300 outflow). It is evident that the velocity map in Figure 2.3*a* shows a ^{13}CO structure different from the other velocity maps. In addition, the position angle of the short and long axes of the $3.79 < v < 5.77$ km s^{-1} structure differs from that of the B18w cloud by about 30°. This reconfirms our assumption that the emission from velocities 3.8 to 5.8 km s^{-1} does not come from the B18w cloud, but from another cloud (cloud A) on the same line-of-sight.

The integrated velocity map over the range $5.77 < v < 7.09$ km s^{-1} is shown in Figure 2.3*b*. The velocity range of Figure 2.3*b* does not cover the whole range of velocities in which there is emission from the B18w cloud component ($5.77 < v < 8.63$ km s^{-1}) in Figure 2.2. But, even though the map in Figure 2.3*b* only shows emission from 5.77 to 7.09 km s^{-1}, it shows the general ^{13}CO structure of the B18w cloud. Comparing Figure 2.3*b* with an integrated map that covers the whole velocity range of emission from the B18w component ($5.77 < v < 8.63$ km s^{-1}) shows that both maps have essentially the same structure. And, comparing Figure 2.3*b* with a map integrated over just 6.2 to 7.1 km s^{-1}

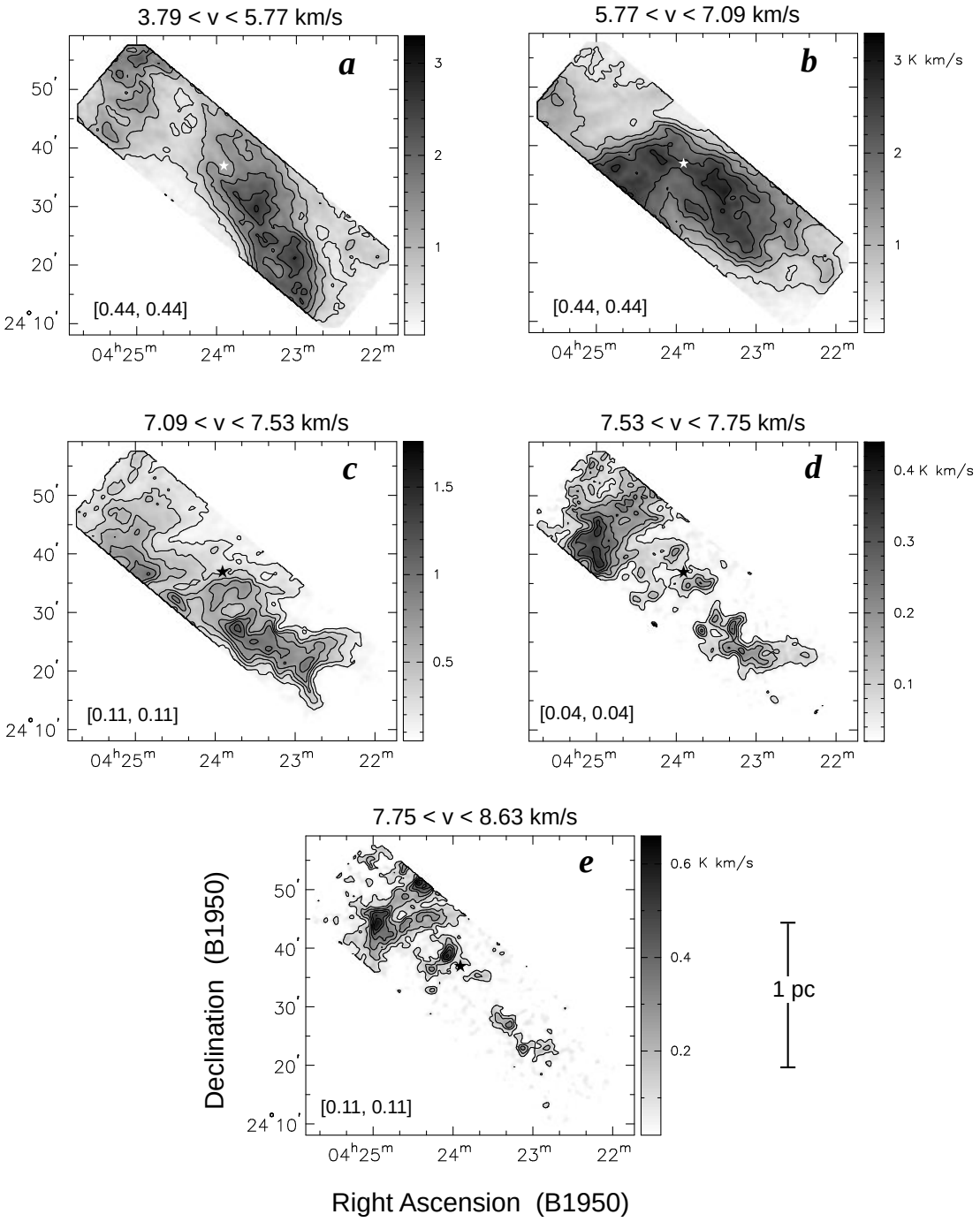

Fig. 2.3.— Velocity-range-integrated intensity maps of the ^{13}CO(1–0) emission. The velocity interval of integration is given on the top of each panel. The first contour and the contour steps are given in parenthesis on the bottom left corner of each panel in units of K km s^{-1}. The position of the outflow source, IRAS 04239+2436, is identified with a star symbol. (*a*) Emission from cloud A. (*b*) Emission from B18w. (*c*) Emission from B18w ambient gas plus HH 300 outflow emission. (*d*) Emission southwest of the outflow source is solely from HH 300 outflow. The emission northeast of the source is from another cloud on the same line of sight. (*e*) Emission southeast of outflow source is from the highest velocity outflowing ^{13}CO gas.

also shows that they have similar structure. In addition, the shape of the ^{13}CO emission of these maps is very similar to the shape of the B18w dark cloud as seen in the optical image of RBD. Therefore, the emission from the B18w cloud is predominantly from gas at velocities between 6.2 and 7.1 km s^{-1}, the peak emission range for the spectra in Figure 2.2.

The integrated intensity map over $7.09 < v < 7.53$ km s^{-1} has a very peculiar structure (Figure 2.3*c*). The long and short axis, as well as the position angle of this structure are similar to those of the $5.77 < v < 7.09$ km s^{-1} (Figure 2.3*b*) structure. Also, the $7.09 < v < 7.53$ km s^{-1} structure bears some resemblance to the ^{12}CO(1–0) outflow in the velocity range of $7.53 < v < 7.97$ km s^{-1} (see §2.3.2). The local maximum in ^{13}CO at R.A. $4^h22^m50^s$, decl. $24°21'30''$(B1950) is at the tip of the most prominent bow shock-like clump (clump R3; see §2.3.2, and ^{12}CO outflow maps in that section) in the ^{12}CO outflow. Although it is tempting to conclude that most of the emission at these velocities comes from the "slow-moving" outflowing gas, the velocity of this structure (about 7.75 km s^{-1}) is still very close to the line center velocity ($V_{LSR} = 6.67$ km s^{-1}). Thus, we expect some contribution to the emission at $7.09 < v < 7.53$ km s^{-1} to come from the turbulent gas in B18w unaffected by the outflow. We are convinced that ^{13}CO emission from both slow-moving outflowing gas and ambient cloud gas are present in the integrated intensity map in the velocity range of $7.09 < v < 7.53$ km s^{-1} (see §2.3.3 for a quantitative discussion).

Figure 2.3*d* shows the integrated intensity for the velocity range $7.53 < v < 7.75$ km s^{-1}. There is no doubt that the ^{13}CO emission in this velocity range, southwest of IRAS 04239+2436 is due to gas that has been put in motion by the outflow. The ^{13}CO emission coincides in position with the medium-velocity structure seen in the ^{12}CO outflow velocity maps (see §2.3.2, and ^{12}CO outflow figures). The emission detected northeast of the outflow source at these redshifted velocities, with respect to the ambient cloud velocity ($V_{LSR} = 6.67$ km s^{-1}), is not associated with the HH 300 flow. Instead, this emission comes from an elongated structure perpendicular to the HH 300 flow's axis, associated with the B18 molecular cloud, as can be seen in the large scale, 2.7′ resolution, ^{13}CO velocity

maps of Taurus by Mizuno et al. (1995). The integrated intensity map over the range $7.75 < v < 8.63$ km s^{-1} (see Figure 2.3*e*) shows the highest (red) velocities of the HH 300 outflow in ^{13}CO emission. The knotty features of these high velocity ^{13}CO coincide with the position of the high-velocity features in the ^{12}CO outflow (again, see §2.3.2 and figures in that section). These knotty features are well defined in space and velocity.

2.3.2 ^{12}CO Maps

In Figures 2.4 and 2.5 we show ^{12}CO(2–1) and ^{12}CO(1–0) velocity maps of the HH 300 molecular outflow. The ^{12}CO(1–0) data set covers more area and has a better spectral resolution than the ^{12}CO(2–1) data. On the other hand, the ^{12}CO(2–1) data has a better spatial resolution and sensitivity than the ^{12}CO(1–0) data. Regardless of the differences in spectral and spatial resolution, area and sensitivity, the ^{12}CO(2–1) and ^{12}CO(1–0) maps look very similar for similar velocity ranges (see Figures 2.4 and 2.5). The most notable characteristic of the HH 300 molecular outflow is its very clumpy structure. In Figure 2.6 and Table 2.1 we show how five named clumps (R1 to R5) are identified.

We believe that all five clumps mentioned above are associated with the HH 300 outflow and each clump represents a different ejection event. Clumps R1 and R2 have "blobby" structures like the high-velocity CO bullets found in HH 111 by Cernicharo & Reipurth (1996). Clump R3 has a shape reminiscent of a bow shock, with wings pointing in the direction of the outflow source (see Figures 2.4*b* and 2.5*b*). There is stronger ^{12}CO emission in the south wing than in the north wing of the bow structure. This asymmetry in the bow wings of R3 is most probably due to the underlying distribution of molecular gas in the cloud, since there is more gas emission south of clump R3, than to its north. Recent high spatial resolution observations of outflows (e.g., Yu et al. 1999, Lee et al. 2000) have found that bow shape CO structures are common. The CO bow structures presumably are created by the interaction between a bow shock from an underlying jet, and the ambient gas. Clump R4 is barely distinguishable as a separate clump

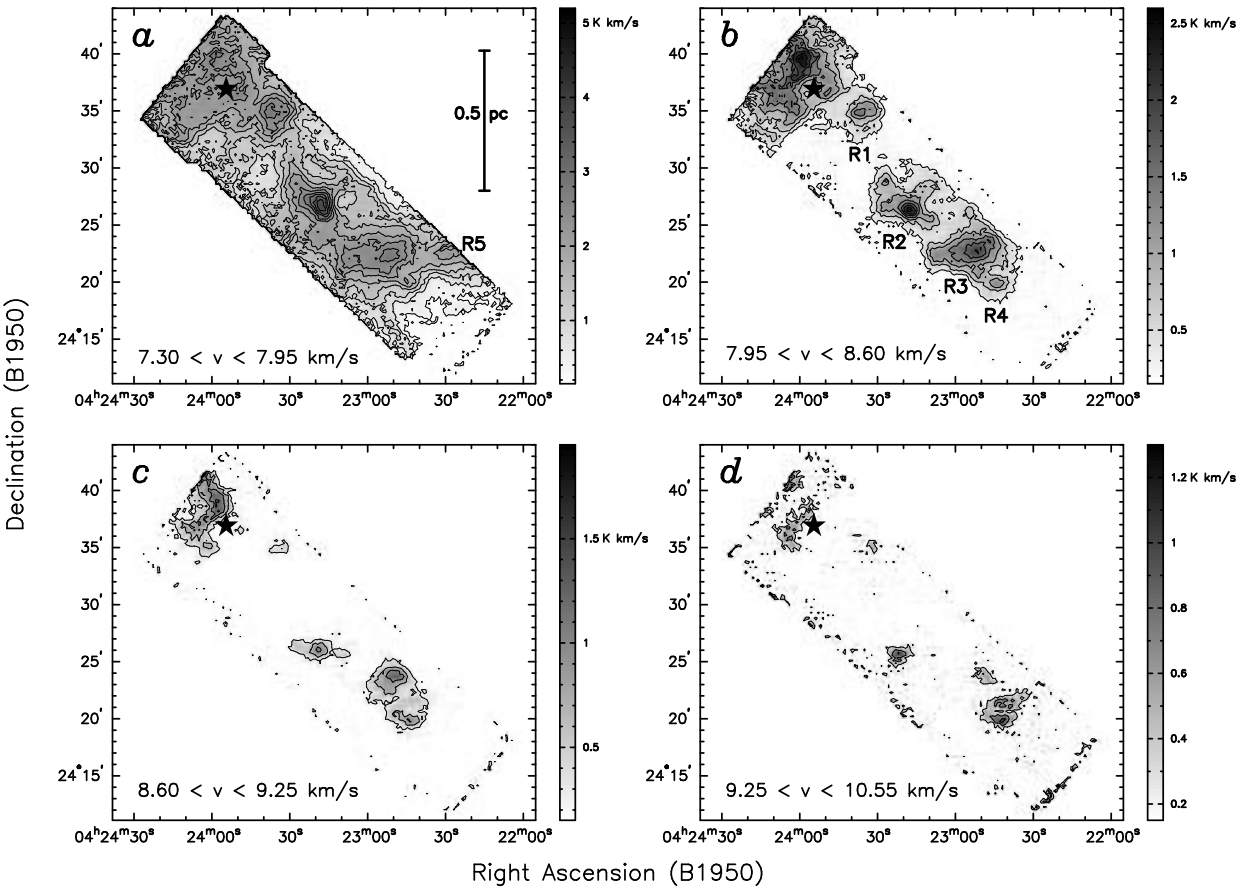

Fig. 2.4.— Velocity-range-integrated intensity maps of the ^{12}CO(2–1) emission from the redshifted lobe of the HH 300 molecular outflow. The velocity interval of integration is given on the bottom of each panel. The first contour and the contour steps are 0.325 K km s^{-1} for all maps. The position of the outflow source, IRAS 04239+2436, is identified with a star symbol. The five outflow clumps R1, R2, R3, R4, and R5 are labeled.

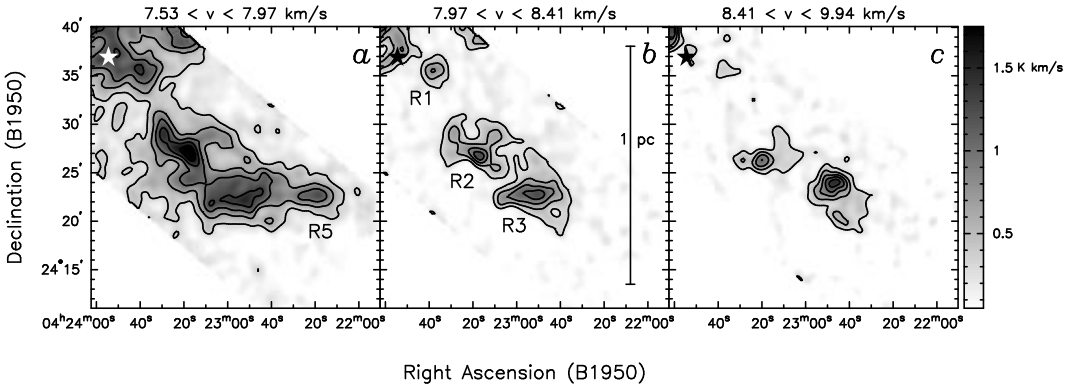

Fig. 2.5.— Velocity-range-integrated intensity maps of the ^{12}CO(1–0) emission from the redshifted lobe of the HH 300 molecular outflow. The velocity interval of integration is given on the bottom of each panel. The first contour and the contour steps are 0.22 K km s^{-1} for all maps. The position of the outflow source, IRAS 04239+2436, is identified with a star symbol. Four of the five outflow clumps (R1, R2, R3, and R5) are labeled.

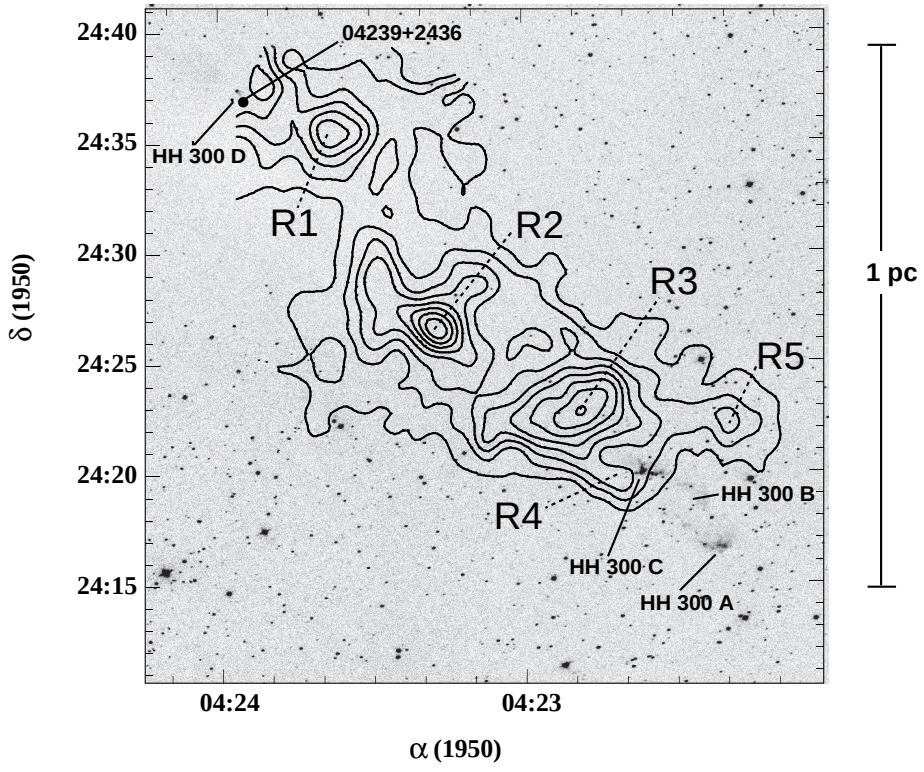

Fig. 2.6.— Integrated intensity contour map of the ^{12}CO(1–0) emission over the range 7.53 < v < 9.94 km s^{-1}, superimposed on a wide-field Hα+[S II] (optical) CCD image from Reipurth, Bally, & Devine (1997). The starting contour of the integrated intensity map is 0.55 K km s^{-1}, and the contour steps are 0.275 K km s^{-1}. The A, B, C, and D HH knot groups from the HH 300 flow are labeled. We also label the molecular outflow clumps R1, R2, R3, R4, and R5. The location of the deeply embedded outflow source, IRAS 04239+2436, is shown. The B18w cloud is seen in the optical image as a region with no background stars (due to extinction).

Table 2.1. Detectability of Clumps in HH 300 Redshifted Lobe

	Integrated Intensity Maps[a]			Position-Velocity Diagrams[b]	
Clump	^{13}CO	^{12}CO(1–0)	^{12}CO(2–1)	^{12}CO(1–0)	^{12}CO(2–1)
R1	yes	yes	yes	yes	yes
R2	yes	yes	yes	yes	yes
R3	yes[c]	yes	yes	yes	yes
R4	no	...[d]	yes	...[e]	yes
R5	no	yes	yes[f]	no	yes

[a]Here we note if the clump structure can be seen in any of the velocity-integrated maps of the different molecular lines (Figures 2.3, 2.4 and 2.5)

[b]Here we note if the clump shows a velocity increase in the the position-velocity (PV) diagrams (Figures 2.9 and 2.10).

[c]The R3 clump is seen as two clumps in ^{13}CO(1–0).

[d]There is ^{12}CO(1–0) emission at the position of clump R4, but the ^{12}CO(1–0) maps do not show the same, clearly defined, clump structure as in the ^{12}CO(2–1) velocity maps.

[e]There is not a clear peak in the velocity at the position of clump R4 in the ^{12}CO(1–0) PV diagram, though there is high-velocity gas (see Figure 2.10).

[f]Clump R5 can only be seen partly in the ^{12}CO(2–1) data because of the limited extent of the ^{12}CO(2–1) map (see Figure 2.4*a*).

from R3, but it is still clear that R4 exhibits a local maximum of CO emission and that it diverges from the bow structure of R3 (see Figure 2.4*b*). We are confident that R4 is associated with the HH 300 outflow not only due to its relatively (redshifted) high-velocity, but also because it coincides in position with the optical knot HH 300C (see Figure 2.6). The molecular clump R5 is the clump with the slowest velocities, and can only be seen in the velocity maps with velocities close to the cloud velocity. It has an elongated drop-like structure, as if it were a bow-shock, with only one wing. The same effect that produces asymmetric bow wings in R3, could be producing the structure of R5, but in a more dramatic way. In the case of R5, there is practically no molecular emission north of the clump, but there is some emission south of it. It is very probable that we do not see a north bow wing in R5, since there is essentially no gas to the north of the clump to produce a ^{12}CO

Table 2.2. Physical Properties of Clumps in HH 300 Redshifted Lobe

Clump	d[a] [pc]	Angle[b] [deg]	Age[c] [yr]	Mass[d] [$M_\odot$]
R1	0.16	250	800	0.07
R2	0.53	221	2500	0.21
R3	0.81	228	4000	0.23[e]
R4	0.98	225	4800	...[e]
R5	1.03	238	5000	0.02[f]

[a]Distance from the outflow source to the maximum emission point on clump

[b]Position angle (east of north) of line intersecting outflow source and maximum emission point on clump.

[c]Dynamical age of the clump assuming mass ejection from source, responsible for the clump, has a tangential velocity of 200 km s^{-1}.

[d]Mass of clump for $v_{out} \geq 0.97$ km s^{-1}, uncorrected for cloud emission. Emission at $v_{out} \geq 0.97$ km s^{-1} is dominated by outflow clump emission, cloud emission dominates at slower velocity channels.

[e]Clump R3 and R4 are indistinguishable (unresolved) in ^{12}CO(1–0) and ^{13}CO lines, the total mass of both is given in the R3 mass entry.

[f]Unlike the other clumps, clump R5 is seen better at lower velocities, $v_{out} \sim 0.75$ km s^{-1}. Mass of clump R5 for $v_{out} \geq 0.75$ km s^{-1} is 0.11 $M_\odot$.

wing. Table 2.2 shows the distance from the source and the position angle, as well as other physical properties of each of the molecular clumps.

2.3.3 Outflow Physical Properties

In order to study the effects of a molecular outflow on its environment, it is essential to calculate its mass, momentum, and energy in the most precise way possible. There are several potential pitfalls which, if not avoided or compensated for, can reduce the precision of the calculation of an outflow's physical properties.

Major dangers include: (1) not accounting for the inclination of the flow's axis to the plane of the sky; (2) assuming that the molecular spectral line being used to obtain the physical properties is optically thin when in reality it is optically thick; and (3) not counting slow-moving outflow gas which is "hidden" by the ambient cloud molecular emission as part of the flow. With our data, we have found a way to tackle the uncertainties produced by (2) and (3). On the other hand, (1) remains a problem.

Inclination

The most accurate way of obtaining i for a molecular outflow is to observe the tangential (V_t) and radial velocities (V_r) of an HH object associated with the molecular outflow being studied. Assuming that the HH object travels through space along a straight line and that the molecular gas from the molecular outflow associated with the HH object will move in the same direction, then $i = \arctan(V_t/V_r)$. Unfortunately, no proper motions study of the HH 300 optical knots has been done, thus we do not know the transverse velocities of the HH 300 knots. Other methods of estimating the value of i for molecular outflows use a simple geometrical and velocity field model for the flow, combined with the observed data of the outflow (see Liseau & Sandell 1986; Cabrit et al. 1988). Using these models results in i values with large uncertainties, but at least they give a rough estimate to the value of i, when otherwise there would be none. The clumpy structure of the HH 300 molecular outflow (very different from the molecular outflow cone geometry assumed by the models listed above), and the fact that it is impossible to detect any blueshifted CO emission from the HH 300 outflow due to contamination from cloud A, makes it impossible to use the simple geometric models to estimate i for HH 300. In addition, if the HH 300 outflow is precessing and episodic (see §2.4.3), then each mass eruption could have been ejected at a different angle with respect to the plane of the sky, so that using a single value of i for HH 300 would be an incorrect assumption.

The HH 300 flow most likely lies very close to the plane of the sky. Most of

the giant HH flows for which the inclination angle is known have been found to have small values of i. By definition, giant HH flows are flows which are observed to extend more than 1 pc in length on the sky. The smaller the angle between the flow's axis and the plane of the sky, the longer the projected (on the plane of the sky) size of a flow will be, for a given flow length. Thus, it is not surprising that there is a bias toward small values of i in giant HH flows. The small maximum outflow radial velocities ($\sim$ 3 to 4 km s^{-1}) that the HH 300 molecular outflow exhibits, as well as the morphology of the near-infrared nebula surrounding the outflow source (as observed by Reipurth et al. 2000) further confirm that HH 300 lies very close to the plane of the sky. We believe that the (average) axis of the HH 300 flow must have an inclination angle with respect to the plane of the sky between 5 and 15 degrees. In this chapter, all outflow velocities quoted for HH 300 *are not corrected by inclination angle*, unless otherwise noted.

Opacity Correction

Using an optically thick line to study an outflow will cause an underestimation of the mass and kinetic energy in the flow. Not only should one worry about the line core opacity, but also the dependence of the line opacity on velocity. Using the outflow mass estimation methods of Bally et al. 1999 (hereafter BRLB) and Yu et al. 1999 (hereafter YBB), with our ^{13}CO(1–0) and ^{12}CO(1–0) data in HH 300, we believe we have obtained a fairly accurate estimate of the outflow mass.

We do not strictly follow BRLB's or YBB's method, but use a combination of the two, with our own modifications. First, we take an average of all the ^{13}CO(1–0) and ^{12}CO(1–0) spectra in the area southwest of IRAS 04239+2436, where the outflow lies. Then, we plot the ratio of the lines as a function of velocity (see Figure 2.7*a*). The ^{12}CO(1–0) line is optically thick over all velocities where there is detectable ^{13}CO(1–0), as the line ratio is always less than 60. It is clear that the line ratio (and thus the opacity) is not constant over velocity, and that it has a parabolic shape. Assuming a constant opacity for the ^{12}CO(1–0) line, as in most studies which claim to correct for the ^{12}CO(1–0) opacity using the ^{13}CO(1–0) line,

is *not* an accurate assumption. It is imperative to take the velocity dependence of the opacity into consideration.

Using the average spectra of the two molecular lines, we obtain the value of the main beam temperature (T_{mb}) for each 0.22 km s^{-1} wide channel, and calculate the ratio of main beam temperatures. We then make a second-order polynomial fit to the ratio of ^{12}CO(1–0) to ^{13}CO(1–0) intensity, $R_{12/13}$, as a function of velocity. The fit is constrained to have a minimum at the velocity of the ambient cloud (equal to the velocity where the average ^{13}CO spectrum peaks), $V_{LSR} = 6.67$ km s^{-1}. We exclude the five velocity channels closest to the ambient velocity from the fit, as they are the velocities at which the ^{13}CO emission is slightly optically thick (see below) and the ^{12}CO emission is extremely optically thick. Also, we use only the points that lie between the velocities 5.8 and 8.2 km s^{-1}, in order to exclude cloud A and low-S/N velocities. We use the $R_{12/13}(v)$ parabolic fit to extrapolate $R_{12/13}$ to the high-velocity wings of the outflow, where the ^{13}CO line is too weak to be reliably detected.

We estimate the mass in the following way. If the ^{13}CO emission at a velocity v_i, at a certain position (x_i, y_i) is greater than or equal to twice the RMS noise of the spectrum at that position, we use the main beam temperature value at the given velocity ($T^{13}_{mb}(x_i, y_i, v_i)$). If the ^{13}CO emission is less than twice the RMS noise, then we use the ^{12}CO(1–0) spectrum at the given position (x_i, y_i) and velocity v_i to estimate $T^{13}_{mb}(x_i, y_i, v_i) = T^{12}_{mb}(x_i, y_i, v_i)[R_{12/13}(v_i)]^{-1}$. Similar to what BRLB and YBB do, the function $R_{12/13}(v)$ is truncated at a value of 62, the assumed isotopic ratio (Langer & Penzias 1993). If both the ^{13}CO and the ^{12}CO(1–0) emissions at (x_i, y_i, v_i) are less than twice the RMS noise, then essentially there is no signal from which we can estimate a value of $T^{13}_{mb}(x_i, y_i, v_i)$.

Once we obtain the value of $T^{13}_{mb}(x_i, y_i, v_i)$, we can get the value of the opacity, assuming that the ^{13}CO line is optically thin. Using our C^{18}O data we are able to estimate the opacity of the ^{13}CO emission at several positions. The C^{18}O observations were made where strong ^{13}CO emission was found, i.e., regions where the ^{13}CO emission might be optically thick. From the ^{13}CO to C^{18}O ratio we

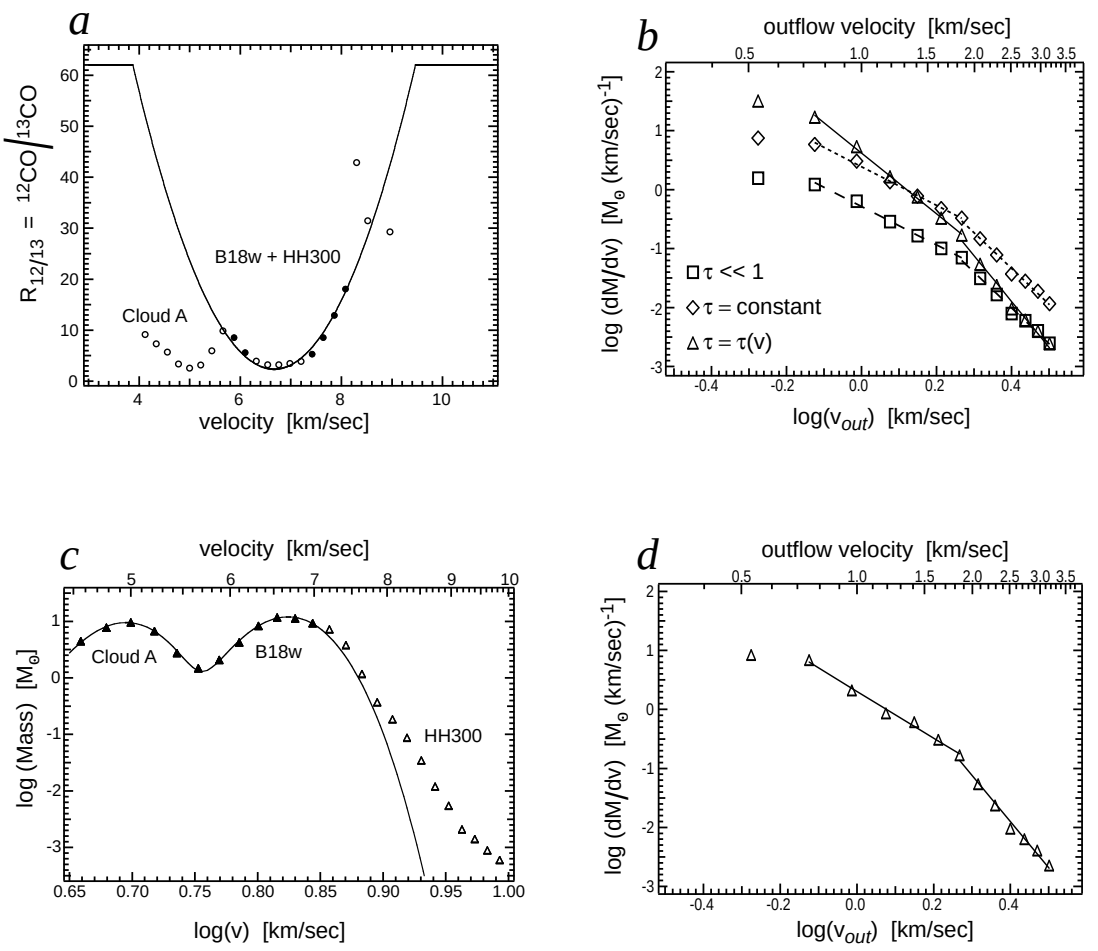

Fig. 2.7.— (*a*) Main beam temperature (or intensity) ratio of ^{12}CO(1–0) to ^{13}CO(1–0), also denoted in the text as $R_{12/13}$, as a function of observed velocity (v). The filled circle symbols are the points used for the second-order polynomial fit to $R_{12/13}$. The solid line is the resulting fit. (*b*) Mass spectrum, or mass in a 0.22 km s^{-1}-wide channel as a function of outflow velocity ($v_{out} = v - V_{LSR}$), for the red lobe of the HH 300 molecular outflow. The squares denote the mass obtained assuming that ^{12}CO(1–0) is optically thin (Mass $\propto \int T_{mb} dv$). The diamonds represent the mass obtained assuming that the ^{12}CO(1–0) line opacity is constant ($R_{12/13} = 13$). The triangles denote the mass assuming that $R_{12/13}$, and thus the opacity of the ^{12}CO(1–0) line, varies as a function of velocity, as shown in Figure 2.7*a*. For each of these three different mass estimates we show two power-law fits, one for low outflow velocities between 0.75 and 1.85 km s^{-1}, and another for high outflow velocities between 1.85 and 3.17 km s^{-1}. The points at $v_{out} = 0.53$ km s^{-1} are real, but are excluded from the fits, as they lie too close to the ambient line core. Velocities are *not* corrected for outflow inclination. The long and short dashed lines are power-law fits to the optically thin mass estimate and the constant opacity mass estimate, respectively. The solid lines show power-law fits to the velocity-dependent opacity corrected mass spectrum. The power-law exponents from the fits are as follows. $\tau << 1$: -3.3 ± 0.1 (low velocity); -6.1 ± 0.2 (high velocity). τ = constant: -3.3 ± 0.1 (low velocity); -6.1 ± 0.2 (high velocity). $\tau(v)$: -5.2 ± 0.1 (low velocity); -7.8 ± 0.4 (high velocity). (*c*) Mass in a 0.22 km s^{-1}-wide channel, as a function of observed velocity. Solid line is a two-Gaussian fit to the filled triangle symbols (points that are not "contaminated" by emission from the HH 300 outflow). (*d*) Mass spectrum corrected for ambient cloud emission. The mass is corrected for ambient cloud emission by subtracting the modeled ambient cloud mass (given by the Gaussian fit in [*c*]) from the velocity-dependent opacity corrected mass (shown in [*b*] in triangle symbols). See discussion in text (§2.3.3). Similar to Figure 2.7*b*, the resultant power-law fits are shown by solid lines. The slopes of the fits are -4.0 ± 0.2 and -7.8 ± 0.4.

estimate the opacity of the ^{13}CO line (as a function of velocity) at the limited positions for which we have C^{18}O data. The ^{13}CO to C^{18}O ratios indicate that even in regions with strong ^{13}CO emission, the opacity of the ^{13}CO line at line core velocities ($6.2 < v < 7.0$ km s^{-1}) does not exceed a value of 3, and for other velocities the ^{13}CO emission is optically thin. Since we are mainly interested in the outflow mass our assumption that ^{13}CO is optically thin is an excellent assumption.

At each position and at each velocity for which we have an estimate of $T_{mb}^{13}(x_i, y_i, v_i)$, we calculate the ^{13}CO opacity, $\tau_{13}(x, y, v)$, using:

$$\tau_{13}(x, y, v) = -\ln[1 - \frac{T_{mb}^{13}(x, y, v)}{\frac{T_o}{\exp(T_o/T_{ex})-1} - 0.87}] \tag{2.1}$$

from (Rohlfs & Wilson 2000). Here $T_o = h\nu/k$, which for ^{13}CO is 5.29. The value of τ_{13}, from equation 2.1, agrees with the value of the ^{13}CO opacity obtained using the ^{13}CO to C^{18}O line ratio in the limited number of positions where we measured the C^{18}O emission. The excitation temperature, T_{ex}, is obtained by assuming that the ^{12}CO(1–0) line core is optically thick. We take an average spectrum of the ^{12}CO(1–0) data over all of the area southwest of the source for which we have ^{12}CO(1–0) data, and measured the peak temperature (corrected for main beam efficiency) to be $T_{peak} = 9.6$ K. Solving the radiative transfer equation for the excitation temperature, assuming that the line is optically thick, we obtain this expression:

$$T_{ex} = \frac{5.53}{\ln[1 + \frac{5.53}{T_{peak}+0.82}]} \tag{2.2}$$

from (Estalella & Anglada 1997). The resultant T_{ex} is 13 K, the same value that Mizuno et al. (1995) quote for the whole Taurus molecular cloud complex. Then, at each position and velocity the column density, $N_{13}(x, y, v)$, can be calculated with the following equation from Bourke et al. (1997):

$$N_{13}(x, y, v) = 2.42 \times 10^{14}(T_{ex} + 0.88)\frac{\tau_{13}(x, y, v)dv}{1 - \exp(-T_o/T_{ex})} \tag{2.3}$$

The outflow (molecular hydrogen) mass at each position pixel and each velocity channel is given by

$$M(x, y, v) = m_{H_2} N_{H_2}(x, y, v)A \tag{2.4}$$

where m_{H_2} (which is equal to 2.72 times the mass of a hydrogen atom) is the mean molecular weight, N_{H_2} is the molecular hydrogen column density which is obtained using the relation $N_{H_2} = 7 \times 10^5 N_{13}$ (Frerking, Langer, & Wilson 1982), and A is the physical area of the pixel at the distance of the source. We then sum over the area of the outflow ($M(v) = \sum_{area} M(x, y, v)$) to obtain the outflow mass as a function of velocity, and then sum over velocity ($M_{total} = \sum_v M(v)$) to obtain the total outflow mass. The uncertainty in the mass estimates comes mainly from the uncertainty in the N_{H_2} to N_{13} ratio, thus the uncertainty in the mass estimates is about a factor of 2 (Frerking et al. 1982).

Using this method we can calculate the mass per 0.22 km s^{-1}-wide velocity channel [$dM(v)/dv$] in the HH 300 flow. In Figure 2.7*b* we plot our results for outflow velocities (v_{out}) greater than 0.5 km s^{-1}, where v_{out} is the observed velocity (v) minus the cloud velocity ($V_{LSR} = 6.67$). Figure 2.7*b* shows that the observed mass (per 0.22 km s^{-1}-wide velocity channel), corrected only for the velocity-dependent opacity of the ^{12}CO(1–0) line, has a power-law dependence on velocity for v_{out} between 0.75 and 1.85 km s^{-1}. For outflow velocities higher than 1.85 km s^{-1}, the mass has an even steeper power-law dependence. A power-law fit to each of these two trends yields a slope of -5.2 ± 0.1 for the low-velocity points, and a slope of -7.8 ± 0.4 for the high-velocity points.

Correction for Ambient Cloud Emission

We suspect that some velocity channels have emission from both the low-velocity outflowing gas and the ambient cloud. Thus, in order to obtain an accurate estimate of the outflow mass it is essential to correct for the "extra mass" at low velocities due to ambient cloud "contamination". In order to make this correction, we use our calculations of the mass per velocity channel (see above) for $4.5 < v < 9.8$ km s^{-1}. Using the overall (cloud A + B18w + HH 300) mass spectrum in Figure 2.7*c*, we fit a two-Gaussian function to the points which define the clouds (cloud A and B18w) and we are sure are not "contaminated" by the HH 300 outflow (see Figure 2.7*c*). The Gaussians, which seem a good fit to the relevant ambient emission, give us

a value of $V_{LSR} = 6.67$ km s^{-1} as the center velocity of the B18w component, which is the value we use as the velocity of the cloud throughout the paper, and a center velocity for cloud A of 4.95 km s^{-1}. The outflow emission can clearly be seen in Figure 2.7*c* as a deviation from the Gaussian shape at redshifted velocities. To obtain the corrected outflow mass ($M_{cor}(v)$), we subtract the value of the fit at the velocity of interest ($M_{fit}(v)$) from the observed mass ($M_{obs}(v)$). Using the simple relation $M_{cor}(v) = M_{obs}(v) - M_{fit}(v)$ we obtain an outflow mass which is presumably free from the cloud emission. We display the mass-velocity relation using the corrected mass in Figure 2.7*d*. It can be seen that the low-velocity power-law slope of the mass spectrum (Figure 2.7*d*) becomes shallower, with a slope of -4.0 ± 0.2, after the correction. From here on all the outflow mass (and momentum) values given in this chapter are corrected for ambient cloud emission, unless otherwise noted.

We note that this method will result in an underestimation of mass in the lowest outflow velocity channels, if the emission were extremely optically thick at these velocities or if the points used for the "cloud" fit were heavily affected by outflow emission. As discussed above, neither of these two scenarios is our case, so we are confident that our underestimation of low-velocity outflow mass is minimal. The mass and the power-law slope at high outflow velocities ($v_{out} > 1.85$ km s^{-1}) are unchanged after the ambient cloud correction, since there is no contamination from the ambient cloud at those velocities.

Effects of Inclination, Opacity and Ambient Contamination

In estimating an outflow's momentum and energy, corrections for inclination can have profound effects, since we can only *observe* a radial velocity. On the other hand, the slope of the mass spectrum (see Figure 2.7*b*) is not affected by a flow's inclination. Correcting the velocity for projection effects will just re-scale the velocity axis of the mass spectrum plot, but the slope of the power-law mass spectrum will remain the same, assuming that all parts of the flow have roughly the same inclination angle, i.

The effects that velocity-dependent opacity correction have on the outflow's mass and mass spectrum can be seen clearly in Figure 2.7*b*. In this figure we plot the mass spectrum of the red lobe of HH 300, using three different assumptions. The square symbols denote the mass spectrum obtained assuming that the ^{12}CO(1–0) line is optically thin, so that mass is proportional to $\int T_{mb} dv$. The diamond symbols represent the mass spectrum obtained by assuming that the ^{12}CO(1–0) line opacity, and thus $R_{12/13}$= $I(^{12}\mathrm{CO})/I(^{13}\mathrm{CO})$, is constant. We use the area- and velocity-averaged value of $R_{12/13}$, over the velocity range between 7.3 and 8.5 km s^{-1} (or outflow velocities between 0.75 and 1.85 km s^{-1}) as an average ratio, $\bar{R}_{12/13}$. The mass is then calculated using equations 2.1, 2.3, and 2.4, and assuming that $T^{13}_{mb} = T^{12}_{mb}/\bar{R}_{12/13}$, with $\bar{R}_{12/13} = 13$. The triangle symbols show the mass spectrum obtained using the technique described above.

From Figure 2.7*b* it is clear that assuming ^{12}CO(1–0) is optically thin greatly underestimates the mass (by a factor of ten) compared to the opacity-corrected estimates. The constant opacity correction gives a more realistic estimate of the total mass. The shape and slopes of the mass spectrum using the constant opacity correction and the mass spectrum obtained using the optically thin assumption are basically the same. Assuming that the opacity of the ^{12}CO(1–0) is constant implies that the high-velocity ^{12}CO(1–0) emission is optically thick. Since it is clear that the ^{12}CO(1–0) line is optically *thick* at outflow velocities close to the cloud V_{LSR} and it is optically *thin* at high velocities, a more precise approach is to assume that the ^{12}CO(1–0) line opacity depends on velocity. The velocity-dependent opacity correction results in low-velocity mass estimates which are close to the constant opacity assumption, and at high velocities the mass estimates converge to the optically thin assumption estimates. This steepens the mass spectrum in both the low and high velocity regimes.

Comparing Figures 2.7*b* and 7*d* we see that the correction for ambient cloud emission makes the mass spectrum shallower. This is because there is more contamination from the ambient cloud at lower velocities than at higher velocities. Not correcting for such contamination results in an overestimation of the mass at lower velocities. Thus, correcting for a velocity-dependent opacity and correcting

for ambient cloud emission have opposite effects on the mass spectrum slopes. Most previous outflow studies do neither of the two corrections, so it could be that their estimates of the mass spectrum slope are reasonable by chance.

2.4 Discussion

2.4.1 Mass and Energetics

The total mass of the red lobe of the HH 300 outflow, using the method described above, for $v_{out} \geq 0.75$ km s^{-1}, is 2.4 M$_\odot$. As can be seen in Figure 2.7*d*, the mass-velocity relation at velocities between 0.75 and 1.85 km s^{-1} follows a power-law trend, $dM(v)/dv \propto v^{-\gamma}$. A second power-law, with a steeper slope, is present for velocities greater than 1.85 km s^{-1}. This broken power-law trend is typical of many outflows (see §2.4.2). If we take the "outflow mass" to include only mass at velocities which follow the broken power-law trend, then we find 2.4 M$_\odot$ in the outflow. Notice the lone point at $v_{out} = 0.53$ km s^{-1}, which lies below the extrapolation of the power-law trend in Figure 2.7*d*. If we add the mass at this very slow outflow velocity (corrected by ambient emission, as explained above), we then find the total mass of the red lobe of HH 300 outflow to be 4.3 M$_\odot$, for $v_{out} \geq 0.53$ km s^{-1}. The mass of the ambient cloud gas that surrounds the red lobe of HH 300 (only the B18w gas southwest of IRAS 04239+2436) is 57 M$_\odot$, thus the mass in the outflow, including the slowest velocity material we can reliably call "outflow", is 7% of the mass of its surrounding cloud.

The total (line-of-sight) momentum in the red lobe of the HH 300 molecular outflow, for $v_{out} \geq 0.75$ km s^{-1} is 2.2 M$_\odot$ km s^{-1}, and for $v_{out} \geq 0.53$ km s^{-1} is 3.2 M$_\odot$ km s^{-1}. The amount of momentum that has been deposited in the cloud by HH 300 presumably should be substantially more, as we have only considered the line-of-sight velocity component. If we assume that i is between 5° and 15°, then the outflow momentum would be between 12 and 37 M$_\odot$ km s^{-1}, for $v_{out} \geq 0.53$ km s^{-1}. Thus, our ignorance of i brings huge uncertainties to

Table 2.3. Mass, Momentum, and Kinetic Energy of the Redshifted Lobe of HH 300

Parameter	$v_{out} \geq 0.75$ km s^{-1}	$v_{out} \geq 0.53$ km s^{-1}
Mass [M$_\odot$]	2.4	4.3
Momentum [M$_\odot$ km s^{-1}]	2.2 $(\sin i)^{-1}$	3.2 $(\sin i)^{-1}$
Kinetic Energy [$\times 10^{43}$ erg]	2.1 $(\sin i)^{-2}$	2.6 $(\sin i)^{-2}$

the value of the outflow momentum. The kinetic energy of the outflow is even more uncertain, as it depends on $(\sin i)^{-2}$. The kinetic energy of the outflow for $v_{out} \geq 0.75$ km s^{-1} is 2.1 $(\sin i)^{-2} \times 10^{43}$ erg, and for $v_{out} \geq 0.53$ km s^{-1} is 2.6 $(\sin i)^{-2} \times 10^{43}$ erg. So, for example, if $i = 10°$, the kinetic energy is about 8×10^{44} erg. The mass, momentum, and kinetic energy estimates of the HH 300 outflow are listed in Table 2.3.

Independent of the real (angle-corrected) momentum, we can still map line-of-sight outflow momentum. In Figure 2.8 we show a contour plot of the total momentum for $v_{out} \geq 0.97$ km s^{-1} (*not* corrected for inclination angle). We are sure there is very little or no emission from the ambient cloud at these velocities. The momentum plot shows distinctive peaks along the outflow axis. These peaks coincide with the different clumps discussed in §2.3.2. The peaks are surrounded by a ~ 0.3 pc wide and ~ 1 pc long, lower-level, momentum distribution.

We assume that the dimension along the line of sight of both B18w and the HH 300 outflow are similar to their respective short axes. Using the maps in Figure 2.8, we estimate their volumes to be $1.7 \times 0.7 \times 0.7 \sim 0.83$ pc^3 and $1.0 \times 0.3 \times 0.3 \sim 0.09$ pc^3, respectively. Hence, we may conclude that a notable fraction (0.09 pc^3/0.83 pc^3 $\sim 11\%$ of the volume) of the B18w filamentary dark cloud is being injected with momentum from the red lobe of the HH 300 outflow.

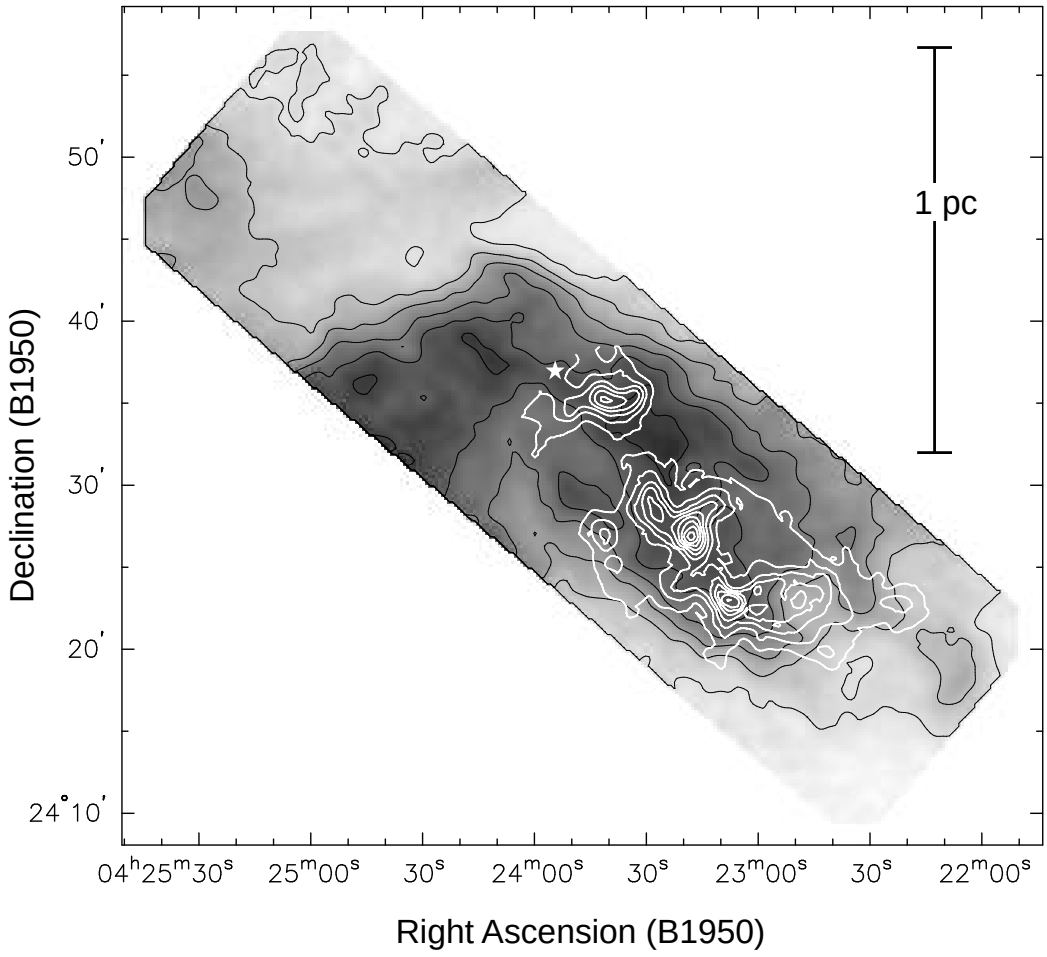

Fig. 2.8.— Contour map of outflow total momentum, *not* corrected for inclination angle, for outflow velocities greater than 0.97 km s^{-1}. The momentum contour map is superimposed on a B18w grey-scale map of ^{13}CO integrated intensity for $5.8 < v < 7.1$ km s^{-1}, as shown in Figure 2.3*b*. The momentum was obtained using the velocity-dependent opacity correction technique described in the text. The starting contour and the contour steps on the momentum map are both 1.5×10^{-4} $M_\odot$ km s^{-1}.

2.4.2 Mass-Velocity Relation

An interesting aspect of the HH 300 outflow is the steep power-law slopes we find in the mass-velocity relation ($\gamma = 4.0$ for v_{out} 0.75 to 1.85 km s^{-1}, and $\gamma = 7.8$ for $v_{out} \geq 1.85$). All molecular outflows exhibit a power-law mass-velocity relation in which there is more outflowing mass at low velocities than at higher velocities, that is, $dM(v)/dv \propto v^{-\gamma}$, where $\gamma > 0$. Most outflows show a break in the power-law relation and a steeper power-law dependence at high velocities. Recently, Richer et al. (2000) compiled existing data on 22 molecular outflows with central source luminosity ranging from 0.58 $L_\odot$ to 3×10^5 $L_\odot$. The low-velocity ($v < 10$ km s^{-1}) mass spectra γ's for the 22 sources ranges from about 0.25 to 2.5, with most of the values concentrating between 1.25 and 2. For high velocities, γ ranges from 2.5 to 7.5, with most of the values between 3 and 4.

Numerical and theoretical studies have also shown that the mass spectrum has a power-law dependence. The models of Zhang & Zheng (1997) and Smith, Suttner, & Yorke (1997), in which a molecular outflow is produced by the entrainment of the ambient gas by a bow shock, find a γ of about 1.8, and steepening of the mass-velocity relation at high velocities. Downes & Ray (1999), with their numerical bow shock models, find that the slope of the power-law mass spectrum ranges between $\gamma = 1.58$ and $\gamma = 3.75$ (depending on the parameters of the simulation). Both Smith et al. (1997) and Downes & Ray (1999) find that γ increases with time. On the other hand, the analytical study by Matzner & McKee (1999) finds that $\gamma = 2$ for all times, independent of the time history of the driving wind and for a wide variety of ambient density distributions. The study of Matzner & McKee (1999) differs from the other ones listed above in that the outflow is not specifically created by the entrainment of the ambient gas by a bow shock, but rather by a wide-angle wind which sweeps the ambient gas into a momentum-conserving shell.

The majority of observations and models in the literature to date seem to indicate that $\gamma \sim 2$. Our observations indicate that the HH 300 outflow has a much steeper ($\gamma \sim 4$) mass spectrum than most outflows (from low and intermediate-mass

Table 2.4. Comparison of γ for Different Velocity-Dependent Opacity Corrected Outflows

Outflow	Average γ[a]		References
	Without ambient cloud correction	With ambient cloud subtracted	
Circinus Flow A	4.0	...[b]	1
Circinus Flow B	3.7	...[b]	1
Circinus Flow C	3.8	...[b]	1
B5-IRS 1	3.9	2.7	2
MMS 9	3.8	1.8	3
HH 300	5.2	4.0	4

[a]The number given is the average value of γ, over both lobes of the given outflow (except for HH 300, where only one lobe was studied). The value of γ is defined to be the power-law slope in the relation $dM(v)/dv \propto v^{-\gamma}$. For the two outflows with mass spectra exhibiting power-laws (HH 300 and MMS 9), we show the "low-velocity" γ.

[b]There is no mass spectrum with ambient cloud subtracted for these outflows.

References. — (1) Bally et al. 1999; (2) Yu et al. 1999; (3) Yu et al. 2000; (4) This Chapter.

stars), both observed and modeled. On the other hand, our results are similar to the outflows analyzed by BRLB, YBB, and Yu et al. 2000 (hereafter, YBSBB). In Table 2.4 we show the average value of γ for the outflows where mass estimates have included a correction for velocity-dependent ^{12}CO line opacity. From Table 2.4 we can see that, after this correction, most of the outflows have power-law slopes larger than 2. A small difference between the results in this paper and those of BRLB and YBB is that we find a steepening of the mass spectrum power-law for high velocities in HH 300, whereas BRLB and YBB state that the outflows in their studies do not show such steepening. Examining the mass spectrum plots of BRLB and YBB, it is clear that some of them do not show a break in the power-law. Yet, others of their mass spectrum plots could be fitted with two distinct power-laws, where the high-velocities would have a steeper γ than the low-velocities.

There is no question that the ^{12}CO line is optically thick in the HH 300 flow, and that its opacity depends on velocity, as the ^{12}CO(1–0)/^{13}CO(1–0) plot (Figure 2.7*a*) demonstrates. The same is true for the Circinus (BRLB), the

B5-IRS 1 (YBB) and the MMS 9 (YBSBB) outflows. It is safe to say that the ^{12}CO line of most, if not all, outflows is optically thick at low velocities and that its opacity is velocity dependent. Thus, if low-velocity ^{12}CO emission is used to estimate the outflow mass, and no correction is made for a velocity-dependent opacity, the resultant mass spectrum power-law slope will be *underestimated*. This can be shown using our data. If we assume that ^{12}CO(1–0) is optically thin or that it has a constant (velocity-independent) opacity; we obtain $\gamma \sim 3.2$ for the HH 300 outflow mass spectrum (uncorrected for ambient emission), while the velocity-dependent-opacity-corrected value is ~ 5.2 (see Figure 2.7*b*). But, the fact that the HH 300, B5 IRS 1, and Circinus outflows all have large values of γ does not necessarily mean that γ would dramatically increase for all other outflows if they were to be corrected for velocity-dependent opacity. The values of the "low-velocity" γ's for some young outflows, such as L1448 (data from Bachiller et al. 1990, plot from Bachiller & Tafalla 1999) and NGC 2264G (Lada & Fich 1996), were calculated from fits to the mass spectra only for velocities greater than 7.0 km s^{-1} from the line core, where the assumption that the line is optically thin is not a bad one. Thus, for those flows we would not expect the value of γ to change significantly if a velocity-dependent-opacity correction of the ^{12}CO line were included in the analysis. Ultimately, we expect that if all mass spectra were corrected for opacity, one would find a significant spread in the values of γ perhaps even without a concentration of values around $\gamma \sim 2$.

There are a number of possible explanations for the relatively large value of γ in HH 300. In their paper, YBB present a list of factors that could modify the slope of the mass spectrum. We offer a similar list of factors here, but we focus on the elements that could give rise to a steep slope in HH 300.

YBB state that their outflow mass estimates are affected by the velocity at which they choose to define an optically thin limit for $R_{12/13}$, that is, the velocity at which $R_{12/13}$ is set to the carbon isotopic ratio (see §2.3.3 and Figure 2.7*a*). In our case, changing the isotopic ratio from 62 (the value assumed in this chapter), to 89 (the solar ratio) changes the total mass of the red lobe of the HH 300 outflow by less than 1%, as this change only affects the "high outflow velocity"

($1.9 < v < 3.2$ km s^{-1}) masses. Using any value for the isotopic ratio from 50 to 89 leaves the power-law slope of the low-velocity ($0.7 < v < 1.9$ km s^{-1}) mass spectrum unchanged. The high-velocity γ increases by a maximum of 4%. Thus, the value of the carbon isotopic ratio does not affect our results considerably. (If we had used only a single power-law fit, the isotopic ratio would significantly effect the power-law slope, as in YBB.)

The outflow orientation with respect to the plane of the sky is another factor which can modify the mass spectrum slope. As shown in Smith et al. (1997), where molecular outflows are modeled as entrainment of ambient gas by a bow shock, the value of γ increases as inclination angle (of the flow axis with respect to the plane of the sky) decreases. Specifically, the results of Smith et al. (1997) show one model where decreasing the angle between the outflow axis and the plane of the sky, from 60° to 15°, raises γ from ~ 1.2 to ~ 1.5. Although it is very probable that the axis of the HH 300 outflow is close to the plane of the sky ($i \lesssim 15°$), this would not be enough, by itself, to explain the high value of γ (~ 4) in the red lobe of HH 300.

Contamination from cloud emission can also affect the slope of the mass spectrum. If one does not take the ambient cloud emission into consideration when estimating the outflow mass, one will overestimate the outflow mass at low velocities, and thus the mass spectrum slope will be overestimated. This was shown in § 2.3.3, where it can be seen that the value of γ before correcting for the ambient cloud emission was larger before correction ($\gamma = 5.2 \pm 0.1$) than after it ($\gamma = 4.0 \pm 0.2$). In order to check if we made a good correction, we constructed a mass spectrum of a limited area around clump R3. We made a power-law fit to only the channels between outflow velocities of 1.1 and 1.9 km s^{-1}, which have predominantly outflow emission (based on the appearance of channel maps), and *very little or no ambient cloud emission*. The resulting mass spectrum, uncorrected for ambient cloud emission, has a $\gamma = 3.9 \pm 0.2$, consistent with the mass spectrum of the whole outflow, corrected for ambient cloud emission, which is $\gamma = 4.0 \pm 0.2$. Thus, we are convinced that our correction for ambient cloud emission is a good one, and that the steep value of γ we obtain for the red lobe of the HH 300 outflow is not due to any residual ambient cloud emission at low velocities.

We believe the most important factor in steepening the slope of the HH 300 mass spectrum is outflow evolution. Both the models of Smith et al. (1997) and Downes & Ray (1999) find that the power-spectrum slope of the mass spectrum changes over time. Both studies find that γ steepens as the outflow ages. The ambient material that once was accelerated by bow shock entrainment, slows down as time goes by, meaning more slow gas is accumulated, resulting in a steepening of γ. The simulated outflows of Smith et al. (1997) and Downes & Ray (1999) are relatively young, (600 and 300 years, respectively), but their results seem to indicate that the increasing trend of γ with age would continue as the outflow evolves in time.

Richer et al. (2000; hereafter RSCBC) do not find any indication of time evolution of the low-velocity ($v < 10$ km s^{-1}) γ from outflow from low-luminosity ($L_{bol} < 10^3$ $L_\odot$) sources[2]. The lack of a trend in their results might be explicable in two ways. First, RSCBC estimate the age of the outflows using their dynamical age. The dynamical age of an outflow is estimated using an average or typical velocity for the source being studied and dividing that velocity by the extent of the outflow lobe. This is known to be a poor estimate of the age of an outflow (it could be off by as much as a factor of 10 to 50) as it assumes that the outflow has kept the same "typical" velocity throughout its life and also because it assumes that all outflowing material comes from the immediate vicinity of the source (Masson & Chernin 1993). Second, the outflow masses are obtained without correcting for a velocity-dependent opacity in the CO line, so there could be an underestimation of the value of γ for some of the outflows in RSCBC's sample.

If our physical reasoning for the steepening of γ is correct, we would then expect that γ would evolve differently for outflows in physically different environments. Outflows in much denser mediums will decelerate more rapidly than outflows in

[2]YBSBB show a similar compilation of γ values as a function of outflow dynamical age and as a function of outflow source luminosity. Their compilation is slightly larger than that of RSCBC and includes the B5-IRS 1 and MMS 9 outflows. Unlike RSCBC, YBSBB only use the steeper value of γ (which in most outflows is the "high-velocity γ") for sources that have broken power-law. Similar to RSCBC, YBSBB's small sample makes it hard to state any definitive conclusion about outflow evolution.

low density mediums if the entrainment mechanism is a momentum-conserving one, as it probably is (Masson & Chernin 1993). It would be interesting to conduct a survey of outflows in similar environments, with mass corrected for CO velocity-dependent opacity and with accurate age estimates, in order to test how γ evolves over time.

The analytical study by Matzner & McKee (1999) find that it is hard to obtain a value of the power-law mass spectrum slope very different from 2. This value of $\gamma \sim 2$ is independent of the time history of the driving wind, including its momentum input as a function of time, and applies to a wide variety of ambient density distributions. The entrainment mechanism of the ambient medium in the Matzner & McKee (1999) study does not specifically involve a bow shock, instead a collimated wind sweeps the ambient gas into a momentum-conserving shell, following the models of Shu et al. (1991) and Li & Shu (1996). The Matzner & McKee (1999) model does not take into account an episodic, precessing outflow which could be modifying the underlying density and velocity distribution of the surrounding gas with each mass ejection episode. As an episodic and precessing outflow changes direction, different mass outflow ejection episodes may be able to entrain new ambient material that previous ejections were not able to effect, as well as to reaccelerate gas that had already been put in to motion by a previous ejection. These processes will certainly effect the mass spectrum slope of an outflow over time. More on this is discussed in Chapter 3/Arce & Goodman (2001a).

2.4.3 The episodic and precessing nature of the flow

The most striking thing about the morphology of the HH 300 outflow is its clumpy structure. The velocity maps in Figures 2.4 and 2.5 show discrete clumps in space and velocity. It is also notable that the outflow lobe axis does not have a fixed position angle in the plane of the sky. By drawing a line from the source to the maximum emission point for each of the 5 (redshifted) clumps in the outflow, we obtain position angles in the plane of the sky ranging from 250° to 221° (see Table 2.2). One unlikely interpretation of the flow's appearance is that the

underlying wind that drives the outflow is a wide-angle wind, with an axis very close to the plane of the sky. In this interpretation most of the wind is not detected as the slow radial velocities are hidden under the ambient cloud emission. The redshifted clumps we detect could then be where the wide angle-wind is interacting with pre-existing cloud clumps, which have been moved to those redshifted velocities by the wind. This scenario seems untenable for several reasons. First, in a momentum-conserving wind-clump interaction, the lightest clumps should be the fastest moving clumps. This is not the case for the HH 300 clumps, where, for example, the heaviest clump (R2) has greater velocities than other, much lighter clumps. Second, if bow-shock shapes are caused by the wind-clump interaction, one would expect them to have "downstream" wings. On the contrary, the several clumps that have bow shock like structures have all wings pointing back to the source.

A more plausible explanation is that HH 300 is a precessing and episodic outflow, and that the outflow clumps are made of swept-up ambient gas. The density of the ambient gas in the B18w region should be on the order of 5×10^3 cm^{-3}, and each outflow clump has a mass less than 0.5 M$_\odot$ (see Table 2.2). In order to form a clump of about 0.5 M$_\odot$ by sweeping up gas with density of 5×10^3 cm^{-3} a volume of about 4×10^{52} cm^3 is needed. A cube of side 0.12 pc (or $3'$ at a distance of 140 pc) is more than enough to account for such volume. From the integrated intensity maps (Figures 2.4, 2.5, and 2.6) we see that the clumps have sizes comparable to or are bigger than 0.12 pc. So, it is realistic to say that most of the mass in the clumps could come from gas that has been accelerated very close to the current position of the clump. Another possible scenario is that the clumps formed (by swept-up ambient gas) at a position closer to IRAS 04239+2436 and then moved to their current position (see §2.4.5).

Position-velocity ($p - v$) diagrams of HH 300, constructed by summing all spectra along an axis with a position angle of 220° (which hereafter will be called the outflow axis) are shown for the ^{12}CO(2–1) and ^{12}CO(1–0) lines in Figures 2.9 and 2.10, respectively. It can be seen that at the position of all the clumps, except R5, there is an increase in the extreme emission velocity. The velocity

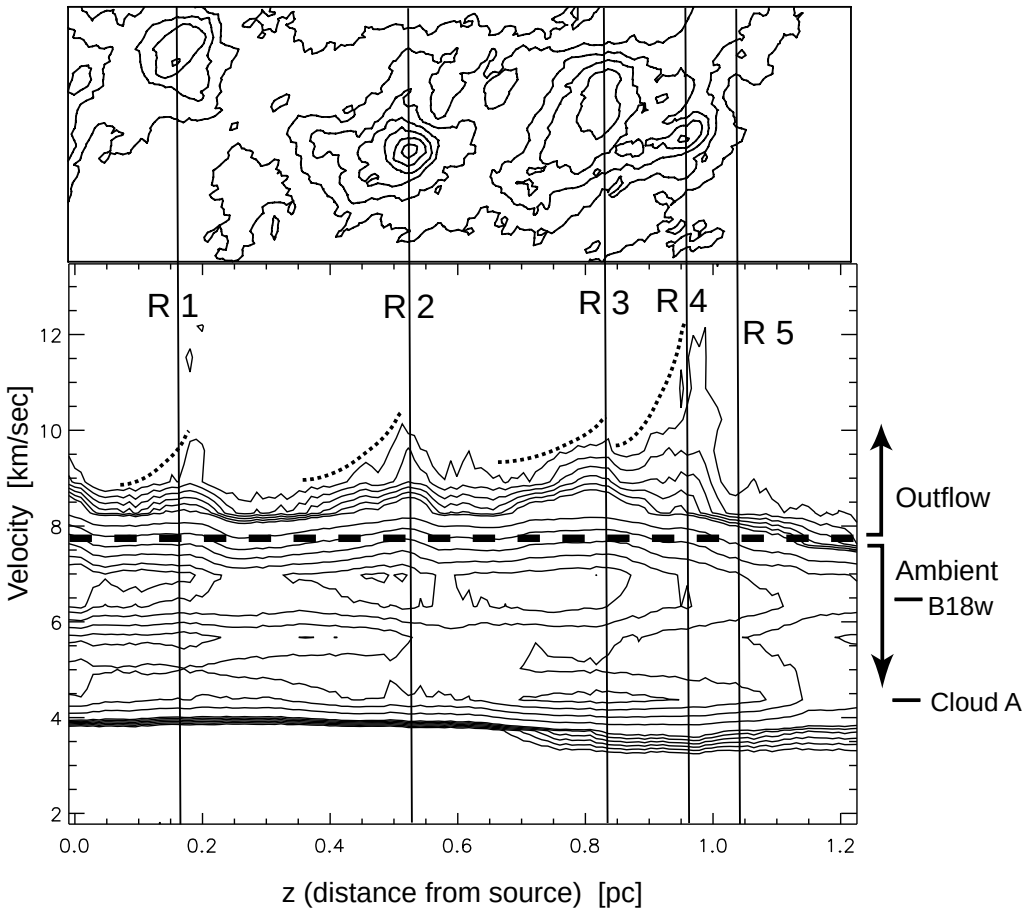

Fig. 2.9.— (*Top*) ^{12}CO(2–1) integrated intensity contour map for velocities between 7.30 and 10.55 km s^{-1}. (*Bottom*) ^{12}CO(2–1) Position-Velocity diagram of the redshifted lobe of HH 300. The outflow velocities, as well as the ambient gas velocities of the B18w cloud and of cloud A, are indicated on the right of the bottom panel. The position of each clump along the outflow axis is marked with a vertical solid line. Notice how at the position of each molecular outflow clump there is an increase in the velocity. The increase in velocity at most of the clump positions, as shown with the dotted curved lines, follows a "Hubble-law", where the velocity increases proportionally to the distance from the source. This velocity structure is consistent with the outflow clumps being produced by bow shock prompt entrainment from an underlying wind (see §2.4.3 for discussion).

structure at the position of each of these clumps is characteristic of the prompt entrainment mechanism, which will produce the highest velocities at the "hot spots" (or local CO maximum of clump), and decreasing velocity trend towards the source (Bence et al. 1996). The kinematic behavior where the velocity of an outflow increases nearly linearly with distance from the outflow source is referred to as the "Hubble-law" for outflows. Thus, in our case, we can say that there is a different outflow Hubble-law associated with each clump. For bow shock models (e.g, Zhang & Zheng 1997; Smith et al. 1997; Downes & Ray 1999) the Hubble-law is a natural consequence of the fact that the highest velocities are found at the head of the bow shock, while the velocity decreases towards the wings. Wide-angle wind models of entrainment (Shu et al. 1991; Matzner & McKee 1999) only produce a single Hubble-law velocity field. We can best explain the Hubble-law "bumps" at the position of the clumps in Figures 2.9 and 2.10 as each being produced by a bow shock at the position of the clumps.

In the bottom panel of Figure 2.10 we show a plot of the total momentum per unit length (measured in cuts perpendicular to the outflow axis), as a function of distance from the source along the flow axis (z), similar to what Chernin & Masson (1995) do for several outflows. It is clear that at the position of each redshifted clump there is a peak in the momentum. The plot in the bottom panel of Figure 2.10 looks very similar to the plots produced by the precessing jet model of Cliffe, Frank, & Jones (1996). In their models, each momentum peak corresponds to different shock structures in a precessing jet.

In HH 300, from the morphology of the knots in the outflow, the $p-v$ diagram, and the momentum distribution all support a picture where the outflow is made up of several bow shocks along its axis, where each shock corresponds to a different ejection event, with a different ejection axis.

Recently, it has been established that it is common for the ejection axis of outflows to precess or wander (e.g., RBD). It is believed that outflow precession is due to the precession of the outflow source, which could itself be caused by the tidal interaction between the circumstellar disk of the outflow source and one (or

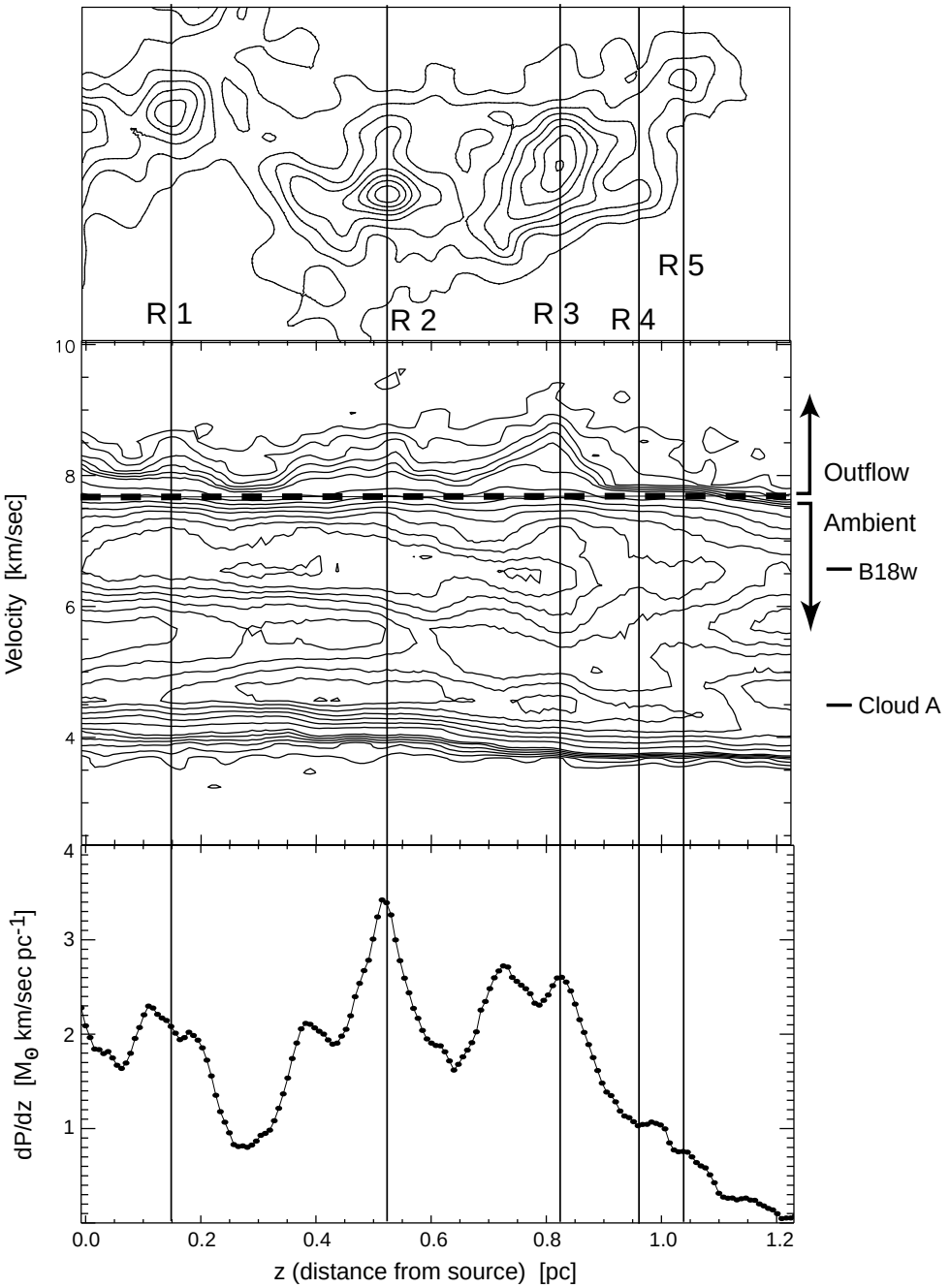

Fig. 2.10.— (*Top*) ^{12}CO(1–0) integrated intensity contour map, as shown in Figure 2.6. (*Middle*) ^{12}CO(1–0) Position-Velocity diagram of the redshifted lobe of HH 300. (*Bottom*) Distribution of the outflow momentum per unit length (dM/dz) along the HH 300 outflow axis. The filled circles represents the total momentum over the width of the outflow lobe. The outflow velocities, as well as the ambient gas velocities of the B18w cloud and of cloud A, are indicated on the right of the middle panel. The position of each clump along the outflow axis is marked with a vertical solid line. Notice that at the positions of the R1, R2, and R3 clumps, the 3 most prominent clumps in ^{12}CO(1–0) , there is an increase in velocity and momentum (see §4.3 for discussion).

many) stellar companion(s) of the source (e.g., Terquem et al. 1999). Reipurth et al. (2000) find that the source of the HH 300 jet is a binary with a separation of only 42 AU, which could explain the precessing nature of the HH 300 outflow. If we assume that clumps R1 and R2, the two clumps with the most extreme position angles, are close to the edges of the precession cone, then the precession period is approximately twice the difference in eruption age, $2(\tau_{dyn,R2} - \tau_{dyn,R1}) \approx 3400$ yr (see Table 2.2). Terquem et al. (1999) give an approximate expression for the precession period of a disk around a young star in a binary system, where the disk surrounds only the primary star. The expression is given in terms of the primary mass, the mass ratio of the two stars, and the ratio of the disk radius to the binary orbit radius. If we assume a primary mass of 0.5 $M_{\odot}$, and a primary to secondary mass ratio of about 1.6, the precession period is about 4000 yr. Hence, it is plausible that the precessing nature of the HH 300 outflow could be explained by the fact that its source lies in a multiple-star system.

2.4.4 Effects on the cloud

Although the HH 300 outflow is not impressively massive or energetic (like R Mon, Wolf et al. 1990), it is still an "average" outflow (in the context of the outflow catalog of Wu et al. 1996), which can apparently significantly effect the velocity structure of its host cloud. We have already shown that the HH 300 flow is depositing a fair amount of momentum over a notable volume of its environment. Another way of assessing the effect that an outflow has on the parent cloud is by studying the behavior of the velocity dispersion as a function of position. By doing so we can examine the effects that the flow has on the cloud kinematics. To do this, we fitted a single Gaussian to the ^{13}CO spectral component associated with B18w, for all spectra southwest of the source. We then made a grey-scale plot of the velocity width (Δv) obtained through the Gaussian fit (Figure 2.11). It appears that the outflow clumps are associated with peaks in the ^{13}CO velocity width. Many of the ^{13}CO spectra at the large Δv positions exhibit two peaks. We interpret these two separate velocity components as one arising from the cloud

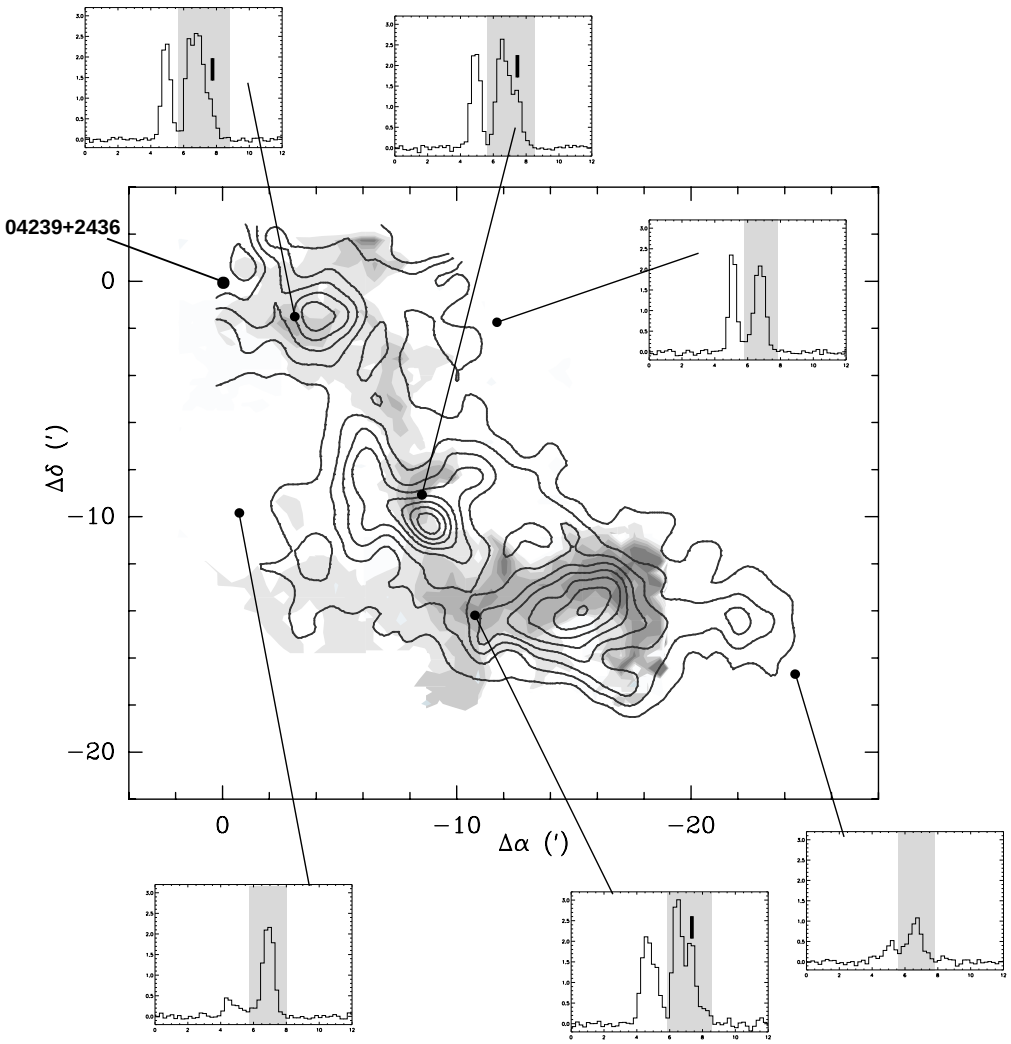

Fig. 2.11.— ^{12}CO(1–0) integrated intensity map of the HH 300 outflow, as in Figure 2.6, superimposed on a grey-scale map of ^{13}CO line width (FWHM). First grey tone corresponds to a width of 1.0 km s^{-1}. Between each grey tone there is an increment of 0.2 km s^{-1}. Coordinate offsets are given with respect to the outflow source's position at $(\alpha,\delta)_{1950} = (4^h23^m54^s.5, 24°36'54'')$. Six example ^{13}CO spectra at different position are shown. In all spectra, the cloud A and the B18w spectral components can be seen. The B18w (+ HH 300 in some cases) spectral component is highlighted in grey. Three spectra are from regions presumably unaffected by the HH 300 outflow, and three are from regions of the cloud affected by the outflow. On these last three, a vertical solid line indicates the position of the separate spectral component, presumably due to the outflow. All spectra are plotted with the same axes ranges: 0 to 12 km s^{-1} in the velocity axis; and -0.2 to 3.2 K on the antenna temperature axis.

emission, and one arising from both cloud and outflowing ^{13}CO emission. The existence of these multiple peaks implies that in certain positions the outflow has put substantial amounts of gas in motion in order for the outflow spectra to appear as a separate velocity component from that of the cloud, rather than just a low-emission high-velocity wing in the cloud component. Hence, detecting one (or more) easily identifiable velocity components attributable to an outflow is yet another indication that the flow is having a major effect on the cloud gas kinematics.

Different velocity components in outflow spectra from high-density tracers have been observed in the Mon R2 outflow (Tafalla, Bachiller & Wright 1994). The clumps responsible for the multiple peaks in the CS spectra of the Mon R2 outflow have been interpreted as gas from the dense core that has been put into motion (Tafalla et al. 1997). On the other hand, the multiple velocity components arising from outflow ^{12}CO spectra observed in some low- and medium-mass stars (e.g., L1448, Bachiller et al. 1990; IRAS 03282+3035, Bachiller, Martín-Pintado, & Planesas 1991; HH 111, Cernicharo & Reipurth 1996), usually called high-velocity bullets, have masses of the order of 10^{-3} M$_\odot$ (e.g., Hatchell, Fuller, & Ladd 1999), and are thought to be composed of jet material. The HH 300 redshifted clumps have relatively large masses (~ 0.1 M$_\odot$, see Table 2.2), which makes it probable that they are mainly made up of swept-up material, more like the high-density clumps of the Mon R2 outflow. Therefore, we conclude that the ^{13}CO clumps in HH 300 consist of medium-density ($n \sim 10^3$ cm^{-3}) gas entrained by the outflow.

We can quantify the effect that the HH 300 flow has on its parent cloud using different methods.

One method is to compare the flow's total energy with the cloud's total turbulent kinetic energy. The total kinetic energy of a cloud where thermal motions are a negligible part of ΔV, is given by $E_{turb} = \frac{3}{16 \ln 2} M_c \Delta V^2$, where M_c is the cloud mass and ΔV is the observed FWHM velocity line width. In our case, from the ^{13}CO data, the mass of the whole B18w filamentary structure (seen in Figure 2.3*b*) is $M_c = 72$ M$_\odot$. The velocity width is $\Delta V \sim 0.8$ km s^{-1}, so $E_{turb} \sim 3 \times 10^{44}$ erg.

The outflow kinetic energy is about 2.6 $(\sin i)^{-2} \times 10^{43}$ erg, thus the HH 300 outflow has the potential of making a substantial contribution to the turbulent energy of the cloud. For $i = 17°$, the outflow kinetic energy is equal to the kinetic energy of the B18w region. Armstrong & Winnewisser (1989) discovered that the kinetic energy of a parsec-scale outflow in L673 could be 6 to 0.4 times (depending on the assumed projection angle and the amount of mass "hidden" under the line core) the turbulent energy in the cloud. At the time Armstrong & Winnewisser (1989) made their study, astronomers had no idea of the common occurrence of parsec-scale HH flows from young stellar objects. Now, with the discovery that HH flows may typically extend for several parsecs (RBD) we should reconsider the role of outflows in driving the turbulent energy of molecular clouds.

We can also asses the importance of the HH 300 outflow energy input on its parent cloud by using the results of numerical simulations. The self-consistent magnetohydrodynamics (MHD) simulations of Gammie & Ostriker (1996) study MHD turbulence under density, temperature and magnetic field conditions representative of those found in Galactic molecular clouds. The models use "slab symmetry", in which all variables are a function of one independent spatial variable x and time t. Using equation 34 in Gammie & Ostriker (1996), we can derive the input power needed to support a molecular cloud in equilibrium. We approximate the "linear" dimension (L) of B18w to be twice the geometric mean of its axes ($\sim$ 1.1 pc). We assume a mean density of 5×10^3 cm^{-3}, and a β parameter[3] of 0.01. Using these approximations we find that we would need about 0.4 $L_\odot$ of input power at a scale of 1 pc (the size of the outflow lobe) to counter the dissipation of MHD turbulence in the B18w region and thus support it against gradual gravitational contraction.

The power of an outflow is usually estimated by dividing the outflow kinetic energy by the dynamical age of the outflow. The conventional way to estimate the dynamical age of a molecular outflow assumes that all the gas in the outflow originates at the young star. This assumption is wrong, since the vast majority

[3]The β parameter is defined as the ratio of the square of the sound speed to the square of the Alfvén speed in the cloud, that is $\beta = c_s^2/v_A^2$

of the gas in a molecular outflow comes from the entrained gas in the host cloud (along the extent of the outflow) that has been put in motion by the underlying stellar wind. Since there is no way to obtain an accurate estimate of the outflow lifetime, we estimate a lower and an upper bound to the dynamical age in order to estimate an upper and lower bound to the outflow power. We estimate the dynamical age lower limit to be the time it has taken HH 300A (the HH knot which currently lies further to the source) to travel to its current position. The distance from the source to HH 300A is 1.2 pc, and if we assume a typical HH jet velocity of 200 km s^{-1}, we then obtain a dynamical age of about 5900 yr. As an upper limit on the age we use 2×10^5 years, the statistical lifetime of outflows as derived by the study of Parker, Padman, & Scott (1991). We then estimate the lower and upper limits of the outflow power to be 1.1×10^{-3} $(\sin i)^{-2}$ to 3.6×10^{-2} $(\sin i)^{-2}$ $L_\odot$. If we assume that $i \sim 10^\circ$, then the outflow power's lower limit is only about a factor of ten less than what is needed to drive the MHD turbulence in B18w. Thus, the HH 300 outflow has the potential to make a substantial contribution to the power needed to sustain the MHD turbulence in B18w.

Yet another way to estimate the effects of the flow on the cloud is to compare the flow's energy with the cloud's binding energy. The B18w cloud binding energy ($\sim GM_c^2/R_c$), where we estimate R_c to be the geometric mean of the short and long axes of B18w, is about 8×10^{44} erg. Hence, if $i \sim 10^\circ$ the HH 300 outflow would have enough kinetic energy to potentially disperse a major fraction of the B18w region. From our estimates (see §2.4.1) we see that HH 300 is effecting a notable fraction of B18w, so whether most of the outflow kinetic energy will be converted to turbulent energy or it will be used to directly disperse the cloud gas (see §2.4.6 for more on this), it is clear that the HH 300 outflow will have a major effect on the evolution of B18w.

2.4.5 The structure of B18w

The axis of the HH 300 redshifted outflow lobe is parallel to B18w's long axis, as can be seen in both Figure 2.2 and 2.6. The B18w region looks like a protuberance

that sticks out from the main B18 molecular cloud (see Figure 2.1). Given the nice positional coincidence of the outflow's and the dark cloud's axes, in addition to the particular shape of B18w and its position with respect to the rest of the B18 cloud, we originally flirted with the idea that the HH 300 outflow was creating the B18w dark cloud. We hypothesized that the outflow was dragging gas and dust from the star-forming core and forming the B18w dark cloud. Without calculating any estimates of mass for HH 300 and B18w, this seemed like a reasonable idea. Similarly, Bence et al. (1996) speculate that the RNO 43 outflow's most southerly bow shock could be responsible for ejecting material from the main cloud and creating a spur of cloud material, seen in ^{12}CO emission and in extinction (see their Figure 19). But, once we estimated the mass of the outflowing material to be only 7% that of the surrounding ambient gas, in addition to studying the kinematics of the gas, we concluded that what we observe to be the "current" HH 300 molecular outflow has not created the B18w region. Moreover, if this scenario were true one would expect the blue and the red lobes to drag along similar amounts of gas. As seen in Figures 2.1 and 2.8, the B18w cloud extends southwest with respect to the outflow source but does not extend northeast of the source, where one would expect the blue lobe to be. Such a high asymmetry in the "dragging process" is highly unlikely. Even if this scenario does not apply to the HH 300 outflow, we still believe that the process in which an outflow ejects and/or drags gas and dust from a dense core (or any other dense region in the parent cloud) and moves it to distances of the order of 0.1 to 1 pc could take place in other sources (e.g., see Chapter 4). If HH 300 is not "producing" the B18w region, then the fact that B18w and HH 300 have long axes with similar position angles is a coincidence. In that case, HH 300 has a shape similar to B18w because B18w is the cloud that "supplies" the gas that the HH 300 molecular outflow is made of. That is, the parent cloud is constraining the morphology of the *observed* molecular outflow.

2.4.6 The cumulative effect of outflows

Our observations clearly show that even low-mass young stellar objects with a luminosity of about 1 $L_{\odot}$ can affect their surrounding density and kinematical distribution on parsec scales. From our results, we can speculate that the cumulative action of many outflows, from different YSOs could have a profound effect on a cloud's evolution and fate. The cumulative effect of many outflows could be: 1) to produce just enough turbulent energy to support the cloud against gravitational collapse; 2) to greatly increase the turbulent energy to more than the binding energy of the cloud; or 3) to put enough ambient gas into motion as to directly disperse the cloud. If enough gas is moved out of the gravitational potential well of the cloud, the cloud would eventually disperse. If the ambient density is relatively high and the outflow momentum is relatively low, then the outflowing material will eventually slow down through the interaction with the ambient medium, mixing with its surroundings, and feeding the turbulent energy of the cloud. On the other hand, if the ambient density is relatively low and the outflow momentum is high, the swept-up gas will barely decelerate and it could eventually be "pushed away" from the cloud. It is hard to conclude which of these two scenarios will prevail in a given cloud, without modeling the interface between outflow and cloud. Further theoretical and numerical investigations should concentrate on how efficiently bulk motions, produced by outflows, can decay to produce turbulence as a function of a cloud's density and outflow energy. Now that it has been established that individual outflows are energetic enough, and large enough to substantially affect a big portion of their host cloud, observational studies should concentrate in investigating the cumulative effects that many outflows have on a molecular cloud and on a cloud complex (e.g., see BRLB).

2.5 Conclusion

We mapped the red lobe of the giant molecular outflow associated with the HH 300 flow in the ^{12}CO(2–1) line, with a beam size of 27″. We also made a

more extended map of the gas surrounding the HH 300 flow at the ^{12}CO(1–0) and ^{13}CO(1–0) lines, with 45″ and 47″ beam sizes, respectively. By observing a large extent of the gas surrounding the outflow we are able to study the outflow in the context of its surrounding medium. Also, the ^{13}CO observations help us assess the effects the outflow has on the surrounding moderate-density ($n \sim 10^3$ cm^{-3}) gas structure and kinematics. In addition, the combined ^{12}CO(1–0) and ^{13}CO(1–0) line observations enable us to estimate the mass of the outflow by correcting for the velocity-dependent opacity of the ^{12}CO(1–0) line. Due to "contamination" from emission of another molecular cloud along the same line-of-sight we are not able to study the blue lobe of the HH 300 outflow.

Our results show that the HH 300 outflow has a very clumpy structure. We identify five ^{12}CO redshifted clumps, each of which is readily apparent in position-position-velocity space. They each have masses of the order of a few 10^{-1} M$_\odot$ and reach radial velocities of about 3 km s^{-1} from the ambient cloud velocity. Given the low inclination of the outflow with respect to the plane of the sky, the deprojected velocities of these clumps are likely to be higher than 15 km s^{-1}. Such high masses and low velocities suggest that these clumps are made of swept-up ambient gas. The spatial distribution of the clumps, the velocity structure, and the momentum distribution of the outflow indicate that these clumps arise from prompt entrainment, most probably produced by bow shocks, arising from the young star's mass ejection episodes. Each of these clumps has a different orientation on the plane of the sky (or position angle) with respect to the outflow source. We conclude that HH 300 is a precessing and episodic outflow.

We obtain a power-law mass spectrum slope of -4.0 ± 0.2 for low outflow velocities and a slope of -7.8 ± 0.4 for high outflow velocities, for the red lobe of HH 300. These slopes are steeper than the average for other outflows. To obtain the outflow mass we used a velocity-dependent ^{12}CO(1–0) optical depth, and we corrected the low-velocity outflow mass for "contaminating" ambient cloud emission. Previous outflow studies, with the exception of Bally et al. (1999), Yu et al. (1999), Yu et al. (2000) from which we obtain the idea, do not correct for the velocity-dependent opacity of the line, when obtaining outflow parameters from

their ^{12}CO data. As we have shown, not applying this correction will underestimate the low-velocity outflow mass. We believe that some low-velocity outflows will exhibit a steeper mass spectrum power-law slope (γ) once their masses have been corrected for the velocity-dependence of the ^{12}CO line. Thus, we expect that for a sample of outflows (with different ages) the value of γ will have a wider range of values than what is currently found in the literature. The fact that HH 300 has a steep mass spectrum power-law slope ($\gamma \sim 4$) is most probably due to the evolution of outflow mass kinematics. Ambient material accelerated by several episodes of mass ejection by the young star will eventually slow down, leading to accumulation of slow gas, and a steepening of γ.

The HH 300 outflow, although not extremely powerful, is depositing a fair amount of momentum ($3.2\ (\sin i)^{-1}$ M$_\odot$ km s^{-1}) and kinetic energy ($2.6\ (\sin i)^{-2} \times 10^{43}$ erg) over a notable volume ($\sim 11\%$) of its parent dark cloud (B18w). We qualify the effects that the HH 300 flow has on its host cloud by using three different methods. If HH 300 has an inclination to the plane of the sky (i) of about 10°, then the red lobe of the HH 300 molecular outflow has more than enough energy to supply the turbulent energy of B18w, more than enough energy to gravitationally unbind the B18w region, and enough power to make a substantial contribution to the power needed to sustain the MHD turbulence in B18w. In addition, the ^{13}CO data indicate that the HH 300 flow is having a major effect on the cloud gas kinematics, and is able to redistribute considerable amounts of its surrounding medium-density ($\sim 10^3$ cm^{-3}) gas.

Our study clearly shows that even low-mass young stellar objects of about 1 L$_\odot$ can produce drastic changes in their surrounding environment, and affect a notable volume of their parent clouds. This is probably a characteristic of giant HH flows, which typically extend over a few parsecs on the sky, and precess. Giant outflows have the potential of modifying the velocity and density structures not only of their host core, but also of their host cloud, even at parsec-scale distances from the source. The cumulative action of giant outflows from young stellar objects will certainly have a profound effect on a cloud's evolution and fate.

Chapter 3

The Mass-Velocity and Position-Velocity Relations in Episodic Outflows

ABSTRACT

While observational evidence for the episodic nature of young stellar outflows continues to mount, existing numerical and theoretical models of molecular outflows assume they are formed by the interaction of a non-episodic wind from a young stellar object with an ambient cloud. In this chapter we estimate and discuss the effects of episodicity on the mass-velocity and position-velocity relations observed in molecular outflows. We explain how many recent observational results disagree with the predictions of non-episodic outflow models, and we offer simple explanations for the discrepancies. In particular, we discuss how an episodic stellar outflow can steepen the power-law slope of the mass-velocity relation in a molecular outflow. And, we illustrate how an episodic outflow can produce multiple "Hubble-wedges" in the position-velocity distribution of a molecular outflow. With a little more information than we have now, it may be possible to use the "fossil record" embedded in a molecular outflow's mass-velocity and position-velocity relations to reconstruct the history of a young stellar object's mass ejection episodes.

Published in: *The Astrophysical Journal*, 551, L171–174, 2001 by H. G. Arce & A. A. Goodman

3.1 Introduction

As forming stars accrete mass inside molecular clouds, they simultaneously throw away a large fraction of that mass in a vigorous outflow. So-called "molecular" or "CO" outflows are one of several manifestations of these mass outflows from young stellar objects (YSOs). The molecular outflows consist primarily of swept-up ambient cloud material, and are most likely driven by an underlying (faster) flow emanating from the forming star and/or its circumstellar disk.

Spectral-line observations of molecular outflows have shown that they exhibit several common observational characteristics. A log-log plot of outflow mass as a function of velocity (a.k.a. a "mass spectrum"), usually shows power-law mass-velocity ($M - v$) relations where $dM(v)/dv \propto v^{-\gamma}$. Position-velocity relations of outflows often exhibit another common characteristic —a so-called "Hubble-law" where the maximum velocity of the outflowing gas increases nearly linearly with distance from the source.

Many observational and theoretical studies have found that molecular outflows have a mass spectrum with $\gamma \sim 2$ (e.g., Lada & Fich 1996; Smith, Suttner, & Yorke 1997; Matzner & McKee 1999), and that the outflows can be characterized by a single Hubble-law (e.g., Meyers-Rice & Lada 1991, Shu et al. 1991; Lada & Fich 1996; Matzner & McKee 1999). But, recent outflow studies (e.g., Yu et al. 1999; Chapter 2/Arce & Goodman 2001b) have shown γ to be much steeper than 2 in some cases. Furthermore, the position-velocity diagrams of those steep-mass-spectrum molecular outflows are characterized by several Hubble-law "wedges," rather than a single one. In this *Letter*, we show how an *episodic*[1] outflow could easily produce mass spectra with $\gamma > 2$ and multiple Hubble wedges.

[1]We use the term "episodic outflow" to mean an outflow that varies in shape, mass loss rate, direction, and/or velocity in an unpredictable way and it is "not-strictly-periodic". Episodic outflows (with ages about 10^4 to 10^5 yr) are characterized by events of violent mass ejection ($\dot{M}_{out} \sim 10^{-5}$ to 10^{-4} $M_\odot$ yr^{-1}) every 500 to 10^3 yr or so, with states of no, or very low ($\dot{M}_{out} \sim 10^{-8}$ to 10^{-7} $M_\odot$ yr^{-1}) mass ejection between the violent outburst episodes. Several mechanisms which produce episodic outflows from young stars have been discussed in the literature (e.g., self-regulated thermal disk instabilities, Bell & Lin 1994; companion-disk interactions in a multiple stellar system, Reipurth 2000, and references therein).

3.2 Mass-Velocity Relation

3.2.1 Observing the $M - v$ Relation

Observers measure molecular outflow mass as a function of velocity using molecular spectral line maps, usually of the ^{12}CO(1–0) line. In practice, the mass-velocity relation is obtained by calculating mass per δv-wide velocity bin and plotting mass as a function of velocity offset from the host cloud's mean velocity. The observed mass-velocity relations to date always imply more mass at low outflow velocities than at higher outflow velocities. Usually, $\log(dM/dv)$ vs. $\log(v)$ has a broken-power-law appearance, with $dM(v)/dv \propto v^{-\gamma_{low}}$ for "low" outflow velocities, and $dM(v)/dv \propto v^{-\gamma_{high}}$ for "high" velocities. The border between "high" and "low" is set by the break in the power law, and $\gamma_{high} > \gamma_{low}$ (see Bachiller & Tafalla 1999 and references therein). Hereafter γ is used to mean γ_{low} whenever $\log(dM/dv)$ has a broken power-law appearance.

Most observational outflow studies estimate outflow mass by assuming either that ^{12}CO emission is optically thin at all outflow velocities, or by correcting for a constant (velocity-independent) ^{12}CO line opacity. In the majority of studies where the outflow mass is obtained in this conventional way, γ ranges from about 0.5 to 3.5, with a concentration of values near $\gamma \sim 2$ (e.g., Richer et al. 2000). In fact, however, the ^{12}CO line is often optically thick, and the exact value of opacity depends on velocity. Not correcting for the velocity-dependent opacity will, in most cases, underestimate the value of γ. A few very recent outflow studies have explicitly taken the velocity-dependent opacity of the ^{12}CO line into account when estimating outflow mass, and these studies generally find $\gamma > 2$ (Bally et al. 1999; Yu et al. 1999; Yu et al. 2000; Chapter 2). Discussions on the possible factors that may produce a large value of γ can be found in Yu et al. (1999) and Chapter 2. But, just because these studies have yielded a steeper mass-spectrum slope, on average, than the "conventional" outflow studies, does not necessarily mean that γ would dramatically increase for all outflows if they were corrected for the velocity-dependent opacity of ^{12}CO. In some cases, usually involving very fast

outflows, the assumption that the ^{12}CO is optically thin at the outflow velocities is fine, and there is no need for opacity correction. In general, though, we expect that a compilation of velocity-dependent-opacity-corrected mass spectra would yield a distribution of γ's, with mean $\gamma > 2$. As discussed in §3.2.3 below, episodic outflows could produce such a distribution of observed γ's.

3.2.2 Modeling the $M - v$ Relation

Numerical and theoretical studies predict that a molecular outflow mass spectrum should have a power-law dependence. In the numerical models of Zhang & Zheng (1997) and of Smith et al. (1997), molecular outflows are produced by the entrainment of ambient gas by a bow shock, and γ is found to be ~ 1.8 over most of the outflow velocity range. Both models also find a turn-down in the mass spectrum at very high velocities, where $\gamma >> 1.8$. In their numerical models, Downes & Ray (1999) find that the mass spectrum has a single slope which ranges between 1.58 and 3.75, depending on certain parameters of the simulation (i.e., molecular fraction in the jet, amplitude of the jet velocity variation,[2] and the ratio of jet to ambient density). Both Smith et al. (1997) and Downes & Ray (1999) find that γ increases as the jet ages. According to those models, the ambient material that once was accelerated by bow shock entrainment slows down as times goes by, which steepens the mass spectrum by shifting mass from the "fast" end of the mass-velocity relation to the "slow" end. The simulated outflows of Smith et al. (1997) and Downes & Ray (1999) are relatively young (600 and 300 years, respectively), but it seems reasonable to expect that the qualitative trend of increasing γ with age would continue as the outflow evolves in time, and once-fast gas slows down. Very recent bow shock modeling by Lee et al. (2001) finds that γ also depends sensitively on the inclination of the outflow axis to the line of sight.

In contrast to the numerical results, the recent analytical study by Matzner & McKee (1999; hereafter MM) concludes that it is hard to obtain a value of the

[2]The models of Smith et al. (1997) and Downes & Ray (1999) include the effects of rapidly periodic pulsed jets, but these pulsations are too rapid and regular to be "episodic" in our definition.

power-law mass spectrum slope that is not very close to 2, for all times. Unlike the numerical studies listed above, however, the entrainment of the ambient medium in MM is not specifically caused by a bow shock; rather, it is caused by a collimated wind which sweeps the ambient gas into a momentum-conserving shell, following the models of Shu et al. (1991) and Li & Shu (1996).

3.2.3 The $M - v$ Relation in Episodic Outflows

As a framework for a future analytic model of an episodic outflow, consider a flow as the sum of many collimated MM-like outflows, each of which originates at a different time, with a slightly different orientation. In this hypothetical picture, the episodic "bursts" need not all have the same total mass or ejection velocity. As a result, the bursts can even run over themselves in space, with very fast young bursts overtaking older, slower ones. In this picture, an observed molecular outflow represents the *time and space superposition* of many MM-like individual outflow events. In cases where many events of comparable energy have taken place within a few dynamical times of each other, the effects of episodicity will be noticeable in the mass-velocity (and position-velocity, see §3.3) relations measured for the outflow. In addition, in order for a burst to effect the molecular outflow, the ejection angle between the different bursts should be enough so that each travels through regions of the cloud that have not yet been cleared out of gas by previous bursts. Given that most stellar jets have opening angles of a few degrees (e.g., Mundt, Ray, & Raga 1991) a change in ejection angle of only a few degrees between different bursts is enough for a burst to easily encounter "fresh and unperturbed" cloud material. In the case where the kinetic energy of one of those events completely dominates any others, the effects of episodicity will be less noticeable.

MM show that for any stellar wind with a momentum injection rate distributed in space in proportion to $1/\sin^2\theta$, any momentum-conserving interaction between that wind and an ambient medium with a power-law density profile will have a mass spectrum with $\gamma \sim 2$.[3] So, for the hypothetical episodic flow described

[3]Hydromagnetic winds naturally collimate and their resultant force distribution is proportional

above, we can assume that each outburst of an episodic (hydromagnetic) wind has a $1/\sin^2\theta$ force distribution. Each outburst of outflowing material will not necessarily interact with the same ambient gas conditions, as each successive burst can change the density, velocity and/or temperature distribution of the ambient gas surrounding the wind. But, MM clearly explain that a value of γ close to 2 is obtained *independent* of the density, velocity and temperature distributions in the ambient gas. So, in an episodic outflow, we can assume that each independent outburst is responsible for putting ambient gas into motion with a power-law mass-velocity relationship with $\gamma \sim 2$.

So, what will the *cumulative* observed γ for an episodic outflow be? MM say that "$\gamma \sim 2$" regardless of the time history of the flow, but that is for a "time history" where the same flow is just turned on and off, flowing into an ambient medium with a power-law density distribution. If instead we envision the bursty flow described above, where variable amounts of ambient material are accelerated to assorted maximum velocities (due either to variations in the wind, or in the ambient medium), the observed mass spectrum will be the result of superimposed bursts, and will steepen (see Figure 3.1).

Figure 3.1 shows a mass spectrum for a hypothetical episodic outflow. Each molecular outflow episode is represented as a power-law going back to zero-velocity[4] with $\gamma = 2$, but with a unique total mass and maximum velocity. The observed molecular outflow mass spectrum is the superposition (sum) of all past episodes' mass spectra. A power-law fit to the sample "observed" mass spectrum in Figure 3.1 results in an "observed" γ of 2.7. Thus, an episodic wind composed of a series of MM-like ($\gamma = 2$) outbursts is able to create a molecular outflow with $\gamma \geq 2$. In fact, without additional constraints on the maximum velocity or total mass of any outburst, practically any value of $\gamma \geq 2$ can be created in this way.

to $1/\sin^2\theta$ (see MM and references therein).

[4]This is for illustrative purposes only, as in reality $\log(dM/dv)$ should flatten at very low velocities.

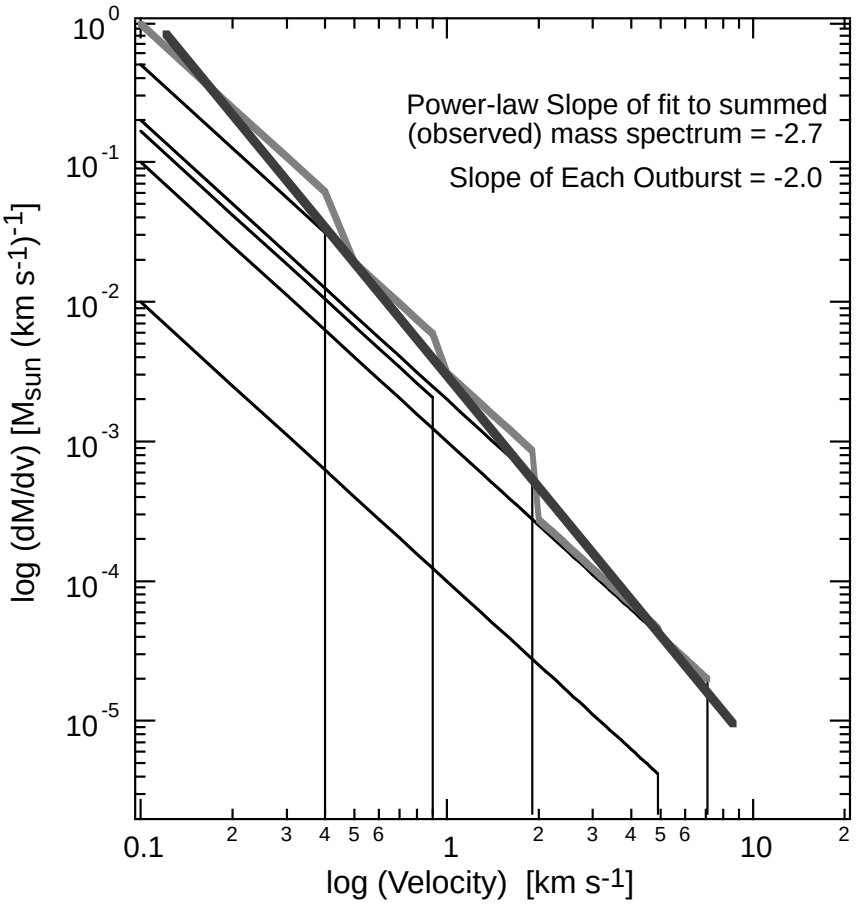

Fig. 3.1.— Molecular outflow mass spectrum for a hypothetical episodic outflow. Thin dark lines represent the mass spectrum produced by different ejection episodes. The thick grey line is the sum of all the episodes, and represents the observed mass spectrum. The thick dark line is a fit to the observed mass spectrum. See §3.2.3.

3.3 Position-Velocity Relation

3.3.1 Observing *p(v)*

One of the best kinematic diagnostics of outflows is a position-velocity (*p*-*v*) diagram. The typical molecular outflow *p*-*v* diagram is constructed by summing spectra in strips perpendicular to the assumed outflow axis, and then contouring line intensity as a function of position along the outflow axis and velocity (see Figure 3.2).

The simplest molecular outflow *p*-*v* diagrams show maximum outflow velocity increasing approximately linearly as a function of distance from the source. Clear examples of this kind of "Hubble-law" velocity distribution are seen in Mon R2 (Meyers-Rice & Lada 1991) and NGC 2264G (Lada & Fich 1996; also see bottom panels of Figure 3.2). In other cases, *p*-*v* diagrams exhibit more complicated behavior, which can often be described as a series of "Hubble-wedges" distributed at various distances from the source (see top panels of Figure 3.2). These multiple wedges are seen in small molecular outflows (0.4 pc long) from Class 0 sources (e.g., L 1448, Bachiller et al. 1990) as well as in large ($\sim$ 1 pc long) outflows from Class I sources (e.g., L1551, Bachiller, Tafalla, & Cernicharo 1994; B5 IRS1, Yu et al. 1999; HH 300, Chapter 2).

3.3.2 Modeling *p(v)*

Outflow models can easily produce a *single* Hubble-law position-velocity relation, but so far, we do not know of any model that produces multiple Hubble-wedges.

The numerical simulations of Smith et al. (1997), Zhang & Zheng (1997), and Downes & Ray (1999) in which outflows are created by the entrainment of ambient gas by a single bow shock, all reproduce the Hubble velocity law. In these models, the Hubble velocity law is in part due to the geometry of the bow shock. A simplified explanation is that the highest forward (in the traveling direction of the jet) velocities are found in the apex of the bow shock, which is also the

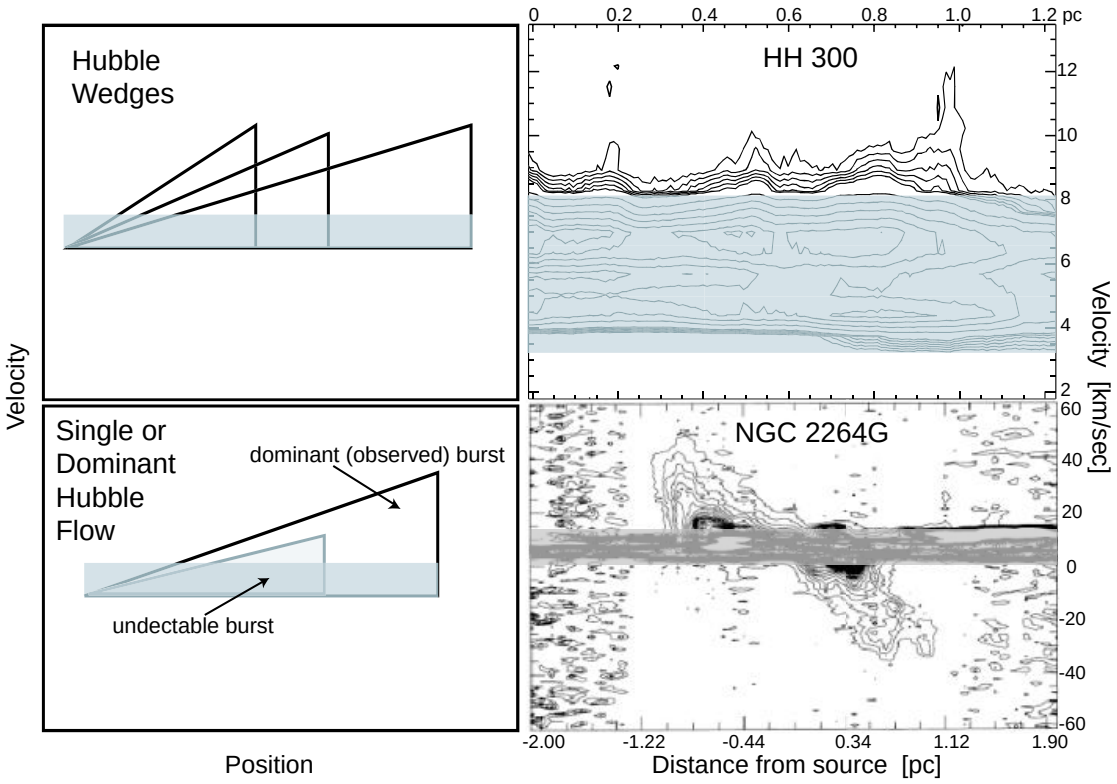

Fig. 3.2.— (*Top-Left*) Schematic picture of the position-velocity diagram of an episodic outflow. (*Top-Right*) Example of an episodic outflow (HH 300), from Chapter 2. (*Bottom-Left*) Schematic picture of the position-velocity diagram of an outflow with only one burst or with one dominant burst. (*Bottom-Right*) Example of a molecular outflow (NGC 2264G) with a single Hubble-law velocity distribution (panel based on Figure 4 of Lada & Fich [1996]). The grey area represents the ambient cloud velocities in which outflow emission cannot be detected, as it is indistinguishable from the ambient cloud emission.

point furthest away from the source. The forward velocities decrease toward the wings of the bow shock, and the farthest away from the apex (or closer to the outflow source) the slower will be the entrained gas (see Figure 3 of Masson & Chernin 1993; and Figure 12 of Lada & Fich 1996).

Bow shock models are not the only ones that produce the Hubble velocity law; the studies of Shu et al. (1991), Li & Shu (1996) and MM also obtain molecular outflows with Hubble velocity laws as a natural consequence of their being created by a momentum-conserving wind. This behavior is easy to understand as "velocity-sorting," since faster material *ejected contemporaneously* with slower material will travel farther from the source.

3.3.3 The *p(v)* in Episodic Outflows

An episodic stellar wind interacting with ambient gas through bow shock prompt entrainment could produce a *p-v* diagram with several Hubble wedges. In an episodic flow with a significantly varying mass-ejection rate, outflowing gas would show a Hubble-like velocity distribution for each mass-ejection episode, with the tip of each Hubble wedge at a source offset corresponding to a bow-shock apex in the outflow map. Since not all outbursts from an episodic source necessarily have the same angle with respect to the plane of the sky or accelerate the ambient gas to the same maximum velocity, each "Hubble wedge" will not necessarily have the same maximum radial velocity, and the maximum velocity can change over time.

If a wind either has had only a single outburst or is dominated by one particularly strong outburst, a molecular outflow with a *single* Hubble velocity law can result (see Figure 3.2). Outflow evolution may also be responsible for creating a single Hubble law. A molecular outflow from an episodic wind which had its last outburst (or has not had an outburst in a considerable amount of time) will be subject to the same kind of velocity-sorting mentioned above, and would produce a single Hubble law in its *p-v* diagram.

3.4 Discussion and Conclusions

Taken together, $M - v$ relations with $\gamma > 2$ and p-v relations showing multiple Hubble wedges provide very strong evidence that "episodicity" is a key feature of molecular outflows from young stars.

3.4.1 Reconstructing History

It is tempting to try to reconstruct the outburst history of an episodic outflow by combining information from $M - v$ and p-v diagrams. In very simple cases, where two or three outbursts dominate the flow, this is possible (e.g., Gueth, Guilloteau, & Bachiller 1996; Narayanan & Walker 1996). In perhaps more typical cases though, where important bursts are separated by much less than the dynamical time scale for each burst, modeling is considerably more complicated —in that uniqueness problems plague the search for solutions. We expect though, that if an *a priori* model of the underlying jet can be made (based on either the molecular line map or other data), the consistency of this model with both the $M - v$ and p-v relations can be tested.

3.4.2 The need for new models

Almost since the day they were discovered, molecular outflows have been thought of as a possible (re-)supplier of the turbulent energy needed to support molecular clouds against rapid gravitational collapse (e.g. Norman & Silk 1980 and citations thereto). It has also been suggested that a molecular outflow may be able to disrupt its host core (e.g, Tafalla & Myers 1998), and/or that a combination of outflows may "churn" (Bally et al. 1999) or disrupt (Knee & Sandell 2000) a whole molecular cloud complex.

Now, dozens of observational papers, only some of which are mentioned above, have pointed to the "episodic" nature of young stellar outflows. Simply put, observers are now *sure* that these outflows originate from a bursty source. The

outflow source may also be precessing and/or moving through the ISM, and each of its bursts may accelerate a *different* amount of ambient matter to a *different* velocity. In this chapter, we have shown that the episodic nature of outflows causes their M-v and p-v relations to be very different from those predicted by any existing analytic model.

In order to correctly asses the energetic role of outflows in a magnetized ISM, it is now necessary to account for the time history of their interaction with their surroundings. The episodic nature of outflows does not affect the *total* momentum injected in the ISM by outflows, and thus it does not matter in most of the ISM feedback theories (e.g., Norman & Silk 1980, and citations thereto). On the other hand, outflow episodicity may change the effective length and time scales on which the momentum is injected, which is important for a magnetized ISM with MHD turbulence (e.g., Padoan & Nordlund 1999, and references therein). We offer this study as a motivation for would-be modelers. Any detailed realistic model of a molecular outflow must include its episodic nature.

Chapter 4

The Great PV Ceph Outflow: A Case Study in Outflow-Cloud Interaction

ABSTRACT

We present a set of detailed molecular line maps of the region associated with the giant Herbig-Haro flow HH 315, from the young star PV Cephei, aimed at studying the outflow-cloud interaction. Our study clearly shows that the HH 315 flow is effecting the kinematics of its surrounding medium, and has been able to redistribute considerable amounts of the surrounding medium-density ($\sim 10^3$ cm^{-3}) gas in its star-forming core as well at parsec-scale distances from the source. The single-dish observations include a map of the outflow in the ^{12}CO(2–1) line, with a beam size of 27″, and more extended maps of the outflow region in the ^{12}CO(1–0) and ^{13}CO(1–0) lines, with 45″ and 47″ beam sizes, respectively. The next chapter (Chapter 5) presents higher-resolution (IRAM 30-m) observations, and discusses their implications.

The giant molecular outflow HH 315 is a highly asymmetric bipolar flow with a projected linear extent of about 2 pc. Our results indicate that the two lobes of the outflow are each interacting with the ambient medium in different ways. The southern (redshifted) lobe, with a mass of 1.8 $M_\odot$, interacts with a dense ambient medium, very close to the young stellar outflow source, and its kinetic

energy is comparable to both the turbulent and gravitational binding energy of its host cloud (of order 10^{44} erg). In addition, we find evidence that the southern lobe is responsible for the creation of a cavity in the ^{13}CO emission. In contrast, the northern (mainly blueshifted) outflow lobe, with a total mass of 4.8 $M_{\odot}$, extends farther from PV Ceph and interacts with ambient gas much less dense than the southern lobe. There is very little ^{13}CO emission north of the outflow source, and the only prominent ^{13}CO emission is a shell-like structure coincident with the outer edge of the northern lobe, about 1.2 pc northwest of PV Ceph. It appears that the northern lobe of the HH 315 outflow has been able to "push" aside a substantial fraction of the gas in the area, piling it in a dense shell-like structure at its edges. In addition, we find that about 50% of the gas in the region of the northern lobe has been put in motion by the outflow, and that the northern outflow lobe is responsible for a velocity gradient in the ambient gas.

4.1 Introduction

As stars form inside molecular clouds, they gravitationally gather gas from their surroundings, while simultaneously spurting out vast amounts of mass in a bipolar flow. The young stellar wind may reveal itself in different ways. Among the many manifestations of a nascent star's mass loss process are Herbig-Haro (HH) objects and molecular outflows. An HH object is a nebulous knot, mainly seen at optical wavelengths, which delineates the shock arising from the interaction of a high-velocity flow of gas ejected by a young stellar object (YSO) and the ambient medium. A chain of these HH objects (or knots) is usually referred to as an HH flow. One or more shocks associated with an HH flow can accelerate entrained gas to velocities greater than those of the quiescent cloud, transferring momentum and energy into the host molecular cloud, thereby producing a molecular outflow.

Since their discovery, molecular outflows have been thought to supply their host cloud with energy (e.g., Norman & Silk 1980). Yet, the (past) notion that outflows rarely extended to more than 1 pc in length, and that they only effected a

minor volume of the cloud, made it difficult to believe that stellar outflows could be important to the energetics of their host cloud. This picture is now changing. Recent studies have shown that outflows from young stars have an enormous potential to influence their parent cloud's structure and lifetime. Optical and near-infrared observations have revealed that giant —parsec-scale— HH flows exist and that they are common (Eislöffel & Mundt 1997; Devine et al. 1997; Reipurth, Bally, & Devine 1997, hereafter RBD; Mader et al. 1999; Eislöffel 2000; Stanke, McCaughrean, & Zinnecker 2000). Giant HH flows have sizes about an order of magnitude larger than the cloud cores from which they originate, and many are found to extend to distances well outside the boundary of their parent dark cloud. The colossal size of a giant HH flow enables it to entrain molecular material at parsec-scale distances from the source, and thus it may effect the kinematics and density of a substantial volume of its parent molecular cloud.

Recent millimeter-wave studies (Bally et al. 1999; Knee & Sandell 2000) show that molecular outflows from a group (or cluster) of stars in a molecular cloud can interact with a substantial volume of the cloud, while criss-crossing and interacting with each other. The final outcome of this many outflows-cloud interaction could be the "churning" (Bally et al. 1999) or disruption (Knee & Sandell 2000) of the entire parent cloud. In addition, by moving gas and dust around, and compressing dust and gas shells, outflows may be able to trigger star formation (e.g., Warin et al. 1996; Sandell & Knee 2001).

In order to study the effects an outflow has on its environment's kinematic and density structure, it is imperative to observe a large area of the cloud gas surrounding the outflow, in addition to the outflow itself. The observations should preferably be of more than one molecular line transition, probing a range of densities, and at least one of the lines should be relatively optically thin, in order to take line opacity into account. Also, if one is to avoid source confusion, one should study regions with a very low density of young stellar objects.

The HH 315 flow, from the young star PV Cephei (or PV Ceph) is a perfect laboratory to study outflow-cloud interaction without any serious source confusion.

There are no known outflow-powering YSOs, other than PV Ceph, in a 30′ radius centered on PV Ceph. There is still the possibility that PV Ceph is a member of a tight binary system, with a separation between components of $\lesssim 50$ AU (Leinert et al. 1997; RBD), or the very slim possibility that PV Ceph is a member of a, yet undetected, small group of forming stars. But, even in the case that PV Ceph is not the sole young star in the region, it is the only source of a very powerful, giant outflow. As a bonus, each of the lobes of the PV Ceph flow interact with drastically different environments, making it a nice laboratory for studying outflow-cloud interaction.

The giant HH 315 flow was discovered independently by Gómez, Kenyon & Whitney (1997, hereafter GKW) and RBD. The presumed source of the HH 315 flow is PV Cephei, a variable Herbig Ae/Be pre-main sequence star located at the northeastern edge of the L1158 and L1155 group of dark clouds, which are believed to be at a distance of 500 pc (Cohen et al. 1981). A brief literature review of the observations of PV Ceph is given by GKW. The HH 315 flow (see Figure 4.1) consists of six major condensations (which are named knot A, B, C, D, E, F), and each major condensation (or knot) is made of two or more individual small HH knots (identified F1, F2, F3, etc.). In addition, a group of knots, which were originally discovered by Neckel et al. (1987), are seen 20″ to 55″ north of PV Ceph, and are identified as HH 215. RBD state that HH 215 and HH 315 are all part of a single 2.6 pc-long (in projection) HH flow which, all together, are commonly referred to as the HH 315 flow. The northern lobe of the HH 315 flow is made of HH 215, and knots A, B, and C. The southern lobe is made of knots D, E, and F (see Figure 4.1). The spectra of several knots (Devine 1997) show that the northern lobe is blueshifted and the southern lobe is redshifted.

RBD affirm that the distances from the source to knot A, B, and C are within 10% of the distance from the source to knots D, E, and F, respectively (see Figure 4.1). They argue that the coincidence in the distance from the source to the knots, and the S-shaped point symmetry of the two lobes around the source (see below) are evidence that the six knots come from three major mass ejection eruptions. In this picture the oldest eruption is responsible for the C-F knot pair,

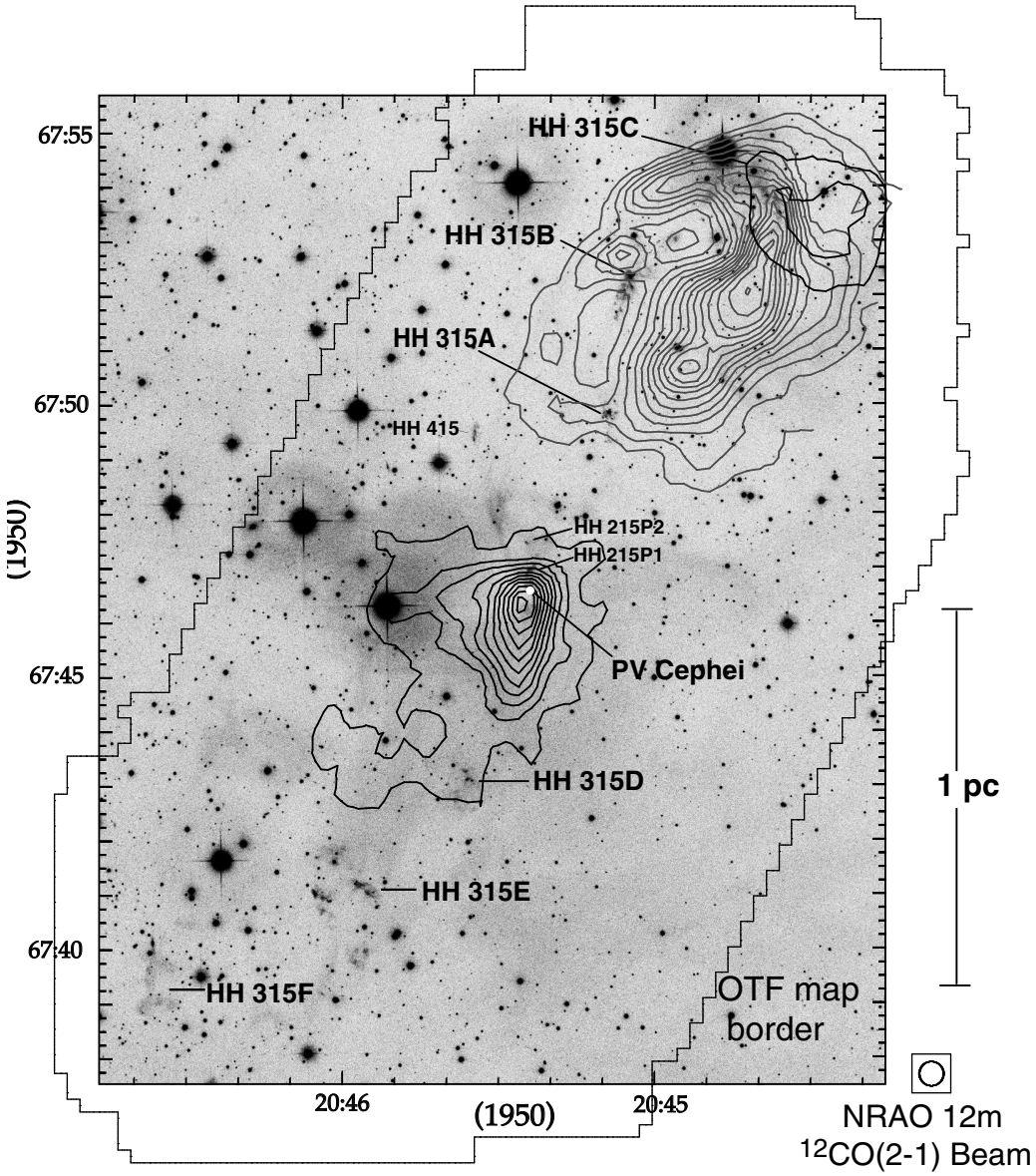

Fig. 4.1.— Integrated intensity contour map of the ^{12}CO(2–1) HH 315 outflow superimposed on a wide-field Hα+[S II] (optical) CCD image from RBD. The blueshifted lobe, which is integrated over the velocity range $-2.55 < v < 0.7$ km s^{-1}, is represented by the light grey contours. The first contour and contour steps of the blueshifted lobe are 1.04 and 0.52 K km s^{-1}, respectively. We cut out the contribution from cloud X from the integrated intensity map of the blueshifted lobe, hence the cut contours at the westernmost edge of the lobe. The redshifted emission is represented by the dark contours. The redshifted emission in the north lobe is integrated over the velocity range $2.65 < v < 3.30$ km s^{-1}. The southern redshifted lobe is integrated over the velocity range $3.30 < v < 6.55$ km s^{-1}. The first contour and contour steps of both north and south redshifted integrated intensity emission all have a value of 0.52 K km s^{-1}. The position of the HH knots in the optical map, and the position of PV Ceph are shown. The extent of the OTF map is indicated by the jagged thin line. The FWHM beam of the NRAO 12 m telescope is shown on the bottom-right corner.

followed by the eruption responsible for the B-E pair, which is followed by the eruption responsible for the A-D pair. The most recent eruption is responsible for the HH 215 knots, and a counter-knot to HH 215 is not observed south of PV Ceph presumably because is heavily obscured by the dense gas near PV Ceph (RBD). Assuming a tangential velocity of 200 km s^{-1} for each knot, RBD estimate that the major eruptions in PV Ceph have occurred every 2000 yr, starting with the C-F eruption about 6500 yr ago.

A very peculiar aspect of HH 315 is that the knots trace a roughly sinusoidal path, or S-shaped point symmetry around PV Ceph. RBD and GKW argue that this particular flow morphology strongly suggests that the ejection axis of PV Ceph is wandering or precessing (i.e., changes over time). GKW modeled the HH 315 flow with a simple precessing jet model. In their model the jet axis precesses on a cone with full opening angle, θ, inclined to the plane of the sky at an angle i, and the jet is assumed to have a constant velocity and a constant precession velocity. GKW state that assuming a jet velocity of 200 km s^{-1}, with $i \sim 10°$, $\theta \sim 45°$, and a precession period of about 8300 yr their model can produce a jet consistent with the HH 315 flow morphology. It is also possible to explain the knot position angles and symmetries with a model where PV Ceph is moving at a substantial velocity ($\sim$ 10 km s^{-1}) and pairs of knots are emitted at varying angles as the source travels through space (see Goodman & Arce 2002).

The molecular outflow associated with the HH 315 flow was first observed by Levreault (1984). The low resolution ^{12}CO(1–0) map of Levreault (1984) shows that the HH 315 molecular outflow is asymmetric. The redshifted lobe has a circular morphology with a diameter of $\sim$ 0.3 pc, and the blueshifted lobe has an elongated morphology which extends up to $\sim$ 1.2 pc northwest from PV Ceph. Here we present new, more sensitive, and higher spatial resolution ^{12}CO(2–1), ^{12}CO(1–0), and ^{13}CO(1–0) observations of the HH 315 molecular outflow, its surroundings, and a large fraction of its parent dark cloud. Our analysis focuses on the effects of the giant HH 315 outflow on its host cloud.

In §4.2 we give a description of our observations, and in §4.3 we describe

our results. In §4.4 we discuss the mass and energetics of the HH 315 flow and the effects that the HH 315 flow has on its parent cloud. We devote §4.5 to our conclusions. A study of the kinematics of the HH 315 outflow and the entrainment mechanism is discussed in Chapter 5, using even higher angular and velocity resolution (IRAM 30 m telescope) molecular line data of the gas immediately surrounding PV Ceph (the HH 215 region) and the HH 315B and HH 315C knots.

4.2 Observations

4.2.1 ^{12}CO(2–1) Data

The ^{12}CO(2–1) line data were obtained using the on-the-fly mapping technique at the National Radio Astronomy Observatory (NRAO) 12 m telescope on Kitt Peak, Arizona, in December 1998. At the observed frequency of 230 GHz, the telescope's half-power beam width, main beam efficiency, and aperture efficiency are 27″, 0.32 and 0.44, respectively. The spectrometer used was a filter bank with 250 kHz resolution, with two independent sections of 128 channels each. The filter bank was put in parallel configuration, in which each of the two sections received independent signals with a different polarization. The parallel configuration was chosen so that ultimately the two polarizations could be averaged to produce better signal-to-noise spectra. At a frequency of 230 GHz, the resultant velocity resolution for this setup is 0.65 km s^{-1}.

The on-the-fly (OTF) mapping technique was used to observe an area of about 215□′ surrounding the HH 315 flow. The OTF technique allowed the extended area to be mapped in a more efficient way than the conventional point-by-point mapping. The telescope in OTF mode moved across the source at a constant speed of 30″ s^{-1}, while a spectrum was acquired every 0.1 seconds. In order to map the desired area more efficiently, the total area was mapped by combining three overlapping regions of different sizes and orientation. The largest region (hereafter central region) has a size of 11′ × 13′, oriented at a position angle of -26° centered

around the position of PV Ceph, at R.A. $20^h45^m23^s.3$, decl. $67°46'36''$ (B1950). The second region (hereafter SE region) is a rectangle of about $10.5' \times 6.5'$, and it is centered southeast of PV Ceph at R.A. $20^h45^m58^s$, decl. $67°40'15''$ (B1950). The third region (hereafter NW region) is a rectangle, of about $10.5' \times 6.5'$, and it is centered northwest of PV Ceph at R.A. $20^h44^m52^s$, decl. $67°53'00''$ (B1950). Each region was scanned in both the directions perpendicular and parallel to its long axis. The separation, in the direction perpendicular to the scanning direction, between subsequent rows was $7.2''$ for the central region and $8''$ for the SE and NW regions. The telescope was pointed to an OFF position after every other row, where it would observe the OFF position for 10 sec and then vane calibrate for 5 sec. We used a different OFF position, depending on the region observed in order to reduce the time needed to move from the "ON" area to the OFF position. The central region and the NW region used the same OFF position, located at R.A. $20^h45^m26^s$, decl. $67°56'22''$ (B1950) and for the SE region we use a different OFF, located at R.A. $20^h45^m26^s$, decl. $67°56'22''$ (B1950). Deep observations at the OFF positions show that there is very faint emission at these positions in the velocity range between 0.5 and 3.0 km s^{-1}, with $0.1 \lesssim T_A^* \lesssim 0.3$ K, and no emission greater than 0.1 K at other velocities. Most of the outflow emission is at velocities less than 0.5 km s^{-1} and at velocities greater than 3.0 km s^{-1}. Therefore, the very small amount of ^{12}CO(2–1) cloud emission at velocities between 0.5 and 3.0 km s^{-1} at the OFF positions does not affect our outflow data. The different regions were observed several times to improve the signal-to-noise in the spectra. The system temperature was measured to be in the range between 350 and 800 K. Our goal was to maintain a constant noise level through the whole map, so regions that were mapped with a higher system temperature were given comparatively more integration time.

The raw OTF data were reduced using various AIPS OTF tasks. A first-order baseline was fitted and subtracted to each spectrum, and the two polarizations were averaged. The different mapped regions were combined and averaged. The map was then convolved onto a grid with $14''$ pixels (Nyquist sampled). The resultant RMS noise in each 0.65 km s^{-1} channel was 0.1 K, for most (non border) spectra.

The intensity scale of the spectral data presented in this chapter is in units of T_A^* (Kutner & Ulich 1981) unless otherwise stated.

4.2.2 ^{12}CO(1–0), ^{13}CO(1–0), and C^{18}O(1–0) Data

In order to study the effect of the HH 315 outflow on a larger scale and to obtain a better estimate of the outflow mass, we observed the ^{12}CO(1–0) line in a region 17.6′ by 29.3′ and the ^{13}CO(1–0) line in a region 11.7′ by 23.5′, both along a position angle of -30°, surrounding PV Ceph. The data were obtained using the SEQUOIA 16 element focal plane array receiver of the Five College Radio Astronomy Observatory (FCRAO) 14 m telescope. The observations were done over the course of three different observing rounds, which took place in April 1999, December 1999, and February 2000. The backend used for observing both lines was the Focal Plane Array Autocorrelator Spectrometer, with a channel spacing of 78 kHz (0.21 km s^{-1}) for ^{12}CO(1–0), at a frequency of 115 GHz, and a channel spacing of 20 kHz (0.05 km s^{-1}) for ^{13}CO(1–0), at a frequency of 110 GHz. The ^{12}CO(1–0) line was observed in position switching mode, with a single OFF position located at R.A. $20^h46^m50^s$, decl. 68°01′36″ (B1950). Observations at the OFF position reveal no significant ($T_A^* \lesssim 0.2$ K) emission. The ^{13}CO line was observed in frequency switching mode. The telescope half-power beam widths for the ^{12}CO(1–0) and ^{13}CO(1–0) lines are 45″ and 47″, and the main beam efficiencies are 0.45 and 0.54, respectively. Both lines were observed on a 22″ grid (Nyquist sampled), and with an integration time of 100 sec for each position. The system temperature of our ^{13}CO(1–0) observations was about 250 K, and for our ^{12}CO(1–0) observations it ranged between 500 and 900 K.

Observations of the C^{18}O(1–0) emission were also made using the same telescope and backend configuration as the ^{13}CO(1–0) observations. We made one 5.5′ × 5.5′ FCRAO-SEQUOIA footprint centered at the position of PV Ceph. The telescope half-power beam width and main beam efficiency for C^{18}O(1–0), at a frequency of 109 GHz, are 47″ and 0.54, respectively. Each position was observed for 210 sec, with a system temperature of about 280 K.

The ^{12}CO(1–0) and ^{13}CO(1–0) data were reduced with the CLASS and MIRIAD packages. For the purpose of obtaining the molecular gas mass (see §4.3.5), the original spectra from both lines were smoothed and resampled to a channel spacing of 0.22 km s^{-1}. The spectra were spatially linearly interpolated and a data cube of 11.5″ pixels was produced for each line. The data cube was then smoothed by convolving it with a Gaussian with a FWHM of 46″. The resultant RMS noise of the spectra in the ^{12}CO(1–0) and ^{13}CO(1–0) smoothed maps is 0.14 K and 0.04 K for each 0.22 km s^{-1} channel, respectively. Interpolating the ^{12}CO(1–0) and the ^{13}CO(1–0) data to this common position-velocity grid allowed us to use them in concert when calculating the mass estimates presented in §4.3.5.

4.3 Results

4.3.1 ^{12}CO(2–1) Maps

In Figure 4.1 we show the integrated velocity map of the molecular outflow associated with the HH 315 flow, created by integrating over wide blue- and red-shifted velocity ranges. The integrated velocity map is overlaid on an optical image of the region (from RBD). The large extent of the flow is clearly seen. The blueshifted lobe (northwest of PV Ceph) is about 0.6 pc wide and 0.8 pc long, and the redshifted lobe is about 0.3 pc wide and 0.5 pc long.[1] Another striking aspect of this molecular outflow, besides its large extent, is the difference in size and morphology of the two outflow lobes. The blue lobe shows a bow shock-like appearance, with an axis of P.A. $\sim -26°$, and with its northern edge coincident with the optical knot HH 315C. Most of the blueshifted emission resides in a region near the optical knot HH 315C and HH 315B, and does not extend all the way to source. In contrast, most of the red lobe's emission is concentrated in a collimated north-south structure that extends from PV Ceph south about 0.3 pc. The redshifted lobe also includes a more extended, wider region of low intensity

[1]The full flow, measured as the distance between the outermost HH knots, is 2.6 pc long (see Figure 4.1).

emission which has its southern edge near the position of the optical knot HH 315D. In addition to the morphological differences, the lobes also have different maximum outflow velocities. Our large scale map, shows ^{12}CO(2–1) blueshifted lobe velocities up to $\sim$ 16.0 km s^{-1} away from the central velocity of the ambient cloud. On the other hand, the ^{12}CO(2–1) red lobe shows maximum outflow velocities of only up to $\sim$ 6.5 km s^{-1}.

In Figure 4.2 we show 12 velocity-binned ("channel") maps of the ^{12}CO(2–1) data. It is clear that most of the ^{12}CO(2–1) emission comes from the (0.65 km s^{-1}-wide) velocity channels centered at 0.38, 1.03, 1.68, 2.33, and 2.98 km s^{-1}. The central velocity of the ambient gas associated with PV Ceph is about 2.5 km s^{-1} (see Cohen et al. 1981, and §4.3.3), thus most of the ambient cloud emission surrounding PV Ceph comes from the channels centered at 2.33 and 2.98 km s^{-1}. The emission at these two velocity channels concentrates around (and south of) the location of PV Ceph, but there is also a local peak in the emission about 9′ northwest of the source.

It should be noted that in our ^{12}CO(2–1) map we also detect emission from another cloud which is unrelated to the cloud associated with the young star PV Ceph. This cloud (hereafter cloud X) contributes a major fraction of the total emission seen at velocity channel (v_{chan}) 1.03 km s^{-1}, and is also detected at v_{chan} = 0.38 and v_{chan} = $-$0.28 km s^{-1} (see Figure 4.2). Cloud X has a filamentary structure with a northwest-southeast long axis, most clearly seen in v_{chan} = 0.38 km s^{-1}, and may also be seen, less clearly at v_{chan} = 1.03 and -0.28 km s^{-1}.

The blueshifted lobe of the PV Ceph molecular outflow is easily discernible at v_{chan} = 0.38 km s^{-1}, where the structure of the ^{12}CO(2–1) gas about 9′ northwest of the source, has a bow shock-like appearance. This bow-shock-like structure is coincident with the position of the HH 315C optical knot (see also Figure 4.1), and can also be clearly seen at the velocity channels centered at -0.28, -0.93, and -1.58 km s^{-1} , and less clearly at v_{chan} = $-$2.23 km s^{-1}. At v_{chan} = $-$0.28 km s^{-1}, this structure is about 0.5 pc wide and 0.75 pc long.

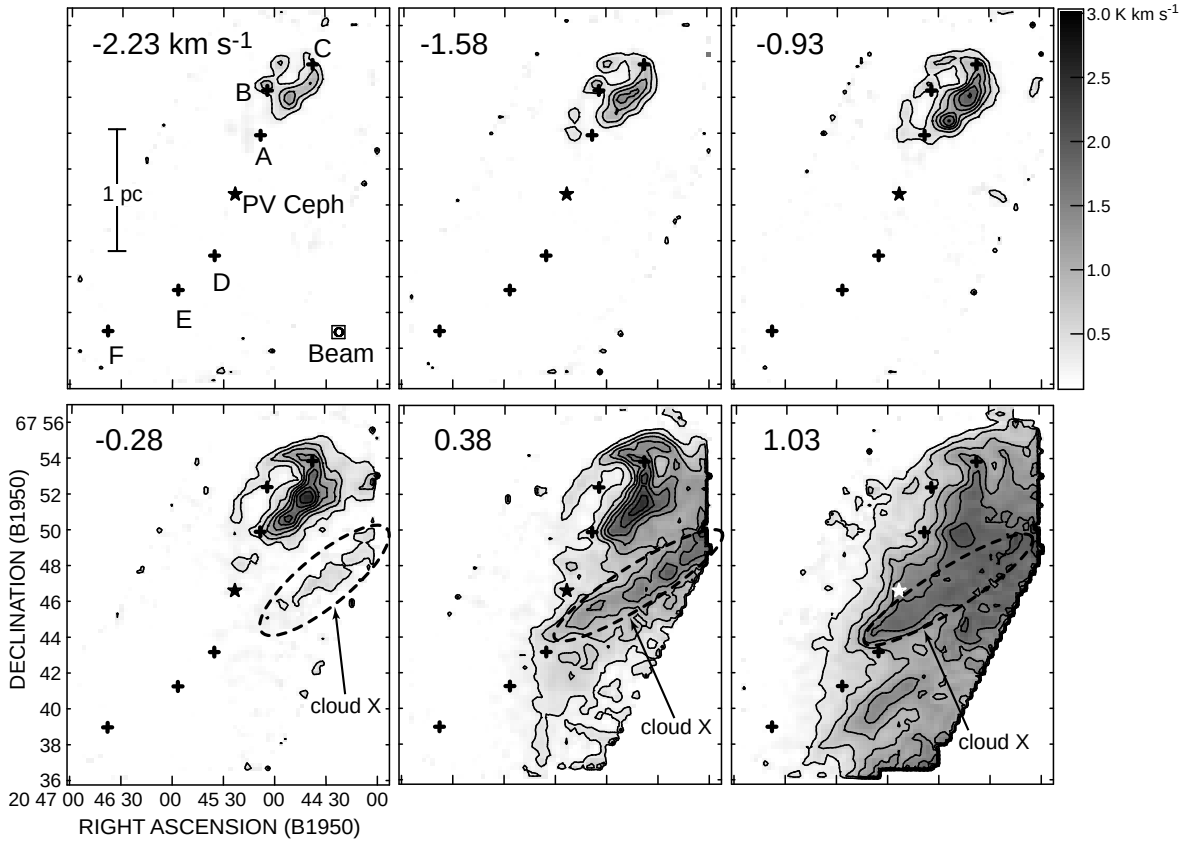

Fig. 4.2.— Velocity channel maps of the ^{12}CO(2–1) emission. Each velocity channel is 0.65 km s^{-1} wide. The center velocity of the channel (v_{chan}) is shown on the upper-left corner of each panel. The starting contour and the contour steps are both 0.325 K km s^{-1} for all panels. The position of the outflow source (PV Ceph) is represented by the star symbol, at the center of each panel. The crosses show the position of the brightest (optical) point of the different HH knots which make the HH 315 flow, knots C, B, A, D, E, F (from top to bottom) (RBD). We also identify the cloud structure we define as cloud X. The linear scale, assuming a distance to the source of 500 pc, is shown. The FWHM beam of the NRAO 12 m telescope is also shown.

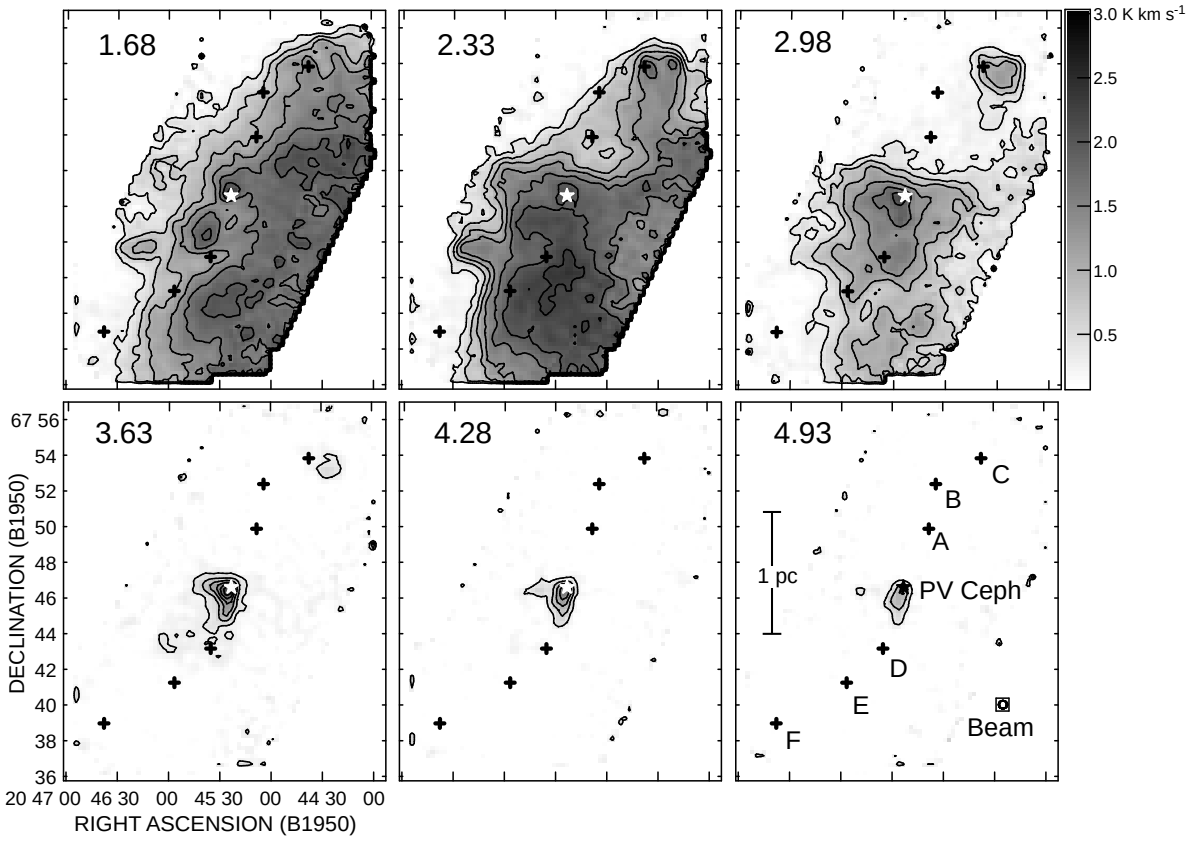

Fig. 4.2.— Continued.

Other high spatial resolution studies of molecular outflow have found bow shock-like CO structures coincident with optical HH knots or near-infrared H_2 knots (e.g., Davis, Smith, & Moriarty-Schieven 1998; Yu et al. 1999; Lee et al. 2000). In these studies the CO bow shock structure is attributed to the interaction between a bow shock from an underlying jet, and the ambient gas. We believe the same is happening in the blueshifted lobe of PV Ceph, as the (blueshifted) bow shock-like shaped optical knot HH 315C is perfectly spatially coincident with the blueshifted CO bow shock structure, which has wings pointing in the direction of the outflow source. The observed asymmetry in the bow wings is most probably due to the underlying distribution of molecular gas in the cloud. As can be seen in the velocity channels close to the central velocity of the cloud ($v_{chan} = 1.68$ km s^{-1}, $v_{chan} = 2.33$ km s^{-1}), the edge of the ambient gas emission is just east of the bow shock structure, and there is more ambient gas emission on the west side of the bow shock structure. Thus, it is likely that the asymmetry in the bow shock wings is due to the fact that the west wing has more gas to interact with than the east wing.

A bow-shaped shock front should accelerate ambient gas both towards and away from the observer (e.g., Cabrit, Raga, & Gueth 1997, and references therein; Lee et al. 2001). We detect redshifted emission at a distance of $\sim 9'$ northwest of the source, near the position of the HH 315C knot, at $v_{chan} = 2.98$ and $v_{chan} = 3.63$ km s^{-1}. The average axis of the HH 315 flow is believed to be close to the plane of the sky (GKW). Thus it is reasonable to assume that the redshifted emission near HH 315C comes from the gas accelerated away from us, on the "back side" of the HH 315C bow shock.

At higher blueshifted velocity channels ($v_{chan} = -0.93, -1.58, -2.23$ km s^{-1}) some of the bow shock-like structure can be seen near HH 315C, in addition to emission at the positions of the optical knots HH 315A and HH 315B. The blueshifted gas emission near HH 315A is very faint, and dispersed. On the other hand, the ^{12}CO(2–1) associated with the HH 315B blueshifted optical knot is relatively strong and has a defined knot-like structure, with a peak ^{12}CO(2–1) emission coincident with the location of the peak in the HH 315B optical emission

(see Figures 4.1 and 4.2).

The redshifted velocity channel maps show a very different morphology than the blueshifted channels. At $v_{chan} \geq 3.63$ km s^{-1} most of the ^{12}CO(2–1) emission is limited to a small region close to PV Ceph. In $v_{chan} = 3.63$ km s^{-1}, in addition there is also some faint ^{12}CO(2–1) emission near the position of the redshifted optical knot HH 315D, and some faint emission near HH 315C. At $v_{chan} \geq 4.28$ km s^{-1} all of the emission is concentrated very close to the source, mostly in a north-south structure.

The ^{12}CO(1–0) velocity maps show basically the same structure as the ^{12}CO(2–1) maps. Our ^{12}CO(1–0) data set is not as sensitive as our ^{12}CO(2–1) data set, thus for illustrative purposes we only show the ^{12}CO(2–1) maps.

4.3.2 ^{13}CO(1–0) Maps

Most of the ^{13}CO(1–0) emission in this region of the sky is optically thin, and thus is a good probe of the structure of the medium density ($n \sim 10^3$ cm^{-3}) gas. The ^{13}CO(1–0) opacity may be estimated with C^{18}O(1–0) observations of the same region (e.g., Heyer et al. 1987). Our 5.5′ by 5.5′ map of C^{18}O(1–0) centered on PV Ceph shows that the C^{18}O emission is concentrated around the young star, at velocities between 2.1 and 3.2 km s^{-1}, and that there is no C^{18}O detectable emission at other velocities nor at distances greater than 2′ from PV Ceph. The maximum emission in our ^{13}CO map (Figure 4.3) is near PV Ceph, and hence it is fair to assume that all other local peaks in the ^{13}CO emission far from PV Ceph are less optically thick than the emission near PV Ceph. Thus, we assume that the ^{13}CO emission in the area we studied is only mildly optically thick very near PV Ceph and other local ^{13}CO maxima (and only at ambient cloud velocities) and it is optically thin everywhere else. On the other hand, the ^{12}CO emission is optically thick almost everywhere (see §4.3.5), so the ^{13}CO emission is a much better probe of the cloud structure.

In Figure 4.3 we show six ^{13}CO maps, integrated over six different velocity

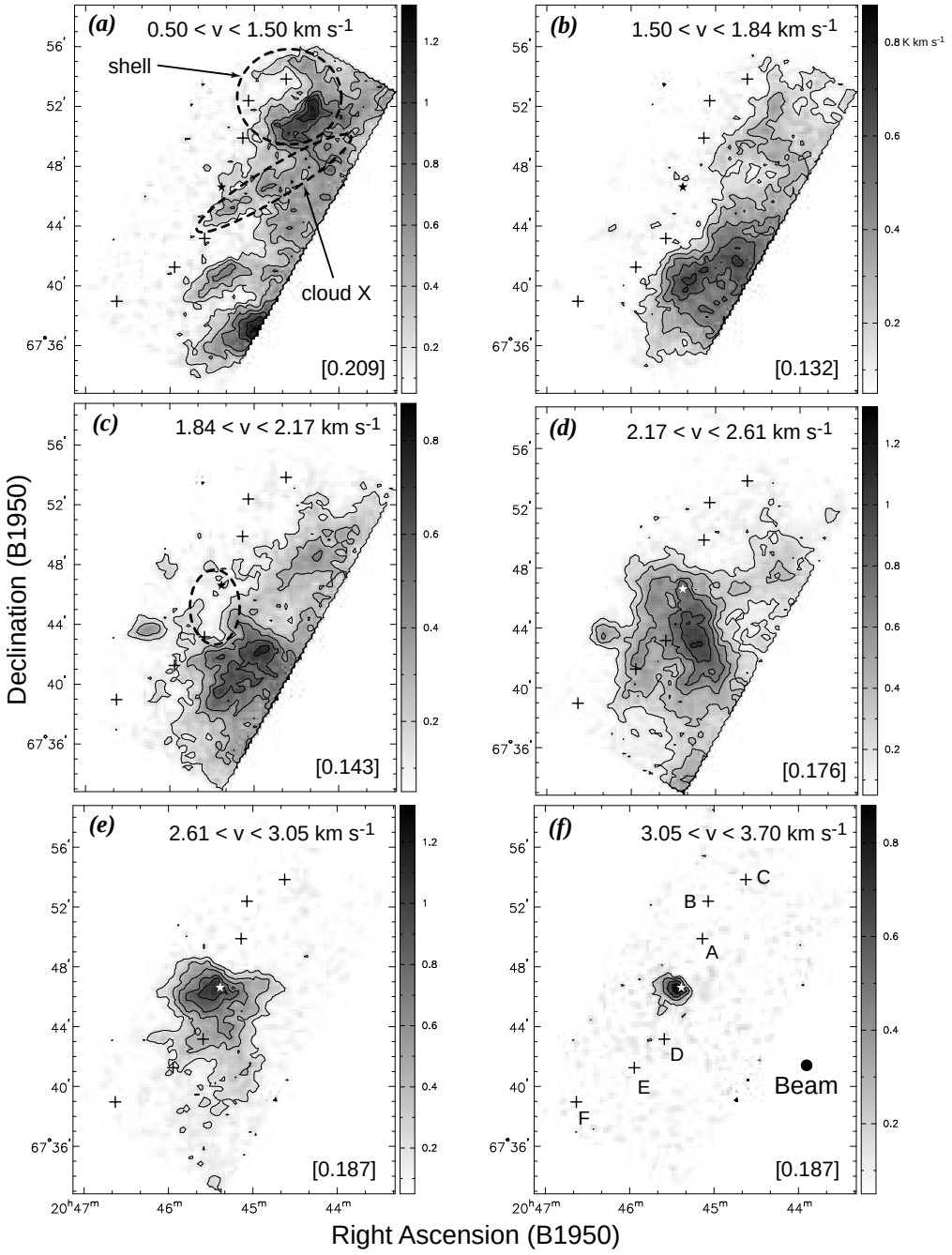

Fig. 4.3.— Velocity-range-integrated intensity maps of the ^{13}CO(1–0) emission. The velocity interval of integration is given on the top of each panel. The first contour, which is also the value of the contour steps, is given inside brackets on the bottom-right corner of each panel in units of K km s^{-1}. The position of the outflow source, PV Ceph, is identified with a star symbol. The cross symbols indicate the position of the HH knots, the same as in Figure 4.1. In panel *(a)* we identify the filamentary structure associated with cloud X. We also indicate the shell-like structure formed by the blueshifted lobe of the HH 315 outflow (see §4.4.2). In panel *(c)* we show the cavity in the ^{13}CO emission presumably formed by the redshifted (southern) lobe of HH 315 (see §4.4.2).

ranges. It should be noted that the velocity ranges shown in each panel of Figure 4.3 are not of equal width. The velocity ranges were chosen to show the velocity-dependent structure of the cloud, so all the velocity channels inside the velocity range of integration show similar structures in the ^{13}CO emission.

The first map is integrated over the velocity range of $0.50 < v < 1.50$ km s^{-1} (Figure 4.3*a*). At these velocities most of the emission is concentrated west and northwest of PV Ceph. Cloud X, which is clearly seen in ^{12}CO(2–1) at $v_{chan} = 0.38$ km s^{-1} and $v_{chan} = -0.28$ km s^{-1} (see Figure 4.2), can also be seen in ^{13}CO emission at these velocities. An interesting feature seen in Figure 4.3*a* is the shell-like structure about 9′ northwest of PV Ceph. This structure encloses the bow shock-like blueshifted ^{12}CO(2–1) lobe of the HH 315 molecular outflow (see Figures 4.1 and 4.2). It appears that the blueshifted lobe of the HH 315 flow has "pushed" aside ambient gas, piling it in a dense shell-like structure at the edges of the blue lobe (see §4.4.2 for a discussion of this).

Figures 4.3*b* and 4.3*c* show the ^{13}CO integrated emission over the ranges $1.50 < v < 1.84$ km s^{-1} and $1.84 < v < 2.17$ km s^{-1}, respectively. The ^{13}CO emission in Figure 4.3*b* is concentrated near the western edge of our map. The ^{13}CO emission in Figure 4.3*c* is also mainly concentrated near the western edge of the map, but, it is more spread out (towards the east) than the emission seen in Figure 4.3*b*. It is at the velocities of Figure 4.3*c* ($1.84 < v < 2.17$ km s^{-1}) where we start to detect ^{13}CO associated with the cloud that harbors PV Ceph (see below). The ^{13}CO emission over the velocity ranges $2.17 < v < 2.61$ km s^{-1} and $2.61 < v < 3.05$ km s^{-1} (Figures 4.3*d* and 4.3*e*, respectively) show the main ^{13}CO structure of the cloud associated with the PV Ceph young star. The cloud's northern edge is just north of PV Ceph, and the cloud extends mainly towards the south-southwest of the young star. The ^{13}CO structure at these velocities is very similar to the ^{12}CO(2–1) structures seen at $v_{chan} = 2.33$ and 2.98 km s^{-1} (see Figure 4.2).

In Figure 4.3*f* we show the ^{13}CO integrated intensity map over the velocity range $3.05 < v < 3.48$ km s^{-1}, which reveals the most redshifted ^{13}CO emission

of our map. All of the ^{13}CO emission is concentrated at the position of PV Ceph. This (unresolved) redshifted ^{13}CO emission most probably comes from the medium-density gas very near PV Ceph that has been accelerated by the HH 315 flow, or could also be due to the motion of PV Ceph (see Goodman & Arce 2002).

4.3.3 Dissecting the PV Ceph cloud

This subsection is intended to explain certain definitions we will use in the discussion that follows. Table 4.1 summarizes the definitions. We use the term "PV Ceph cloud" to refer to the cloud associated with the formation of the young star PV Ceph. We define the area and velocity limits of the PV Ceph cloud based on the ^{13}CO density and velocity structure. The central velocity of the PV Ceph cloud is 2.5 km s^{-1} (from our own spectral data, see below, and Cohen et al. 1981), and the slowest (detected) redshifted molecular outflow velocity is 0.7 km s^{-1} from the central velocity (see §4.3.5). Thus, we assume that 0.7 km s^{-1} "blue-ward" and 0.7 km s^{-1} "red-ward" of the central velocity, that is $1.8 < v < 3.2$ km s^{-1}, is the range of velocity of the PV Ceph ambient cloud emission. It can be seen, from the ^{13}CO velocity channels, that it is at these velocities ($1.8 < v < 3.2$ km s^{-1}) where there is ^{13}CO emission surrounding PV Ceph, which does not come from cloud X.

In Figure 4.4 we plot the ^{13}CO position-velocity diagram of the mapped region, constructed by summing all spectra along an axis with a position angle of -26° over the whole width of the ^{13}CO map. In Figure 4.4, the lower dashed box delimits the "PV Ceph Cloud," and the upper box defines the "North Cloud" (see Table 4.1). The box defining the PV Ceph cloud avoids the high-velocity ^{13}CO feature at velocities greater than 3.2 km s^{-1}. The box limits also avoid the ^{13}CO emission at velocities lower than 1.8 km s^{-1}, south of PV Ceph, which is due to the ^{13}CO clump south-southwest of PV Ceph (Figure 4.3*b*) which is not part of the cloud associated with the formation of PV Ceph. The small velocity gradient south of PV Ceph is mainly due to the velocity distribution of the large scale ^{13}CO emission.

The integrated intensity map of the ^{13}CO emission integrated over $1.8 < v < 3.2$ km s^{-1} is shown in Figure 4.5. The east edge of the cloud is easily

Table 4.1. Description of Features in the Region Surrounding HH 315

Feature	Description	Number Value or Range	See also
PV Ceph Cloud	medium-density gas condensation associated with the formation of PV Ceph	$1.8 < v < 3.2$ km s^{-1} $20^h44^m32^s < \alpha_{1950} < 20^h46^m30^s$ $67^o36'30'' < \delta_{1950} < 67^o48'40''$	Figs. 4.4 and 4.5, §4.3.3
North Cloud	medium-density gas condensation north of PV Ceph, associated with gas of northern outflow lobe	$0.8 < v < 2.2$ km sec^{-1} area same as northern outflow lobe (see below)	Figs. 4.5 and 4.6, §4.3.3
v_{o_south}	Central velocity of ambient PV Ceph cloud gas	2.5 km s^{-1}	Fig. 4.7*a*, §4.3.3
v_{o_north}	Central velocity of north cloud	1.5 km s^{-1}	Fig. 4.7b, §4.3.3
Southern lobe area	Area used to estimate the mass of the southern molecular outflow lobe	$20^h45^m10^s < \alpha_{1950} < 20^h46^m05^s$ $67^o41'30'' < \delta_{1950} < 67^o48'05''$	Fig. 4.6
Northern (blue) lobe area	Area used to estimate the mass of the blueshifted molecular gas of the northern lobe	Non-square area, see Fig. 4.6	Fig. 4.6
Northern (red) lobe area	Area used to estimate the mass of the redshifted molecular gas of the northern lobe	$20^h44^m08^s < \alpha_{1950} < 20^h44^m44^s$ $67^o51'30'' < \delta_{1950} < 67^o54'50''$	Fig. 4.6

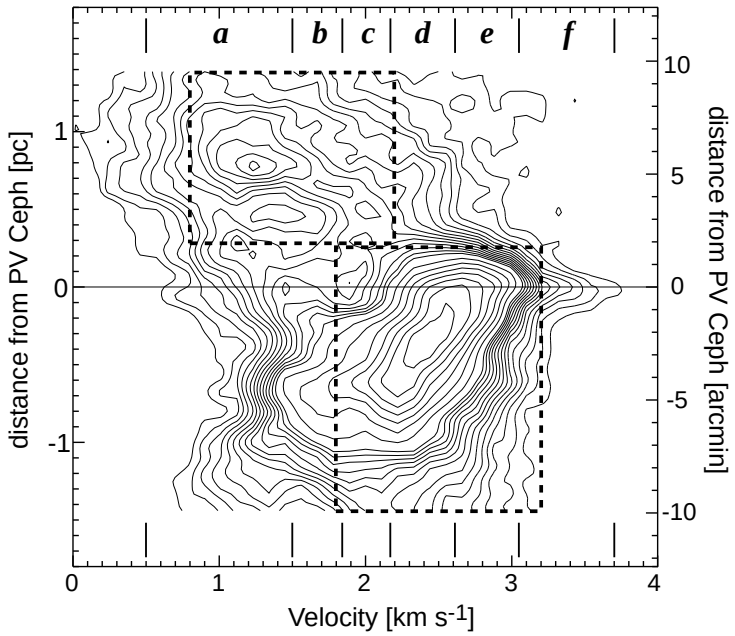

Fig. 4.4.— Position-Velocity ($p-v$) diagram of the ^{13}CO(1–0) emission, constructed by summing all spectra along an axis with a P.A.=-26° (the outflow "average" axis), over the width of the map. The ^{13}CO $p-v$ digram is obtained from a smoothed cube of our ^{13}CO data with a velocity resolution of 0.11 km s^{-1}, and 11.5″ by 11.5″ pixels (see §4.2.2). The contours are from 4 to 30 K, in steps of 2 K, and from 35 to 90 K in steps of 5 K. The dashed square on the bottom denotes the limits of our definition of the PV Ceph cloud (see §4.3.3). The dashed square on the top denotes the limits of what we define in the text as the Northern Cloud (see §4.3.3). The vertical lines at the top and bottom denote the velocity range of integration of the ^{13}CO velocity maps shown in Figure 4.3. The letter at the center of each velocity range indicates the panel in Figure 4.3 which corresponds to the given velocity range.

defined by the drop in ^{13}CO emission. The western edge is not so clear, but it seems that R.A. $20^h44^m32^s$ (B1950) is a reasonable choice. Figure 4.3 shows that most, if not all, of the ^{13}CO emission at the defined velocities of the PV Ceph cloud ($1.8 < v < 3.2$ km s^{-1}) lies east of $20^h44^m32^s$ (B1950). The northern edge of the PV Ceph cloud is marked by the sudden drop of ^{13}CO emission (see Figure 4.5). Similar to our definition of the western edge, we choose the southern edge, at 67°36′30″ (B1950), through visual inspection of the ^{13}CO velocity maps (Figures 4.3 and 4.4). Recapitulating, we define the PV Ceph cloud as the ^{13}CO emission in our map that lies east of $20^h44^m32^s$ and between 67°48′40″ and 67°36′30″ (B1950), at velocities between 1.8 and 3.2 km s^{-1}.

In Figure 4.6 we show the area that we later use to calculate the mass of

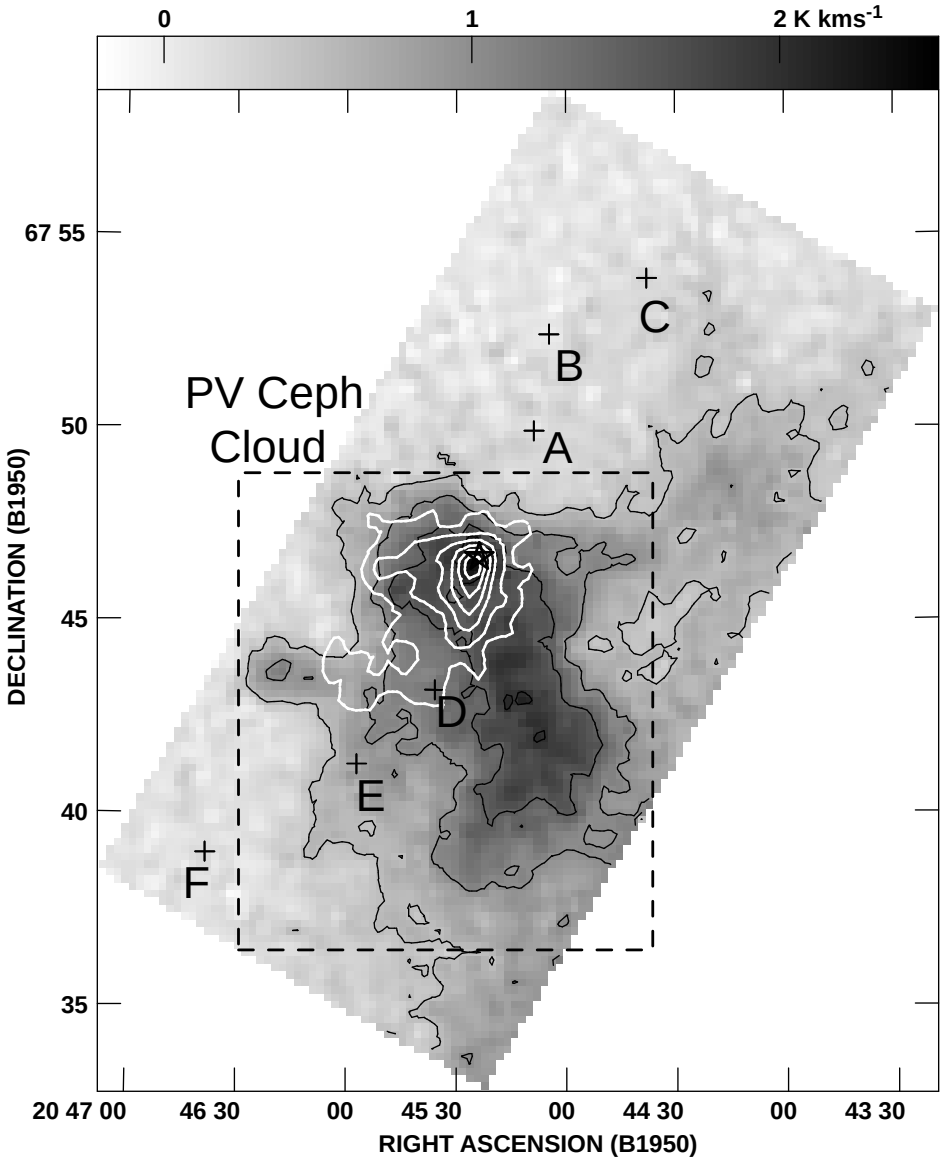

Fig. 4.5.— Integrated intensity grey-scale map of the ^{13}CO(1–0) PV Ceph cloud. The velocity range of integration is $1.8 < v < 3.2$ km s^{-1}. The value of the starting contour and contour step for the black contours is 0.5 K km s^{-1}. The dashed square denotes our definition of the PV Ceph cloud area (see §4.3.3). The white contours represent the ^{12}CO(2–1) integrated intensity of the redshifted outflow lobe. The contours are the same as in Figure 4.1, except that here, we only show the 0.52 × (1, 2, 4, 6, 8, 10) K km s^{-1} contours.

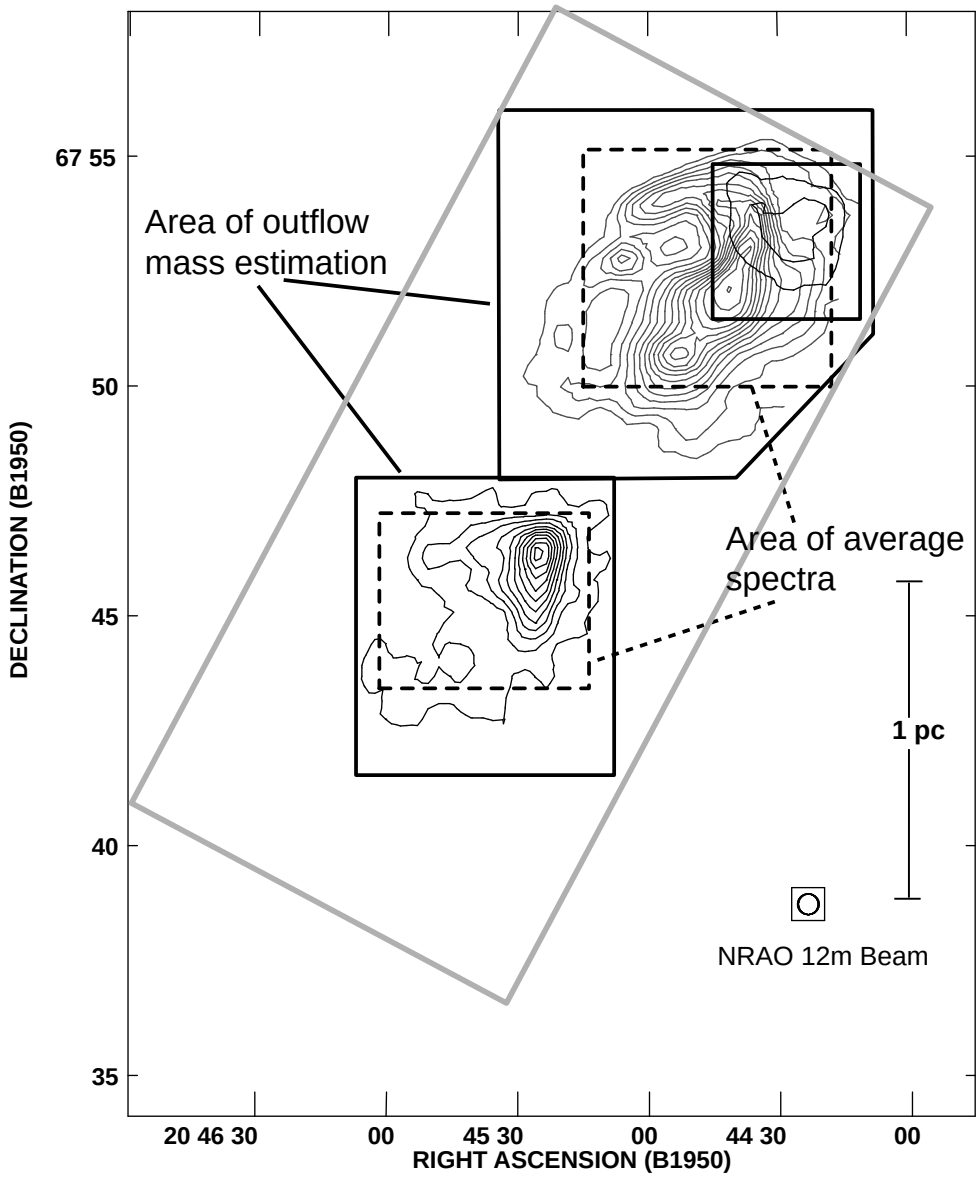

Fig. 4.6.— Map showing different regions defined in the text. The contours are the same as the contours in Figure 4.1. The dashed square around the blueshifted (northern) lobe and around the southern (redshifted) lobe indicate the region used to obtain the average ^{12}CO(1–0) and ^{13}CO(1–0) spectra shown in Figure 4.7. The solid square around the blueshifted lobe and around the southern lobe indicate the region used to obtain the outflow mass of each lobe. The solid square around the redshifted emission in the *northern* lobe indicates the region used to obtain the average ^{12}CO(1–0) and ^{13}CO(1–0) spectra shown in Figure 4.8, and the mass of the northern redshifted outflow emission. The solid grey tilted rectangle shows the area used to obtain the ^{12}CO(2–1) position-velocity diagram of Figure 4.13.

each molecular outflow lobe (see §4.3.5). We also show in Figure 4.6 the area used to estimate the velocity dependence of the ^{12}CO(1–0) line opacity for each outflow lobe region, as discussed in §4.3.5. These smaller areas were chosen to have CO emission representative of the larger (outflow mass) areas, with as little contamination from unwanted cloud (and velocity) structures (e.g., cloud X) as possible. The "ambient" velocity for the Southern lobe, v_{o_south}, is obtained from a two-Gaussian fit to the average ^{12}CO(1–0) spectrum shown in Figure 4.7*a*. The resultant value, for the narrow velocity component is $v_{o\_south} = 2.5$ km s^{-1}.

It is evident that the molecular gas north of PV Ceph exhibits a large-scale velocity gradient. The overall gradient is in the sense that the ^{12}CO and ^{13}CO emission (with cloud-like morphology, presumably non-outflow gas) is shifted to the blue towards the north-northwest of the map (see Figures 4.2, 4.3, and 4.4). The central velocity of the northern lobe region (or "Northern Cloud") is $v_{o\_north} = 1.5$ km s^{-1}, obtained using the same procedure described above for v_{o_south}. We define the "Northern Cloud" to be in the velocity range $0.8 < v < 2.2$ km s^{-1} , and to have an area shown by the box in Figure 4.6 (see also Table 4.1 and Figure 4.4). Later, we argue that the sense of the overall velocity gradient is not an accident, and that most of the mass in the northern cloud has been accelerated to blueshifted velocities by the HH 315 flow (see §4.2.2).

4.3.4 The flow in context with its parent cloud's structure

Levreault (1984) suggested that the asymmetry in the lobes' morphology and velocity distribution is due to the underlying density distribution in the PV Ceph region. Now that we have a map of the ^{13}CO gas we can state for sure that Levreault's original suggestion that there is a factor of 10 difference between the ambient density gas north and south of PV Ceph, is accurate. As can be seen in the ^{13}CO integrated intensity map (see Figure 4.5) there is almost no ^{13}CO gas (associated with the PV Ceph cloud) north of PV Ceph, and there is strong ^{13}CO emission south of PV Ceph. A difference in the ambient gas density of a factor of ten between north and south of the young star is able to produce the

discrepancy in the ^{13}CO emission (see also §4.4.2 for a quantitative discussion on this). Thus, there is no question that the red lobe of the HH 315 flow interacts with much denser gas than the blue lobe. The smaller maximum outflow velocity and extent of the red lobe, compared to the blue lobe is explained by the fact that molecular outflows are formed by the momentum-conserving interaction between an underlying stellar wind and the ambient cloud (see §4.4.1 for a discussion).

4.3.5 Outflow Mass

Procedure

To obtain the outflow mass we use the method described in §2.3.3. This method, which is based on the method employed by Bally et al. (1999) and Yu et al. (1999), uses the ^{12}CO(1–0) to ^{13}CO(1–0) ratio to estimate the opacity in the ^{12}CO(1–0) line, as a function of velocity. In most cases the ^{12}CO(1–0) line is optically thick, and its opacity varies with velocity. Typically, the highest-velocity gas in the line wings is optically thin, and the optical depth increases as velocities approach the line center. Using an optically thick line, without properly correcting for its velocity-dependent opacity, will result in an underestimation of the outflow mass, momentum and kinetic energy.

Here we give a brief description of the method used to estimate the outflow's mass (see Chapter 2 for detail). First, in order to estimate the ratio of ^{12}CO(1–0) to ^{13}CO(1–0) as a function of velocity, we calculate average spectra of ^{13}CO(1–0) and ^{12}CO(1–0) over the region where most of the outflow emission is found (see Figure 4.6). We did this for two different regions, one for each outflow lobe. The average spectra of these two regions are shown in Figures 4.7*a* and 4.7*b*. In Figures 4.7*c* and 4.7*d*, we present the ratio of ^{12}CO(1–0) to ^{13}CO(1–0) main beam temperature (T^{12}_{mb}/T^{13}_{mb}), as a function of velocity for the average spectra of the south (red) and north (blue) lobe regions, respectively. The line ratios, hereafter denoted $R_{12/13}(v)$, were each fit with a second-order polynomial, as described below.

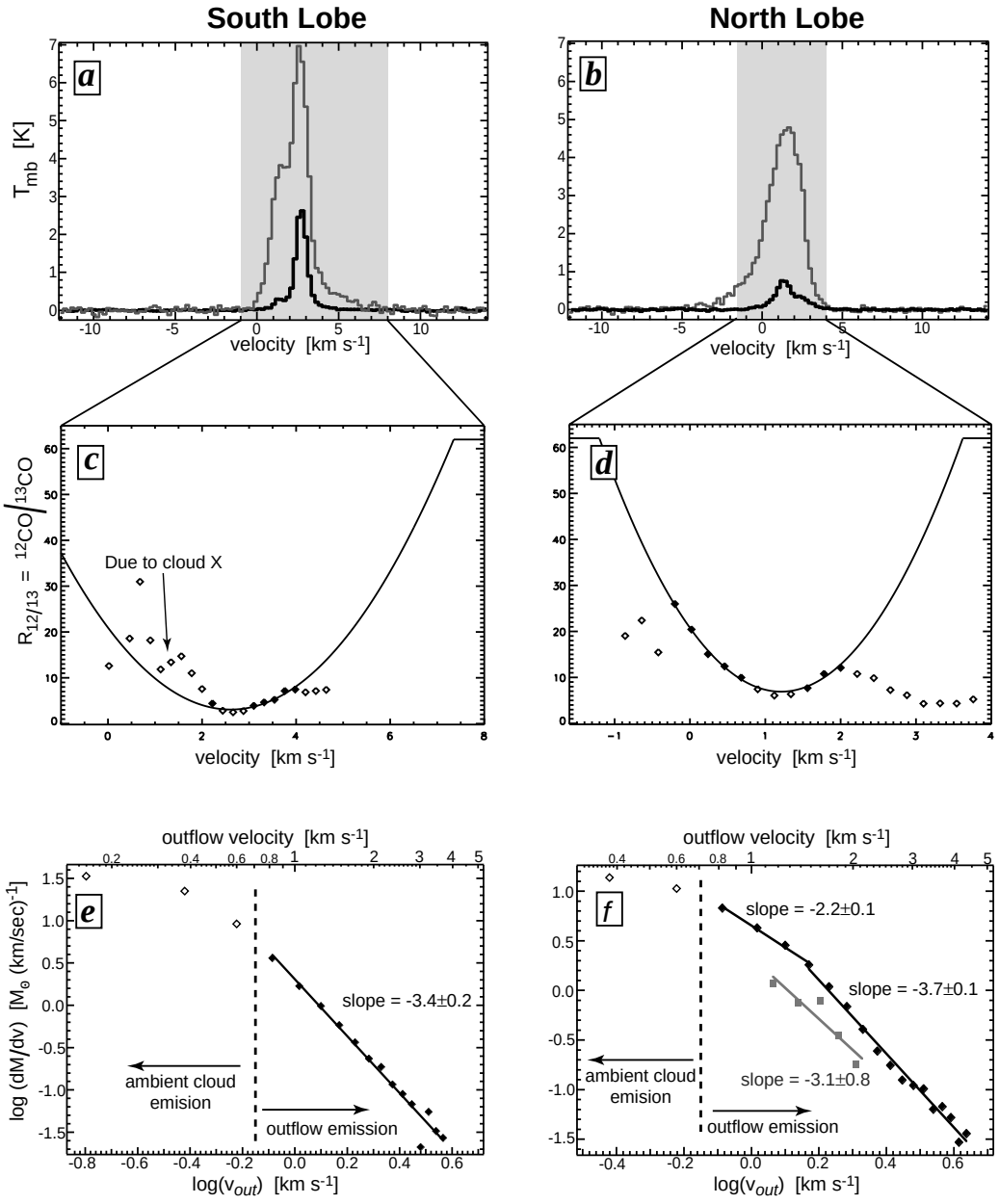

Fig. 4.7.— (a) Average spectra over the redshifted (southern) lobe region indicated in Figure 4.6. Dark line indicates the ^{13}CO(1–0) average spectrum, the light line indicates the ^{12}CO(1–0) average spectrum. (b) The same as [a], but for the blueshifted (northern) lobe. (c) Main beam temperature (or intensity) ratio of ^{12}CO(1–0) to ^{13}CO(1–0), using the average spectra in the above panel, as a function of observed velocity (v). This ratio is denoted in the text as $R_{12/13}$. The filled circle symbols are the points used for the second-order polynomial fit to $R_{12/13}$. The solid line is the resulting fit. (d) The same as [c], but for the blueshifted lobe. (e) Mass spectrum, or mass in a 0.22 km s^{-1}-wide channel as a function of outflow velocity ($v_{out} = v - v_o$), for the red (southern) lobe of the HH 315 molecular outflow. The filled diamonds represent the outflow, and the unfilled diamonds represent the ambient cloud. The solid line shows a power-law fit to the filled diamonds. The slope of the fit is -3.4 ± 0.2. (f) Similar to [e], but for the northern lobe. The dark diamond symbols represent the blueshifted emission. The grey squares represent the redshifted emission in the northern lobe. We made two power-law fits to the blueshifted emission in the northern lobe. The slopes of the fits are -2.2 ± 0.1 for the low-outflow velocity range and -3.7 ± 0.1 for the high-outflow velocity range. The grey line shows a power-law fit to the northern lobe redshifted outflow emission. The slope to this fit is 3.1 ± 0.8.

The fits to $R_{12/13}(v)$ are each a truncated parabola with fixed minimum at the velocity where the average ^{13}CO(1–0) spectrum peaks (this velocity is obtained by a two-Gaussian fit to each of the average ^{13}CO spectra in Figures 4.7*a* and 4.7*b*). We exclude the three velocity channels closest to the ^{13}CO peak velocity from the fit to $R_{12/13}(v)$, as they are the velocities at which the ^{13}CO emission might be slightly optically thick and where the ^{12}CO emission is probably extremely optically thick. In both the red and the blue lobe's average ^{13}CO spectra there are "contaminating" velocity components (e.g., cloud X; see Figure 4.7*a* and 4.7*b*). This contamination is at blueshifted velocities in the red lobe, and redshifted velocities for the blue lobe. So, after editing for this contamination, eliminating low signal-to-noise points, and the three points near the line core, we use only the points shown as filled symbols in Figures 4.7*c* and 4.7*d* in the final fits. The $R_{12/13}(v)$ parabolic fit is then used to extrapolate $R_{12/13}$ to the high-velocity wings of the outflow, where the ^{13}CO line is too weak to be reliably detected (see below).

To calculate the outflow mass at a given (x, y) position, we directly use the ^{13}CO emission at low outflow velocities. At high outflow velocities, or wherever the ^{13}CO has not been reliably detected, we use the ^{12}CO(1–0) data and the fit to $R_{12/13}(v)$, to estimate the value of $T^{13}_{mb}(v)$ at the given velocity and position, using the simple relation $T^{13}_{mb}(x,y,v) = T^{12}_{mb}(x,y,v)[R_{12/13}(v)]^{-1}$. The function $R_{12/13}(v)$ is truncated at a value of 62, the assumed isotopic ratio (Langer & Penzias 1993). Once we estimate a value of $T^{13}_{mb}(x,y,v)$, we can obtain a value of the ^{13}CO opacity ($\tau_{13}(x,y,v)$), from which we then obtain a value of the ^{13}CO column density ($N_{13}(x,y,v)$) and then the mass, using Equations 2.1, 2.3, and 2.4.

It should be noted that the ^{13}CO(1–0) excitation temperature (T_{ex}) is needed in order to obtain an estimate of $\tau_{13}(x,y,v)$ from $T^{13}_{mb}(x,y,v)$ (see Equation 2.1). A value of T_{ex} is obtained by assuming that the excitation temperature for ^{12}CO(1–0) and ^{13}CO(1–0) are the same, and that the ^{12}CO(1–0) emission is optically thick at the line core. To obtain T_{ex}, we use an average spectrum of the ^{12}CO(1–0) data over a region 5.75′ by 9.58′, centered on $20^h45^m24.7^s$, 67°42′19″ (B1950). This region is where most of the ^{13}CO emission lies, and thus we are confident that the ^{12}CO emission at ambient cloud velocities in this region is extremely optically

thick. The peak main beam temperature of the average spectrum is about 7.1 K, and using Equation 2.2, we find that $T_{ex} \sim 10.5$ K.

The value of $T_{ex} \sim 10.5$ K should be taken as a lower limit, as other studies have shown gas in most outflows is usually warmer (by a factor of a 1 to 10) than the ambient cloud gas (e.g., Snell, Loren, & Plambeck 1980; Fukui et al. 1993; Bence, Richer, & Padman 1996; Hatchell, Fuller & Ladd 1999; Davis et al. 2000). Our high spatial resolution data taken with the IRAM 30 m telescope (see Chapter 5) include simultaneous observations of the ^{12}CO(2–1) and ^{12}CO(1–0) lines, at the same position, which can be used in concert to obtain an estimate of T_{ex} (e.g., Levreault 1988). Our estimates (see Chapter 5 for specifics) indicate that in most places $10 \lesssim |T_{ex}| \lesssim 15$, and that there are only very few positions with $T_{ex} > 30$ K. Changing the excitation temperature from 10.5 K to 15 K, the outflow mass estimate would increase by a factor of only 1.1. A change in T_{ex} from 10.5 K to 30 K, increases the outflow mass estimate by a factor of 1.76. Thus, since most of the outflow gas is at temperatures between 10 and 15 K, assuming $T_{ex} = 10.5$ K does not lead to a significant uncertainty in the outflow mass estimate.

Mass-Velocity Relation

Outflows usually show a mass-velocity relation (mass spectrum) in which $dM(v)/dv \propto v^{-\gamma}$, and γ may differ for "high" and "low" velocities in the flow (see Chapter 3 for a detailed discussion). Using the method described above, we calculate the mass per 0.22 km s^{-1}-wide velocity channel in the redshifted and blueshifted lobes of the HH 315 molecular outflow. The southern lobe redshifted gas mass as a function of outflow velocity is shown in Figure 4.7*e*. The outflow velocity (v_{out}) is defined as the observed velocity (v) minus the "ambient" molecular cloud velocity in the redshifted lobe region ($v_{o\_south} = 2.50$ km s^{-1}, see §4.3.3 and Table 4.1). We confidently detect redshifted outflow emission at outflow velocities between 0.71 and 3.79 km s^{-1} (that is, from the 0.22 km s^{-1}-wide channel centered at outflow velocity 0.82 km s^{-1} to the channel centered at $v_{out} = 3.68$ km s^{-1}). At outflow velocities lower than 0.71 km s^{-1} the structure of the molecular gas (both

^{12}CO and ^{13}CO) is nothing like the structure of the higher velocity outflowing gas, and resembles the PV Ceph cloud structure. Therefore, we are confident that all of the molecular gas at $v_{out} > 0.71$ km s^{-1} is outflow emission. The upper value of the redshifted velocity ($v_{out} = 3.68$ km s^{-1}) is constrained by the sensitivity of our observations. Figure 4.7*e* shows that the observed mass (per 0.22 km s^{-1}-wide velocity channel) has a single power-law dependence on velocity for the range of outflow velocities in which we detect redshifted outflow emission. A power-law fit yields a slope of -3.4 ± 0.2. We estimate a total redshifted outflow mass, within the box shown in Figure 4.6, in the velocity range $0.71 < v_{out} < 3.79$ km s^{-1}, of 1.8 M$_{\odot}$.

The northern lobe blueshifted gas mass as a function of outflow velocity is shown in Figure 4.7*f*. We detect blueshifted outflow emission at outflow velocities between -0.71 and -4.45 km s^{-1}. Similar to the southern lobe region, outflow velocities in the northern region are defined as the observed velocity minus the "ambient" central velocity. In the northern outflow region the ambient velocity is $v_{o\_north} = 1.5$ km s^{-1} (see §4.3.3 and Table 4.1). At outflow velocities slower than -0.71 km s^{-1} the structure of the ^{12}CO starts to be much more extended than the ^{12}CO bow-shock like structure seen at faster outflow velocities, and thus we do not include any emission at v_{out} slower than -0.71 km s^{-1} in our blue lobe mass estimate. The CO data we use in this paper show low level blueshifted outflow emission at $|v_{out}| > 4.45$ km s^{-1}, but not at high enough signal-to-noise levels to study it. The higher resolution data in Chapter 5 show the high velocity structure of the CO outflow clearly, and we discuss its importance there. Figure 7*e* shows that the observed mass per 0.22 km s^{-1}-wide velocity channel (or mass spectrum) has a power-law dependence on outflow velocity for $0.8 \lesssim |v_{out}| \lesssim 1.5$ km s^{-1}, with a slope of -2.2 ± 0.1, and for the velocity range of $1.5 \lesssim |v_{out}| \lesssim 4.2$ km s^{-1}, the mass spectrum has slope of -3.7 ± 0.1. We obtain a total blueshifted outflow mass in the velocity range $-4.45 < v_{out} < -0.71$ km s^{-1}, within the box shown in Figure 4.6, of 4.1 M$_{\odot}$.

The blueshifted molecular outflow lobe of HH 315 has a $\gamma = 2.2 \pm 0.1$ for velocities $-1.59 < v_{out} < -0.71$ km s^{-1} (see Figure 4.7*f*). At this velocity range

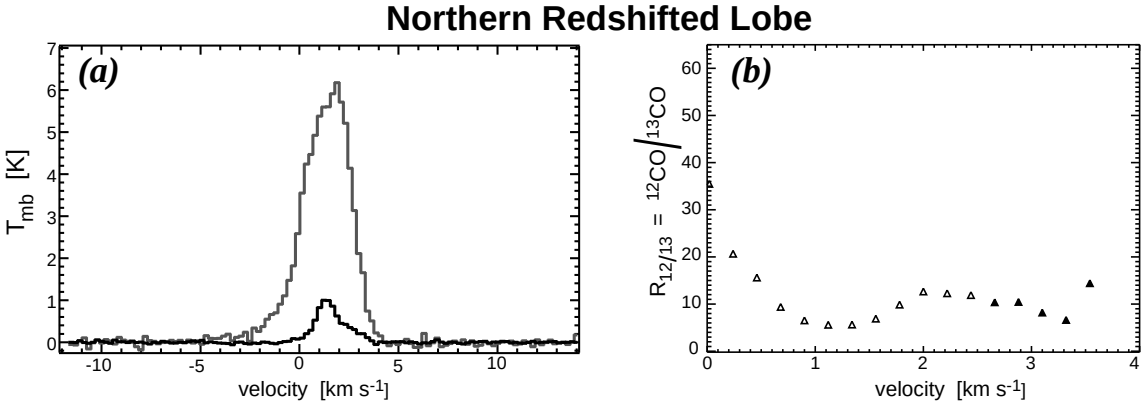

Fig. 4.8.— (*a*) Average spectra over the northern redshifted outflow emission region indicated in Figure 4.6. Dark line indicates the ^{13}CO(1–0) average spectrum, the light line indicates the ^{12}CO(1–0) average spectrum. (*b*) Main beam temperature (or intensity) ratio of ^{12}CO(1–0) to ^{13}CO(1–0) —also denoted in the text as $R_{12/13}$— as a function of observed velocity (v), using the average spectra in panel [*a*].

the only molecular outflow structure observed is the bow shock-like structure coincident with HH 315C. This structure was presumably formed, *solely*, by the interaction of the HH 315C mass ejection event with the ambient cloud. Thus the value of $\gamma = 2.2 \pm 0.1$ is consistent with the value predicted for an outflow created by one mass ejection episode (see Chapter 3/Arce & Goodman 2001a; Matzner & McKee 1999). The episodic nature of the HH 315 outflow is further discussed in Chapter 5.

The ^{12}CO(2–1) channel maps (Figure 4.2, $v_{chan} = 2.98$, 3.63 km s^{-1}) show that there is localized redshifted emission in the same region of the main blueshifted outflow lobe (near HH 315C). We mentioned earlier (§4.3.1) that it is likely that this redshifted emission comes from gas that has been accelerated by the "back side" of the HH 315C bow shock. Therefore, it should also be considered as outflow emission, and should be included in the mass and energy estimates of the outflow. Hereafter we refer to the blueshifted and redshifted outflow emission north of PV Ceph as the northern lobe. In Figure 4.6 we indicate the region used to calculate the mass of the northern lobe redshifted emission. The average ^{12}CO(1–0) and ^{13}CO(1–0) spectra in this region (see Figure 4.8) indicate that the ratio of these two lines ($R_{12/13}$) is approximately constant in the velocity range where there is redshifted outflow emission ($2.55 < v < 3.65$ km s^{-1}), with an average line

ratio ($\bar{R}_{12/13}$) of 10. We therefore estimate the redshifted outflow mass in the north lobe using the same method described above, but instead of assuming a velocity-dependent ^{12}CO(1–0) line opacity, we assume that the opacity is constant with $\bar{R}_{12/13} = 10$. The resultant molecular outflow mass of the northern lobe redshifted emission over the outflow velocity range $1.05 < v_{out} < 2.15$, in the area shown in Figure 4.6, is 0.7 $M_\odot$.

Unlike Chapter 2 (HH 300), we do not subtract for the ambient cloud emission contribution to the outflow emission at low outflow velocities (see §2.3.3). In the case of the HH 315 molecular outflow there is no indication that at the chosen outflow velocities there is "contamination" from the ambient cloud emission. As discussed above, the molecular gas emission (at the velocities used for calculating the outflow mass) has a structure very different from that of the ambient cloud and a structure which is consistent with that of an outflow lobe. Thus, we are confident that we *do not* need to correct our HH 315 CO outflow mass estimate by the "contamination" of ambient cloud emission.

4.4 Discussion

4.4.1 Mass and Energetics of the Outflow

The southern lobe

The total mass of the southern (redshifted) lobe is 1.8 $M_\odot$. The mass of the PV Ceph cloud (as defined in §4.3.2, also see Figure 4.5) is about 74 $M_\odot$. Hence, the detectable redshifted outflow lobe mass is only $\sim$ 2% of the PV Ceph cloud mass. The mass of the PV Ceph cloud in the redshifted lobe area (as defined in Figure 4.6) is 29 $M_\odot$. Even in this localized area, the detectable redshifted outflowing mass is only about 4% of the cloud mass. The measured (line-of-sight) momentum ($\Sigma m(v_i)v_i$) of the redshifted outflow lobe, for $0.71 < v_{out} < 3.79$ km s^{-1}, is 2.1 $M_\odot$ km s^{-1}. The true momentum in the redshifted outflow lobe should be substantially more, as we have only considered the line-of-sight velocity component.

If we assume that the angle, i, between the plane of the sky and the outflow's "average" axis is about 10° (GKW), then the outflow momentum would be about 12.1 $M_\odot$ km s^{-1}. Our ignorance of the exact value of i brings large uncertainties to the value of the outflow momentum. For example, a change in the value of i from 10° to 15° changes the value of the red lobe momentum from 12 to 8 $M_\odot$ km s^{-1}. The kinetic energy is even more uncertain, as it depends on $(\sin i)^{-2}$. We estimate the kinetic energy $[(\,^1/_2)\,\Sigma m(v_i)v_i^2]$ of the red lobe, for $0.71 < v_{out} < 3.79$ km s^{-1}, to be 2.9 $(\sin i)^{-2} \times 10^{43}$ erg. Using $i = 10°$, the kinetic energy is then 9.6×10^{44} erg.

The northern lobe

The mass of the blueshifted gas at the outflow velocity range $-4.45 < v_{out} < -0.71$ km s^{-1} in the north lobe of the PV Ceph molecular outflow is 4.1 $M_\odot$. If we include the 0.7 $M_\odot$ of outflowing redshifted emission (at $1.05 < v_{out} < 2.15$ km s^{-1}) detected near the HH 315C optical knot, then the total mass of the northern outflow lobe is 4.8 $M_\odot$. We estimate the mass of the Northern Cloud (see §4.3.3), from the ^{13}CO emission, to be 13.5 $M_\odot$. Comparing this amount of mass, with the total northern lobe mass, we see that the outflowing mass in the north region is about one third of what one would naively consider the "ambient" cloud mass. Later, we show that about half of the mass of the medium-density gas which we at first naively define as the ambient north cloud gas, is in fact gas that has been accelerated by the HH 315 flow (see §4.4.2).

We obtain a line-of-sight momentum of 5.1 $M_\odot$ km s^{-1} for the blueshifted outflow emission and a line-of-sight momentum of 1.0 $M_\odot$ km s^{-1} for the redshifted outflow emission in the north lobe, for a sum of 6.1 $M_\odot$ km s^{-1}. Assuming $i = 10°$, then we obtain a total north lobe momentum of 35.1 $M_\odot$ km s^{-1} . The kinetic energy estimates for the north lobe are 7.6 $(\sin i)^{-2} \times 10^{43}$ erg for the blueshifted gas and 1.5 $(\sin i)^{-2} \times 10^{43}$ erg for the redshifted gas. If we assume $i = 10°$, then the total kinetic energy of the north lobe is 3.0×10^{45} erg. The mass, momentum, and kinetic energy estimates of the HH 315 outflow are listed in Table 4.2.

Table 4.2. Mass, Momentum, and Kinetic Energy of the HH 315 Molecular Outflow

	Southern Lobe		Northern Lobe			
	Redshifted gas[a]	If $i = 10°$[b]	Blueshifted gas[c]	Redshifted gas[d]	Total	If $i = 10°$[b]
Mass	1.8	···	4.1	0.7	4.8 $M_\odot$	···
Momentum	2.1 $(\sin i)^{-1}$	12.1	5.1 $(\sin i)^{-1}$	1 $(\sin i)^{-1}$	6.1 $(\sin i)^{-1}$	35.1 $M_\odot$ km s^{-1}
Kinetic Energy	2.9 $(\sin i)^{-2}$	96	7.6 $(\sin i)^{-2}$	1.5 $(\sin i)^{-2}$	9.1 $(\sin i)^{-2}$	302×10^{43} erg

[a]In the southern lobe we only detect redshifted gas. The mass, momentum, and kinetic energy are obtained from the gas in an area shown in Figure 4.6, over the velocity range $3.21 < v < 6.29$ km s^{-1}

[b]Value of physical parameter assuming that the angle between the plane of the sky and the outflow "axis" (i) is 10°.

[c]Obtained from the blueshifted gas in the area shown in Figure 4.6, over the velocity range $-3.95 < v < 0.79$ km s^{-1}

[d]Obtained from the redshifted gas in the area shown in Figure 4.6, over the velocity range $2.55 < v < 3.65$ km s^{-1}

The effects of the ambient medium on the outflow's physical properties

The most notable aspect of the HH 315 molecular outflow is the striking difference in the morphology, kinematics, mass, momentum and kinetic energy between the two lobes. The difference between the two lobes is most probably due to the difference in the cloud structure and density between the region south and north of PV Ceph (see Levreault 1984 and Cohen et al. 1989 for illustrations). Molecular outflows are thought to be formed by the momentum-conserving interaction of an underlying stellar wind and ambient cloud gas. The southern HH flow lobe interacts with the densest parts of the PV Ceph cloud, and thus it is no surprise that the southern molecular lobe is constrained to a smaller area and exhibits lower maximum outflow velocities than the northern molecular lobe. It is striking, though, that the southern lobe has a smaller momentum than the northern lobe. Each lobe of a bipolar stellar wind (or HH flow) is expected to have equal amounts of momentum, thus each of the two lobes of a molecular outflow produced in a momentum conserving wind-cloud interaction should have similar amounts of momentum.

The high ambient cloud density south of PV Ceph, and the low inclination angle of the "average axis" of the HH 315 flow with respect to the plane of the sky ($i \sim 10^{\circ}$), both contribute to the fact that the observed redshifted emission in the southern outflow lobe exhibits low outflow velocities, compared to the northern lobe and to other observed molecular outflows (e.g., Orion B, Richer, Hills, & Padman 1992; NGC 2264G, Lada & Fich 1996; HH 111, Cernicharo & Reipurth 1996). It is very probable then, that an unknown amount of (redshifted) outflow mass is undetectable, as its velocity is so slow that its emission is hidden under the ambient cloud emission. Other studies estimate the presumed undetectable outflow mass hidden under the ambient cloud emission by extrapolating the mass-velocity power-law relation to lower outflow velocities (e.g., Margulis & Lada 1985; Bally et al. 1999; Yu et al. 1999). Extrapolating the mass-velocity relation in the HH 315 southern (red) lobe (Figure 4.7*e*) to an outflow velocity of about 0.4 km s^{-1}, adds an additional 12 $M_{\odot}$ and 5 $M_{\odot}$ km s^{-1} to the mass and (line-of-sight) momentum,

respectively, of the southern lobe. If we add this extra momentum to our original estimate, the southern lobe would then have a similar amount of momentum as the northern lobe. Though it is probable that some of the outflow mass is hidden under the ambient cloud emission, estimating the actual amount, and adding it in, is a very uncertain process. Instead, we will treat the estimated southern lobe mass, momentum, and kinetic energy at $0.71 < v_{out} < 3.59$ as lower limits.

4.4.2 The effects of the outflow on the ambient gas

The southern lobe and the PV Ceph Cloud

As shown in Figure 4.5, the projected overlap between outflowing gas and the PV Ceph cloud (as defined in Table 4.1) is quite small. Nonetheless, it is still interesting to consider what effect(s) the outflow may have on the overall evolution of the PV Ceph cloud. Since the large-scale ^{12}CO velocity maps in this paper (Figure 4.2) show no blueshifted outflow lobe emission superimposed on the PV Ceph cloud we only consider the effects of the redshifted lobe in estimating the effects of the HH 315 flow on the dense portion of the star-forming cloud. Note, though, that our higher resolution observations (Chapter 5) *do* detect a small amount of blueshifted outflow emission just north of PV Ceph.

One method to quantitatively study the effects of an outflow on its parent cloud is to compare the outflow's energy with the cloud's binding energy. The cloud's binding energy is given by $E_{grav} \sim GM_c^2/R_c$, where we estimate R_c to be the geometric mean of the short and long axes of the PV Ceph cloud (~ 0.7 pc), and M_c, the mass of the cloud, is ~ 74 M$_\odot$. Using these values we obtain that the cloud's binding energy is about 6.7×10^{44} erg. If the HH 315 flow has an inclination to the plane of the sky of $i \sim 10°$, then the southern lobe of HH 315 has enough kinetic energy (9.6×10^{44} erg) to gravitationally unbind its parent cloud —if that energy is efficiently coupled to the cloud (see below). Given the substantial amount of kinetic energy in the southern lobe, the flow might be able to disperse a major fraction of the very dense gas, where most of the binding mass is located. This in

turn would alter the gravitational potential well of the cloud.

We may indeed already be seeing the start of the PV Ceph cloud's disruption by the HH 315 flow. In Figure 4.9*a* we plot, in contours, the integrated intensity of the HH 315 molecular outflow's south lobe, superimposed on the ^{13}CO integrated intensity over the velocity range $1.84 < v < 2.17$ km s^{-1}. It can be seen that the molecular outflow's southern lobe fits in the ^{13}CO cavity seen just south of PV Ceph. This spatial coincidence suggests that the cavity was formed by the outflow-cloud interaction. In addition, the peak ^{13}CO integrated intensity over the velocity range $2.17 < v < 2.61$ km s^{-1} borders the southern lobe's position (see Figure 4.9*b*). This structure in the ^{13}CO also suggests that the southern lobe has pushed and redistributed the medium-density ambient gas.

In order to further investigate the hypothesis that the southern molecular outflow lobe is responsible for the minimum in the ^{13}CO distribution observed south of PV Ceph, we studied the velocity distribution of the ^{13}CO in the region (see spectrum in Figure 4.10). We made an average of the ^{13}CO emission in the cavity and fit it with a two-Gaussian function (the small blueshifted velocity component is due to cloud X). The fit yields a central velocity of 2.6 km s^{-1} for the velocity component associated with the PV Ceph cloud. This is only 0.1 km s^{-1} larger than v_{o_south}. Even though the difference is small, it is still significant as the 1-σ error in the central velocity fit is about 0.01 km s^{-1}.

In Figure 4.11 we show (in white contours) a ^{12}CO(2–1) position-velocity ($p-v$) diagram superimposed on a grey-scale ^{13}CO(1–0) $p-v$ diagram. Both $p-v$ diagrams are constructed by summing all spectra over the width of the ^{13}CO cavity seen in Figure 4.9*a*. The cavity is seen as a minimum in the ^{13}CO emission at velocities between $\sim$ 1.5 and $\sim$ 2.2 km s^{-1}, and at 0 to -2.5′ offset from the position of PV Ceph. This minimum in the ^{13}CO emission (or cavity) is bordered to the north and south by emission from the PV Ceph cloud. The redshifted border of the cavity is formed by the emission of the PV Ceph cloud and the blueshifted "border" is defined by emission from Cloud X. At the same position of the cavity there is a notch in the ^{12}CO(2–1) $p-v$ diagram. This notch indicates that there is

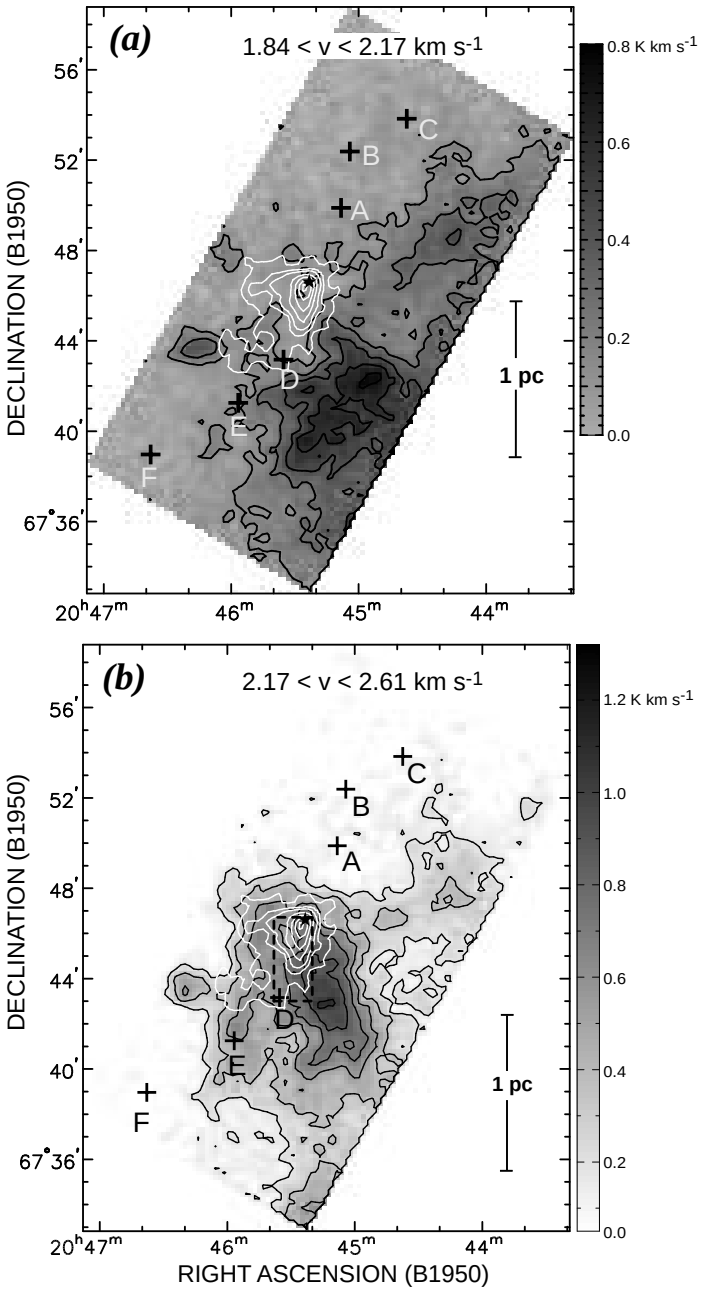

Fig. 4.9.— (*a*) Same grey-scale map as in Figure 4.3*c*, but with different grey-scale range. In addition, we superimpose the integrated intensity contours (white lines) of the ^{12}CO(2–1) southern lobe shown in Figure 4.1. Notice that the integrated intensity contours of the southern lobe fit well in the ^{13}CO "cavity" (or minimum). (*b*) Grey-scale map similar to Figure 4.3*d*. In addition, we superimpose the integrated intensity contours (white lines) of the ^{12}CO(2–1) southern lobe shown in Figure 4.1. Notice that the maximum ^{13}CO emission borders the western edge of the molecular outflow lobe. The dashed rectangle shows the area used to obtain the average ^{13}CO(1–0) spectrum shown in Figure 4.10.

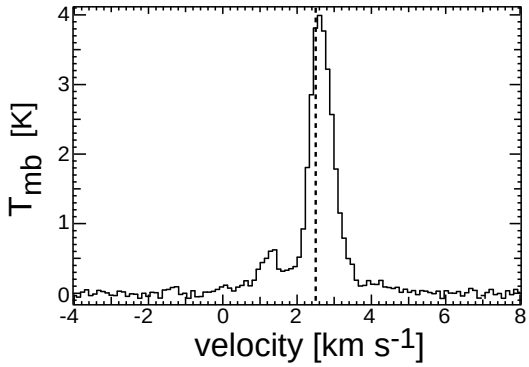

Fig. 4.10.— Average ^{13}CO spectrum over the cavity south of PV Ceph. The area is indicated by a dashed box in Figure 4.9*b*.

also a minimum in the ^{12}CO(2–1) emission at the position and velocity of the ^{13}CO cavity, and that there is a bulk shift in the velocity distribution of the ^{12}CO(2–1) gas towards redshifted velocities.

One possible scenario which fits the data is that the south molecular (redshifted) lobe pushed and accelerated the ambient cloud gas. The cavity can only be seen at low blueshifted velocities (relative to the PV Ceph cloud's central velocity, $v_{o\_south} = 2.50$ km s^{-1}) since the redshifted outflow lobe has only been able to slightly change the velocity distribution (toward redshifted velocities) of the dense gas it has interacted with, and it yet has to clear the region completely. If the outflow does not turn off, then given more time, more ambient gas will be shoved away and accelerated, making the cavity larger and visible at all velocities.

We may also estimate the role of the HH 315 flow in the PV Ceph cloud by comparing the southern lobe's kinetic energy with the cloud's turbulent kinetic energy. The total kinetic energy of a cloud where thermal motions are a negligible part of ΔV (the observed FWHM velocity line width), is given by $E_{turb} = \frac{3}{16 \ln 2} M_c \Delta V^2$, where M_c is the cloud mass. The average ^{13}CO velocity width in the PV Ceph cloud is $\Delta V \sim 0.6$ km s^{-1}, so $E_{turb} \sim 1.2 \times 10^{44}$ erg. The outflow kinetic energy is about 2.9 $(\sin i)^{-2} \times 10^{43}$ erg in the southern lobe, thus, even if $i = 29°$, the southern lobe kinetic energy exceeds the cloud's turbulent kinetic energy. Similar to what is observed in the giant molecular outflow HH 300

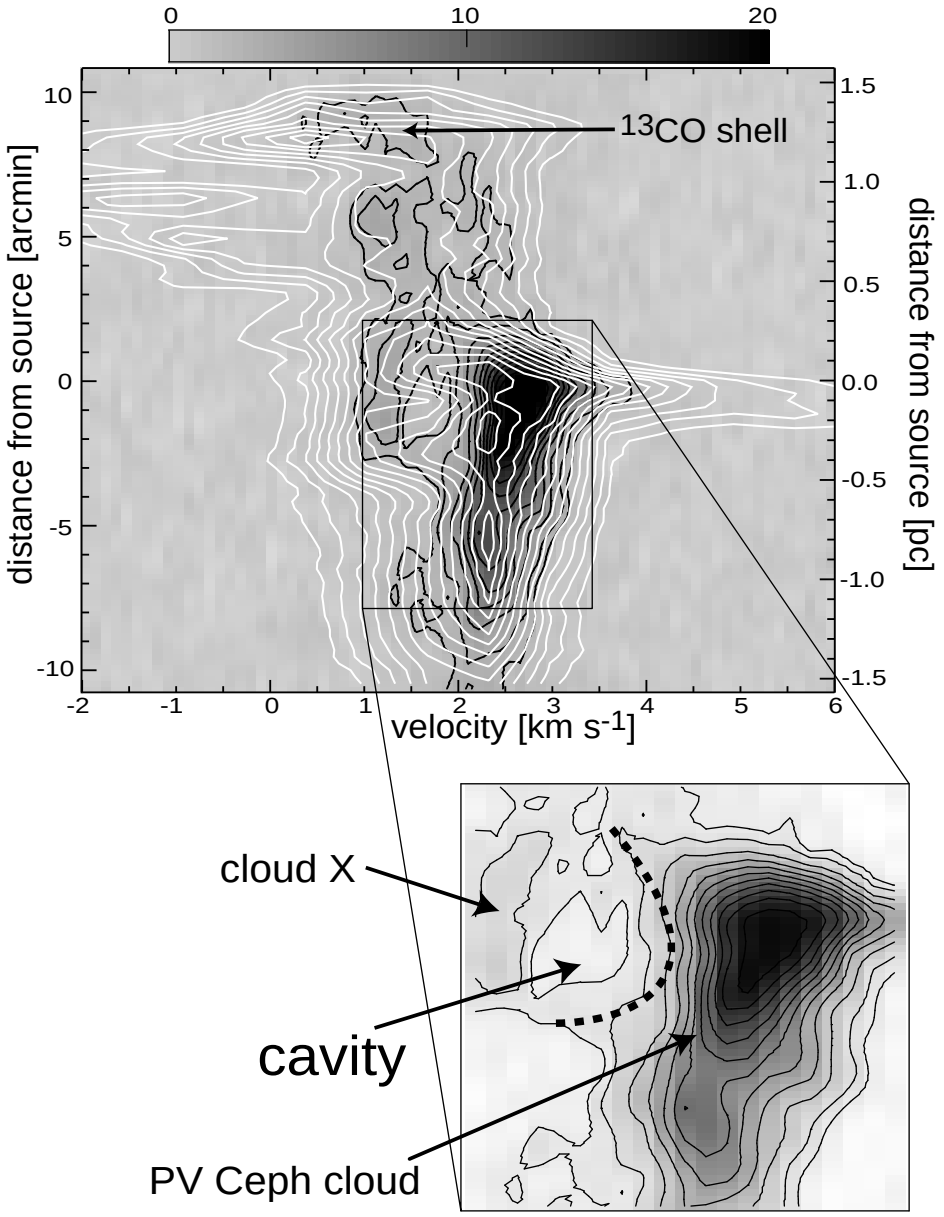

Fig. 4.11.— ^{12}CO(2–1) position-velocity diagram (white contours) superimposed on a ^{13}CO grey-scale position-velocity diagram. Both $p-v$ diagrams are constructed by summing all spectra over the width of the ^{13}CO cavity seen in Figure 9*a*. The contours in the ^{12}CO(2–1) $p-v$ diagram are 4 to 30 K, in steps of 2 K. The contours in the ^{13}CO(1–0) $p-v$ diagram are 2, 3, 5, 7, 9, 11, 13, 15, 17, 19, 21 K. The box encloses the region of the ^{13}CO $p-v$ diagram shown in more detail in the bottom panel. Several velocity features are identified.

(Chapter 2/Arce & Goodman 2001b), the southern lobe of the HH 315 molecular outflow has enough kinetic energy to potentially feed the turbulence in its parent cloud.

Yet another way to asses the importance of the HH 315 outflow energy input on its parent cloud is by comparing the flow's power with the power needed to maintain the magnetohydrodynamic (MHD) turbulence in the PV Ceph cloud. The three-dimensional numerical simulations of Stone, Ostriker, & Gammie (1998) and Mac Low (1999) study MHD turbulence under density, temperature and magnetic field conditions representative of those found in Galactic molecular clouds. Using equation 7 in Mac Low (1999), we can estimate the input power needed to maintain MHD turbulence in the PV Ceph cloud (shown in Figure 4.5). We use the estimated mass of the PV Ceph cloud (74 $M_{\odot}$) and the average velocity line width of the ^{13}CO (0.6 km s^{-1}). Using these values we find that about 0.01 $L_{\odot}$ of input power at a scale of 0.5 pc (the approximate length of the southern lobe) are needed to counter the dissipation of MHD turbulence in the PV Ceph cloud.

The power of an outflow is usually estimated by dividing the outflow kinetic energy by the dynamical age of the outflow. The conventional way to estimate the dynamical age of a molecular outflow assumes that all the gas in the outflow originates at the young star. This assumption is wrong, since the vast majority of the gas in a molecular outflow comes from the entrained gas in the host cloud (along the extent of the outflow) that has been put in motion by the underlying stellar wind. Since there is no way to obtain an accurate estimate of the outflow lifetime, we estimate a lower and an upper bound to the dynamical age in order to estimate an upper and lower bound to the outflow power. We estimate the lower limit to be the time it has taken HH 315F (the HH knot which currently lies farthest from the source) to travel to its current position. The distance from PV Ceph to HH 315F is 1.41 pc (RBD), and if we assume a tangential velocity of 200 km s^{-1}, we then obtain a dynamical age of about 6900 yr. As an upper limit on the age we use 2×10^5 years, the statistical lifetime of outflows as derived by the study of Parker, Padman, & Scott (1991). We then estimate the lower and upper limits of the outflow power to be 1.2×10^{-3} $(\sin i)^{-2}$ to 3.4×10^{-2} $(\sin i)^{-2}$ $L_{\odot}$. If

we assume that $i \sim 10°$, then the southern lobe's power is more than the estimated power needed to maintain the MHD turbulence in the PV Ceph cloud.

Note that we only compare the outflow power to that needed to sustain the MHD turbulence and stop gravitational collapse in the cloud in order to quantify the possible effect that outflows have on their parent cloud: by no means we are implying that molecular clouds *need* to be maintained in gravitational equilibrium. Our results for HH 315 (this chapter) and HH 300 (Chapter 2) imply that outflows are sources of non-negligible power in clouds, and they should be treated as such in numerical simulations of MHD turbulence in star-forming clouds (see also Chapter 6).

The energy in the HH 315 outflow southern lobe is comparable to, or larger than, the binding energy, and the turbulent energy, of the PV Ceph cloud. But, this does not necessarily mean that the outflow will be able to unbind the cloud or turn all its energy into cloud turbulent energy. We would be able to make a rough prediction of the PV Ceph cloud's future from our observations, if we knew how well the outflow energy couples to the cloud. The ^{13}CO cavity coincident with the southern outflow lobe, the ^{13}CO shell structure in the north, coincident with the outer edge of the northern blueshifted lobe, and the velocity gradient in the velocity of the ambient gas (see below) are all examples that there is some degree of coupling between the outflow and the ambient gas. Just from observational data, though, it is very hard to predict the outflow-cloud coupling efficiency of any outflow. No sufficiently good episodic outflow-cloud interaction model exists (see Chapter 3). There is a need for theoretical and numerical studies which concentrate on studying how efficiently can bulk motions, produced by outflows, unbind a cloud and/or produce turbulence, as a function of cloud density and outflow energy.

The northern lobe and the Northern Cloud

The northern lobe of the PV Ceph molecular outflow is characterized by its bow shock-like structure, coincident with the optical knot HH 315C, most evident at low outflow velocities (see Figure 4.2). A shell-like structure, surrounding the

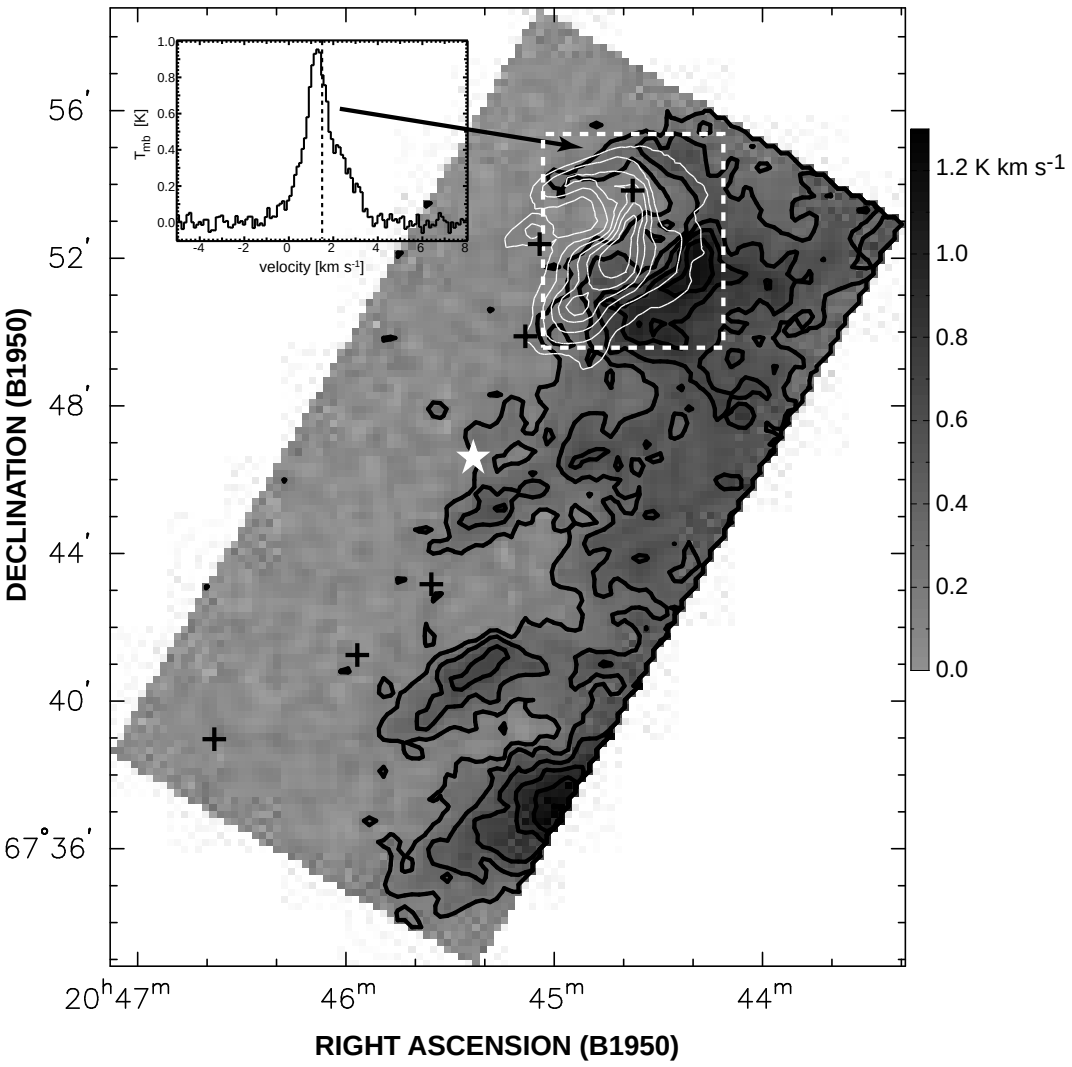

Fig. 4.12.— Grey-scale map similar to Figure 4.3*a*. In addition we superimpose the ^{12}CO(2–1) integrated intensity contours (white lines) of the blueshifted (northern) lobe. Notice the shell-like structure in the ^{13}CO surrounding the outer edge of the ^{12}CO(2–1) outflow lobe. The spectrum shown is an average over the area inside the white dashed box. The spectrum has a velocity range of $-5 < v < 8$ km s^{-1} and a main beam temperature range of $-0.1 < T_{mb} < 1.0$ K. The vertical dashed line in the spectrum indicates the position of $v = 1.5$ km s^{-1} in the velocity axis.

blueshifted outflow lobe, can be seen in ^{13}CO emission at very low (between 0.79 and 1.45 km s^{-1}) velocities (see Figures 4.3*a* and 4.12). Most of the northern lobe region is essentially devoid of ^{13}CO emission, and the majority of the ^{13}CO emission present in the region surrounds the western and northern edge of the ^{12}CO bow shock structure (see Figure 4.12). It appears that the HH 315 flow has been able to push gas north of PV Ceph, piling it in a dense shell-like structure surrounding the outflow lobe, which we detect in ^{13}CO(1–0).

Using the ^{13}CO emission surrounding the blueshifted lobe at velocities between 0.79 and 1.45 km s^{-1}, we estimate the shell structure's mass to be 6.8 M$_\odot$ and momentum to be 2.5 M$_\odot$ km s^{-1}. The line-of-sight momentum of the shell is sightly smaller than the line-of-sight momentum of the blueshifted outflow emission (which is equal to 5.1 M$_\odot$ km s^{-1}). The morphology of the shell-like structure (which surrounds the blueshifted outflow lobe), its slow blueshifted velocity, and the fact that its momentum is similar to the blueshifted outflow momentum are all consistent with the ^{13}CO shell having been formed by (momentum-conserving) entrainment of the ambient molecular gas by the HH 315 flow.

The velocities at which the ^{13}CO shell structure is seen fall inside the range of velocities which we defined earlier (§§4.3.3 and 4.4.1) as the north cloud ambient cloud. Thus, in fact we see that a substantial fraction (6.8/13.5 $\sim$ 50%) of what we had earlier naively defined as "Northern Cloud ambient gas" in reality is medium density gas that has been accelerated by the outflow. In fact, the peak ^{13}CO emission shell structure can be nicely seen in the ^{13}CO $p-v$ diagram (Figure 4.4), at about 6′ ($\sim$ 0.75 pc) from the source (along the P.A.=-26° axis), at a velocity of about 1.35 km s^{-1}. Thus, most of the cloud structure in the northern lobe region, as defined by the ^{13}CO emission, comes from gas that has been greatly affected by the outflow. One might say that in this region "the cloud is the outflow and the outflow is the cloud".

In Figure 4.13 we plot the ^{12}CO(2–1) position-velocity ($p-v$) diagram of the mapped region, constructed by summing all spectra along an axis with a position angle of -26°. By summing the ^{12}CO(2–1) spectra over a limited width

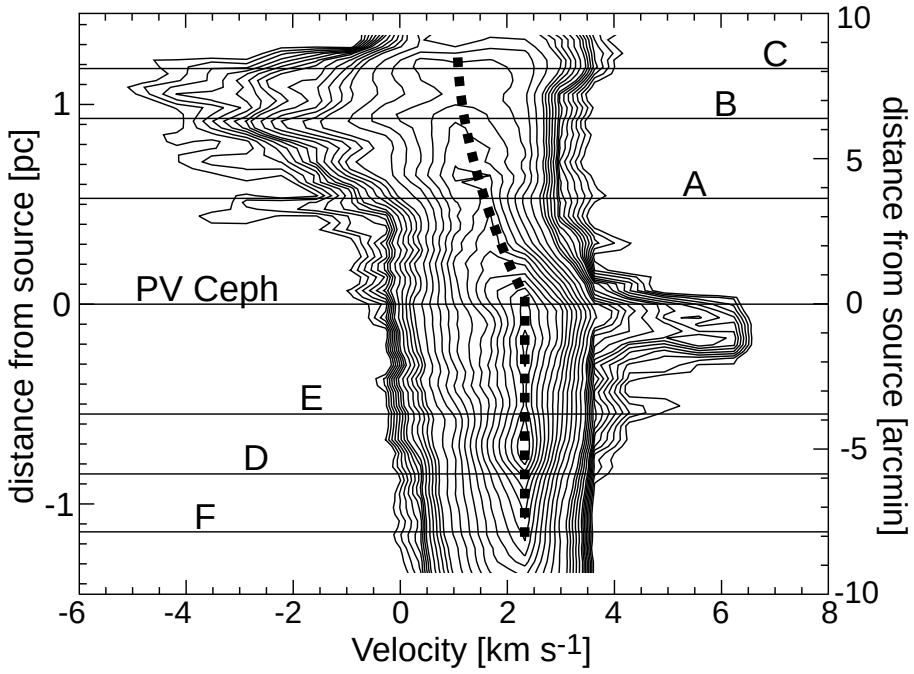

Fig. 4.13.— ^{12}CO(2–1) Position-Velocity ($p-v$) diagram of the HH 315 molecular outflow, constructed by summing all spectra along an axis with a P.A.=-26° (the outflow "average" axis), over an area shown in Figure 4.6. The contours are 3 to 10 K in steps of 1 K, 12 to 20 K in steps of 2 K, and 25 to 85 K in steps of 5 K. The positions of the brightest (optical) point of the six major HH knots in the flow, along the average outflow axis, are marked with a horizontal solid line. The thick black dash line traces the maximum contour along the outflow axis, indicating the presumed ambient cloud gas central velocity. Notice the velocity gradient north of PV Ceph.

(see Figure 4.6) of the ^{12}CO(2–1) map, we avoided including most (but not all) of the region where cloud X lies, so that its emission would not "contaminate" the ^{12}CO(2–1) $p-v$ diagram. The main features of the ^{12}CO(2–1) $p-v$ diagram are the peaks in the maximum velocity associated with the blueshifted (north) and redshifted (south) lobes. A local increase in the maximum velocity may be seen at the position (along the average axis) of the optical HH knots A, B, C, and D, and close to the position of PV Ceph. The velocity structure at the position of each of these optical knots is characteristic of the bow shock (prompt) entrainment mechanism, which will produce the highest velocities at the head of the shock (the position of the HH knot) and a decreasing velocity trend towards the source (e.g., Bence et al. 1996; Lee et al. 2001). The fact that we see several of these velocity increases (or bumps) in the $p-v$ diagram, and each is coincident with a different HH knot is also evidence that HH 315 flow is an episodic outflow (see Chapter 3). The increase in redshifted velocities at about -1$'$ offset from the source position is mainly due to the redshifted outflow lobe. We further discuss this velocity feature, and the kinematics of HH 315 molecular outflow in Chapter 5.

In addition to the kinematical structure associated with the HH knots, the north half of the $p-v$ diagram shows evidence for a velocity gradient in the ambient gas' central velocity. The ambient cloud's central velocity may be approximated as the velocity where the peak contour, in the $p-v$ diagram, lies. In the ^{12}CO(2–1) $p-v$ diagram, the peak contour is seen to shift from about 2.5 km s^{-1} at the position of PV Ceph down to about 1.5 km s^{-1} near HH 315A. We believe that the northern lobe of the HH 315 outflow is responsible for the gradient in the central velocity of the ambient cloud. In addition, the fact that more than half of the gas mass in the northern region has been accelerated by the outflow gives additional support to our hypothesis.

In any volume of momentum-conserving wind-cloud interaction high-density gas will be accelerated less than gas at low densities. This is what we observe in the ambient gas surrounding HH 315. The ambient gas north of PV Ceph (where we detect an obvious velocity gradient) is much less dense than the ambient gas to the south (where we cannot easily detect a large-scale velocity gradient

in the CO emission). The ambient density contrast between north and south of PV Ceph is clear from our ^{13}CO integrated intensity map (Figure 4.5) and from the relative extinction measurements between the region around HH 315B and HH 315D (GKW). We may also estimate the density contrast, from the ambient gas velocity gradient in each region. We assume that the velocity gradient in the ambient gas central velocity (Δv_a) is wholly due to the momentum conserving stellar wind-ambient gas interaction, and that the stellar wind deposits all its momentum ($\rho_w v_w$) on the ambient gas, so that $\rho_w v_w \approx \rho_a \Delta v_a$. We assume that the wind momentum of each lobe is the same. The ^{12}CO(2–1) $p-v$ diagram shows a velocity gradient to the north of ~ 1 km s^{-1} (see Figure 4.13). The ^{12}CO(2–1) $p-v$ diagram shows no velocity gradient in the ambient gas south of PV Ceph due to the coarse velocity resolution (0.65 km s^{-1}) of the ^{12}CO(2–1) data. But, the ^{13}CO data shows a velocity shift of ~ 0.1 km s^{-1} in the southern molecular outflow lobe region (see above, and Figure 4.10). Thus, we estimate that the ambient gas density south of PV Ceph is about a factor of 10 larger than the ambient gas density north of PV Ceph.

4.5 Summary and Conclusion

We mapped the giant molecular outflow associated with the HH 315 flow, from the star PV Cephei, in the ^{12}CO(2–1) line, with a beam size of 27″. We also made more extended maps of the gas surrounding the HH 315 flow in the ^{12}CO(1–0) and ^{13}CO(1–0) lines, with 45″ and 47″ beam sizes, respectively. By observing a large extent of the gas surrounding the outflow we are able to study the outflow in the context of its surrounding medium. Also, the ^{13}CO observations help us assess the effects the outflow has on the surrounding moderate-density ($n \sim 10^3$ cm^{-3}) gas structure and kinematics. In addition, the combined ^{12}CO(1–0) and ^{13}CO(1–0) line observations enable us to estimate the mass of the outflow by correcting for the velocity-dependent opacity of the ^{12}CO(1–0) line.

The outflow source, PV Ceph, is a young star forming in the northern *edge*

of its dark cloud. Hence, the northern and southern lobes of the HH 315 outflow are interacting with environments with drastically different densities. The southern lobe has a mass of 1.8 $M_\odot$ and interacts with the dense region we define as the PV Ceph cloud. We quantify the effects that the HH 315 flow has on the PV Ceph cloud by using different methods. Assuming that HH 315 has an inclination to the plane of the sky (i) of about 10°, then the southern lobe of the HH 315 molecular outflow has a momentum of 12.1 $M_\odot$ km s^{-1} and a kinetic energy of 9.6×10^{44} erg. The kinetic energy of the southern outflow lobe is enough to supply the turbulent energy of the PV Ceph cloud (1.2×10^{44} erg), and enough energy to gravitationally unbind it (the gravitational binding energy of the PV Ceph cloud is $\sim 6.7 \times 10^{44}$ erg). We compare our estimate of the southern lobe's mechanical power, with that of the power needed to sustain the MHD turbulence in the PV Ceph cloud (using the numerical models of Stone, Ostriker, & Gammie 1998 and Mac Low 1999). If we assume that $i \sim 10°$, then the southern lobe's power is more than the estimated power needed to maintain the MHD turbulence in the PV Ceph cloud. In addition, the ^{13}CO data indicate that the southern HH 315 flow is having a major effect on the distribution of the ambient cloud gas. We detect a cavity in the distribution of the ^{13}CO in the PV Ceph cloud region. The ^{13}CO gas velocity and density distribution, and the morphology of the outflowing ^{12}CO(2–1) gas suggest that the cavity has been formed by the southern outflow lobe interaction with its surroundings.

The northern (mostly blueshifted) lobe has a total mass of 4.8 $M_\odot$ and interacts with an environment which is much less dense (by about a factor of ten) than the environment south of PV Ceph. There is much less ^{13}CO emission north of PV Ceph, and most of the ^{13}CO emission is concentrated in a shell-like structure about 1.2 pc northwest of PV Ceph, coincident with the outer edge of northern outflow lobe. It appears that the northern lobe of the HH 315 molecular outflow has "pushed" aside ambient gas, piling it in a dense shell-like structure at its edges. The morphology of the shell-like structure, its slow blueshifted velocity, and the fact that its momentum is very similar to the blueshifted outflow lobe momentum are all consistent with the shell being formed by the (momentum-conserving)

entrainment of the ambient molecular gas in the HH 315 flow. Adding the mass in the northern molecular outflow, and the mass of the ^{13}CO shell, we find that more than 50% of the total gas mass in the region of the northern outflow lobe has been put into motion by the outflow. The northern outflow lobe of HH 315 is having a major impact on the structure of the ambient medium, even at a distance of about 1 to 1.4 pc from the outflow source.

In addition, we detect a velocity gradient in the ambient cloud's central velocity north of PV Ceph. The gradient is towards blueshifted velocities, in the same sense as the vast majority of the outflowing gas in the northern outflow lobe. We argue that the gradient in the cloud's central velocity is due to the HH 315 outflow, as the gradient is consistent with it being formed by a momentum-conserving outflow-cloud interaction. The fact that the outflowing gas mass north of PV Ceph is a major fraction of the total gas mass supports our picture in which the HH 315 flow is responsible for the velocity gradient in the ambient gas north of PV Ceph.

Our study clearly shows that the HH 315 flow is effecting the kinematics of its surrounding medium, and has been able to redistribute considerable amounts of its surrounding medium-density ($\sim 10^3$ cm^{-3}) gas in its star-forming core as well at parsec-scale distances from the source. These are necessary steps in the clearing of the gas surrounding a forming star and the eventual (total) disruption of the parent cloud. We conclude that the giant outflow from PV Ceph is having a profound effect on its host cloud's evolution and fate. It is tempting to generalize this result, along others like it, and suggest that outflows have great influence on the sculpting of star-forming molecular clouds.

Chapter 5

Molecular bow shocks, jets and wide-angle winds: a high resolution study of the entrainment mechanism of the PV Ceph Outflow

ABSTRACT

We present a new set of high-resolution molecular line maps of the gas immediately surrounding various Herbig-Haro (HH) knots of the giant HH flow from the young star PV Cephei (HH 315). The observations, aimed at studying the entrainment mechanism of the 2.6 pc-long HH 315 flow, include IRAM 30 m maps of the ^{12}CO(2–1), ^{12}CO(1–0), and ^{13}CO(1–0) lines, with beam sizes of 11″, 21″, and 22″, respectively. We compare the morphology and the kinematics of the outflow gas, as well as the temperature and momentum distribution of the molecular outflow with those predicted by different entrainment models. With our detailed study we are able to conclude that jet bow shock entrainment by an episodic stellar wind, with a time-varying axis, produces most of the high-velocity molecular outflow observed far from the source. In addition, near PV Cephei we find evidence for a poorly collimated, wide-angle, molecular outflow *and* a collimated wiggling jet-like molecular outflow. We propose that the poorly collimated component is entrained

by a wide-angle wind, and the collimated component is entrained by a variable jet with internal working surfaces. Thus, a stellar wind model which allows for the coexistence of a wide-angle component *and* a collimated (jet-like) stellar wind component is needed to explain the observed properties of the PV Ceph outflow. The wiggling axis of the redshifted molecular outflow lobe indicates that the outflow ejection axis is changing over time. We find that the timescale of the axis variation shown by the molecular outflow lobe is about a factor of 10 less than that shown by the large-scale optical HH knots.

5.1 Introduction

In order to better understand the effects of winds from young stars on the ambient molecular cloud, it is essential to study how the wind interacts with its surrounding medium. The best evidence that winds from young stars interact with their surrounding ambient gas is the existence of molecular outflows. Many molecular outflows have masses that are larger than their powering young star, by a factor of a few up to an order of magnitude (e.g., Wu et al. 1996). It is, therefore, highly unlikely that the mass in CO outflows comes directly from the forming star and/or the circumstellar disk, and so molecular outflows consist mainly of swept-up ambient material.

The mechanism by which a wind from a young stellar object entrains and accelerates the ambient gas, thereby producing a molecular outflow, is still a matter of debate, even though several models have been proposed. The three most popular entrainment models are the turbulent jet model, the bow shock model, and the wide-angle wind model.

In the turbulent jet entrainment model (e.g., Cantó & Raga 1991; Stahler 1994; Lizano & Giovanardi 1995), the ambient gas is entrained on the sides of a jet (or wind) through a turbulent viscous mixing layer formed by Kelvin-Helmholtz instabilities.

In the bow shock model (e.g., Raga & Cabrit 1993; Stone & Norman 1993a;

Masson & Chernin 1993; Stone & Norman 1994; Suttner et al. 1997; Zhang & Zheng 1997; Smith, Suttner, & Yorke 1997; Downes & Ray 1999; Lee et al. 2001) a highly-supersonic collimated wind or jet propagates into the ambient medium, forming a bow shock surface at the head of the jet. The jet carves into the cloud, interacting with the ambient gas, producing a molecular outflow around the jet. Velocity variations in the jet produce bow shocks along the body of the jet, also referred to as internal working surfaces (e.g., Raga et al. 1990; Raga & Kofman 1992; Cantó, Raga, & D'Alessio 2000), which can also help entrain ambient gas.

In the wide-angle wind model (Shu et al. 1991; Li & Shu 1996; Matzner & McKee 1999; Lee et al. 2000; 2001), the outflow is produced when a momentum-conserving wide-angle wind from a young stellar object interacts with the ambient gas. The wind power is dependent on polar angle, has a constant velocity and blows into a core with radial density profile and angular dependence. The ambient medium is swept up into a shell by a shock at the wind bubble-ambient cloud interface. The molecular outflow is then identified as the molecular gas in the entrained shell.

In Table 5.1 we summarize the expected molecular outflow characteristics (i.e., gas morphology, temperature, velocity and momentum distribution), for these three entrainment models.

On the observational front, recent high angular resolution studies of molecular outflows (e.g., Richer, Hills, & Padman 1992; Bence, Richer, & Padman 1996; Cernicharo & Reipurth 1996; Lada & Fich 1996; Davis, Smith, & Moriarty-Schieven 1998; Shepherd et al. 1998; Gueth & Guilloteau 1999; Yu, Billawala, & Bally 1999; Davis et al. 2000; Lee et al. 2000; Arce & Goodman 2001b/Chapter 2) have provided important information on the physical parameters of outflows and the entrainment mechanism. These studies have revealed a wide variety in the properties of molecular outflows leaving us in need of even more observations before we can understand the entrainment mechanism, and further constrain theoretical and numerical models.

In the previous chapter we studied the interaction of the HH 315 flow with its

Table 5.1. Molecular outflow properties predicted by entrainment models

Model	Stellar Wind	Predicted property of molecular outflow			
		Morphology	Velocity	Temperature	Momentum [a]
Turbulent Jet	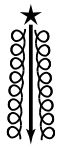				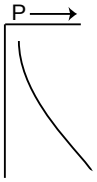
Jet Bow Shock	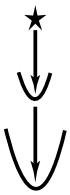		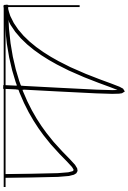		
Wide-angle Wind	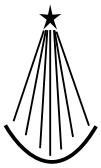	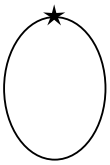			

[a] Momentum distribution along the outflow axis, assuming a underlying density distribution of r^{-1} to r^{-2}.

parent cloud on large scales. In this chapter, we zoom in on the gas immediately surrounding several HH knots and the outflow source (PV Ceph), in order to study the entrainment mechanism of the HH 315 outflow. In particular, we study the temperature distribution, kinematics, momentum distribution, and morphology of the outflow gas. The results are then used to compare all of these observed outflow characteristics with those expected from different entrainment models. Along with the information from earlier high resolution studies, our results provide important constraints to be considered by future theoretical entrainment models.

In the following section we will describe the observations. This is followed by a section where we describe our results. We later use our results to compare them with the results of the three molecular outflows entrainment models shown in Table 5.1. Subsequently, we discuss the episodic and wandering (or wiggling) nature of the HH 315 outflow. Lastly, we give a summary of our findings.

5.2 Observations

In order to study in detail the interaction between the HH 315 flow and the surrounding gas, we made high spatial- and velocity- resolution observations of the gas around several of the HH knots in the flow. The data were obtained using the IRAM 30 m telescope in Pico Veleta, Spain, in September 1999. The ^{12}CO(1–0), ^{12}CO(2–1), and ^{13}CO(1–0), lines were observed simultaneously using three spectral line SIS receivers. The spectrometer used was an autocorrelator split in three parts, each connected to a different receiver. The $J = 1 \rightarrow 0$ lines were observed with a spectral resolution of 40 kHz and a bandwidth of 20 MHz, and the ^{12}CO(2–1) line was observed with a spectral resolution of 80 kHz and a bandwidth of 40 MHz. The telescope beamwidth (FWHM) at ^{12}CO(1–0), ^{12}CO(2–1), and ^{13}CO(1–0) are about $21''$, $11''$, and $22''$, respectively. The forward efficiency (F_{eff}) and main beam efficiency (B_{eff}) of the $J = 1 \rightarrow 0$ lines are approximately 0.90 and 0.54, respectively, and for the ^{12}CO(2–1) line $F_{eff} \sim 0.86$ and $B_{eff} \sim 0.42$ (Wild 1999). Unless it is stated otherwise, the intensity scale of the spectral data from the IRAM

Table 5.2. Regions Mapped with the IRAM 30 m telescope

Region Name	Center Position α_{1950}	Center Position δ_{1950}	Region Size
hh315b+c	$20^h44^m49^s.4$	$67°52'49''$	$5.2' \times 4.2'$
hh215	$20^h45^m26^s.4$	$67°46'13''$	$2.2' \times 4.2'$
hh315e	$20^h45^m59^s.6$	$67°40'31''$	$2.3' \times 2.3'$

30 m is in units of main beam temperature (T_{mb}), where $T_{mb} = (F_{eff}/B_{eff})T_A^*$ (Wild 1999; Rohlfs & Wilson 2000).

The on-the-fly mapping technique was used to map three regions of interests. The telescope in OTF mode moved across the source at a constant speed of $2''$ s^{-1}, while a spectrum was acquired every 2 seconds. In order to map the three different desired areas more efficiently, they were mapped by combining several overlapping maps of different sizes. Table 5.2 lists the center position and the size of each of the three major regions (see also Figure 5.1). The regions were all scanned in both the right ascension and declination directions. The separation, in the direction perpendicular to the scanning direction, between subsequent rows was $4''$.

The telescope was pointed to an OFF position, located at R.A. $20^h45^m30.4^s$, decl. $67°55'46.7''$ (B1950), after every other row, where it would observe the OFF position for 10 to 15 sec. A temperature calibration was done every 5 to 10 minutes. Deep observations of the OFF position showed no significant emission. The different regions were observed several times to improve the signal-to-noise in the spectra. A baseline was fitted to and subtracted from each spectrum. The spectral maps of each region were convolved with Gaussian beams of different sizes, and Table 5.3 shows the resultant RMS noise for each spectral line map convolved with different beams.

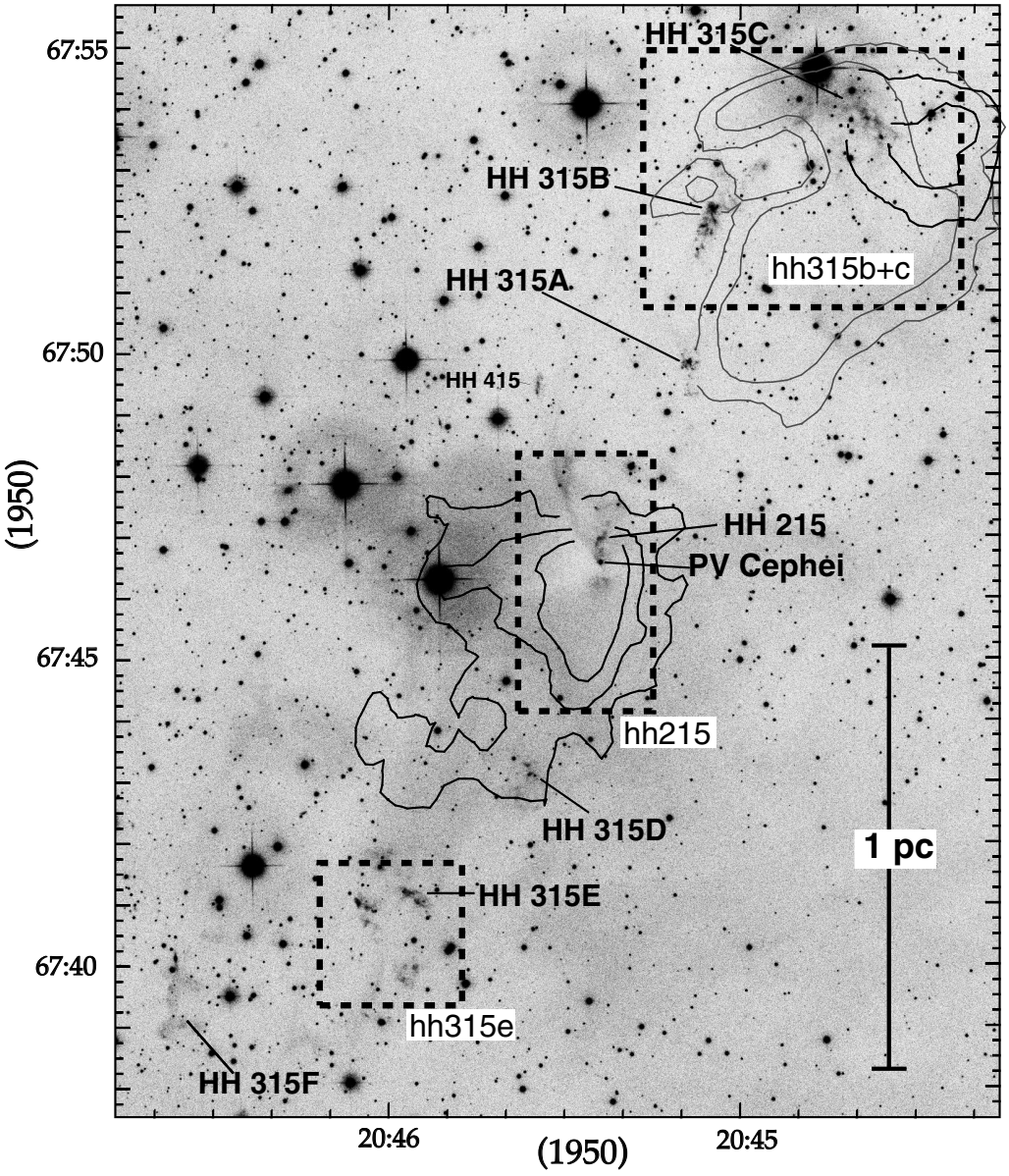

Fig. 5.1.— Wide-field Hα+[S II] (optical) CCD image of the HH 315 giant HH flow, from RBD. The dashed boxes denote the areas mapped with on-the-fly mapping at the IRAM 30 m telescope. The name given to each region is shown at the bottom of each region. We also show selected contours of the large-scale blueshifted (grey) and redshifted (black) ^{12}CO(2–1) outflow gas (based on Figure 4.1). In certain places the contour are cut so that features in the optical image may be seen better. The position of the HH knots, and the position of PV Ceph (the outflow source) are also shown.

Table 5.3. RMS Noise and Velocity Resolution of Spectral Line Maps

Region Name	Molecular Line	Beam[a] [″]	δv[b] [km s^{-1}]	RMS[c] [K]	Where Used
hh315b+c	^{12}CO(2–1)	21	0.22	0.62	Fig. 5.2
	^{13}CO(1–0)	21	0.22	0.20	Fig. 5.4
	^{12}CO(2–1)	24	0.22	0.50	Figs. 5.10, 5.12
	^{12}CO(1–0)	24	0.22	0.28	Fig. 5.10, 5.13, Mass estimates[d]
	^{13}CO(1–0)	24	0.22	0.16	Mass estimates[d]
hh215	^{12}CO(2–1)	14	0.11	0.78	Fig. 5.5
	^{13}CO(1–0)	14	0.11	0.28	Fig. 5.6
	^{12}CO(2–1)	24	0.11	0.49	Fig. 5.11
	^{12}CO(1–0)	24	0.11	0.31	Figs. 5.11, 5.15, Mass estimates[e]
	^{13}CO(1–0)	24	0.11	0.18	Mass estimates[e]
hh315e	^{12}CO(2–1)	21	0.11	0.69	Figure 5.9

[a]The size of the beam the map was convolved with. The size of each pixel in each map is always half the size of the convolution beam.

[b]Velocity resolution (width of velocity channel).

[c]Maximum RMS (in T_{mb} units) of all pixels *not* at the edge of the map.

[d]Outflow mass estimates of the hh315b+c region are shown in Table 5.4

[e]Outflow mass estimates of hh215 region are shown in Table 5.5

5.3 Results

5.3.1 The region surrounding HH 315B and HH 315C (hh315b+c)

Large scale CO maps of the outflow associated with PV Ceph (Levreault 1984; and the results of Chapter 4) show that the region surrounding the optical knots HH 315B and HH 315C (region hh315b+c) is the area where most of the emission from the northern (mostly blueshifted) outflow lobe resides (see Figure 5.1). In this section, we present high spatial resolution maps of hh315b+c, which show the structure of the outflowing gas in detail, and its spatial relation with the HH knots.

^{12}CO(2–1) emission

Figure 5.2 shows ^{12}CO(2–1) velocity-integrated maps of the hh315b+c region, observed with the IRAM 30 m telescope, for 10 different velocity ranges. The emission with the most blueshifted velocities is shown in Figure 5.2*b* and the emission with the most redshifted velocities is shown in Figure 5.2*l*. Notice that not all velocity integration ranges have the same width. The different ranges of integration were chosen to group different channels with similar ^{12}CO(2–1) emission structure. The grey objects shown in each velocity map panel represent the position of the different S[II] knots in the region, as presented by Gómez, Kenyon, & Whitney (1997, hereafter GKW).

The highest-velocity (most blueshifted) CO outflow gas is shown in Figure 5.2*b*. The emission at these velocities is concentrated at the position of the HH 315B optical knot. The lowest (plotted) contour of integrated emission shows wing-like extensions which point towards the position of the outflow source (PV Ceph). The shape of the contours at these high velocities is suggestive of a bow shock morphology.

At slightly lower (less blueshifted) velocities, the outflow gas is concentrated along the main HH 315B optical knot (see Figures 5.2*c* and 5.2*d*). The gas emission surrounding HH 315B in Figures 5.2*c* and 5.2*d* is mainly concentrated south of the emission peak in Figure 5.2*b*, and has an elongated morphology towards the position of PV Ceph. This is consistent with a picture where the highest velocities are at the head of the shock (Figure 5.2*b*), where the gas is currently being entrained, and the slower wake of previously entrained gas is found behind the head of the shock (emission in Figures 5.2*c* and 5.2*d* near HH 315B).

The most striking feature of the velocity maps shown in Figure 5.2 is the bow shock- (or shell-) like structure of the ^{12}CO(2–1) emission, coincident with the HH 315C optical knot. The head of the CO shell coincides with the region of brightest optical emission from HH 315C, and has wings, on both sides of the head, which point in the general direction of PV Ceph. Hereafter we will refer to this structure as the HH 315C CO shell. Figure 5.2*d* shows the outflow gas

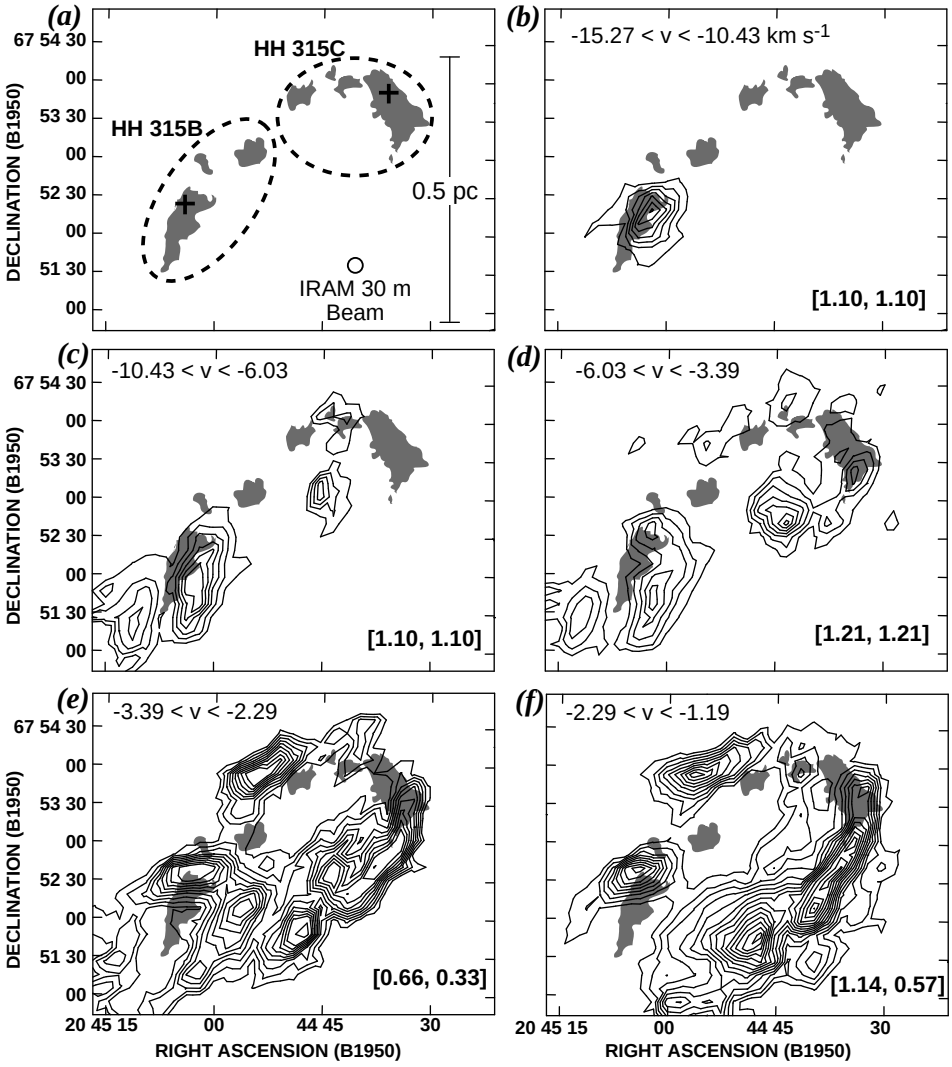

Fig. 5.2.— Velocity-range-integrated intensity maps of the ^{12}CO(2–1) emission surrounding the blueshifted optical knots HH 315C and HH 315B (i.e., the hh315b+c region, see Figure 5.1). The velocity range of integration is shown in the upper-left corner of each panel. The starting contour and the contour steps are given in brackets at the lower-right corner of each panel in units of K km s^{-1}. The grey silhouettes represent the S[II] knots in the region, from GKW. The optical knots are identified in panel [*a*]. Panel [*a*] also shows the IRAM 30 m beam at the ^{12}CO(2–1) frequency (11″), and the linear scale assuming a distance to PV Ceph of 500 pc. In panel [*g*] we show the position from where the spectra in Figure 5.3 are taken. Each letter in panel [*g*] represents the position of the spectrum shown in the panel, in Figure 5.3, with the same letter.

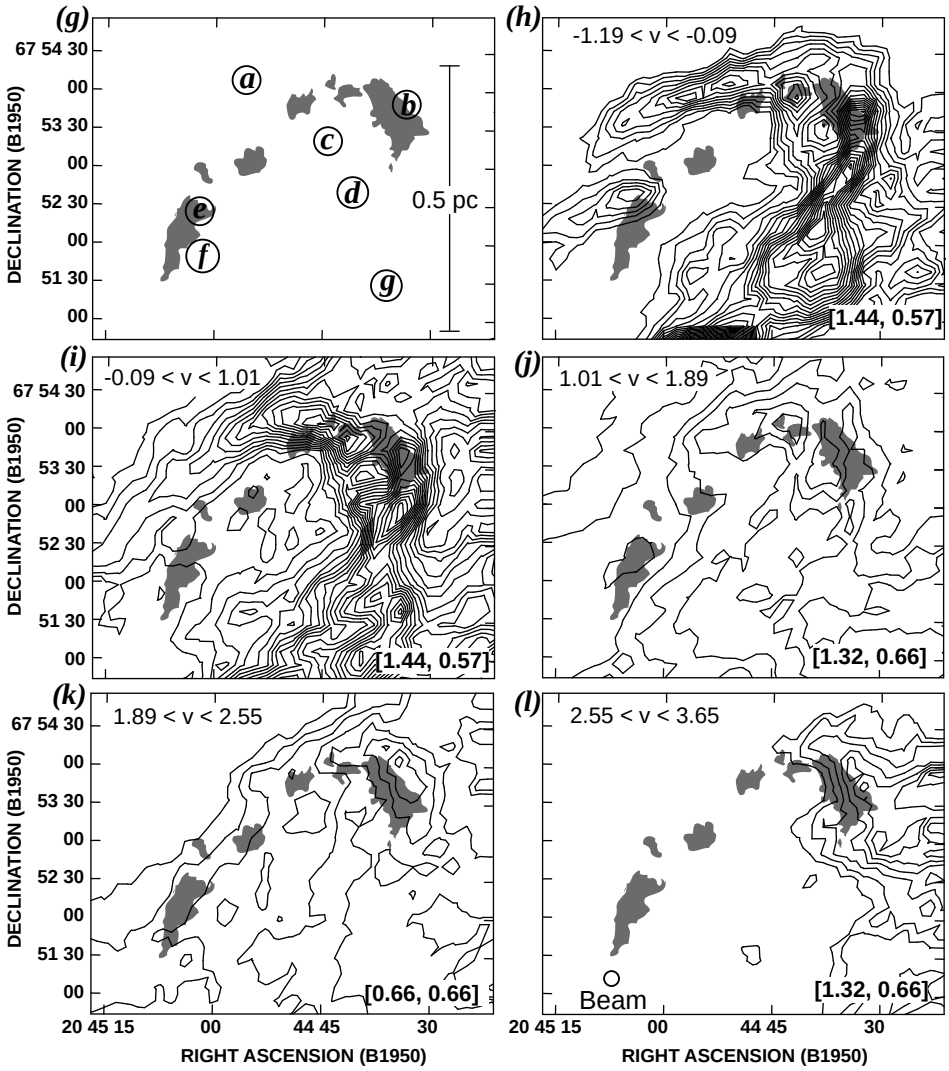

Fig. 5.2.— Continued.

emission with the highest velocities at which the HH 315C CO shell is detected. It can be seen that the HH 315C CO shell is smaller for increasing (blueshifted) outflow velocities. That is, the bow shock wings are further apart from each other, and extend further out from the HH 315C optical knot, for less extreme outflow velocities. For example, the CO bow shock wings in Figure 5.2*i* are about 2′.7 (0.39 pc, at a distance of 500 pc) apart, and the wings extend off the southern and eastern limits of our map. On the other hand, the high-velocity CO bow shock structure seen in Figure 5.2*d* has wings which are about 1.8′ (0.26 pc) apart and extend 1.3′ (0.19 pc) southeast from the position of HH 315C.

In Figure 5.2*j* we show the ^{12}CO(2–1) integrated over the velocities between 1.01 and 1.89 km s^{-1}. The ambient cloud velocity in this region is 1.5 km s^{-1} (see Chapter 4), and so most of the "ambient" cloud is found at this velocity range. In Figure 5.2*k* we plot the ^{12}CO(2–1) integrated over the velocities between 1.89 and 2.55 km s^{-1}. This velocity range also includes emission from "ambient" cloud gas, as the gas emission shows an extended, cloud-like, morphology. In both Figures 5.2*j* and 5.2*k* the density gradient of the cloud is clearly seen, the cloud's edge is in the east and the density increases towards the west. At these "ambient" velocities, there is an increase in the column density at the position of the different small knots which comprise the HH 315C knot. In addition, the ^{12}CO(2–1) contours near the HH 315C knots curve, following the bow-like configuration of the optical knots. Thus, we see that the HH 315C CO shell structure is also detectable at ambient cloud velocities —evidence that the HH 315 flow has altered the ambient gas distribution at distances as far as $\sim$ 1.5 pc from the source (see Chapter 4 for more on this).

The ^{12}CO(2–1) map integrated over the range of $2.55 < v < 3.65$ km s^{-1} (Figure 5.2*l*), which is redshifted with respect to the ambient cloud velocity of the region, shows a "clump" of emission coincident with the HH 315C optical knot. Similar to what is seen in the other (blueshifted) velocity-integrated maps in Figure 5.2, the ^{12}CO(2–1) intensity contours curve, following the bow-like arrangement of the HH 315C optical knots. This redshifted emission is presumably outflowing gas accelerated by the "back side" of the shock front associated with

HH 315C.

In Figure 5.3 we show several sample ^{12}CO(2–1) spectra from the hh315b+c region. It is interesting to note the drastic differences between spectra from regions very close to each other. Also, notice that the outflow emission is not a smooth low-level wing at blueshifted velocities. Instead, it is made of different velocity (spectral) components, which sometimes are stronger than the ambient cloud component.

^{13}CO emission

The ^{13}CO emission in the hh315b+c region has less complicated velocity structure than the ^{12}CO emission. Similar to what is observed in the large-scale map (see Figure 4.3), the ^{13}CO(1–0) emission at velocities greater than 1.5 km s^{-1} in this region is very weak ($T_{mb} \lesssim 0.6$ K), and hence most of the ^{13}CO emission in this region is blueshifted compared to the cloud's ambient velocity. In Figure 5.4 we show three different ^{13}CO velocity-integrated intensity maps. The different ranges of integration were chosen to group different channels with similar ^{13}CO(1–0) emission structure.

The ^{13}CO vaguely follows the ^{12}CO bow shock structure associated with HH 315C. Both the north and the south bow shock wings are clearly present in ^{13}CO emission, yet there is very little ^{13}CO emission at the location of the bow shock apex. The north and south ^{13}CO bow wings are spatially coincident with the ^{12}CO bow wings with similar velocities. We do not detect any ^{13}CO emission associated with the high velocity gas surrounding the HH 315B knot. The structure of the high spatial resolution ^{13}CO is consistent with our original hypothesis (Chapter 4) that the blueshifted northern lobe of the HH 315 molecular outflow has "pushed" aside gas, creating a shell-like structure at its edges, which is dense enough ($n \gtrsim 500$ cm^{-3}) that is detected in ^{13}CO.

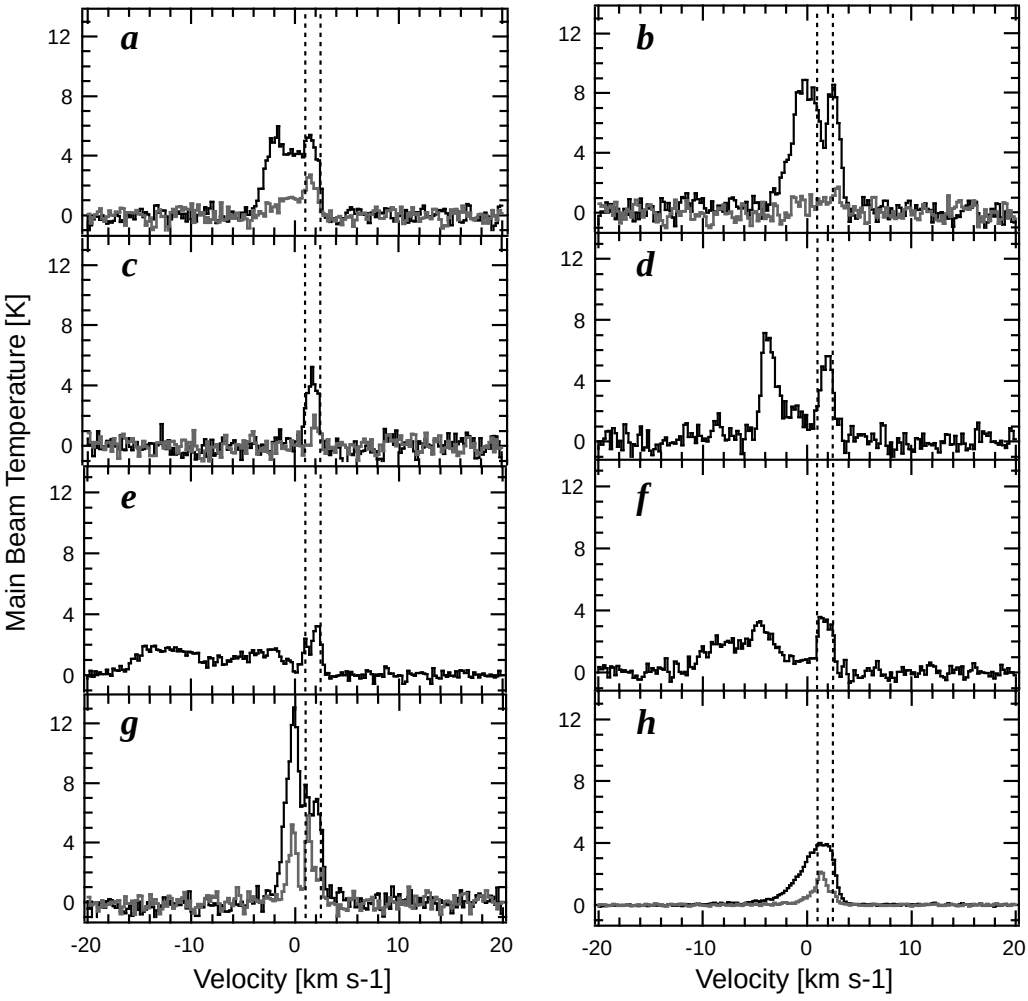

Fig. 5.3.— Sample ^{12}CO(2–1) (black) and ^{13}CO(1–0) (grey) spectra of the hh315b+c region. Panels [*a*] through [*g*] show spectra from the position shown in Figure 5.2*g*. Each spectrum (*a* through *g*) was taken from a single 10.5″ by 10.5″ pixel, of a molecular line map convolved with a 21″ beam. Panel [*h*] shows the average spectra over the whole hh315b+c region. The dotted vertical lines indicate the approximate range of the "ambient" cloud velocities ($1.0 < v < 2.5$ km s^{-1}).

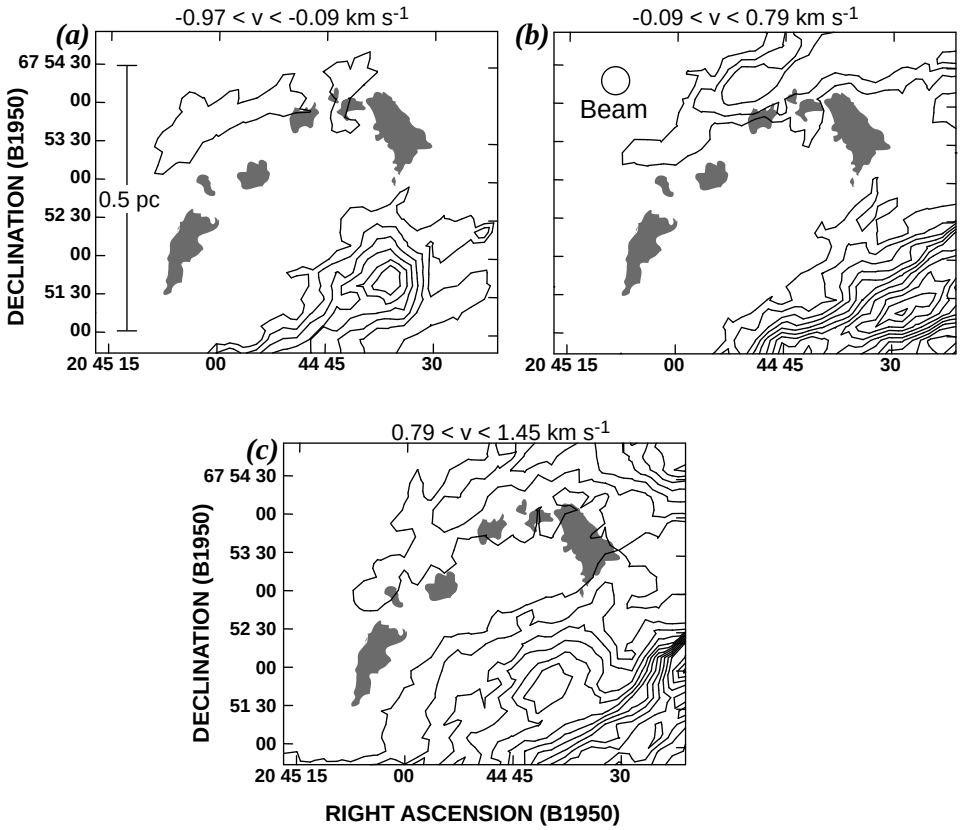

Fig. 5.4.— Velocity-range-integrated intensity maps of the ^{13}CO emission surrounding the blueshifted optical knots HH 315C and HH 315B. The velocity range of integration is shown at the top of each panel. The grey silhouettes represent the S[II] knots in the region, see Figure 5.2. All panels have the same staring contour and contour step value of 0.18 K km s^{-1}. The linear scale is shown in panel [*a*] and the IRAM 30 m beam (22″) at the ^{13}CO(1–0) frequency is shown in panel [*b*].

Table 5.4. Mass at different velocity ranges in hh315b+c

Velocity Range[a] [km s^{-1}]	$\bar{T}_{ex}$[b] [K]	Mass [M$_\odot$]	Momentum[c] [M$_\odot$ km s^{-1}]	Kinetic Energy[c] [10^{43} erg]
$-15.27 < v < -10.43$	21.7	0.01	0.14	1.94
$-10.43 < v < -6.03$	18.6	0.03	0.25	2.27
$-6.03 < v < -3.39$	17.8	0.05	0.30	1.76
$-3.39 < v < -2.29$	15.4	0.07	0.30	1.26
$-2.29 < v < -1.19$	13.0	0.17	0.53	1.64
$-1.19 < v < -0.09$	11.0	0.76	1.52	3.10
$-0.09 < v < 1.01$	10.5	2.88	2.65	2.69
$1.01 < v < 1.89$[d]	10.5	3.92	...	...
$1.89 < v < 2.55$[d]	10.5	1.31	...	...
$2.55 < v < 3.65$	10.5	0.58	0.77	1.08

[a]Velocity ranges are the same ranges as the ones in Figure 5.2.

[b]Average excitation temperature at the given velocity range, using Equation A.9, except for last four rows, where $\bar{T}_{ex} = 10.5$ (from previous chapter).

[c]Radial component only. Value not corrected for the inclination of the outflow axis with respect to the plane of the sky.

[d]Ambient cloud velocity range.

Mass

In Table 5.4 we list the mass for each of the velocity ranges shown in Figure 5.2. The mass was obtained using our high-resolution (IRAM 30 m) ^{12}CO(1–0) and ^{13}CO(1–0) data, with the procedure described in Chapter 4. The only difference in the procedure is the use of the average excitation temperature ($\bar{T}_{ex}$), given in Table 5.4, to estimate the outflow mass of a given velocity range (rather than using $T_{ex} = 10.5$ for all velocities). Notice that the mass of the "ambient cloud" velocity range ($1.01 < v < 2.55$ km s^{-1}) is approximately the same as the sum of the rest of the velocity ranges. This implies that in this region the outflow mass is approximately the "ambient cloud" mass. We first noticed this with our large-scale CO maps (Chapter 4), and its importance is discussed there.

5.3.2 The region surrounding HH 215 and PV Ceph (hh215)

The other region studied at high resolution with the IRAM 30 m telescope is the area surrounding the outflow source, PV Ceph. This area is where most of the southern (redshifted) outflow resides (see Figure 5.1). In addition, the area observed also covers the area north of PV Ceph where the chain of five optical knots that make up HH 215 have been detected (GKW). We call this whole area the hh215 region. We note that in this region, the central ambient cloud velocity is $v_{o\_south} = 2.5$ km s^{-1} (see Chapter 4), and so outflow velocities in the hh215 region are defined as the observed velocity minus 2.5 km s^{-1}.

^{12}CO(2–1) emission

In Figure 5.5 we show the integrated intensity, over different velocity ranges, of the ^{12}CO(2–1) in the hh215 region. Notice that not all velocity integration ranges have the same width. The different ranges of integration were chosen to group different velocity (spectral) channels with similar ^{12}CO(2–1) emission structure.

The most blueshifted velocity range in which we detect ^{12}CO(2–1) emission in this region is shown in Figure 5.5*a*. The blueshifted molecular outflow emission in this velocity range ($-0.15 < v < 0.74$ km s^{-1}) is concentrated at the source and north of it. The emission detected south (and southeast) of the source in Figure 5.5*a* is from another cloud in the same line of sight (cloud X) which we detect in our large scale ^{12}CO and ^{13}CO maps (see Figures 4.2 and 4.3). The blueshifted ^{12}CO(2–1) outflow emission in Figure 5.5*a* is very poorly collimated —unlike the outflowing redshifted emission discussed below— nor does it show the nice bow shock structure observed in the hh315b+c region.

In Figure 5.5*b* we show the (blueshifted) ^{12}CO(2–1) integrated emission over the velocity range between $1.62 < v < 2.06$ km s^{-1}. We do not include an integrated velocity map for velocities between 0.74 and 1.62 km s^{-1}, since at these velocities the ^{12}CO is dominated by the emission from cloud X all through the

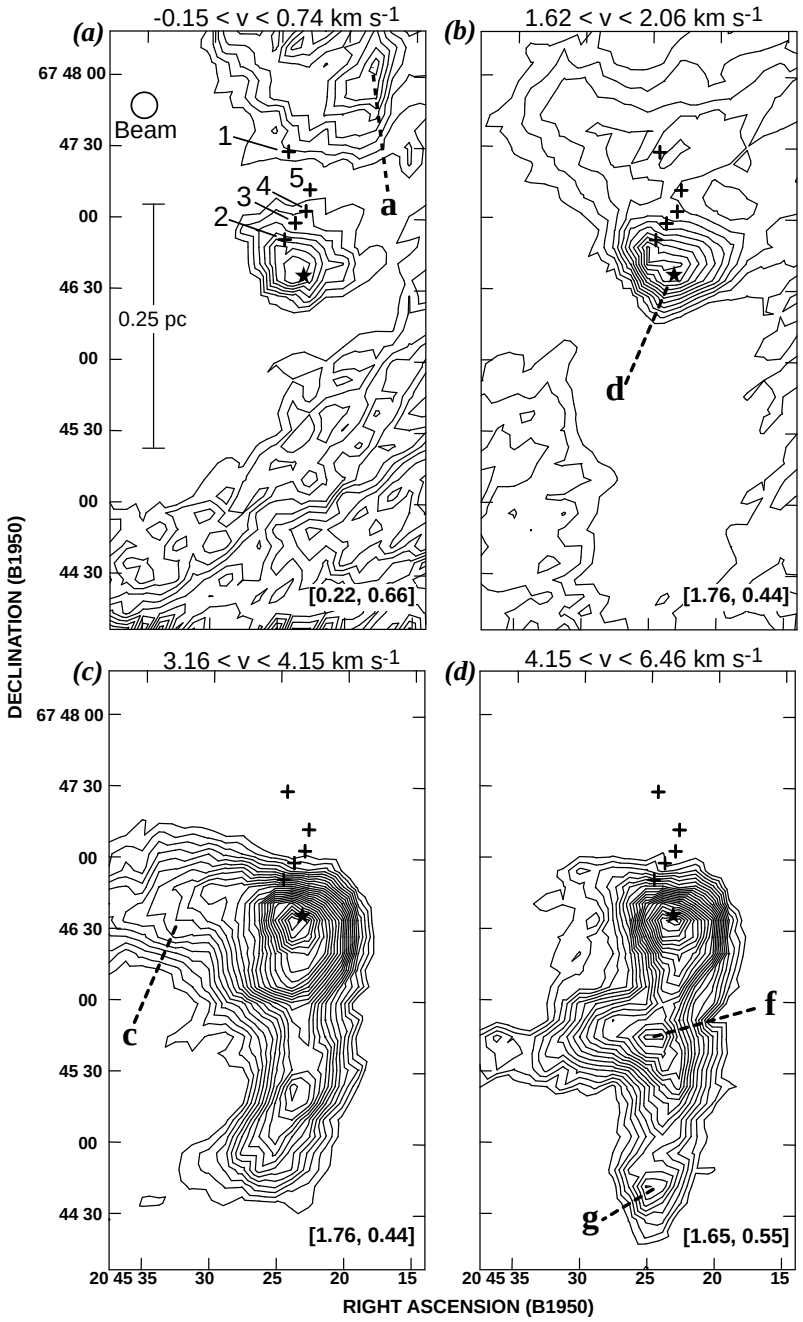

Fig. 5.5.— Velocity-range-integrated intensity maps of the ^{12}CO(2–1) emission surrounding PV Ceph, HH 215, and the southern redshifted outflow lobe (i.e., the hh215 region, see Figure 5.1). The velocity range of integration is shown at the top of each panel. The starting contour and the contour steps are given in brackets at the lower-right corner of each panel in units of K km s^{-1}. The star symbol denotes the position of the outflow source, PV Ceph, and the crosses denote the position of the different HH 215 knots 1 through 5 (from GKW), identified in panel [*a*]. The IRAM 30 m beam at the ^{12}CO(2–1) frequency is also shown on panel [*a*]. The letter inside the panels identify the position from which we obtain the spectra shown in Figure 5.8. Each letter represents the position of the spectrum shown in the panel (in Figure 5.8) with the same letter.

mapped region, and so no outflow features are observed. The velocity range in Figure 5.5*b* includes velocities as close as ~ 0.5 km s^{-1} to the central ambient velocity of 2.5 km s^{-1}, so there is some ambient cloud emission contribution to the ^{12}CO(2–1) emission at these velocities. The contours were chosen to show the brightest features. It can be seen that the emission peaks near the position of PV Ceph and extends north with a fan-like structure (with an opening angle of $\sim 90^{\circ}$). This wide-angle structure does not resemble any cloud structure observed in our large scale maps. Thus, we believe that the emission north of PV Ceph in Figure 5.5*b* comes from the slowest, detectable (blueshifted) outflow emission in the hh215 region. This slow outflow gas has a morphology which is consistent with it being entrained by a wide-angle wind. We further discuss this in §5.4.3.

The emission south of PV Ceph in Figure 5.5*b* is ambient cloud emission, which we easily identify with a structure seen in our large scale maps. Notice that this emission south of PV Ceph in Figure 5.5*b* delineates the walls of the cavity cleared by the redshifted outflow lobe (Figures 5.5*c* and 5.5*d*). This cavity is also observed in our large-scale map and we discuss its importance in Chapter 4.

Between velocities 2.06 and 3.16 km s^{-1}, the detected ^{12}CO(2–1) comes from (extremely optically thick) ambient emission, which shows no (or very little) structure. The slowest detectable redshifted outflow emission is at $v \sim 3.2$ km s^{-1}, and it is easily identified as outflow gas from the obvious non-cloud-like morphology of the gas emission.

The redshifted outflow gas shows a very peculiar structure, very different from the wide-angle blueshifted outflow emission discussed above. At the lowest redshifted velocities (Figure 5.5*c*) the ^{12}CO(2–1) integrated intensity peaks at the position of PV Ceph and has a cometary-like extension towards the east, and a collimated (jet-like) extension towards the south. The east-west cometary-like structure is only clearly detected at the velocities between ~ 3.2 and 4.2 km s^{-1} and extends further than the eastern limits of our map. We believe that this cometary-like structure is associated with the motion of PV Ceph through the cloud (see Goodman & Arce 2002). The north-south structure seen in Figure 5.5*c*

extends about 1.75′ ($\sim$ 0.25 pc), and resembles a curving (or wiggling) CO jet, with an eastward bent at $\sim 1'$ south of PV Ceph.

At high (redshifted) outflow velocities (see Figure 5.5*d*) we detect a north-south ^{12}CO structure similar to the one seen in Figure 5.5*c*. The east-west cometary structure seen in Figure 5.5*c* is not detected at these velocities. About 50 to 60″ south of PV Ceph there is a "bump", where the collimated north-south structure widens. As discussed later (§5.4.3), this bump is most probably due to the entrainment of the ambient gas by a redshifted counter-episode of HH 215 (see Figure 5.5). South of the bump the jet-like structure continues, and it ends about 2′ ($\sim$ 0.29 pc) south of PV Ceph, slightly further south than the north-south structure in Figure 5.5*c*.

^{13}CO emission

In Figure 5.6 we show three different velocity-integrated intensity maps of the ^{13}CO(1–0) emission in the hh215 area. Similar to the other velocity-integrated maps presented here, the ranges of integration were chosen to group different velocity (spectral) channels with similar ^{13}CO(1–0) emission structure.

Figure 5.6*a* shows the most blueshifted ^{13}CO emission in the hh215 area, at velocities between 1.73 and 2.28 km s^{-1}. The velocity range is very narrow (only 0.55 km s^{-1} wide) and the velocities are close to the central ambient gas velocity (2.5 km s^{-1}). The blueshifted ^{13}CO integrated intensity map (Figure 5.6*a*) shows a clear V-shaped structure with its apex at the position of PV Ceph. As shown in Figure 5.7, this ^{13}CO structure is coincident with the the optical reflection nebula north of PV Ceph (Cohen et al. 1981; Gledhill, Warren-Smith, & Scarrot 1987; Levreault & Opal 1987; Neckel et al. 1987 Scarrot, Rolph, & Tadhunter 1991; RBD; GKW), and encloses the wide-angle ^{12}CO(2–1) blueshifted outflow seen in Figure 5.5*b*. Thus, it appears that ^{13}CO in this velocity range traces the limb-brightened walls of a wind-blown cavity. We will discuss this further in §5.4.3.

The other two velocity-integrated intensity maps of ^{13}CO(1–0) come from

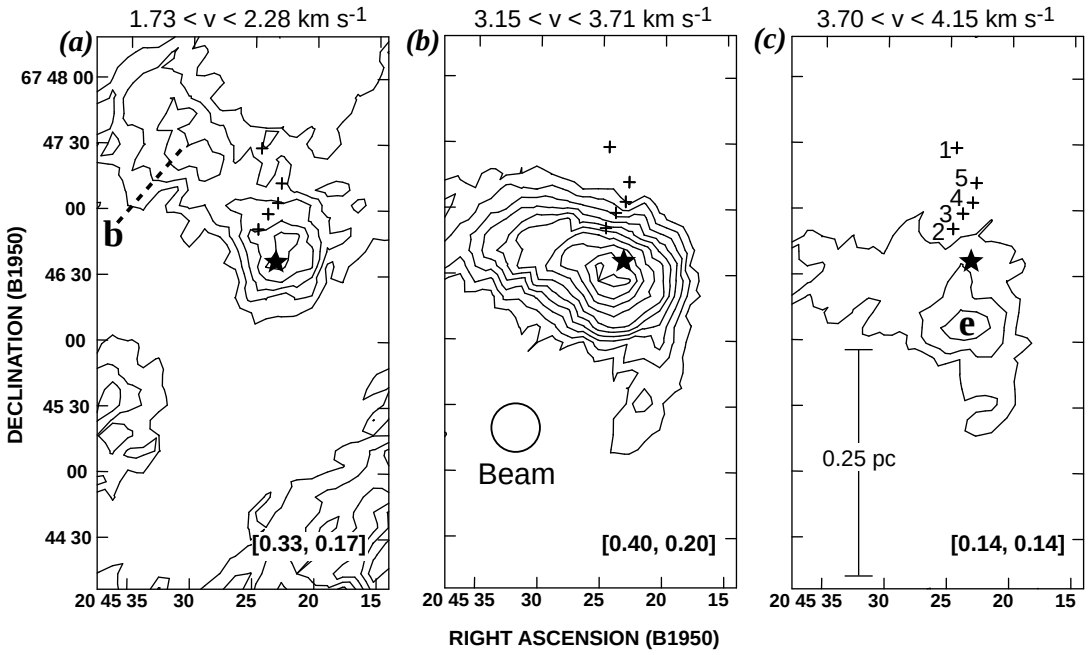

Fig. 5.6.— Velocity-range-integrated intensity maps of the ^{13}CO emission in the hh215 region. The velocity range of integration is shown at the top of each panel. The starting contour and the contour steps are given in brackets at the lower-right corner of each panel in units of K km s^{-1}. The star symbol denotes the position of the outflow source, PV Ceph, and the crosses denote the position of the different HH 215 knots 1 through 5 (from GKW), identified in panel [*c*]. The IRAM 30 m beam at the ^{13}CO(1–0) frequency is shown on panel [*b*]. The letter inside the panels identify the position from which we obtain the spectra shown in Figure 5.8. Each letter represents the position of the spectrum shown in the panel (in Figure 5.8) with the same letter.

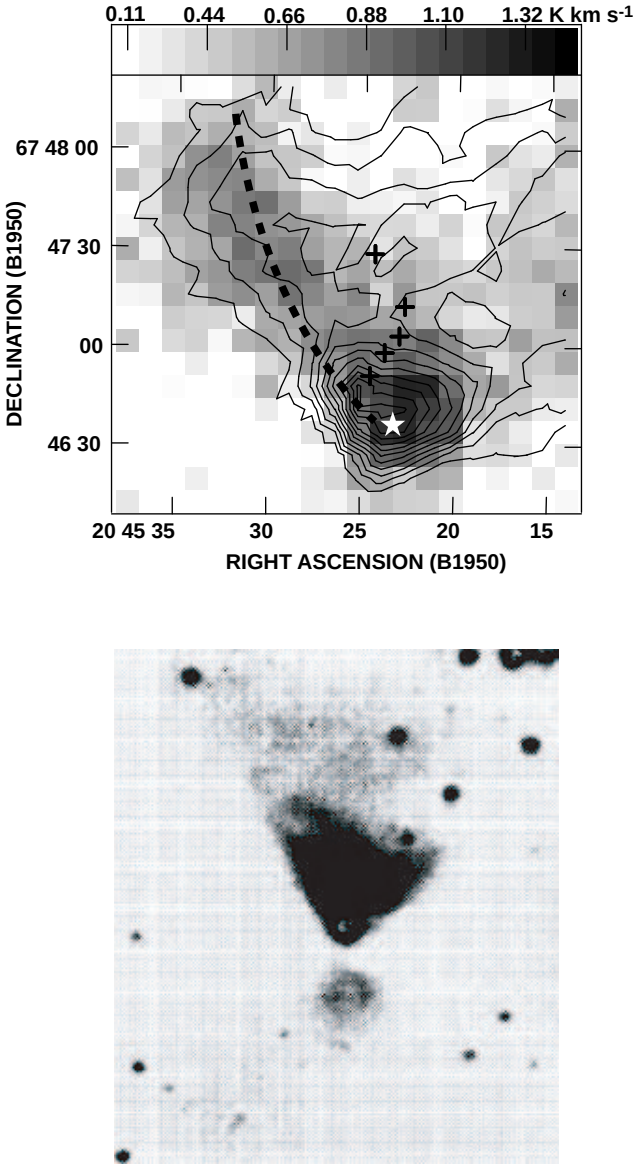

Fig. 5.7.— (*Top*) Velocity-range-integrated intensity contour map of blueshifted ^{12}CO(2–1) emission (within 0.3 pc north of PV Ceph in hh215 region) superimposed on grey-scale map of blueshifted ^{13}CO(1–0) emission of the same area. The velocity range of integration and the contours of the ^{12}CO(2–1) map are the same as Figure 5.5*b*, and the grey-scale map comes from Figure 5.6*a*. The star and cross symbols show the same as previous figures. The dashed dark line represents the eastern edge of the optical nebula north of PV Ceph. (*Bottom*) I_c image of the PV Ceph biconical nebulosity (from Levreault & Opal 1987). The field shown is 2.58′ high.

Table 5.5. Mass at different velocity ranges in hh215

Velocity Range[a] [km s^{-1}]	Mass [M$_\odot$]	Momentum[b] [M$_\odot$ km s^{-1}]	Kinetic Energy[b] [10^{43} erg]
$-0.15 < v < 0.74$	0.01	0.03	0.06
$1.62 < v < 2.06$	0.94	0.43	0.23
$3.16 < v < 4.15$	1.31	1.25	1.28
$4.15 < v < 6.46$	0.27	0.30	1.51

[a]Velocity ranges are the same ranges as the ones in Figure 5.5.

[b]Radial component only. Value not corrected for the inclination of the outflow axis with respect to the plane of the sky.

redshifted velocities (compared to the ambient cloud velocity of 2.5 km s^{-1}). The velocity range of Figure 5.6*b* is $3.15 < v < 3.71$ km s^{-1}, which is the slowest (less redshifted) half of the velocity range in Figure 5.5*c*. The ^{13}CO integrated intensity emission in Figure 5.6*b* resembles (and coincides with) the east-west cometary-like structure in the ^{12}CO(2–1) integrated intensity map in Figure 5.5*c*. In addition to the east-west structure there is a low-emission north-south elongation, which coincides with the north-south ^{12}CO(2–1) jet-like structure in Figure 5.5*c*. The ^{13}CO north-south structure extends only $\sim 1.3'$ (0.18 pc) south of PV Ceph.

The most redshifted ^{13}CO emission in the hh215 region is shown in Figure 5.6*c*. The velocity range of integration is $3.71 < v < 4.15$ km s^{-1}, which is the fastest (more redshifted) half of the velocity range in Figure 5.5*c*. At these velocities the ^{13}CO emission is very weak compared to the other velocities shown, and the maximum emission is just south of PV Ceph. In Figure 5.6*c* the east-west and the north-south structures have the same weak intensities.

In Table 5.5 we list the mass for each of the velocity ranges shown in Figure 5.5. The mass was obtained using our IRAM 30 m ^{12}CO(1–0) and ^{13}CO(1–0) data,

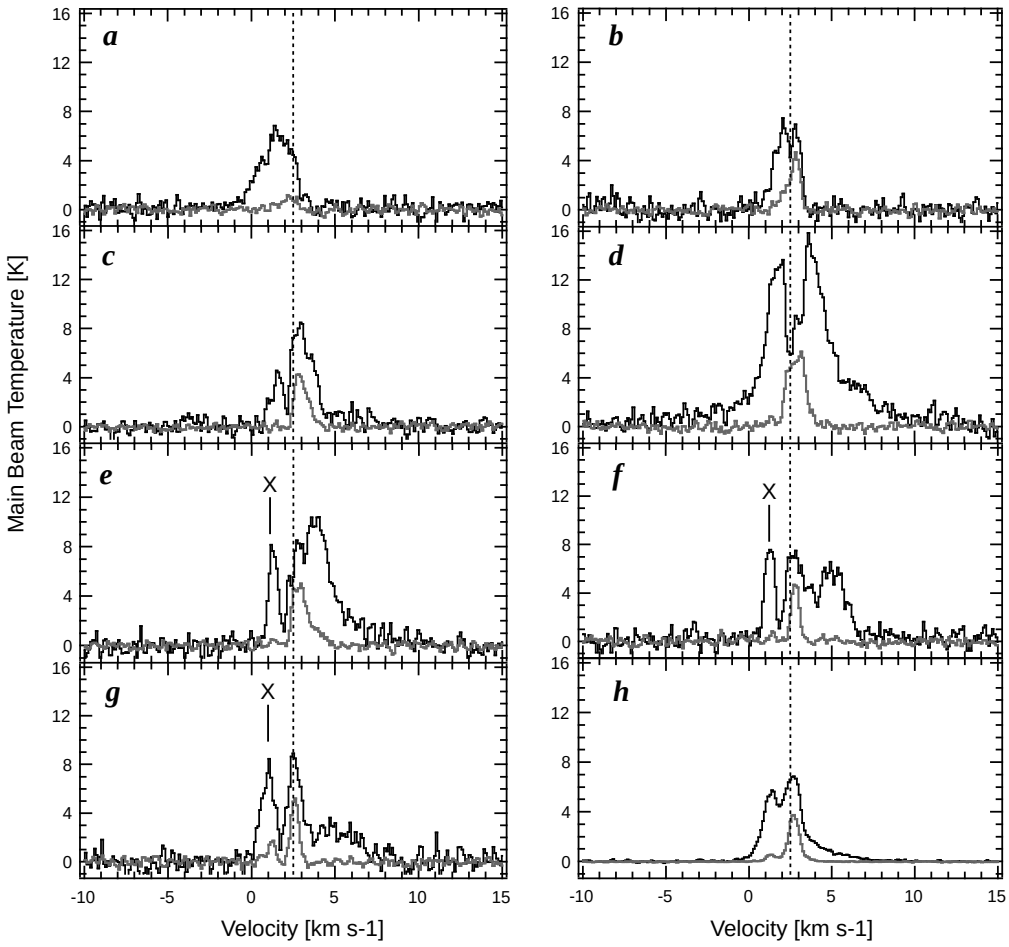

Fig. 5.8.— Sample ^{12}CO(2–1) (black) and ^{13}CO(1–0) (grey) spectra of the hh215 region. Panels [*a*] through [*g*] show spectra from the positions shown in Figures 5.5 and 5.6. The spectra shown in panel [*d*] comes from the position of the outflow source, PV Ceph. Each spectrum ([*a*] through [*g*]) was taken from a single 7″ by 7″ pixel, of a molecular line map convolved with a 14″ beam. In panel [*h*] we show the average spectra over the whole hh215 region. The dotted vertical line indicates the position of $v = 2.5$ km s^{-1}.

using the procedure described in Chapter 4 (with $T_{ex} = 10.5$ for all velocity ranges). In Figure 5.8 we show sample ^{12}CO(2–1) and ^{13}CO(1–0) spectra from the hh215 region.

5.3.3 The region surrounding HH 315E

The sensitivity of our observations in the hh315e region is similar to that of the other regions (see Table 5.3). So, if the column density of the outflowing CO gas in the hh315e region were similar to that of the other regions, then outflowing CO should be easily detectable. But, even though HH 315E is the counter-knot of HH 315B —where we detect CO with the highest blueshifted outflow velocities— we do not detect any outflow emission it the region surrounding the optical knot HH 315E.

In Figure 5.9 we show an average ^{12}CO(2–1) spectrum of the hh315e region. The spectrum does not show any redshifted low-level wing, or another velocity component redshifted from the ambient emission, as might be expected for a redshifted CO outflow lobe spectrum. Instead, the spectrum shows mainly ambient gas emission from the cloud associated with PV Ceph (the "PV Ceph cloud"), which peaks at $v \sim 2.5$ km s^{-1} (see Chapter 4). The bump in the spectrum seen at blueshifted velocities is due to "contaminating" emission from another cloud on the same line of sight (cloud X, see Chapter 4). We fit a double Gaussian to the average spectrum and from the fit we obtain that the PV Ceph cloud component (centered at ~ 2.5 km s^{-1}) has a width (FWHM) of ~ 0.8 km s^{-1}. Even if we fit a single Gaussian, the resultant velocity width is 1.1 km s^{-1}.

A ^{12}CO(2–1) spectrum with such a narrow velocity is usually observed in quiescent ambient gas clouds, rather than in regions affected by stellar outflows. HH knots delineate shocks arising from the interaction of a high-velocity flow of gas ejected by a young stellar object and the ambient medium. Thus, we know that the outflow mass ejection responsible for the HH 315E optical knot is interacting with its surrounding medium because HH 315E is detected. It is strange that even though the column density of the ambient gas in the hh315e region is more than

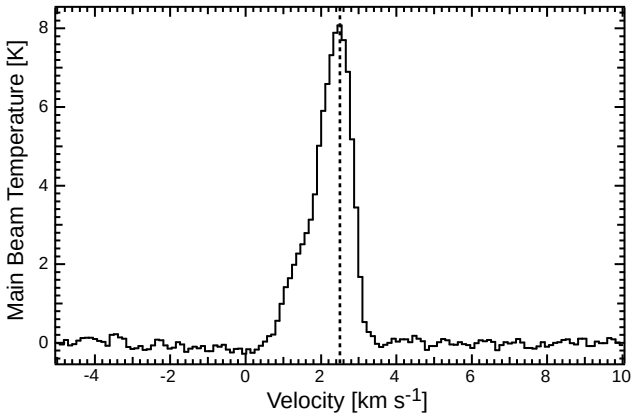

Fig. 5.9.— Average ^{12}CO(2–1) spectrum of the mapped area surrounding the redshifted optical knot HH 315E (i.e., the hh315e region, see Figure 5.1). A dashed line indicates the position of $v = 2.5$ km s^{-1}. The main component, with a peak in T_{mb} at $v = 2.5$ km s^{-1}, is due to ambient gas from the cloud associated with PV Ceph. The bump in the spectrum at blueshifted velocities is due to emission from another cloud on the same line of sight.

the column density of the ambient gas surrounding HH 315B, we see no evidence of outflow-cloud interaction in our CO spectra. One possible explanation is that the relatively high CO column density observed is all (or mostly) due to CO in front of HH 315E, and that HH 315E is interacting only with atomic gas *behind* the PV Ceph cloud.

5.4 Analysis and Discussion

5.4.1 Temperature distribution

We use our ^{12}CO(1–0) and ^{12}CO(2–1) data in concert to study the excitation temperature (T_{ex}) across the mapped regions. We then use the estimate of the temperature variations in our map to discern between different molecular outflow entrainment models. The theory (and equations) used to obtain the excitation temperature from the ^{12}CO(2–1) to ^{12}CO(1–0) ratio are discussed in Appendix A.

Since estimating the excitation temperature of optically thick ($\tau > 1$) gas is very unreliable, we will only try to estimate the excitation temperature of optically

thin ($\tau < 1$) CO gas. And so, in our temperature estimates we will use the optically thin approximation of Equation A.3, that is, Equation A.9.

We warn that Equation A.9 is only exact in the optically thin limit ($\tau << 1$). For example, using Equation A.9 with gas with an opacity as low as $\tau \sim 0.1$ would lead to an underestimation of the real excitation temperature (see Figure A.1). If $\tau \sim 0.1$, the discrepancy stays within 20% for CO line ratios lower than 2.5, but for line ratios higher than 2.8, the error in T_{ex} exceeds 40%. In any case, it still true that for any given opacity, the higher the line ratio, the higher the excitation temperature. So even though Equation A.9 does not give a perfect estimate for $\tau \gtrsim 0.01$, we can still use it to investigate the *relative* temperature distribution.

The hh315b+c region

To estimate the excitation temperature of the outflow gas in the region surrounding the optical knots HH 315B and HH 315C we used velocity-integrated maps of the ^{12}CO(2–1) and ^{12}CO(1–0) lines. For each velocity-integrated map, we produced a map of the line ratio ($R_{12/10}$), and then a map of the excitation temperature, using Equation A.9. Five grey-scale maps of T_{ex} are shown in Figure 5.10 (the velocity ranges of integration are the same as Figures 5.2*b* to 5.2*f*). Gas with velocities close to the ambient velocity are optically thick, and so we do not obtain an estimate of T_{ex} for gas at those velocities. For each grey-scale temperature map, we superimposed the ^{12}CO(2–1) velocity-integrated intensity contours. We only obtain a value of T_{ex} for pixels with a signal to noise ratio of at least 5, in both ^{12}CO(2–1) and ^{12}CO(1–0). We masked (set $T_{ex} = 0$) the low signal-to-noise pixels and those (few) which gave unphysical negative values of T_{ex}.

In all panels of Figure 5.10, there is a discernible trend in which there is a temperature increase in regions with high velocity CO emission (see Table 5.4). In Figures 5.10*a*, 5.10*b*, and 5.10*c*, the temperature peaks of $T_{ex} \sim 23 - 30$ K coincide with (or are very near) the peaks in the integrated intensity. The average excitation temperature in Figure 5.10*a* is higher than the average temperature of Figures 5.10*b* and 5.10*c* (see Table 5.4). As discussed above (§5.3.1), the emission

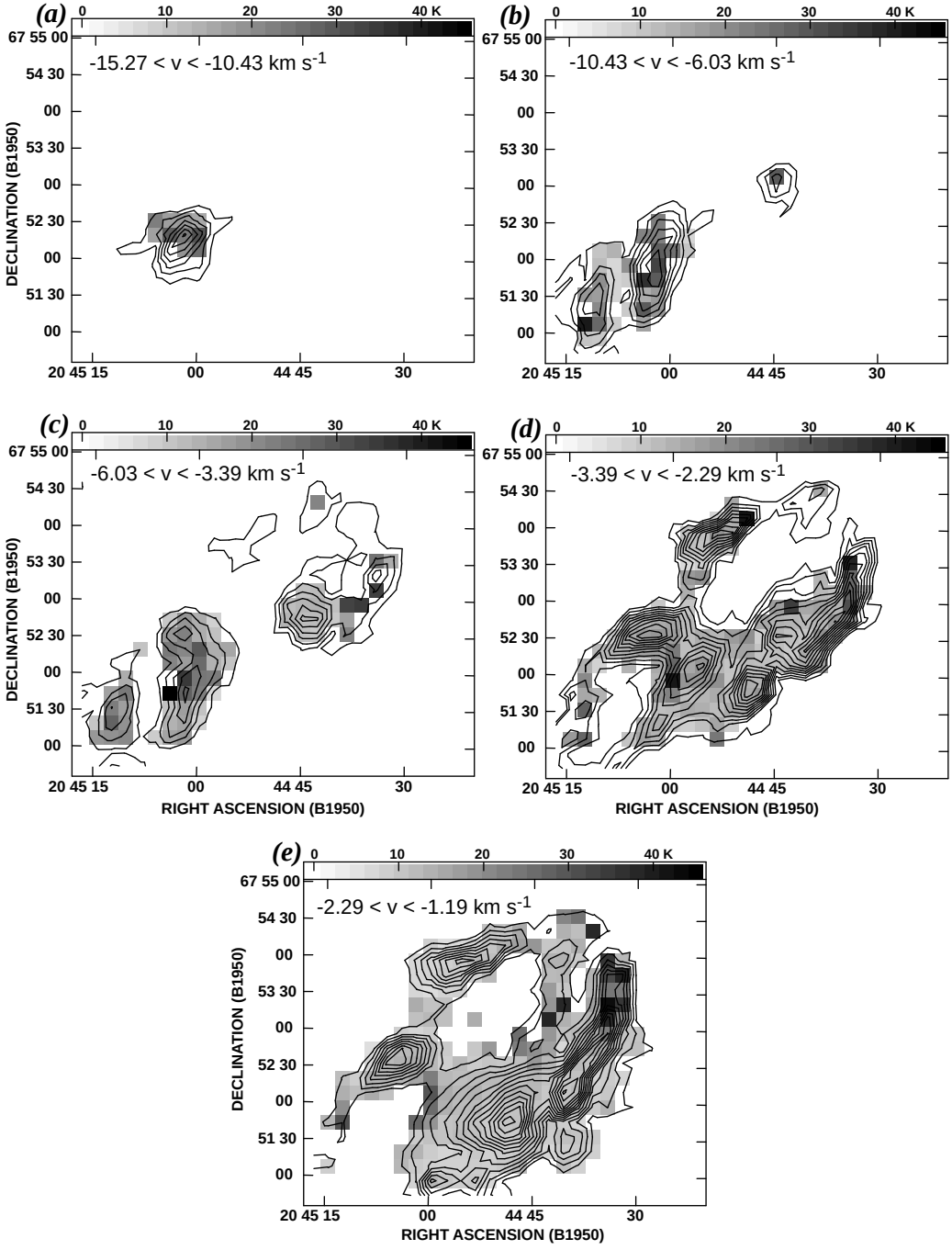

Fig. 5.10.— Grey-scale excitation temperature maps of the CO outflow gas in the hh315b+c region. Superimposed on the grey-scale maps, we show in contours, the ^{12}CO(2–1) velocity integrated intensity. The velocity range of integration is shown at the top of each panel. The first contour and contour steps for each panel are the same as for the corresponding velocity range in Figure 5.2. Each pixel is 12″ by 12″.

at velocities $-15.27 < v < -10.42$ km s^{-1} (Figures 5.2*b* and 5.10*a*) seems to delineate the region where HH 315B is currently entraining the ambient gas (i.e., the shock head in a bow shock-drive outflow). Thus, we see a general increase in excitation temperature towards the presumed shock head in the outflow gas associated with HH 315B.

In Figure 5.10*d*, where the integrated intensity contours clearly show the CO bow-like structure associated with HH 315C, the temperature is approximately constant with a value of $T_{ex} \sim 11 - 13$ K in most of the bow shock structure. Similarly, in Figure 5.10*e* most of the body of the HH 315C CO shell structure shows a higher temperature ($T_{ex} \sim 11 - 13$ K) than the ambient gas temperature of 10.5 K (as derived in Chapter 4). There is also a general increase in the temperature at the head of the CO bow structure (in both Figure 5.10*d* and 5.10*e*), at about $(\alpha, \delta)_{1950} \sim (20^h44^m34^s, 67°53'30'')$, where the outflow gas reaches excitation temperatures of 25 to 35 K.

The spatial temperature distribution of the high-velocity gas in the hh315b+c area is consistent with the temperature distribution expected for a molecular outflow formed by bow shock prompt-entrainment. Analytical and numerical jet-driven bow shock models show that the temperature of the accelerated gas which forms the molecular outflow should be higher than the ambient gas. The temperature is also expected to peak near the bow shock head —where most of the energy input occurs— and decrease toward the source (e.g., Hatchell et al. 1999; Lee et al. 2001) . Similar to the models, our results show that the outflow temperature (with $T_{ex} > 11$ K) is higher that the quiescent ambient gas temperature ($T_{ex} \sim 10.5$ K), and there is a noticeable increase in temperature near the head of the bow shock-like CO structures coincident with HH 315B and HH 315C.

Bow shock entrainment models predict temperatures at the head of the shock of $\sim 10^3$ K (Hatchell et al. 1999) to temperatures of $\sim 10^4$ K (Lee et al. 2001). The discrepancy between our results and the temperatures predicted by models could be due to a variety of factors. First, as stated above, if the gas is not in the optically

thin limit, the temperature obtained using Equation A.9, will be underestimated. Also, it is known that most of the very hot gas (a few 10^3 K) is traced by near infrared lines of H_2 and not by millimeter molecular lines (Bachiller 1996). In any case, even if our results do not show the actual (absolute) excitation temperature of the map, it still gives an indication of the relative temperature variations in the gas.

The hh215 region

The ^{12}CO gas detected (at most velocities) in the hh215 region is moderately optically thick ($\tau \sim 1$, see Chapter 4), and so estimates of the excitation temperature are very unreliable (see Appendix A). Hence, we study the *relative* temperature distribution by studying the spatial distribution of the CO line ratio ($R_{21/10}$).

The map of CO line ratio of the blueshifted outflow gas in the hh215 region does not show any significant structure, and hence is not shown. The only clear trend in this map is that there is an increase in $R_{21/10}$ at the position of the source, implying there is an increase in temperature at the position of PV Ceph.

In Figure 5.11 we plot the average line ratio along the axis of the redshifted molecular outflow lobe. To do this, we determine the average value of $R_{21/10}$ over the width of the jet-like outflow lobe, for each row of pixels, and then plot it as a function of declination offset from the source. The line ratio shown in Figure 5.11 has a maximum at the source position, then it decreases with distance from the source up to about 36″ south of PV Ceph. At about 60″ south of the outflow source position $R_{21/10}$ reaches a local maximum. Further south, along the outflow lobe axis, the CO line ratio stays approximately constant.

Models where the molecular outflow is formed by turbulent mixing of the ambient gas along the sides of a jet or wind predict that the gas temperature should have a maximum temperature at (Cantó & Raga 1991) or very close to (Lizano & Giovanardi 1995) the position of the source, and decrease monotonically

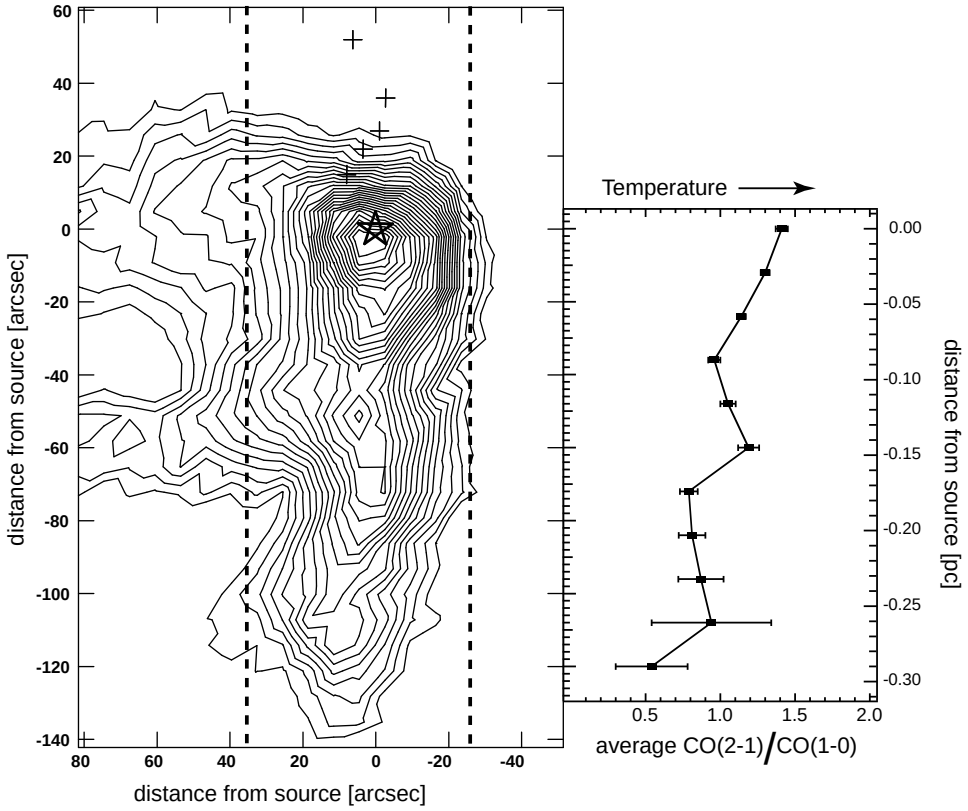

Fig. 5.11.— (*Left panel*) ^{12}CO(2–1) integrated intensity contours of the redshifted emission near PV Ceph (hh215 region). The velocity range of integration is $3.16 < v < 6.46$ km s^{-1}. The starting contour and contour step are 2.64 and 0.88 K km s^{-1}, respectively. The star symbol indicates the position of PV Ceph, and the crosses indicate the position of the HH 215 knots. (*Right panel*) Average ^{12}CO(2–1) to ^{12}CO(1–0) line ratio as a function of distance from the source. The line ratio is averaged over the width of the north-south jet-like structure, indicated by the dark vertical dashed lines on the left panel. The error bars indicate the 1-σ error.

with distance from the source. Entrainment models where the gas is accelerated solely by the leading bow shock in a jet predict that the gas temperature should be minimum at the outflow source, and increase toward the head of the bow shock, where the gas temperature peaks. Therefore, the gas temperature distribution implied by our measurements of $R_{21/10}$ is not entirely consistent with an outflow entrained by the leading jet bow shock nor by a turbulent mixing layer along the sides of a jet.

One alternative explanation is that the outflow is entrained by a time-varying (pulsed) jet. A time-varying jet will have internal bow shocks (usually called internal working surfaces) along its axis (see, e.g., Raga et al. 1990; Stone & Norman 1993b; Lee et al. 2001), and the gas temperature should increase at the head of each internal shock. Thus, each local increase in the CO line ratio could arise from the local increase in temperature expected at the head of each internal bow shock. In this picture, the increase in line ratio 60″ south of PV Ceph could be due to the redshifted counter-knot of HH 215(1) —presumably also responsible for the "bump" in the integrated intensity of the redshifted molecular outflow lobe (see Figure 5.11). We further discuss this in §5.4.3. The increase in temperature at the source position could arise from an unresolved internal working surface very close to PV Ceph.

5.4.2 Kinematics and momentum distribution

Studying the velocity and momentum distribution of the molecular outflow may help us distinguish between different entrainment models. It also helps us better understand how young stellar outflows interact with the ambient gas.

Kinematics of the hh315b+c region

In Figure 5.12 we show a ^{12}CO(2–1) position-velocity ($p-v$) diagram of the hh315b+c region. This $p-v$ diagram was constructed by rotating our image of the hh315b+c region by 43° and summing the ^{12}CO(2–1) spectra at each row of pixels.

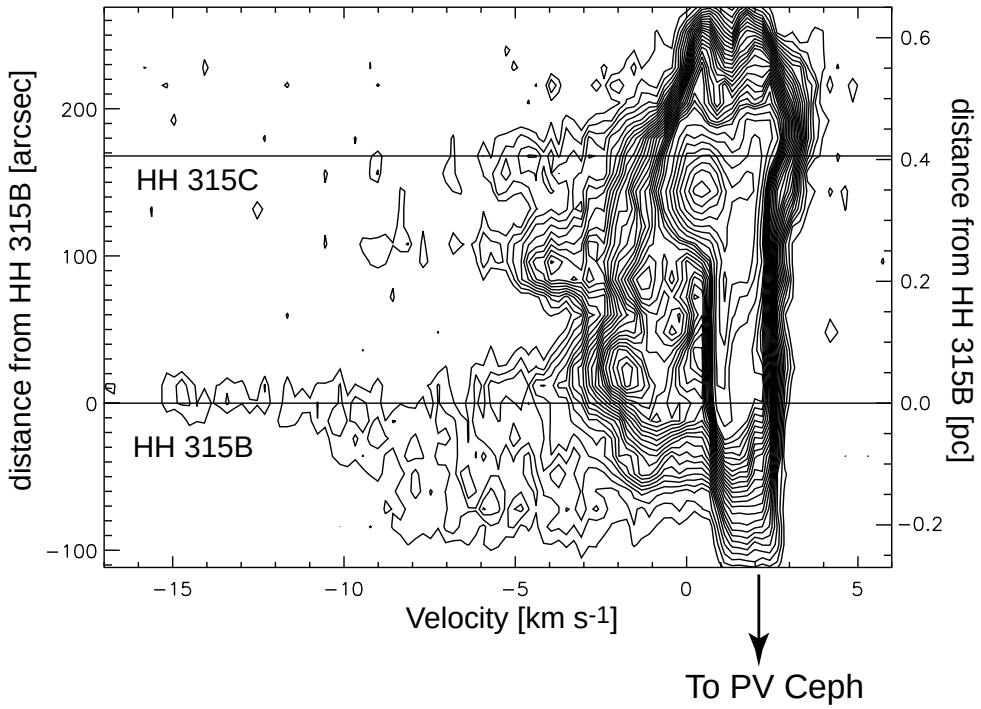

Fig. 5.12.— ^{12}CO(2–1) position-velocity diagram of the hh315b+c region. The $p-v$ diagram was constructed by rotating our ^{12}CO(2–1) map of the hh315b+c region (with 12″ by 12″ pixels, and 0.22 km s^{-1}-wide velocity channels) by 43° and summing the ^{12}CO(2–1) spectra at each row of pixels. The horizontal lines denote the position of the brightest optical emission in the HH 315B and HH 315C knots. Contours are 3 to 51 K in steps of 2 K, and 56 to 91 K, in steps of 5 K.

Figure 5.12 clearly shows that the velocity peaks at the position of HH 315B, and decreases towards the position of the source. This velocity distribution, where the velocity peaks at the shock head and decreases towards the outflow source, is consistent with models of bow shock-entrained molecular outflows. For these models such velocity structure is a natural consequence of the fact that the highest (radial) velocities are found at the head of the bow shock, while the velocity decreases towards the wings.

Lee and coworker's recent analytical (Lee et al. 2000) and numerical (Lee et al. 2001) studies show detail $p-v$ diagrams of wide-angle wind-driven molecular outflows. Their results indicate that the $p-v$ diagrams of wide-angle wind-driven molecular outflows have noticeable differences compared with the predicted $p-v$ diagram for bow shock-entrained molecular outflows (see Table 5.1 for a schematic illustration on this). We do not see any indication in Figure 5.12 of a structure similar to that shown in the $p-v$ diagrams of Lee et al. (2000; 2001) for wide-angle wind-driven molecular outflows.

Figure 5.12 shows that the highest outflow velocities are at the head of the shock (i.e., HH 315B), and that the rise in velocity associated with HH 315B is restricted to a limited region of no more than $100''$ (~ 0.2 pc). This indicates that most, if not all, of the entrainment is taking place at the head of the HH 315B shock. Thus, we totally discard turbulent entrainment along the sides of a jet (or wind) as the mechanism responsible for the outflowing gas associated with the HH 315B optical knot, and we suggest that bow shock entrainment is responsible instead.

North of HH 315B, there are two more local peaks in the velocity (see Figure 5.12). Both of the velocity peaks come from outflowing gas associated with the HH 315C molecular bow structure. The northernmost local velocity peak is coincident with the brightest optical emission in HH 315C, which is also the head of the optical bow shock. The other local peak in velocity associated with HH 315C (at $\sim 100''$ north of HH 315B) comes from outflow gas in the wings of the HH 315C CO bow (see Figures 5.2*c* and 5.2*d*). As discussed above, a bow shock-entrained

molecular outflow should have the peak velocity at the head of the shock, and *no* local peak in velocity is expected at the bow wings. The velocity structure of the outflowing gas associated with HH 315C does not resemble the velocity structure of a wide-angle-wind-driven molecular outflow either (see Lee et al. 2000; 2001). Turbulent entrainment is again discarded as the head of the shock does not show the slowest velocities in the outflow, as predicted by turbulent jet models. Although the kinematics of the molecular outflow associated with HH 315C are not entirely consistent with bow shock entrainment, other pieces of evidence presented here suggest that bow shock entrainment is still the best candidate (see §5.4.3 for further discussion).

Momentum distribution in the hh315b+c region

In order to study the momentum distribution of the blueshifted outflowing gas surrounding HH 315B and HH315C, we constructed a momentum map of the region. The map was produced using the technique to estimate mass described in Chapter 4. With this method we obtain a map of the outflow mass for each position pixel and velocity channel (x, y, v). We multiply the mass at each (x, y, v) by the outflow velocity corresponding to the given velocity channel ($v_{out} = v - v_{o\_north}$) to obtain a momentum at each pixel and channel. By integrating (summing) over velocity channels [$\Sigma m(x, y, v_i)v_{out,i} = P(x, y)$], we obtain a momentum map over a given velocity range.

In Figure 5.13 we show the momentum map of the hh315b+c region, integrated over the velocity range $-15.27 < v < -0.09$ km s^{-1}. The bow-like structure of the outflowing gas associated with HH 315C is clearly seen in the momentum map. In this structure the bow wings show more momentum than the head of the bow. In addition, the southwestern wing has considerably more momentum than the northeastern bow wing. The maximum momentum in Figure 5.13 is nearly coincident with the brightest optical emission in HH 315B, and it is surrounded by a region of relatively high momentum extending south and extending east of the momentum peak. This extension traces the bow wings of the HH 315B CO

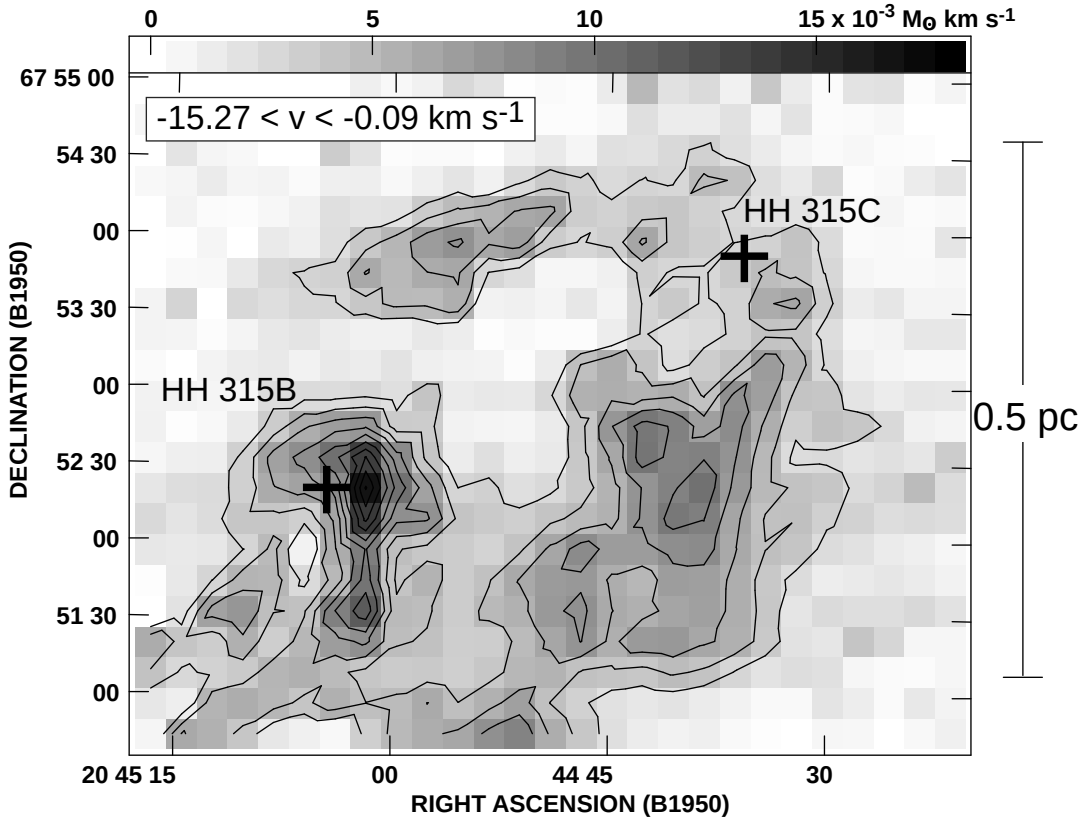

Fig. 5.13.— Momentum map of the molecular outflow gas in the hh315b+c region, over the velocity range $-15.27 < v < -0.09$ km s^{-1}. The first contour and contour step are 3 and 1.5 $\times 10^{-3}$ M$_{\odot}$ km s^{-1}, respectively. The crosses denote the position of the brightest optical emission of the HH 315B and HH 315C knots.

bow shock, similar to what is seen in the HH 315C CO bow shock, but at a smaller scale.

In a bow shock-driven outflow model the outflowing gas velocity peaks at the head of the bow shock. The momentum ($p = mv$), on the other hand, is dependent on the underlying ambient cloud mass distribution (Chernin & Masson 1995). If a bow shock from a stellar wind mass ejection were to interact with an ambient gas with a perfectly uniform density distribution, the resultant molecular outflow momentum would peak at the head of the bow shock. This is not the case for HH 315C. As discussed in §5.3.1, in this region there is a gradient in the ambient cloud density (seen in the ambient CO emission, see Figures 5.2*j* and 5.2*k*), which increases from east to west. This explains why the southwest bow wing has more momentum than the northeast bow wings. Near both southwest and northeast bow wings the gas is denser than the gas at the head of the bow structure (we only detect ^{13}CO emission near the HH 315C CO bow wings, see Figure 5.4). Thus, the increase in momentum along the bow wings with respect to the bow head. We conclude that the momentum distribution of the HH 315C molecular bow structure can be explained by the bow shock entrainment of ambient gas with non-uniform density distribution.

The momentum distribution of the outflowing gas associated with HH 315B follows what is expected for a bow shock-entrained outflow in a relatively flat ambient density distribution. As can be seen in Figure 5.2 the outflowing gas associated with HH 315B is constrained to a small area surrounding HH 315B, and the ambient cloud density is approximately constant within that area. In Figure 5.13, the momentum peaks practically at the presumed bow shock head, and the momentum decreases away from the head, along the wings, towards the direction of the outflow source.

Velocity distribution in the hh215 Region

Similar to hh315b+c, we studied the velocity distribution of the hh215 area by constructing a position-velocity diagram of the ^{12}CO(2–1) emission. The $p - v$,

shown in Figure 5.14, was made by summing all spectra over the width of the hh215 area at each different row of pixels, resulting in a declination-velocity diagram.

There are several interesting features in the hh215 $p-v$ diagram. The redshifted gas, shows two distinctive velocity peaks; one is coincident with the position of PV Ceph, and the other is $\sim 60''$ (0.15 pc) south of PV Ceph. Most of the slow redshifted velocity coincident with the outflow source position comes from the east-west cometary-like structure seen in Figure 5.5*c*. We believe that most of this structure is a result of the motion of PV Ceph through its parent cloud (see Goodman & Arce 2002). So, most of the slow redshifted gas at the position of PV Ceph is not related to the HH 315 outflow. Thus, we only consider the redshifted gas south of PV Ceph as being part of the outflow.

The peak in velocity, ~ 0.15 pc south of PV Ceph, is coincident (within the $11''$ beam of the telescope) with the "outflow clump" (or local maximum in the outflowing CO) south of PV Ceph, seen in the ^{12}CO(2–1) velocity-integrated map shown in Figure 5.5*d*. A peak in outflow velocity coincident with the position of an outflow clump has been attributed, in other outflows, to be evidence for bow shock (prompt) entrainment from a mass ejection episode (e.g., RNO 43, Bence et al. 1996; HH 300, Chapter 2).

We believe the optically undetected redshifted counter-knots of the HH 215 chain of knots (see Figure 5.5) are responsible for the entrainment of the redshifted outflow gas south of PV Ceph. Each of the 3 major blueshifted knots of HH 315 (knots A, B, and C) have a redshifted counter-knot (see Figure 5.1), and for each of the three redshifted-blueshifted knot pairs the distance from PV Ceph to the blueshifted knot is the same (within 10%) to the distance from PV Ceph to the corresponding redshifted counter-knot (RBD). One would reasonably expect the same for the HH 215 knots, and so we believe that the rise in velocity ~ 0.15 pc south of PV Ceph is produced by the (unseen) counter-knot of HH 215(1). It is very probable that optical observations have not detected HH knots in the corresponding location south of PV Ceph because of the high extinction in this region.

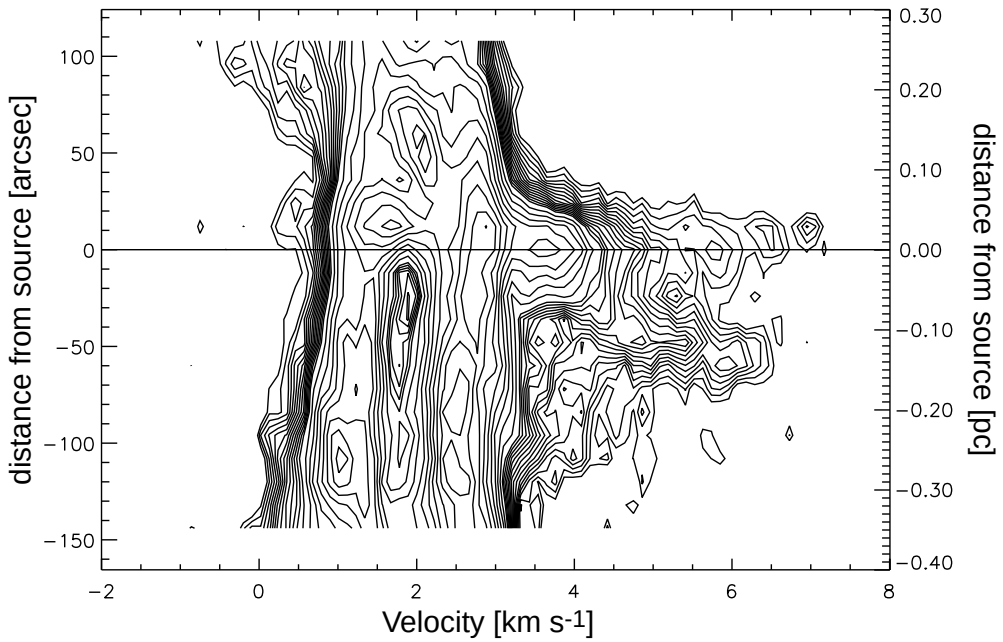

Fig. 5.14.— ^{12}CO(2–1) position-velocity diagram of the hh215 region. The $p-v$ diagram was constructed by summing all spectra over the width of the hh215 area at each different row of pixels, resulting in a declination-velocity diagram. The map used has 12″ by 12″ pixels and a velocity resolution of 0.11 km s^{-1}. The horizontal line indicates the position of the outflow source (PV Ceph). Contours are 7 to 35 K in steps of 2 K, and 40 to 80 K in steps of 5 K.

As discussed in §5.3.2, we detect a wide-angle blueshifted outflow emission north of PV Ceph, in the hh215 region. In the $p - v$ diagram (Figure 5.14), the blueshifted gas shows a Hubble-like velocity distribution; the slowest blueshifted velocities (detached from the ambient cloud emission in the $p - v$ diagram) is at ~ 0.1 pc north of PV Ceph and the average blueshifted outflow velocity increases with distance from the source, off our map limits (see Figure 5.14). Given the limited coverage of the area, we cannot conclude if such velocity distribution is consistent with a bow shock-driven outflow model or a wide-angle wind-driven molecular outflow model.

Momentum distribution in the hh215 region

As discussed in §5.3.2, we are unable to estimate the total mass and momentum from the blueshifted outflow gas just north of PV Ceph (in the hh215 region) because of contamination from the emission from another cloud in the same line of sight. This hinders our ability to compare the *total* blueshifted momentum with that expected by different entrainment models. Hence, we do not consider it here.

One the other hand, we can study the outflow momentum distribution of the redshifted lobe. In Figure 5.15, we plot the average momentum along the redshifted outflow axis, using a momentum map integrated over the velocity range of $3.16 < v < 6.46$ km s^{-1}. This plot was constructed by calculating the average momentum at each horizontal row of pixels along the north-south axis of the outflow, and then plotting the average momentum as a function of distance from the source. In order to avoid redshifted emission not associated with the redshifted outflow lobe (i.e., the cometary-like east-west structure), we averaged the momentum over a restricted area, which only includes the north-south redshifted jet-like outflow structure (see Figure 5.15). The average momentum along the redshifted lobe axis has a maximum at the source position and it decreases with distance from the source. This momentum distribution is very similar to that predicted by Chernin & Masson (1995) for an outflow consisting of material swept-up by a jet bow shock traveling through an ambient cloud with a density

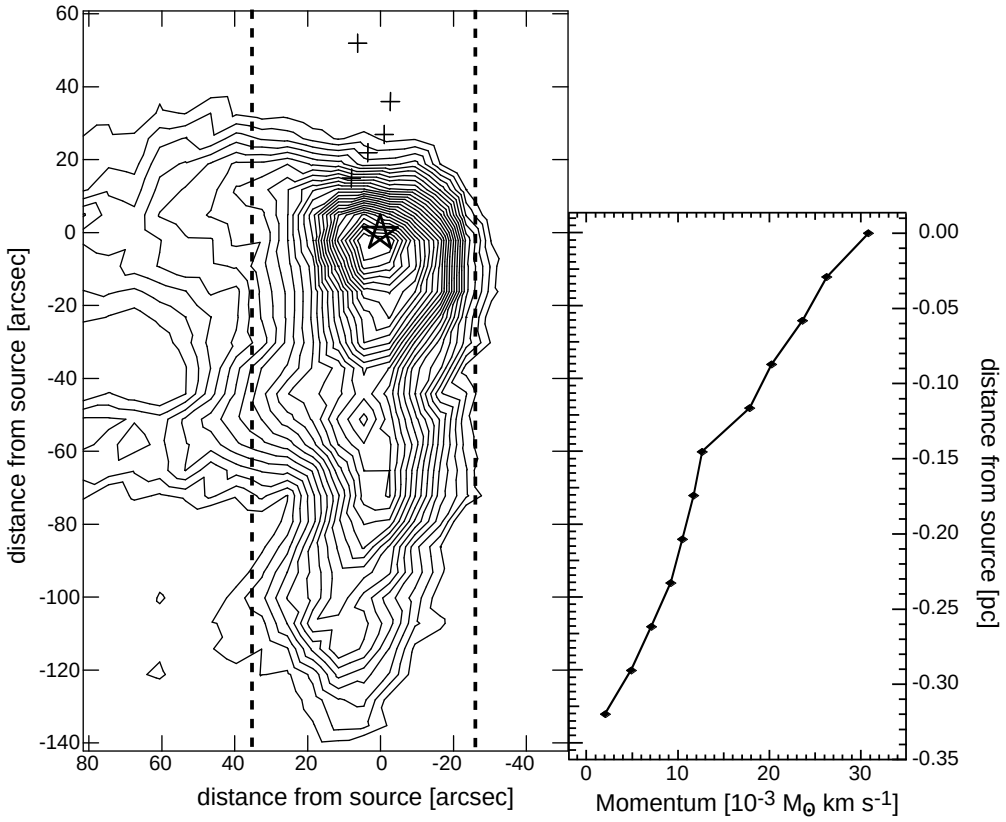

Fig. 5.15.— (*Left panel*) The same as the left panel in Figure 5.9. (*Right panel*) Average momentum in the redshifted outflow lobe as a function of distance from PV Ceph. The momentum was averaged over the width of the redshifted CO jet-like structure, indicated by the black vertical dashed lines on the left panel.

gradient proportional to r^{-a}, where to $1 \leq a \leq 2$. In this model the outflow momentum decreases with distance from the outflow source because the ambient cloud density decreases with distance from the young star. The ambient density of the PV Ceph cloud (as implied by the integrated intensity ^{13}CO maps of the cloud in Chapter 4) monotonically decreases with distance from PV Ceph in the region where we detect the redshifted jet-like outflow feature. Therefore, the bow shock entrainment model of Chernin & Masson (1995) can be used to explain the momentum distribution along the axis of the redshifted outflow lobe in the hh215 region.

5.4.3 Bow shocks, jets, and wide-angle winds

The temperature distribution, the kinematics, the momentum distribution, and the morphology of the outflow gas may all be used to deduce the most likely entrainment mechanism responsible for the molecular outflow. In this section we summarize our results, and discuss which are the most likely entrainment mechanisms that accelerate the molecular gas of the outflow associated with PV Ceph.

Blueshifted CO bow shocks in HH 315C and HH 315B

In Table 5.6 we list the properties of the outflow gas associated with HH 315B. The morphology, as well as the temperature, velocity, and momentum distribution of the outflow gas are all consistent with bow shock entrainment models. Thus we conclude that the outflow gas associated with HH 315B is bow shock-driven.

In Table 5.7 we list the characteristics of the molecular outflow gas associated with HH 315C. Some of the properties listed are both consistent with bow shock and wide-angle wind entrainment. As discussed below, HH 315 is an episodic outflow, in which HH 315C and HH 315B come from consecutive episodes. The mass ejection episode responsible for HH 315B entrains the ambient gas with a bow shock, so the same is expected for HH 315C. It is highly unlikely that two

Table 5.6. Comparison of molecular outflow associated with HH 315B and entrainment models

Parameter	Description	Figure	Consistent with model?		
			Turbulent Jet	Bow Shock	Wide-angle Wind
Morphology	Small bow-like, with wings extending in direction of outflow source	5.2	NO	**YES**	NO
Temperature	T_{ex} of outflow > ambient T_{ex}, also increase in T_{ex} at shock head	5.10	NO	**YES**	NO
Velocity	"Spur-like"—maximum velocity at position of HH 315B (shock head)	5.12	NO	**YES**	NO
Momentum	Maximum at bow head	5.13	NO	**YES**	NO

consecutive mass ejection episodes interact with the environment through two different mechanisms. Thus, we suspect that the outflow gas associated with HH 315B and HH 315C are both produced by the bow shock entrainment of an episodic jet.

We note that there is still the possibility that the underlying stellar wind that produces the outflow in this area is technically not a jet bow shock, but a very collimated angle-dependent wind. How a wide-angle wind interacts with the ambient gas depends on the angular distribution of the wind force (e.g, Matzner & McKee 1999, and references therein). If the wind force is highly concentrated on the pole, then the wind would essentially be jet-like. This jet-like wind would interact with the ambient medium very much like a bona fide jet. Thus, outflows created by a highly collimated angle-dependent wind and outflows created by a jet show very similar morphologies, and velocity and momentum distributions —any differences would be indistinguishable by our observations. Thus, a very collimated angle-dependent wind, and a bona fide jet will produce practically the same entrainment mechanism.

Table 5.7. Comparison of molecular outflow associated with HH 315C and entrainment models

Parameter	Description	Figure	Consistent with model?		
			Turbulent Jet	Bow Shock	Wide-angle Wind
Morphology	Large and wide shell- (or bow-) like, with wings extending in direction of outflow source	5.2	NO	**YES**	**YES**
Temperature	T_{ex} of outflow > ambient T_{ex}, also increase in T_{ex} at shell head (coincident with HH 315C knot)	5.10	NO	**YES**	NO
Velocity	Double-peaked velocity distribution	5.12	NO	NO	NO
Momentum	Higher in bow (shell) wings due to underlying ambient density distribution	5.13	NO	**YES**	**YES**

The redshifted CO jet south of PV Ceph

The properties of the redshifted molecular outflow lobe (south of PV Ceph in the hh215 region) are listed in Table 5.8. The redshifted outflow gas in this region shows a clear jet-like (very collimated) structure that extends south of PV Ceph (see Figure 5.16). Turbulent entrainment has been proposed as an attractive model to explain other molecular outflows with similar highly collimated morphologies (e.g., HH211, Gueth & Guilloteau; and NGC 2024, Richer et al. 1992). But, as can be seen in Table 5.8, the morphology is the only characteristic of the redshifted outflow lobe that is consistent with turbulent jet entrainment models.

Bow shock entrainment by a variable jet with internal working surfaces seems to better explain our results. A major internal working surface at $\sim 60''$ (0.15 pc) south of PV Ceph may naturally explain all of the following characteristics which are seen there: 1) the local increase in outflow gas column density (i.e., outflow clump or hot spot) seen in Figure 5.5*d*; 2) the slight rise in the CO line ratio

Table 5.8. Comparison of redshifted molecular outflow lobe south of PV Ceph and results of entrainment models

Parameter	Description	Figure	Consistent with model?		
			Turbulent Jet	Bow Shock	Wide-angle Wind
Morphology	jet-like, with wiggling axis	5.16	**YES**	**YES**	NO
Temperature	Outflow T_{ex} > ambient T_{ex}, with local maxima at source position and $\sim 60''$ south of source along axis	5.11	NO	**YES**[a]	NO
Velocity	velocity peak at source and $\sim 60''$ south of source	5.14	NO	**YES**[b]	NO
Momentum	Maximum at source, general decrease with distance from source	5.15	NO	**YES**[c]	NO

[a]Consistent with bow shock entrainment by several internal working surfaces, each responsible for the rise in temperature.

[b]Consistent with bow shock entrainment by several internal working surfaces, each responsible for the rise in velocity. Note, most of the low-velocity redshifted emission at the source position is *not* due to the PV Ceph outflow.

[c]Consistent with bow shock entrainment with an underlying ambient density gradient of r^{-a}, where $1 \leq a \leq 2$.

(Figure 5.11); and 3) the peak in outflow velocity (Figure 5.14). We thus conclude that the redshifted outflow gas south of PV Ceph has most likely been entrained by a variable jet with internal bow shocks.

The chain of optical HH knots that form HH 215 is also highly suggestive of a variable jet morphology. The average axis of HH 215 is coincident with the general north-south axis of the redshifted molecular outflow lobe south of PV Ceph (see Figure 5.16). The HH 215 knots show a wiggling pattern somewhat similar to the redshifted outflow lobe axis (see Figure 5.16). In addition, HH 215(1) —the brightest knot in HH 215— is $\sim 55''$ north of PV Ceph. Thus, we strongly believe that the redshifted molecular outflow is entrained by the counter jet of HH 215, and that the features observed $\sim 60''$ south of PV Ceph are produced by the

counter-knot of HH 215(1).

It is interesting to note that although the outflow gas in the hh315b+c region (Figure 5.2) and the redshifted outflow in the hh215 region (Figure 5.16) are both presumably entrained by the same mechanism, they have very different morphologies. The source of this seeming inconsistency is apparent from the morphology of the optical HH 315 flow. Similar to other HH flows [e.g., HH 34 (Reipurth et al. 1986; Devine et al. 1997); and HH 111 (Reipurth et al. 1992; Reipurth et al. 1997; RBD)] the HH objects which make up the HH 315, increase in size, the further away they are from the outflow source. We should expect the redshifted counter-knots of HH 215, south of PV Ceph, to be as compact and small as HH 215. Therefore, the redshifted gas south of PV Ceph has a jet-like appearance because it is most probably entrained by a continuous (unresolved) chain of small bow shocks, which have a jet-like appearance. On the other hand, the transverse size of the bow shock responsible for the blueshifted outflow associated with HH 315C is larger than the shocks associated with HH 215, and so the CO outflow shell-like structure produced is very well resolved by our observations.

Evidence for a blueshifted wide-angle wind north of PV Ceph

The blueshifted ^{12}CO and ^{13}CO gas just north of PV Ceph, in the hh215 region, shows a wide-angle structure. The ^{13}CO integrated emission has a V-like structure which encloses the blueshifted emission seen in CO (see Figure 5.7). In addition, the ^{13}CO V-structure coincides with the walls of the optical conical reflection nebula. Thus, we are confident that the observed blueshifted ^{13}CO structure traces the limb-brightened walls of a wind-blown cavity. This structure is similar to that observed in the inner regions of the B5-IRS1 outflow (Langer, Velusamy, & Xie 1996; Velusamy & Langer 1998; Yu et al. 1999, hereafter YBB).

Approximately coincident with the cavity axis, lie the HH 215 chain of knots. These optical knots trace the gas that has recently been excited by a much more collimated wind than the wind responsible for the blueshifted V-shaped outflow and ^{13}CO cavity walls. Therefore, it seems that we have two different wind components

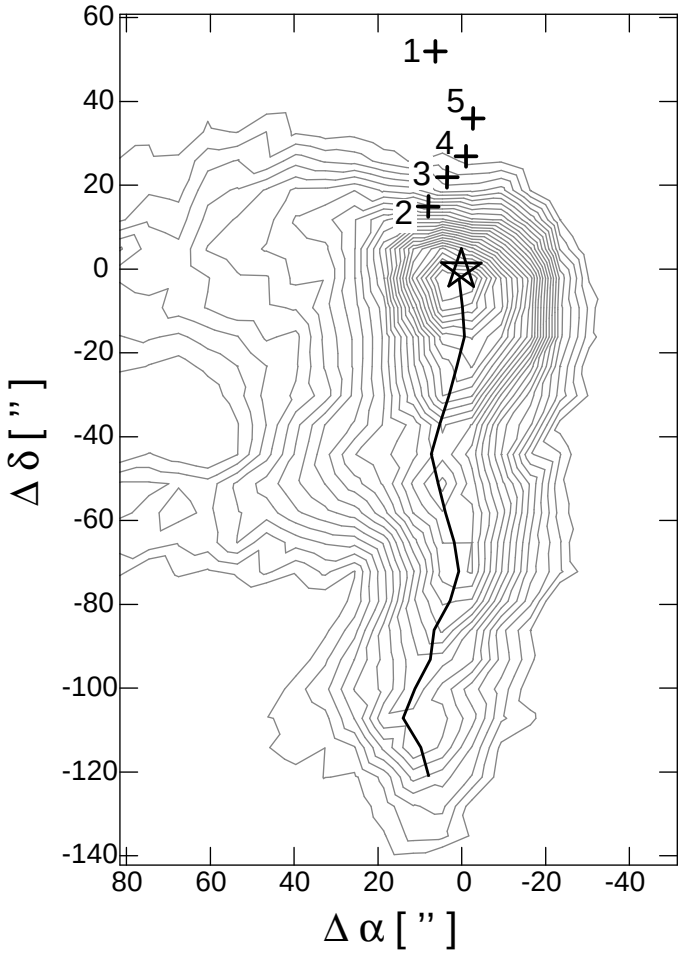

Fig. 5.16.— ^{12}CO(2–1) integrated intensity contours of the wiggling molecular redshifted outflow lobe in the hh215 region, near PV Ceph. The contours are the same as the left panel of Figure 5.9. The emission centroid (obtained from Gaussian fits to the intensity profile) is indicated by the thick black line. The star symbol represents the position of PV Ceph. The crosses represent the position of the HH 215(1) through HH 215(5) knots, and the number beside each cross indicates the HH 215 knot number.

in the northern (blueshifted) lobe close to PV Ceph: 1) a collimated (jet-like) wind responsible for the HH 215 knots; and 2) a wide-angle wind responsible for the poorly collimated blueshifted CO immediately north of PV Ceph, and the ^{13}CO V-shaped structure. A similar two-component wind is observed in the inner region of the B5-IRS1 outflow (see YBB).

There is evidence that a dual wind component is also present in the southern (redshifted) lobe of the outflow associated with PV Ceph. As discussed above, the collimated outflow lobe south of PV Ceph is most probably produced by a variable jet (the counter jet of HH 215). We do not detect a wide-angle wind in the redshifted lobe south of PV Ceph, but optical observations of the region close to PV Ceph (Gledhill et al. 1987; Levreault & Opal 1987; Neckel et al. 1987; RBD) have detected a fan-shaped reflection nebula south of PV Ceph, similar to the reflection nebula north of PV Ceph (see Figure 5.7). It is very probable that the redshifted molecular gas emission of the wide-angle wind south of PV Ceph is "hidden" under the optically thick ambient cloud emission of the region. Interferometric observations of the area will certainly help us detect the limb brightened walls of the southern cavity, as interferometric observations are excellent for filtering out large scale cloud structures.

A model which allows for the coexistence of both wide-angled and a very collimated wind is needed to explain the outflow from PV Ceph, similar to the B5-IRS1 outflow (YBB). So, we come to a similar conclusion as YBB do for B5-IRS1: we can best describe the sum of all the observations of the PV Ceph outflow near the source with a two-component model or a single-wind model in which the wind splits into a very collimated (axial) component and a wide-angle component. Of the latter category of models, the X-wind (Shu et al. 1994a; Shu et al. 1994b; Najita & Shu 1994; Ostriker & Shu 1995; Shu et al. 1995) is the most popular (but there are other models of the same category, e.g., Lery et al. 1999). In the X-wind model the outflow originates in the boundary layer between the accretion disk and the stellar magnetic field (the X-point), and the outflow is accelerated along magnetic field lines. At the base of the outflow (near the X-point) the wind originates as a very wide-angle wind, with all streamlines (except the

equatorial one) slowly converging to the rotational pole of the young star at infinity (Shu et al. 1995). The streamlines closest to the pole will focus towards the pole the closest to the star. Thus, the innermost streamlines will collimate into a "jet-like" wind at distances from the young star as close as $\sim$ 300 AU (Shang et al. 1998). The streamlines which do not focus fast enough towards the pole will produce a wide-angle wind.

As mentioned above, the other possible kind of model which could explain the observed characteristics of the PV Ceph flow near the source, is a two-component wind model. One example is the MHD model of Hirose et al. (1997), where two types of outflows having different origins form in the vicinity of the young star-circumstellar disk system. The highly collimated (or jet-like) component is launched in the interface between the young star's magnetosphere and the circumstellar disk. The other, less collimated (wide-angle) wind component comes from the disk and is accelerated by the large-scale magnetic field which penetrates the extended regions of the circumstellar disk (see also Kudoh & Shibata 1995, and references therein).

5.4.4 Episodicity and axis wandering of the HH 315 flow

Episodicity

Previous optical studies have pointed out the possible episodic nature of the HH 315 giant HH flow (GKW, RBD). The optical evidence for the episodicity of HH 315 comes from the fact that each of the three major HH knots in each lobe is about 0.35 pc from each other, with no HH-like emission between them. An HH knot is produced by the shock arising from the interaction of a high-velocity flow of gas ejected by a young star and the ambient medium. In HH 315, the HH knot pairs C-F, B-E, and A-D (see Figure 5.1) are thought to arise from three different mass ejection episodes.

Our millimeter line data show further evidence for the episodic nature of the HH 315 flow. The outflow gas surrounding the HH 315B and HH 315C knots

has a spatially discrete structure (Figure 5.2) which shows a shell-like or bow-like structure at the position of each of the two knots. At the head of each of these shell-like structures there is an increase in outflow velocity (Figure 5.12). A velocity increase at the position of the optical HH knots A, B, C, and D is also observed in the large-scale ^{12}CO(2–1) $p-v$ diagram of the HH 315 outflow (Figure 4.11). Such morphology and velocity distribution in the molecular outflow gas is not expected if the underlying stellar wind responsible for the creation of the molecular outflow were made of a continuous constant flow of ejected mass. The multiple CO shell structure, and the peak molecular outflow velocity at the head of the shock (the position of the HH knot) is better understood if the molecular outflow from PV Ceph is formed by a wind with sporadic episodes of copious mass loss (see Arce & Goodman 2001a/Chapter 3).

Wandering ejection axis

The fact that the ejection axis of HH 315 changes over time has been well established by the optical images of the flow, where it is clearly seen that the HH knots trace an S-shaped path. Tracing a line from PV Ceph to the location of each knot, it is seen that each major knot has a different position angle on the sky. Each mass ejection should travel in a straight line after being ejected by the young star, unless it collides with a dense clump which could change its trajectory. Our large scale molecular gas maps (Chapter 4) do not show any evidence for dense clumps which could have perturbed the ballistic trajectory of any ejection. Thus, the HH knots in HH 315 are at different angles with respect to PV Ceph, because PV Ceph's angle of ejection is changing over time (i.e., wandering or precessing). GKW have successfully reproduced the morphology of the HH 315 flow with a simple precession model, assuming a jet velocity of 200 km s^{-1}, a precession cone with full opening angle of $\sim 45°$, an inclination to the plane of the sky of $\sim 10°$, and a precession period of about 8300 yr. Goodman & Arce (2002) show that a westward motion of PV Ceph, in addition to a time-varying ejection angle, explain the position of the HH knot pairs (A-D, B-E, and C-F) with respect to the source better than models without transverse source motion.

In addition to the "precession" (or change in ejection angle) traced by the optical HH knots, our millimeter CO data for the redshifted outflow gas in the hh215 region show signs of a small scale time-varying ejection angle. In Figure 5.16 we show the integrated intensity contours of the redshifted gas in the hh215 region, integrated over the velocity range where we detect outflow emission. We made east-west intensity cuts for all pixel rows, for the extent of the north-south (jet-like) outflow structure. Most of the cuts show Gaussian-like intensity profiles, so we fit a Gaussian to each cut and obtained the position of the Gaussian centroid from each fit. In Figure 5.16, the thick black solid line plotted over the intensity contours indicates the position of the integrated emission centroid (obtained from the Gaussian fit) along the length of the redshifted CO jet-like structure. Assuming the emission centroid indicates the position of the outflow axis, we can state that the axis varies in direction over time (it wiggles). Similar wiggling morphology has been detected in optical HH jets (e.g., Heathcote et al. 1996) and other molecular outflows (e.g., Davis et al. 1997).

In Figure 5.17*a* we plot the presumed trajectory of the jet axis, traced by the ^{12}CO(2–1) velocity-integrated intensity centroid. It can be seen in Figure 5.17*a* that the points trace a sine-like path with a slope. We fit the centroid path with a straight line, and we then subtract the fit to the points, and show the result in Figure 5.17*b*. A sine wave was subsequently fitted to the slope-corrected points (see Figure 5.17*b*). Notice that the points at the peaks and valleys (of the sinusoidal trace) increasingly deviate from the sine fit, the furthest away from the source. This behavior, where the axis traces a cone (projected on the plane of the sky) rather than a cylinder, is suggestive of a "precession cone" expected for a flow with a quasi-periodic time-varying ejection axis (due to pure periodic precession or to a quasi-periodic random wandering of the ejection axis).

Assuming the sinusoidal appearance of the redshifted lobe comes from a purely periodic precession in the ejection axis, we may use the "wavelength" ($\lambda \sim 28,820$ AU) of the sine fit made to the points in Figure 5.17*b* to obtain a precession period. If we assume a jet velocity of 200 km s^{-1} (the same as GKW and RBD), we then obtain a precession period ($T = \lambda / v_{jet}$) of ~ 680 yr.

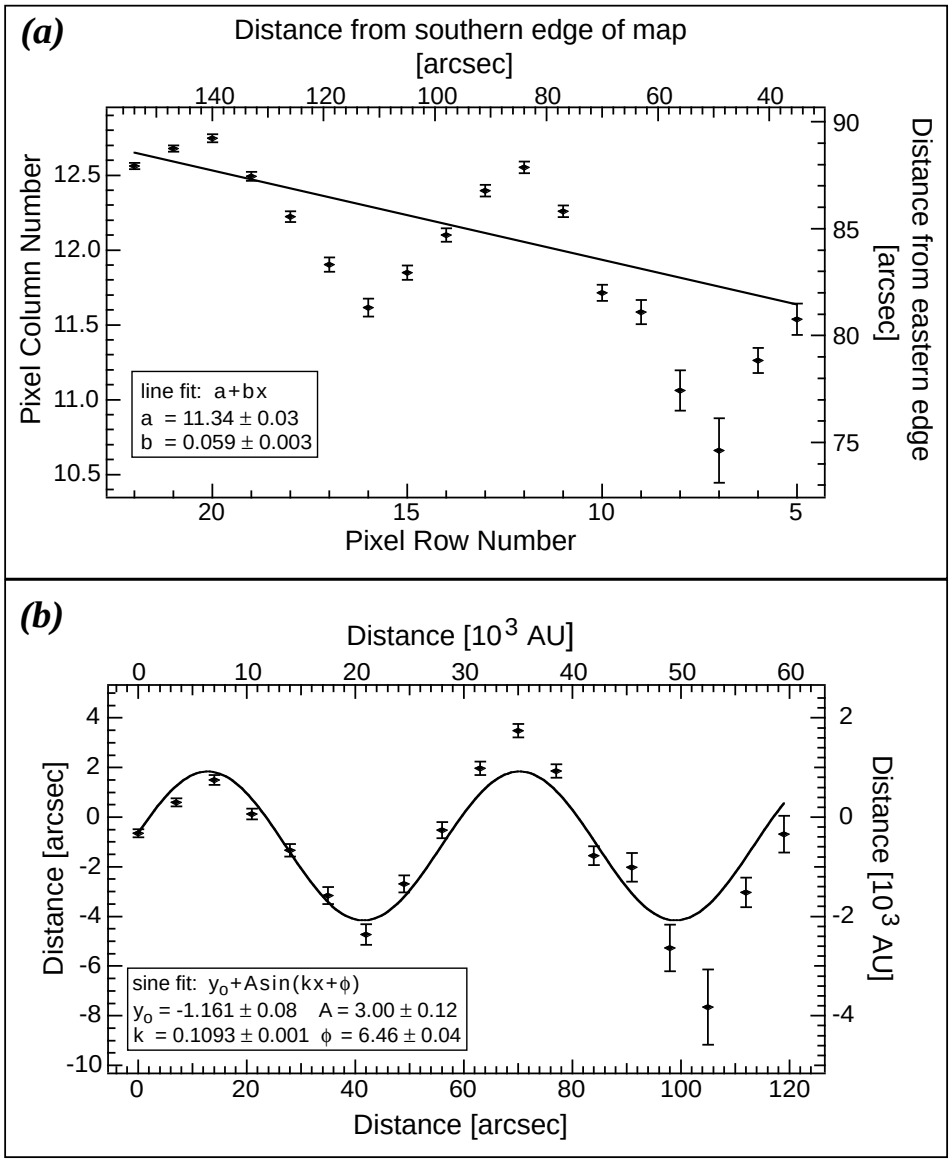

Fig. 5.17.— (*a*) Plot of the redshifted outflow lobe emission centroid position. Distances are given in terms of pixel numbers and arcseconds from the map (Figure 5.16) edges. The straight line fit to the points is plotted, and the fit parameters are shown. (*b*) Plot of the redshifted outflow lobe emission centroid position, corrected for the slope indicated by the line fit in [*a*]. The sinusoidal fit to the points, and the resultant fit parameters are shown. Axes are in arcsecond offsets and distance in AU from the source. In both panels, the errors shown are 3-σ errors.

Tidal interactions between binary components and a circumstellar disk is one possible mechanism which could induce precession on a young star. Terquem et al. (1999) give an approximate expression for the precession period of a disk around a young star in a binary system, where the disk surrounds only the primary star. The expression is given in terms of the primary mass (M_p), the mass ratio of the two stars, the disk radius (R), and the binary separation (D). Observations show that if PV Ceph has a binary companion it must be less than 50 AU apart (Leinert et al. 1997). We can use Equation 1 in Terquem (1999) and solve for the binary separation, to see if a precession period of $\sim$ 680 yr is possible for a binary system with a separation of less than 50 AU between its members. If we assume PV Ceph is the primary star with a mass of 4 $M_{\odot}$ (Fuente et al. 1998a), a primary to secondary mass ratio of about 0.25, and a 15 AU disk radius, then a binary separation of $\sim$ 21 AU would be needed to drive a precession with a period of 680 yr. Even if we were to change our assumptions to a primary-to secondary mass ration of 1 and a disk radius of 25 AU, the binary separation would be 43 AU. Thus, it is possible that the wiggling of the jet is due to precession of the outflow source induced by tidal interactions between PV Ceph, a yet undetected binary companion, and PV Ceph's circumstellar disk.

The precession period of $\sim$ 680 yr, from our observations of the wiggling redshifted CO outflow lobe, is about a factor of 12 less than the precession period obtained by GKW (from modeling the trajectory traced by the optical HH knots in HH 315). This apparent difference in precession period seems to indicate that: 1) the precession period is changing over time; or 2) there are two different mechanisms which are responsible for the different apparent precession-like motions.

Theoretically, the ejection of a third companion in a hierarchical triple system could lead to the formation of a tighter binary (see Reipurth 2000 for more details). But, in the case of PV Ceph the tightening of the binary system would had to occur in a very short time-scale of 2000 yr.[1] In addition, it is extremely coincidental that we would be observing PV Ceph right at the moment after the tightening

[1]This is the approximate time-scale between the eruptions responsible for the HH 215 chain of knots and the HH 315A-D knot pair (see Figure 5.1), assuming $v_{jet} \sim 200$ km s^{-1}.

of the binary system. Thus, it is highly unlikely that this scenario applies to PV Ceph. It seems more likely then, that the large-scale axis wandering is due to some other (unknown) mechanism. Some other possible mechanisms which could produce precession-like motions of the outflow ejection axis are: changes in the outflow source's magnetic field orientation; or a precession-like motion induced by tidal interactions of *multiple* stellar companions and their circumstellar disks.

In summary, we may explain the short-time scale axis wandering observed in the HH 315 outflow by circumstellar disk precession. But, it is highly unlikely that the same mechanism is responsible for the large-scale axis wandering.

5.5 Summary

We observe, at high velocity and spatial resolution, the molecular gas surrounding several knots of the giant Herbig-Haro flow HH 315, from the young star PV Ceph. The observations were aimed at studying the interaction between the HH flow and the ambient gas. The data obtained include simultaneous observations, at the IRAM 30 m telescope, of the ^{12}CO(1–0), ^{12}CO(2–1), and ^{13}CO(1–0), molecular lines. The three regions observed include: 1) an area surrounding two blueshifted knots (HH 315C and HH 315B) about 0.9 to 1.2 pc northwest of PV Ceph; 2) an area which includes the gas surrounding the outflow source, the HH 215 blueshifted optical knots 20″ to 55″ north of PV Ceph, and the collimated redshifted molecular gas south of PV Ceph; and 3) an area surrounding the redshifted optical knot HH 315E, about 0.9 pc southeast from the outflow source. The main points derived from our study can be summarized as follows:

1) We find that the blueshifted outflow gas in the region surrounding HH 315B and HH 315C has clearly been accelerated by bow shock entrainment of an episodic jet. The molecular outflow gas shows a spectacular bow-shock-shaped morphology, which has a width of about 0.4 pc at the slowest outflow velocities. The head of the CO outflow bow structure coincides with the position of the bow-shaped optical knot HH 315C. There is also blueshifted molecular outflow gas coincident with

the optical knot HH 315B which exhibits a structure suggestive of a bow shock morphology. A bow-like structure coincident with each knot, and the fact that both the excitation temperature and the velocity of the outflow gas show peaks at the position of the head of each bow-like structure, are all consistent with an outflow formed by two different bow shocks. Each of these two bow shocks were formed by a different mass ejection episode, where HH 315C is the "leading jet head" of the HH 315 giant flow, and HH 315B is a shock formed by a subsequent mass ejection episode.

2) Near PV Ceph (within 0.3 pc), the stellar outflow shows evidence for the coexistence of a wide-angle wind and a collimated (jet-like) wind. The blueshifted ^{13}CO integrated emission shows a V-shaped morphology with an opening angle of $\sim 90^{\circ}$, which is coincident with an optical reflection nebula. The blueshifted ^{12}CO has a fan-like morphology which fills the cavity delineated by the ^{13}CO V-shape structure. We conclude that the ^{13}CO traces the limb-brightened walls of a wide-angle wind-blown cavity. Along the axis of the wide-angle blueshifted ^{12}CO outflow lie the previously detected optical knots HH 215. These small knots delineate the collimated component of the blueshifted wind north of PV Ceph. We can best describe the sum of all the observations of the PV Ceph outflow near the source with a two-component model (like that of Hirose et al. 1997) or a single-wind model in which the wind splits into a very collimated (axial) component and a wide-angle component (like the X-wind model of Shu et al. 1995).

3) We find that the redshifted molecular outflow lobe south of PV Ceph is most likely entrained by a variable jet with several internal working surfaces (bow shocks). The redshifted outflow has a collimated wiggling jet-like appearance, with an "average" north-south axis, which extends to about 0.3 pc south of PV Ceph. The momentum distribution is consistent with jet bow shock entrainment in an ambient medium with density decreasing with distance from the source. Also the velocity and temperature distribution of the molecular outflow gas are consistent with it being entrained by a jet with several internal bow shocks. We show that the same (bipolar) mass ejection episode responsible for the blueshifted HH 215 knots is also responsible for the entrainment of the redshifted outflow lobe. There

has been no optical detection of the redshifted counter-jet of HH 215 because of the heavy extinction in the region south of PV Ceph.

4) We find that the wiggling observed in the redshifted CO outflow lobe near PV Ceph is most probably due to a time-varying ejection axis. Assuming the wiggling is due to precession of the outflow source, and a jet velocity of 200 km s^{-1}, then the precession period is 680 yr. This is about a factor of 10 less than the precession period deduced from the large-scale optical HH flow. We may explain the short time-scale axis wandering observed in the redshifted molecular outflow lobe by precession induced by tidal interactions between (undetected) binary companions and a circumstellar disk. But, it is highly unlikely that the same mechanism is responsible for the large-scale axis wandering.

5) We do not detect any outflow emission in the region surrounding the HH 315E optical knot. The CO spectra in this region has a FWHM of only $\sim$ 1 km s^{-1}, and shows no evidence of outflow-ambient gas interaction. It is puzzling to find such a narrow CO width in a region presumably affected by a stellar outflow. It is probable that all of the CO observed at the direction of HH 315E is in front of HH 315E (on the same line-of -sight), and that HH 315E is interacting mainly with atomic gas behind the molecular cloud.

Chapter 6

A Quantitative Comparison

ABSTRACT

We present a review of the results presented in this thesis, in the context of previous similar studies. We compile and study a sample of 5 giant molecular outflows (and their parent clouds), including results from our own studies of PV Ceph and HH 300, and three other sources from the literature. The results from this small sample indicate that an "average" single molecular outflow has enough energy and momentum to potentially disrupt a cloud no more massive than ~ 80 $M_{\odot}$. We also investigate the current known outflow activity in the B18 cloud in order to study the potential effects of multiple outflows on their parent cloud. Our findings, combined with other similar studies, suggest that outflows have enough energy and momentum to have a profound effect on a cloud's evolution and fate. We also offer a review of molecular outflow entrainment studies. Most outflow studies suggest that the bow shock entrainment model fits the data best. There are, though, an increasing number of outflow studies which indicate that the observed outflow properties are better explained with a combination of both a wide-angle wind *and* a collimated jet-like wind. The episodic and wandering nature of giant outflows is also discussed.

6.1 Outflow-cloud interaction

6.1.1 Disruption of a cloud by a giant outflow

The results of this thesis have provided a significant contribution to our understanding of giant HH flows effects on their surroundings. Our study of HH 300 (Chapter 2) shows that this giant HH flow has not only been able to create a parsec-scale CO outflow, but also that it has been able to accelerate medium-density gas ($n \sim 10^3$ cm^{-3}) up to distances of about 1 pc away from the outflow source. The linewidth of the medium-density gas (traced by our ^{13}CO observations) has also been enhanced along the 1 pc-length of the outflow. Thus, the HH 300 flow has affected the velocity and space distribution of the medium-density gas in its host cloud, in ways that can lead to cloud dispersal. Our study of the HH 315 flow (Chapter 4) shows that this 2.6-pc long HH flow is severely effecting the density and kinematic distribution of its parent cloud at a distance as far as 1.5 pc from the source. We find that the southern lobe of the stellar wind from PV Ceph has been able to create a cavity in the cloud near the source. The northern lobe has been able to push more than 6 $M_\odot$ of medium-density gas in a shell-like structure, and is also responsible for a velocity gradient in the ambient gas. Moreover, our results indicate that both the HH 300 and HH 315 flows have injected the surrounding molecular gas with kinetic energy comparable to their respective clouds' gravitational binding and turbulent energy.

The results of this thesis, in combination with the other (few) existing studies (see Chapter 1), show the disruptive effects that outflows can have on their parent cloud. But, can we yet generalize and state that giant HH flows could be the main disrupting agent of a molecular cloud?

We searched the literature for parsec-scale HH flows that had created giant (linear extent of 1 pc or more) CO outflows in non-crowed sites of low- to mid-mass star-formation. We restricted our literature search to giant molecular outflows studies which include corrections for gas opacity when calculating the outflow's mass and/or had added the mass of the slow molecular outflow component traced

by ^{13}CO (similar to our studies of HH 300 and PV Ceph). This correction is very important, as not correcting for the opacity of optically thick gas and not including the slowly moving outflowing mass traced by the ^{13}CO may result in an underestimation of the outflow gas by a factor of five to ten (see Chapter 2; Moriarty-Schieven & Snell 1988; Tafalla & Myers 1997). Also, we restricted our search to giant HH flows in clouds which have been mapped in ^{13}CO .

The search yielded only three more outflows in addition to the two outflows presented in this thesis (see Figure 6.1; Tables 6.1 and 6.2). These are: 1) the L1551-IRS5 molecular outflow in the L1551 cloud in Taurus; 2) the L1228 molecular outflow produced by the HH 199 flow, from the source IRAS 20582+7724, in the L1228 cloud; and 3) the B5-IRS1 molecular outflow in the B5 cloud in Perseus. All of the large-scale ^{13}CO cloud maps (from which we obtain the data presented in Table 6.2) have telescope beams no larger than 1.6′. Table 6.1 shows the physical properties of each of the five outflows in our sample. In Table 6.2 we show the properties of the five different parent molecular clouds which harbor the molecular outflows shown in Table 6.1. In Table 6.3 we show the potential effects each outflow has on its parent cloud, using the outflows' and clouds' physical parameters.

As it should be expected, the quantities shown in Tables 6.1, 6.2, and 6.3 have uncertainties. The distance to the cloud has an uncertainty not more than a factor of two. The major source of uncertainty in the estimated mass of the outflows and clouds comes from the uncertainty in the assumed ratio of H_2 column density to ^{13}CO column density (N_{H_2}/N_{13}). The uncertainty in N_{H_2}/N_{13} is about a factor of 2 to 3 (Frerking et al. 1982). The uncertainty in the outflow inclination angle (i) could result in uncertainties in the outflow momentum and kinetic energy by factors of 3 to 4 and 10 to 20, respectively.

The very small sample shown in Table 6.3 (see also Figure 6.2) indicates that most giant molecular outflows have kinetic energies comparable to (or larger than) their host cloud's turbulent energy. So, unless the coupling between outflow energy and cloud turbulent energy is very inefficient, giant molecular outflows should be able to drive the turbulence inside their host clouds.

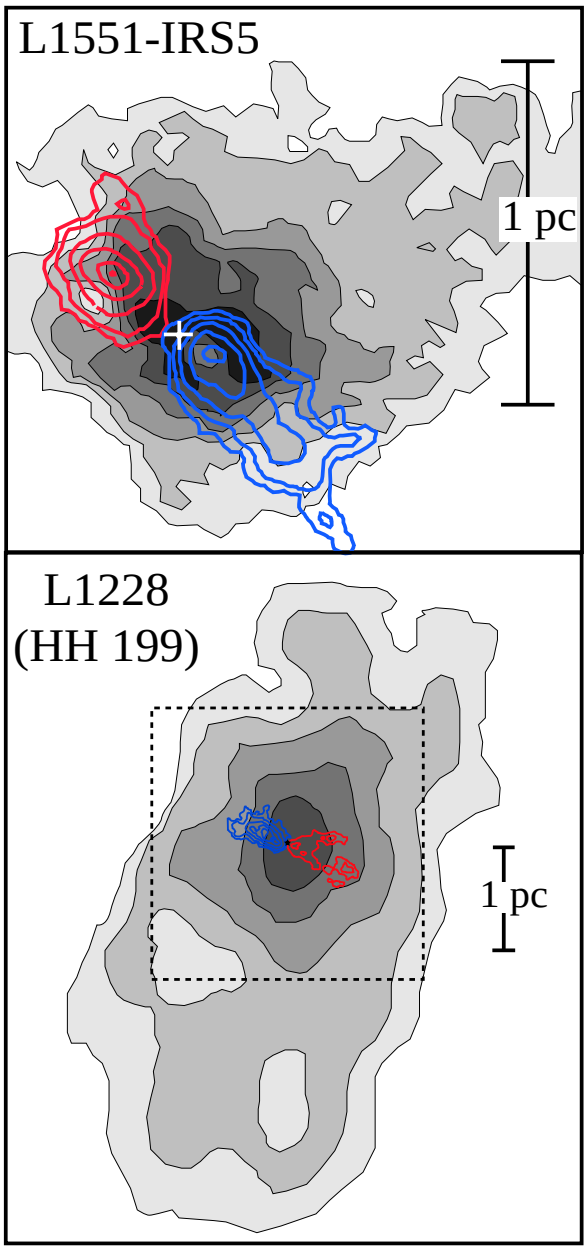

Fig. 6.1.— Maps of 5 giant molecular outflows and their host clouds. The grey-scale in all panels shows the ^{13}CO(1–0) integrated intensity map of the parent cloud. The blue and the red contours represent the blueshifted and redshifted lobes of the ^{12}CO outflow. *L1551-IRS1:* ^{13}CO(1–0) map based on Moriarty-Schieven & Snell (1998); ^{12}CO(1–0) outflow data from Pound & Bally (1991). *L1228:* ^{13}CO(1–0) based on Haikala & Laureijs (1989); ^{12}CO(1–0) outflow data from Tafalla & Myers (1997). The dashed box indicates the 30′ by 30′ region mapped (with a 1.6′ beam) by Bally et al. (1995), from where they obtain the (lower limit) cloud mass estimate (used in this chapter). Haikala & Laureijs (1989) mapped a larger region (shown in this figure) with a larger beam size ($\sim 4'$), but they do not give a mass estimate.

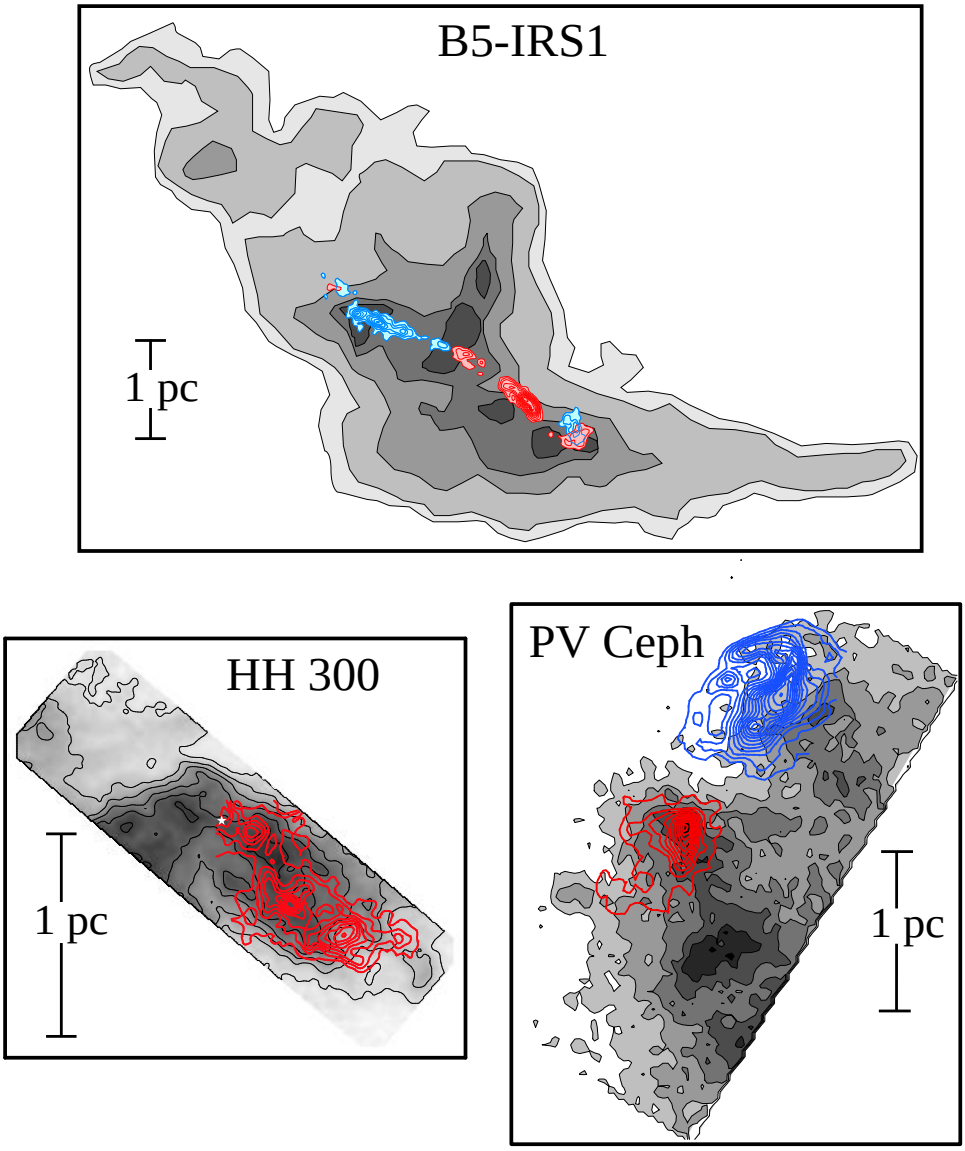

Fig. 6.1.— Continued.
B5-IRS1: ^{13}CO(1–0) map based on Langer et al. (1989); ^{12}CO(2–1) outflow data from Yu et al. (1999). *HH 300:* data from Chapter 2. *PV Ceph:* data from Chapter 4.

Table 6.1. Physical Parameters of Giant Molecular Outflows

Outflow Source	HH flow	i[a] [deg]	L_{flow}[b] [pc]	M_{flow} [$M_\odot$]	P_{flow} [$M_\odot$ km s^{-1}]	E_{flow} [10^{44} erg]	$\dot{E}_{flow}$[c] [$L_\odot$]	Reference
L1551-IRS5[d]	HH 262/264	15	1.2	2.7	46	110	0.45	1, 2
IRAS 20582+7724	HH 199	45	1.7	7.3	11	3	0.01	3
B5-IRS1	HH 366	13	3.1	9.6	51	32	0.13	4
IRAS 04239+2436	HH 300	10	1.0	4.3	18	9	0.03	5, 6
PV Ceph	HH 315	10	0.5	1.8	12	10	0.04	7, 8

[a]Average outflow axis angle with respect to the plane of the sky. The values of the outflow momenta and kinetic energies given in this Table are corrected by i. In the case of HH 199, there is no estimate of i, so we use $i = 45°$.

[b]Length of the molecular outflow which lies *inside* the parent molecular cloud (corrected by i).

[c]Outflow power = E_{flow}/τ_{flow}, where we assume all outflows are of, approximately, the same age: $\tau_{flow} = 2 \times 10^5$ yr (Parker et al. 1991)

[d]Data have been corrected for a distance of 140 pc to the Taurus cloud complex.

References. — (1) Moriarty-Schieven & Snell 1998; (2) Snell & Schloerb 1985; (3) Tafalla & Myers 1988; (4) Yu et al. 1999; (5) Chapter 2; (6) Reipurth et al. 2000; (7) Chapter 4; (8) Gómez et al. 1997.

Table 6.2. Physical Parameters of Clouds with Giant Molecular Outflows

Cloud	R_c[a] [pc]	M_c[b] [$M_\odot$]	ΔV[c] [km s^{-1}]	E_{turb}[d] [10^{44} erg]	E_{grav}[e] [10^{44} erg]	v_{esc}[f] [km s^{-1}]	References
L1551[g]	0.65	38	1.0[h]	2	2	0.7	1
L1228	1.3[i]	181[i]	1.5[h]	22	22	1.1	2
B5	2.2	790	1.0	45	243	1.8	3
B18w	0.55	72	0.8	3	8	1.1	4
PV Ceph	0.7	74	0.6	1	7	0.9	5

[a]The cloud radius is half the geometric mean of the two axes of the cloud.

[b]Mass of cloud obtained from the ^{13}CO(1–0) emission, assuming LTE.

[c]Average FWHM of the ^{13}CO(1–0) line in the cloud.

[d]Turbulent energy given by $\frac{3}{16\ln 2}M_c\Delta V^2$.

[e]Gravitational binding energy given by GM_c^2/R_c.

[f]Escape velocity of the cloud given by $(2GM_c/R_c)^{1/2}$.

[g]Data have been corrected for a distance of 140 pc to the Taurus cloud complex.

[h]ΔV obtained from Miesch & Bally (1994), assuming $\Delta V = 2.355\sigma_t$.

[i]In the case of L1228, the cloud mass and radius are lower limits (see Figure 6.1).

References. — (1) Moriarty-Schieven & Snell 1998; (2) Bally et al. 1995; (3) Yu et al. 1999; (4) Chapter 2; (5) Chapter 4.

Table 6.3. Comparison of Giant Outflows and their Host Clouds

Outflow Source	HH flow	Cloud	E_{flow}/E_{turb} [%]	E_{flow}/E_{grav} [%]	M_{esc}[a] [$M_\odot$]	M_{esc}/M_c [%]	$\mathcal{L}_{MHD}$[b] [$L_\odot$]	$\dot{E}_{flow}/\mathcal{L}_{MHD}$ [%]
L1551-IRS5	HH 262/264	L1551	5500	5500	66	180	0.03	1500
IRAS 20582+7724	HH 199	L1228	10	10	10	5	0.38	30
B5-IRS1	HH 366	B5	70	10	29	5	0.29	50
IRAS 04239+2436	HH 300	B18w	300	110	17	25	0.04	90
PV Ceph	HH 315	PV Ceph	1000	140	13	20	0.03	130

[a] $M_{esc} = P_{out}/v_{esc}$

[b] Input power, at a length scale equal to L_{flow}, needed to maintain MHD turbulence in cloud. The value is given by $\mathcal{L}_{MHD} \sim M_{cl}\ k\ (\Delta V)^3$, where $k = 2\pi/L_{flow}$ (Mac Low 1999; Stone et al. 1998).

In Table 6.3 we also show that each giant molecular outflow posses at least a substantial fraction of the power needed to maintain the MHD turbulence ($\mathcal{L}_{MHD}$) in their parent clouds (see also Figure 6.2). To obtain this estimate we have assumed that the outflow injects energy at a size scale equal to the molecular outflow's length (L_{flow}), and that MHD turbulence is responsible for the ^{13}CO velocity width (ΔV) of the clouds. It should also be noted that the value of $\mathcal{L}_{MHD}$ is based on numerical studies of the energy dissipation from uniformly driven MHD turbulence (Mac Low 1999, Stone et al. 1998). The simulations use parameters that are appropriate to conditions found in molecular clouds. Yet, the space dependence of the driving function in these numerical simulations (which is uniform throughout the simulation cube) differs substantially with the way outflows interact with their parent cloud. The dissipation rate of MHD turbulence and the value of $\mathcal{L}_{MHD}$ could vary depending on the space dependence of the driving force, and thus the numbers given in Table 6.3 are only rough estimates. Even so, our estimates of $\mathcal{L}_{MHD}$ can be used to conclude that giant outflows are a source of non-negligible power in clouds, and they should be treated as such in numerical simulations of MHD turbulence in star-forming clouds.

From our small sample we see that the three giant molecular outflows (L1551-IRS5, HH 300, and PV Ceph) in *small* clouds (with radius and mass less than 0.8 pc and 80 $M_\odot$, respectively) all have kinetic energies comparable to or greater than their parent cloud's binding energy (see Table 6.3, and Figure 6.3). On the other hand, the L1228 and B5-IRS1 outflows, although powerful, do not have enough energy to surpass the binding energy of their respective clouds —which have masses of more than 180 $M_\odot$ and radii of more than 1 pc.

We define the "escape mass" (M_{esc}) as the mass that could potentially be dispersed by the outflow, assuming all the outflow momentum is used to accelerate M_{esc} to the cloud's escape velocity, that is $M_{esc} = P_{flow}/v_{esc}$. We note that the molecular outflows in our small sample *currently* entrain a mass lower than M_{esc}, but by the end of the outflow stage they could easily entrain as much (or more) mass than M_{esc}. Since we do not know how much mass will *eventually* be entrained by the outflow, we use M_{esc} as a measure of the *potential* disruptive effect outflows

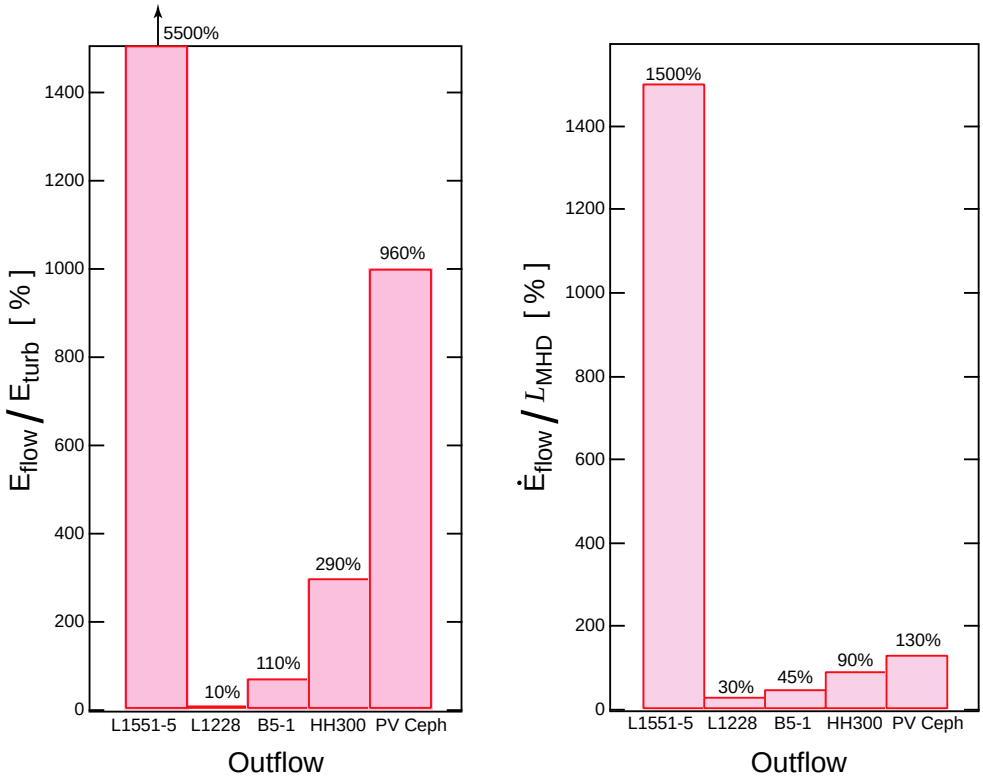

Fig. 6.2.— Comparison of outflow energy and power with cloud turbulence. The *left* plot shows the ratio of outflow kinetic energy (E_{flow}) to cloud turbulent energy (E_{turb}) for the five giant molecular outflows in our sample. The *right* plot shows the ratio of outflow power ($\dot{E}_{flow}$) to the power needed to sustain MHD turbulence in the given cloud ($\mathcal{L}_{MHD}$).

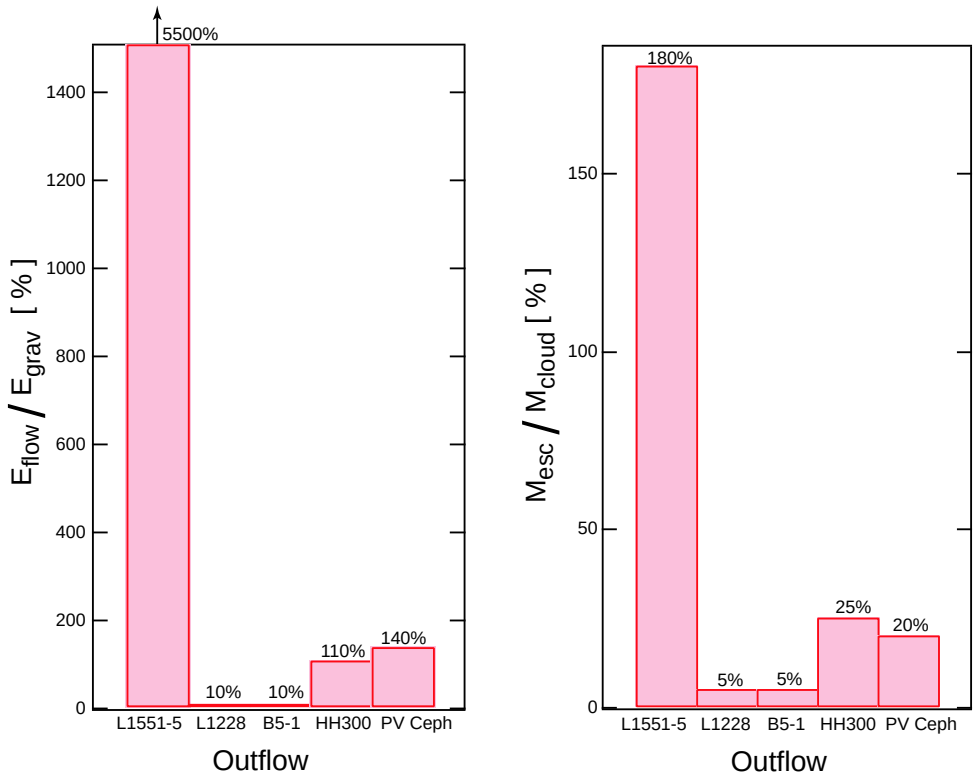

Fig. 6.3.— Comparison of outflow energy and momentum with cloud gravitational binding energy and mass. The *left* plot shows the ratio of outflow kinetic energy (E_{flow}) to cloud gravitational binding energy (E_{grav}) for the five giant molecular outflows in our sample. The *right* plot shows the ratio of "escape mass" ($M_{esc} = P_{out}/v_{esc}$, see text) to cloud mass for all five outflows and their host clouds in our sample.

have on their cloud. The L1551-IRS5, HH 300, and PV Ceph outflows have enough momentum to potentially disperse about 20% or more of their respective cloud's mass (see Table 6.3 and Figure 6.3). This would have a disruptive effect on the cloud, since a loss of 20% of the original mass of a cloud, would translate in a decrease of the gravitational potential energy to 64% of the original value (depending on how the cloud is defined, see §6.1.3). The L1228 and B5-IRS1 outflows lie inside clouds with much more mass than the other three outflows, and so even though L1228 and B5-IRS1 have comparable (or larger) momenta than the other three outflows, they only have the potential to eject about 5% of their respective parent cloud's mass.

We may conclude from our limited sample that a single giant outflow may have a disruptive effect only on relatively small molecular clouds, with linear extents of 1.5 pc ($R_c \sim 0.75$ pc) or less, and mass less than ~ 100 $M_\odot$. Larger clouds, as one might expect, are too massive to be dispersed by the energy and momentum input of a *single* giant outflow.

6.1.2 Many outflows in one cloud

Clouds with mass greater than ~ 100 $M_\odot$ typically harbor more than one young star, so it is possible that a combination of giant (and small) outflows from all the young stars in the cloud could inject enough energy and momentum to their surroundings to be able to disrupt a major fraction of the cloud. An example of such a cloud is B18 in Taurus. This cloud has a mass of 440 $M_\odot$, and long and short axes of 5.3 pc, and 2.5 pc, respectively (Heyer et al. 1987a). Therefore the cloud radius (R_c) is about 1.8 pc; the gravitational binding energy (E_{grav}) is 9.2×10^{45} erg; and the escape velocity (v_{esc}) is about 1 km s^{-1}. The B18 cloud has 18 young stellar systems —each one with one to three members (see Figure 6.4).

In Figure 6.4 we marked the stars which are known to power outflows, through optical studies (HH flows) or millimeter studies (mapped CO outflows or large Δv in the CO spectra surrounding the source), or both (see Table 6.4). We expect that the vast majority (if not all) of the B18 stars are or were outflow sources, but

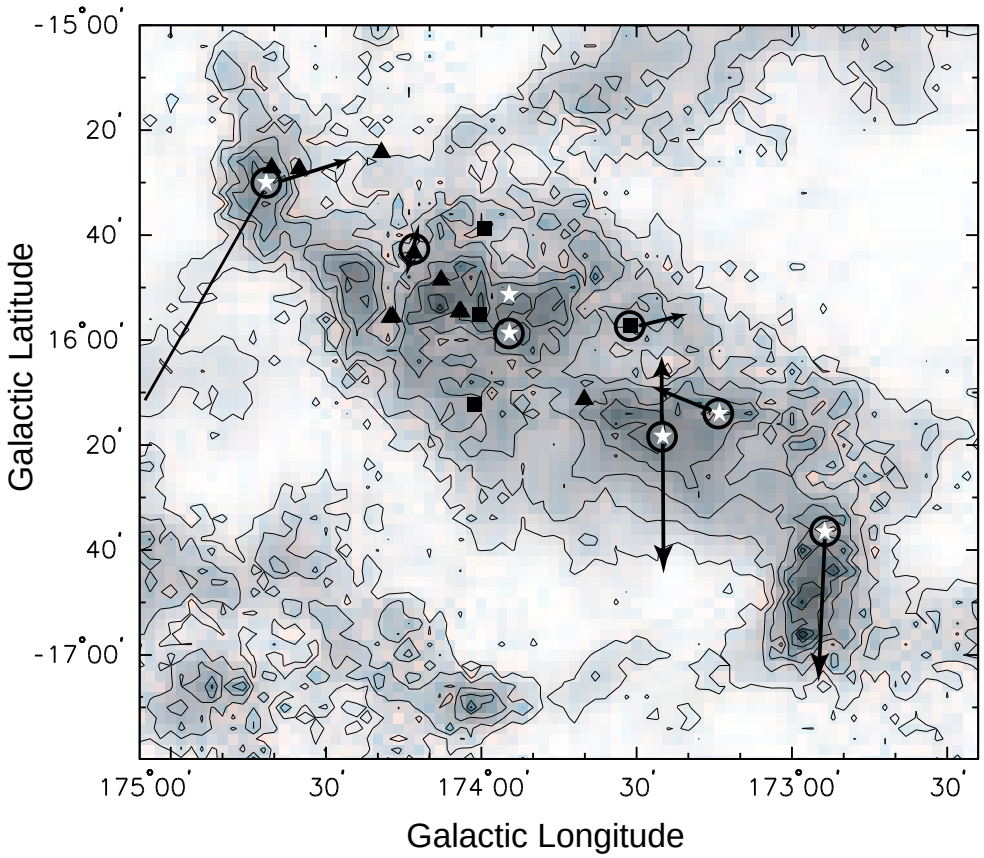

Fig. 6.4.— ^{13}CO integrated intensity map of the B18 cloud in Taurus for the velocity range $2.9 < v < 8.9$ km s^{-1}. The map is part of the large scale ^{13}CO map of the Taurus molecular cloud complex from Mizuno et al. (1995). The young stars associated with the B18 cloud are identified. Class I stars are represented by white stars, Class II stars are represented by solid black triangles, and Class III stars are represented by solid black squares. Known outflow sources are identified with a black circle. The known length of the outflow (through millimeter or optical observations) is indicated by arrows. The outflow source furthest to the left powers an outflow which extends further than the limit of the ^{13}CO map.

Table 6.4. List of known young stars powering outflows in B18

Star	Outflow	Comments	Reference
IRAS 04239+2436	HH 300	giant HH flow, and giant CO outflow mapped	1, 2
IRAS 04264+2433	HH 414/413	small HH jet near source + one HH knot 0.2 pc away, no CO observations	3
GV Tau	HH 410/411	giant HH flow, on source pointing shows wide CO line	3,4,5
ZZ Tau	···	mono-lobe CO outflow mapped	6
HK Tau	···	wide CO spectra on source and north of source	4,7
GK/GI Tau	HH 466–468	several HH knots observed near this binary source, no CO observations	8
IRAS 04325+2402	HH 434–436	one 0.6 pc-long CO lobe mapped and 2.4 pc long HH flow observed (not coincident with CO lobe)	6, 9

References. — (1) Chapter 2; (2) RBD. (3) Devine et al. 1999; (4) Levreault 1988; (5) Terebey et al. 1989; (6) Heyer et al. 1987; (7) Lichten 1982; (8) Aspin & Reipurth 2000; (9) Wang et al. 2001.

the limited past search for outflows (and lack of sensitive deep observations) in the region have resulted in only 7 known outflow sources. Two of the seven outflows [HH 300, powered by IRAS 04239+2436 (Reipurth et al. 1997c), and HH 410/411, powered by GV Tau (Devine et al. 1999)] are "giant" and were discovered within just the past 5 years. So there is a high probability that more, as yet undetected, outflows exist in the B18 cloud, but we will only consider the ones that have been detected.

In Figure 6.4 we show the presumed length of the outflow denoted by the extent of the molecular outflow or by the extent of the HH flow. We can see that the outflows are evenly distributed through the cloud and that they cover a fair amount of area. Out of the seven outflows, only the redshifted lobe of HH 300 has

been carefully mapped in CO and the mass has been estimated by correcting for the optical depth of the ^{12}CO(1–0) line (see Chapter 2). So, we assume that each known (HH or molecular) outflow source in B18 (see Table 6.4) powers a bipolar *molecular* outflow with a momentum and kinetic energy in *each lobe* similar to the redshifted molecular outflow lobe of HH 300 (see Table 6.1). This results in a total momentum and kinetic energy from all (presumed) molecular outflows in B18 of 258 $M_\odot$ km s^{-1} and 12×10^{45} erg, respectively. Thus, the presumed total outflow momentum is enough to potentially disperse $\sim 60\%$ of the cloud's mass ($M_{esc} = 258$ $M_\odot$), and the estimated total kinetic energy of all outflows is larger than the gravitational binding energy of the cloud. Given the current distribution of outflow lobes, the momentum and kinetic energy input to the cloud would be approximately evenly distributed, and thus the cloud could potentially be disrupted by the young stellar outflows.

Recent studies of regions with many outflow sources have also found that outflows acting in concert have a disruptive effect on their parent cloud or cloud complex. Bally et al. (1999) suggest that the same process which, at small scales (0.3-0.5 pc), is currently making the cavities seen in the region of HH 56/57 (Reipurth et al. 1997a, see Figure 1.7) produces the "Swiss cheese" appearance of the Circinus dark cloud complex (see Figure 6.5). That is, past outflow events from young stars which currently do not power molecular outflows were able to create the many ~ 1 pc cavities now seen in the Circinus cloud complex. Knee & Sandell (2000) studied the molecular outflows from the stars in NGC 1333, which are clustered in a region about 0.5 by 0.7 pc. They estimate that if the current energy injection rate from the outflows to the cloud is maintained over $\sim 10^7$ yr, it would be enough to disperse the whole NGC 1333 cloud. In addition, the data suggest that the outflows have been able to break up the star-forming core into cavities and shells (see Figure 1.9; Knee & Sandell 2000; Sandell & Knee 2000). So, evidence is mounting for the disruptive power of outflows in a molecular cloud.

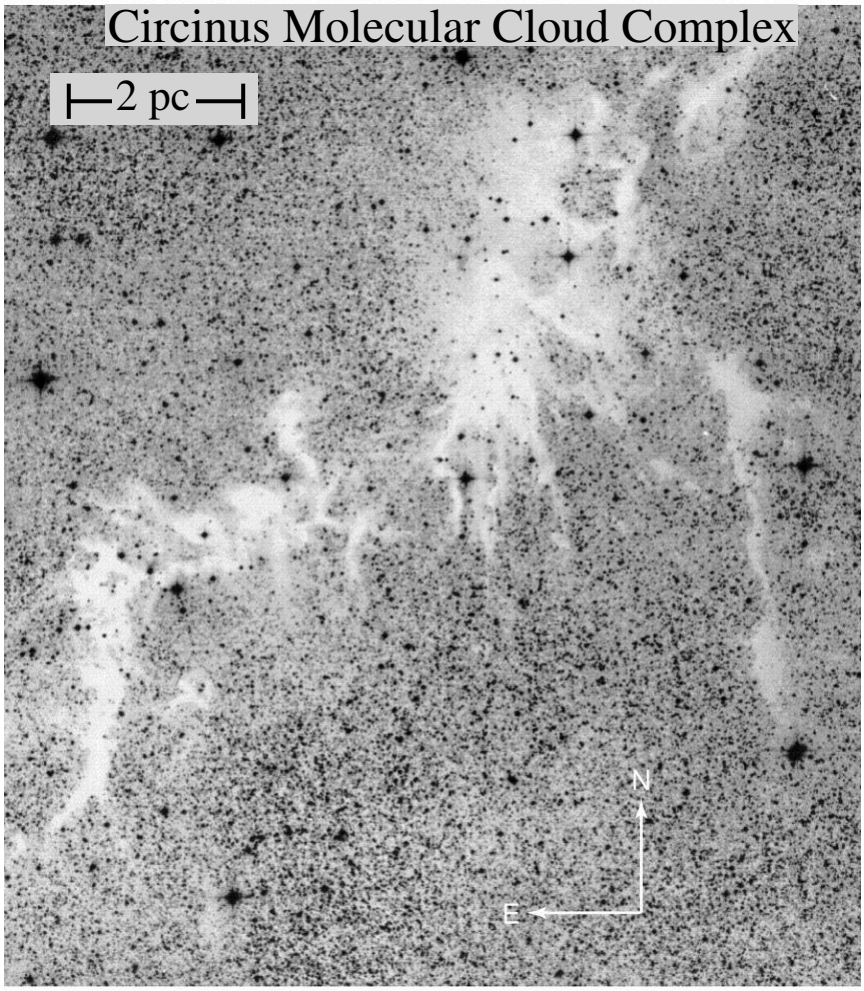

Fig. 6.5.— *R*-band photograph of the Circinus cloud complex from Bally et al. (1999). Notice the many cavities, about 1 pc in size, revealed as regions of lower extinction.

6.1.3 Recipe for destruction

In principle, there are two ways in which outflows could destroy their parent cloud: 1) via "cloud evaporation"; and 2) by "ripping them apart". Molecular clouds may be "evaporated" if outflows inject sufficient turbulent energy on the molecular gas as to gravitationally unbind it. In this picture the bulk motions of the entrained gas eventually decay to produce turbulence in the cloud. If outflows were to be the sole suppliers of turbulent energy in the cloud, then:

$$M_c \ \sigma_{turb}^2 \sim \epsilon \ \bar{E}_{flow} \ N_{flow}, \tag{6.1}$$

where σ_{turb} is the turbulent velocity dispersion in the cloud, $\bar{E}_{flow}$ is the average *molecular* outflow kinetic energy, N_{flow} is the number of outflows in the cloud. Also, ϵ is the efficiency of transferring outflow kinetic energy to turbulent motions. The cloud will eventually "evaporate" if the turbulent energy of the cloud becomes much larger than the gravitational binding energy of the cloud:

$$M_c \ \sigma_{turb}^2 \gg \frac{GM_c^2}{R_c} \tag{6.2}$$

We speculate that this process will be rather inefficient. Not all the molecular outflow energy will be converted to cloud turbulent energy since some of that energy is radiated away. In addition, although outflows are usually evenly distributed inside a cloud (e.g., Fukui et al. 1993; also see Figure 6.4) they will not directly affect all the gas inside the cloud. Outflows can excite MHD waves, which can then help propagate the outflow-induced turbulence to other parts of the cloud. Therefore, some of the outflow energy will be spent exciting MHD waves.

A more direct (and efficient) way to destroy a cloud would be for outflows to "rip it apart" by pushing large amounts of gas away from the cloud's gravitational center. In this picture outflows push and accelerate gas to velocities greater than the cloud's escape velocity, thereby unbinding the gas from the gas gravitational potential. If sufficient gas is accelerated to $v > v_{esc}$, then the whole cloud could be dispersed. Say, there are a number N_{flow} of outflows with average momentum $\bar{P}_{flow}$, inside a cloud with mass M_c. Then, the mass which could potentially be

dispersed by the outflows (M_{esc}), is given by:

$$M_{esc} = \frac{\bar{P}_{flow}}{v_{esc}} N_{flow} \tag{6.3}$$

If a total mass of gas M_{esc} is unbounded, then the remaining binding energy of the cloud (E_{grav}) would be:

$$E_{grav} = \frac{G(M_c - M_{esc})^2}{R_c} \tag{6.4}$$

As we have observed, outflows can push gas around producing cavities, and regions of lower density in the cloud, as schematically illustrated in Figure 6.6. The final result of the creation of these cavities (and the regions of less column density) could essentially be to divide the cloud into several "clumps" (see Figure 6.6). If the different clumps have a velocity dispersion (σ_{clumps}), then they will not stay gravitationally bounded if:

$$\sigma^2_{clumps} > \frac{G(M_c - M_{esc})}{R_c} \tag{6.5}$$

Take, for example the B18 cloud (from the previous section). Here $M_c = 440$ M$_\odot$, $R_c = 1.8$ pc, and we estimate that $M_{esc} \sim 258$ M$_\odot$. If the outflows in B18 are able to "divide" the cloud in different clumps by gravitationally unbinding a total mass of M_{esc}, then the clumps will not remain gravitationally bound if they have a velocity dispersion as low as 0.7 km s^{-1}. In any cloud, even if the clumps stay gravitationally bound the outflows will be able to sculpt the cloud, leaving their mark with fossil outflow cavities. A cavity about 0.3 pc wide may last for $\sim 10^5$ yr, after the outflow turns off, assuming a turbulent velocity dispersion in the cloud of ~ 1 km s^{-1}.

6.1.4 Concluding Remarks

Observations reveal that the energy and momentum in outflows is measured to be adequate for cloud disruption. We detect outflow-blown cavities, massive clumps of gas put into motion by outflows, and large-scale velocity gradients induced by outflows on the ambient gas. But, can outflows really evaporate a whole molecular

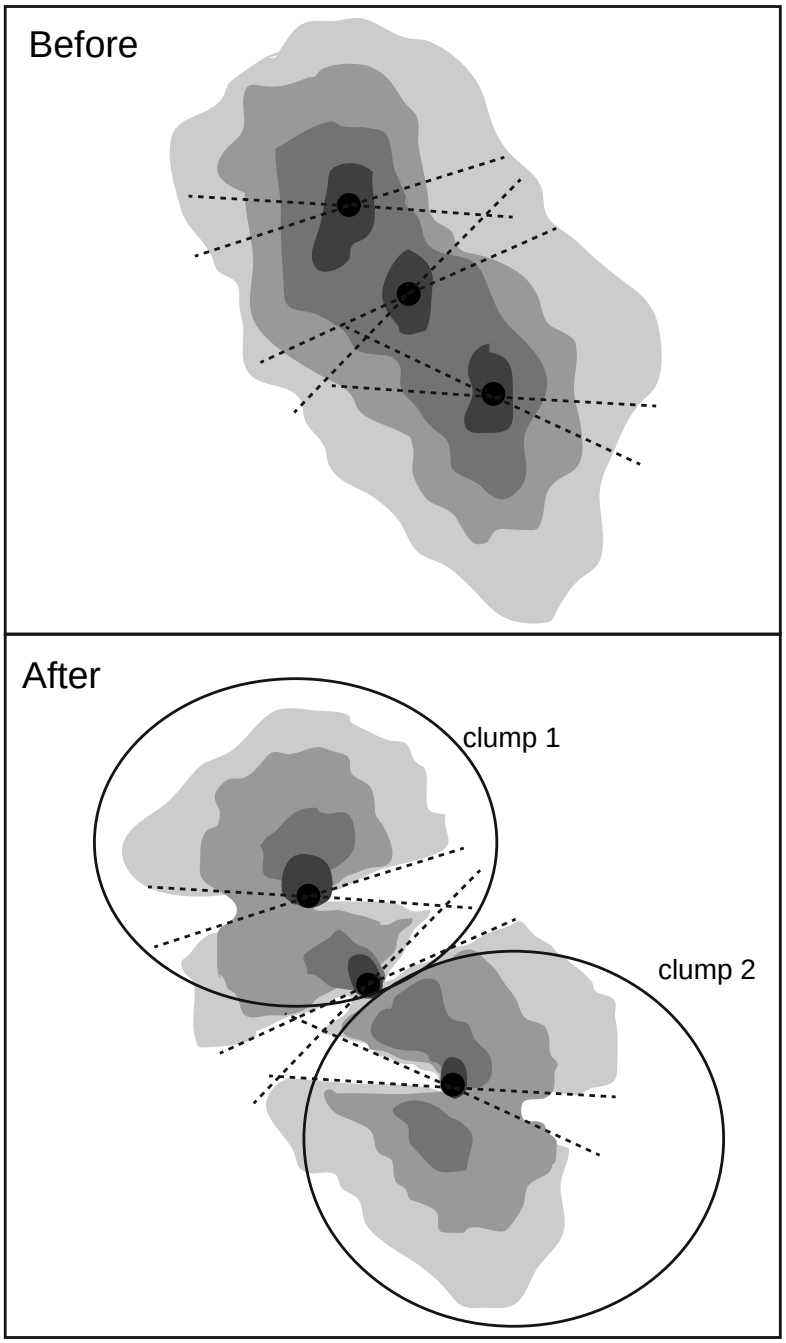

Fig. 6.6.— Schematic illustration of cloud disruption by outflows. *Top.* Initial state of outflow-harboring cloud. Dashed lines delimit the lobes of the three bipolar outflows in the cartoon cloud. *Bottom.* After some time the outflows will push and gravitationally unbind gas, leaving hollowed-out cavities in the cloud. The process could divide the cloud in several "clumps" (as identified in the figure). If the velocity dispersion of the clumps is larger than the remaining gas mass binding energy, the clumps will gravitationally unbind.

cloud? Are outflows the primary agent of molecular gas dispersion, or are just perturbations to the cloud? How well does the outflow energy couple to the molecular clouds? These are among some of the yet unanswered questions that need to be resolved. Clearly, further studies are needed.

With the efficient on-the-fly mapping technique now available in several millimeter-wave telescopes, and the advent of focal plane array millimeter-wave receivers, it is now possible to image large areas on the sky in a relatively short time. These technological advances have made possible the efficient and timely mapping of large outflows and their parent clouds in more than one molecular line, which is essential to the study of the outflow-cloud interaction. With this new technology at hand, we anticipate there will be more work devoted to study the outflow-cloud interaction in different star-forming regions with different environments and at different evolutionary stages. These studies are needed in order to really understand how outflows affect the evolution and lifetime of their parent cloud.

6.2 Driving mechanism

Recent high spatial resolution studies of molecular outflows, with millimeter single dish and interferometric arrays, have made it possible to start testing the different entrainment models with observations. No mechanism seems "perfect," and observations' most important role may be in constraining future entrainment modeling. Most of the high-resolution outflow studies suggest that the best entrainment mechanism for explaining CO outflow is the bow shock (prompt) entrainment model. But, as we explain below, an increasing number of studies suggest that a jet-like wind is not enough to explain the observed properties.

Different pieces of observational evidence are used to conclude that an observed molecular outflow is most likely bow shock-driven:

1) Morphology. Theoretical models and numerical simulations of bow shock jet-driven outflows show that the head of a molecular outflow is expected to have a

bow shock (or shell-like) morphology. Thus, a collimated molecular outflow with a bow shock structure, coincident with HH knots or H_2 knots may be considered to be a jet bow shock-driven outflow, solely based on the morphology of outflowing CO —as in, for example the B5-IRS1 outflow (Yu et al. 1999), and the outflow from PV Ceph (Figure 5.2). Several studies —of both low-mass YSO outflows (e.g., HH 211, Gueth & Guilloteau 1999) and high-mass YSO outflows (e.g., W75N, Davis et al. 1998)— have carried out detailed comparisons of the observed outflow morphology and the bow shock entrainment models, and successfully match observations with the results of the models.

2) Morphology and Kinematics. Some fairly collimated molecular outflows show no clear bow shock structure, but rather one or more CO "hot spots" (or local CO integrated intensity maxima), which most of the time are coincident with the position of HH knots or H_2 knots (see Figure 1.12 for an example). The molecular outflow velocity peaks at the position of the CO hot spots, and decreases towards the outflow source. This morphology and velocity distribution is consistent with an outflow entrained by a jet with several bow shocks, where each CO hot spot coincides with the head of each bow shock. Examples of such outflows include L1448 (Bachiller et al. 1990), IRAS 03282+3035 (Bachiller et al. 1991), RNO 43 (Bence et al. 1996), HH 212 (Lee et al. 2000). When the momentum along the outflow axis is estimated, it is observed to peak at the position of the hot spots, like seen in the RNO 15-FIR (Davis et al. 1997), the HH 25MMS (Gibb & Davis 1998) and the HH 300 (Chapter 2, see Figure 2.10) molecular outflows. Furthermore, Davis et al. (2000), compare the CO outflow mass-velocity distribution along the axis of the V380 Ori-NE outflow, and show that the largest ratios of high-to-low velocity gas mass are detected just behind H_2 shock features. This is exactly what is expected for a shock-driven (prompt entrainment) molecular outflow.

3) Morphology and Chemistry. Further evidence for bow shock-entrained outflows may come from the presence of shock-enhanced molecules (like SiO) coincident (in position, morphology and velocity) with the CO outflow. A fine example of such an outflow is L1157 (Gueth et al. 1998), shown in Figure 1.13, but there are other outflows which also show this (e.g., HH 211, Chandler & Richer

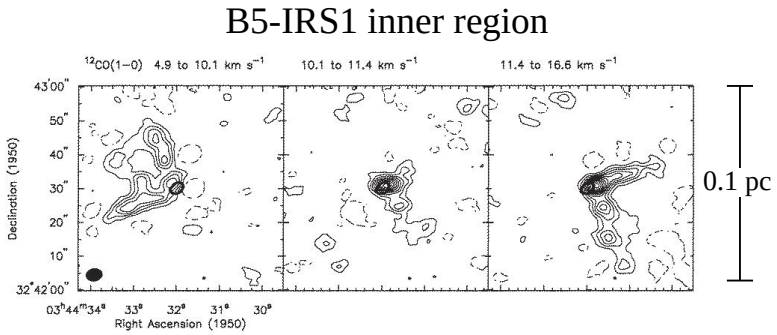

Fig. 6.7.— Wide-angle wind in the B5-IRS1 outflow. ^{12}CO(1–0) velocity-integrated emission maps of the inner region of the B5-IRS molecular outflow. From left to right, the panels show the blueshifted outflow, the ambient gas, and the redshifted outflow. The velocity range of integration is shown on the top of each map. Plot is based on figure from Langer et al. (1996).

2001).

Even though the evidence for bow shock-driven outflows is plentiful, an increasing number of studies suggest that the coexistence of a jet-like wind *and* a wide-angle wind better explain the observed outflow properties. For example, the stellar wind from B5-IRS1 has been able to produce: 1) a very collimated ~ 3 pc CO outflow (see Figure 6.1) consistent with jet (bow shock)-driven models; and 2) a wind-blown cavity with an opening angle of about 90° seen in high velocity CO as a limb-brightened parabolic-shaped cone, which extends less than 0.1 pc from the source (see Figure 6.7). Similarly, PV Ceph shows a very collimated CO outflow, and a wind-blown cavity with an opening angle of $\sim 90°$ (see Figure 5.7) very close to the star ($\lesssim 0.3$ pc). In both cases, the jet bow shock entrainment model can explain the collimated component, but it fails to explain the wide-angle CO outflow.

Evidence for a wide-angle wind (in addition to a collimated wind) also comes from the large-scale morphology of the outflow gas. For example, in the low-mass star L1228 outflow, the chain of HH knots (Bally et al. 1995) trace a collimated flow (HH 199), but the ^{13}CO outflow (Tafalla & Myers 1997) is very poorly collimated (see Figure 1.10), a concurrence hard to explain with any jet-driven models (Tafalla & Myers 1997). Other examples of poorly collimated CO outflows coexisting with a jet-like component include L1551-IRS1 (e.g., Davis et al. 1995), HH 111

(Cernicharo & Reipurth 1996; Nagar et al. 1997; Lee et al. 2000), the massive outflow G192.16 (Shepherd et al. 1998), and possibly also in HH 7-11 (Bachiller & Cernicharo 1990; Bachiller et al. 2000). In addition, observations of the L43 (or RNO 91) molecular outflow show no evidence for jet entrainment, and the data are better explained by solely wide-angle wind entrainment (Bence et al. 1998).

Recently, Lee et al. (2000) obtained high-resolution data for five CO outflows in order to compare the kinematics and morphology of the observed outflow with that predicted by the wide-angle wind and bow shock entrainment models. They found that in two sources (HH 212 and HH 240/241) the CO outflow is best explained by the bow shock model and in other two sources (VLA 05487 and RNO 91) the CO outflow is best explained by the wide-angle wind model. In one source (HH 111), the CO outflow shows characteristics of both models. So, it can be seen that there is no consensus on a single entrainment mechanism to describe all molecular outflows.

One possible scenario that could reconcile the observations is that in all outflows a collimated jet-like wind coexists with a wide-angle wind. One extant model which offers such a scenario is the X-wind model (Shu et al. 1995, and references therein). The X-wind model is a single-stellar wind model in which the wind splits into a very collimated (axial) component and a wide-angle component. In this MHD model, the outflow is accelerated along magnetic field lines. At the base of the outflow (near the X-point) the flow originates as a very wide-angle wind, with all streamlines (except the equatorial one) slowly converging to the rotational pole of the young star at infinity (Shu et al. 1995). The streamlines closest to the pole will focus towards the pole the closest to the star. Thus, the innermost streamlines will collimate into a "jet-like" wind at distances from the young star as close as $\sim$ 300 AU (Shang et al. 1998). The streamlines which do not focus fast enough towards the pole carry a wide-angle wind, which should be colder and less dense than the collimated wind. In addition, if the wind force of an angle-dependent wind is highly concentrated on the poles, then the wind would essentially be a jet-like wind. This jet-like wind would interact with the ambient medium very much like a bona fide jet which entrains the gas through bow

shocks. Outflows created by a highly collimated wind and outflows created by a jet will show very similar shell morphology, kinematics, and momentum distribution —any differences would be indistinguishable by most observations. Thus, an angle-dependent wind which is very collimated, and a jet could essentially produce the same entrainment mechanism.

Whether the observations detect an outflow better explained by a wide-angle wind or a jet-like wind (or both) will depend on the entrainment efficiency of one mechanism over the other, and on the nature of the millimeter line observations. The fact that most high-resolution studies of molecular outflows show that jet-driven models best describe the data, can be explained if in most cases the collimated component is more efficient, at entraining the surrounding ambient gas, than the wide-angle component. It is also possible that the velocity of the outflowing material depends on angle, where the outflowing gas with the highest velocities is entrained by the collimated wind component, and the wide-angle component produces only slowly-moving outflow gas. In fact, many molecular outflows show a dependence of collimation on velocity (e.g., HH 211, L1448, IRAS 03282+3035, NGC 2264G). The L1228 outflow has a wide-angle ^{13}CO outflow component (Figure 1.10) at velocities as low as 0.25 km s^{-1} with respect to the central ambient velocity. Similarly, the the wide-angle outflow component near PV Ceph (Chapter 4) is only detected at outflow velocities as low as 0.5 km s^{-1}. Thus, it could be that a wide-angle wind-entrained component is not observed in many molecular outflows, because the low-velocity outflow gas is hidden under the CO ambient cloud emission.

In addition, it has been suggested that the wide-angle component could be more important at later stages of the star-formation process, when the collimated component might be too weak to effectively entrain gas (Richer et al. 2000). Molecular outflows from Class 0 (deeply embedded, very young) sources are very collimated, while the outflows from more evolved Class I sources are less collimated (e.g., Richer et al. 2000). The RNO 91 molecular outflow in the L43 cloud (powered by a Class II/III star), is thought to be solely entrained by a wide-angle wind. Furthermore, the interferometric study of Velusamy & Langer (1998) shows that

the B5-IRS outflow cavity (see Figure 6.7) has widened with time.

In conclusion, the scenario of two coexisting wind components seems to agree best with the observational data. But, further outflow studies are needed to verify the existence of a wide-angle wind component in more outflows. Also, a consistent study of outflows of different ages, in similar environments, is needed in order to verify the suggestion that outflow opening angle and/or dominant entrainment mechanism changes over time.

6.3 Episodicity

Our results, together with those of several other outflow studies, indicate that episodicity is a common characteristic of stellar winds. Thus, any entrainment or stellar wind model should include the effects of episodic time variability.

Our millimeter observations of HH 300 and PV Ceph, have confirmed the episodic nature of these outflows, first proposed by the optical observations of the HH flows (Reipurth et al. 1997c). We find that a steep mass-velocity relation ($\gamma >> 2$, where $dM/dv \propto v^{-\gamma}$) in the molecular outflow may arise from an episodic stellar wind. The presence of "Hubble-wedges" (or spurs) in the molecular outflow position-velocity ($p-v$) diagram, is another indication that the underlying stellar wind is episodic. In fact, many other molecular outflows show clear evidence of episodicity in their position-velocity diagrams —even though some of the papers presenting the flow data may not address time-dependence (see Chapter 3).

Optical and infrared observations show that giant HH flows are made of well separated HH knots, and in many cases a knot in one lobe has a corresponding counter-knot in the opposite lobe. A continuous jet, with variable outflow velocity can produce multiple, contiguous, emission (HH) knots (e.g., Raga et al. 1990) which would look like the small (0.1 pc) section of HH 111 shown in Figure 1.3. *Giant* HH flows, where contiguous HH knots may be separated by distances of 0.1 to 2.0 pc (or more) and no HH-like emission is detected between contiguous knots, are hard to explain with only variable-velocity models. It is easier to understand

this HH flow morphology with each HH knot (or group of tightly packed knots) being produced by a different mass outflow episode.

By a mass outflow "episode" we mean a sudden increase in the stellar wind's mass loss rate. In this way, we use the term "episodic outflow" to mean an outflow that varies in mass loss rate in an unpredictable way and it is "not-strictly-periodic". In our picture, episodic outflows (with ages about 10^4 to 10^5 yr) are characterized by events of violent mass ejection rate ($\dot{M}_{out} \sim 10^{-5}$ to 10^{-4} $M_\odot$ yr^{-1}) every 500 to 10^3 yr or so, with states of no, or very low ($\dot{M}_{out} \sim 10^{-8}$ to 10^{-7} $M_\odot$ yr^{-1}) mass ejection between the violent outburst episodes (e.g., Hartmann et al. 1993; Bell & Lin 1994; Reipurth 2000). Several mechanisms which produce episodic outflows from young stars have been discussed in the literature (e.g., self-regulated thermal disk instabilities, Bell & Lin 1994; companion-disk interactions in a multiple stellar system, Reipurth 2000, and references therein).

The mass ejection rate from a YSO has the characteristics of a random process. Observations of giant HH flows commonly reveal three to four major ejection episodes, producing large, bright HH knots, with a time interval between episodes of $\sim 1000 - 2000$ yr (e.g., Reipurth et al. 1997; Reipurth 2000). Many of these giant HH flows also show a series of smaller knots with time interval between contiguous ejections of about $30 - 100$ yr[1] (Reipurth 2000). This behavior is similar to what one would expect from a random Gaussian distribution, where the most intense (or violent) events take place much less frequently than moderate events. In Figure 6.8 we show a schematic illustration of this. The plot shows a randomly generated set of points with a Gaussian distribution. As can be seen, large values of the mass ejection rate (corresponding to the mass ejection episodes which produce the widely-spaced large-scale bow shocks in giant HH flows) are much less frequent than values of smaller mass ejection rate (corresponding to the small mass ejection episodes responsible for the small, tightly-packed, knots in HH jets). Definitely, longer time baselines are needed to study the temporal behavior

[1]These small knots are usually found close to the source, and sometimes, the knots with the shortest time intervals may produce what looks like a contiguous jet-like flow. For example, the series of small knots which make up the nice collimated HH jet shown Figure 1.3 (HH 111), have an ejection time interval of about 30 yr.

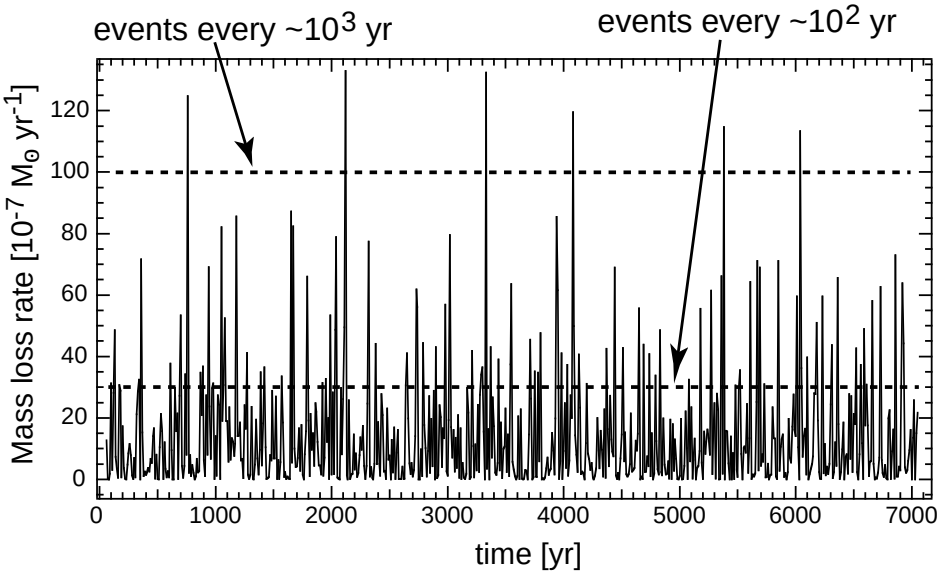

Fig. 6.8.— Schematic illustration of the variation in mass ejection rate for an episodic outflow. The points were randomly generated with a Gaussian distribution, and then squared. The mass ejection rate ($\dot{M}$) is given in units of $M_\odot$ yr^{-1} (y-axis). Notice that the "high-value points" ($\dot{M} \gtrsim 10^{-5}$ $M_\odot$ yr^{-1}) occur less frequent than points with a value of $\dot{M}$ a factor of three smaller, as one would expected for a purely random generated Gaussian noise. The events that occur every $\sim 10^3$ yr are analogous to the mass ejection events which characterize giant HH flows.

of this phenomenon, which will help us understand the cause of outflow episodicity.

Even though the mechanism which produces episodicity remains a mystery, we do know that it is a common characteristic of stellar winds. Thus, it should be taken in consideration when modeling stellar winds, and their effects on the ambient medium. Pulsed jet (or wind) models are not episodic, since in these models only the wind velocity changes in a purely sinusoidal fashion, and in a very short timescale ($\sim 10^2$ yr or less). In order to correctly asses the energetic role of outflows in a magnetized ISM, it is now necessary to account for the time history of their interaction with their surroundings. Outflow episodicity may change the effective length and timescales on which the momentum and energy are injected, which is important in modeling a magnetized turbulent ISM (e.g., Mac Low 1999; Padoan & Nordlund 1999; Ostriker, Stone, & Gammie 2001, and references therein).

6.4 Wandering outflow axis

As more giant HH flows are discovered, it is apparent that outflow axis wandering is a common characteristic among them. Mass ejected from a young stellar object should follow, approximately, a linear trajectory once it leaves the star-disk system from where it originates, unless its trajectory is perturbed by a collision with a dense clump. In a giant HH flow each major HH knot is believed to be caused by a major mass ejection episode (see above). So, HH knots of the same HH flow showing different trajectory angles on the plane of the sky, with respect to the outflow source, most probably have been ejected at different angles; dense clumps that could change an ejecta's trajectory are rarely found. Many, but not all, giant HH flows show such time-varying ejection axis (see, e.g., Eislöffel & Mundt 1997; Reipurth et al. 1997c; Mader et al. 1999; Eislöffel 2000; Stanke, McCaughrean, & Zinnecker 2000)

Our millimeter observations reveal a time-varying axis in both of the sources we studied. In detail, the HH 300 flow is known to have a small ($\sim$ 1000 AU)

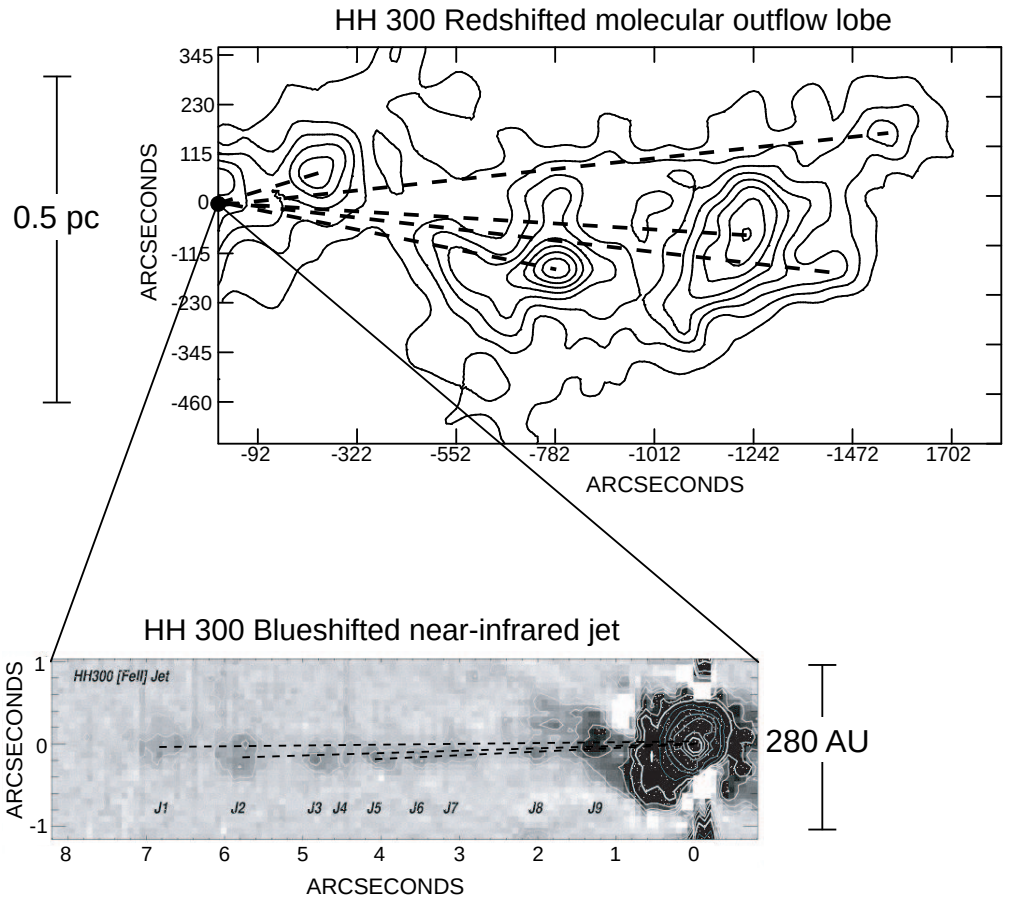

Fig. 6.9.— Comparison of the axis wandering scales in the HH 300 flow. (*Top*) ^{12}CO(1–0) redshifted giant molecular outflow lobe, from Chapter 2. (*Bottom*) Space-based, near-infrared ([Fe II] line) image of the small ($\sim$ 1000 AU) blueshifted jet, from Reipurth et al. (2000). In both panels we show, using dashed black lines, the presumed trajectory from the source to the current position of the ejection episode. Notice the huge difference in the size of the angle variations between the two panels.

wiggling jet near the source (see Figure 6.9), revealed by space-based, near-infrared (NIR) observations (Reipurth et al. 2000). Our millimeter observations show the giant (1.1 pc long) molecular outflow from HH 300 also has a wandering axis (see Figure 6.9) at much larger scales. The small NIR jet shows angle variations in its ejection axis no greater than 3°. On the other hand, the large-scale axis wandering of the molecular outflow has angle variations as big as 30°. The timescale of the large-scale axis wandering in the molecular outflow is about a factor of 50 larger than the timescale of the small-scale axis wandering in the NIR jet.

In the case of PV Ceph, the optical observations of HH 315 show that the HH knots delineate a spectacular S-shaped (2.6 pc long) giant HH flow (see Figure 6.10). The largest change in ejection angle among the HH 315 optical knots is $\sim 20°$. Our millimeter data reveals that the redshifted (~ 0.3 pc long) molecular outflow lobe has a wiggling axis (see Figure 6.10), with angle variations no greater than 12°. The axis wondering that produces the (small-scale) wiggling outflow lobe has a timescale a factor of 12 less than the timescale of the axis variation shown by the (large-scale) HH knots.

Thus, both sources show large- and small-scale axis wandering with different timescales. In both cases, pure precession of the outflow source due to tidal forces between binary components and a circumstellar disk may explain *only one* of the two axis wandering timescales. But, it is very hard to explain the coexistence of *more than one* time- and size-scales in axis angle variation by pure precession of a simple system composed of two stars and a circumstellar disk. It is probable then that more than one mechanism is responsible for the time-varying ejection axis observed in HH 315 and HH 300[2]. Some possible mechanisms include: changes in the outflow source's magnetic field orientation; or a precession-like motion induced by tidal interactions of *multiple* stellar companions and their circumstellar disks.

[2]In HH 300 and HH 315, orbital motions of the outflow source (around a binary) are discarded as a possible explanation to the axis wandering.

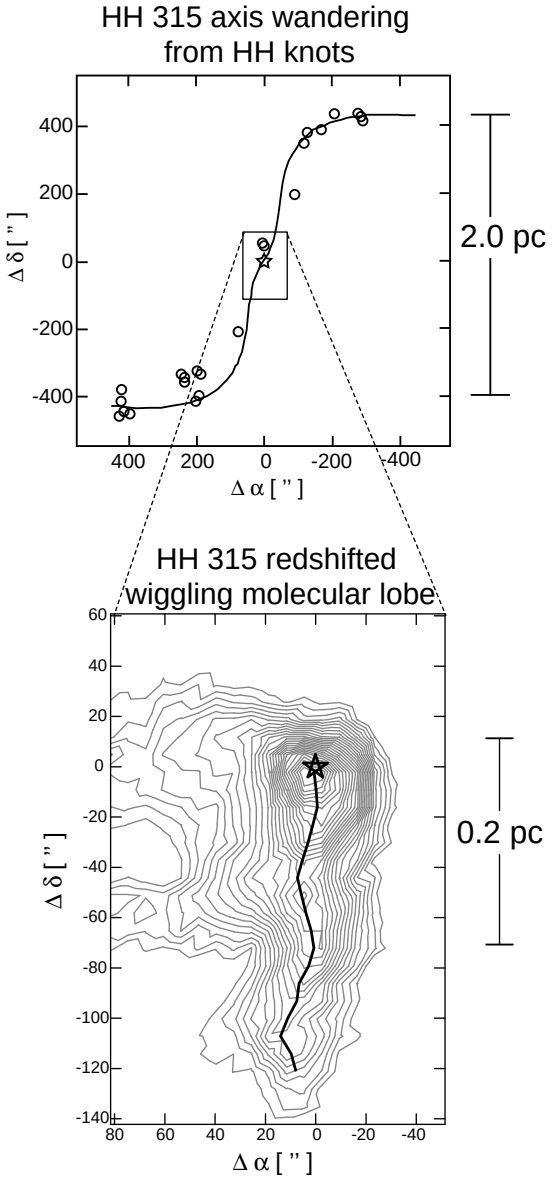

Fig. 6.10.— Comparison of the axis wandering scales in the HH 315 flow. (*Top*) Schematic illustration of the HH 315 flow. The small circles represent the HH knots from Gómez et al. (1997) and Reipurth et al. (1997c). The solid black line represents the results of the precession model from Gómez et al. (1997). The star represents the position of the outflow source, PV Ceph. (*Bottom*) ^{12}CO(2–1) integrated intensity emission of the redshifted outflow lobe near PV Ceph (from Chapter 5). The black line represents the emission centroid along the outflow axis, showing the wiggling axis of the outflow lobe.

Chapter 7

Summary and Future Work

7.1 Summary

We use new millimeter wavelength observations to reveal the important effects that outflows from young stellar objects have on their surroundings. We observed, in great detail, the surrounding gas and parent cloud of two giant (parsec-scale) Herbig-Haro (HH) flows. The HH flows studied were HH 300 from the young star IRAS 04239+2436, at a distance of 140 pc, and HH 315 from the young star PV Ceph, at a distance of 500 pc. These outflows were thoroughly mapped in the ^{12}CO(2–1) line, with a beam size of 27″. These observations were aimed at mapping the giant outflows and investigating their morphology and velocity distribution.

Also, larger maps of the region surrounding each outflow were obtained in the ^{12}CO(1–0) and ^{13}CO(1–0) lines, with 45″ and 47″ beam sizes, respectively. By observing a large extent of the gas surrounding the outflow we are able to study the outflow in the context of its surrounding medium. The ^{13}CO(1–0) observations also help us assess the effects the outflows have on the surrounding medium-density ($n \sim 10^3$ cm^{-3}) gas structure and kinematics. Moreover, the combined ^{12}CO(1–0) and ^{13}CO(1–0) line observations enable us to properly estimate the mass of the outflow by correcting for the velocity-dependent opacity of the ^{12}CO(1–0) line.

We performed higher spatial ($\sim 10''$) and velocity (~ 0.1 km s^{-1}) resolution

observations of the molecular gas surrounding several HH knots of the HH 315 flow. These high-resolution observations were aimed at studying the entrainment mechanism of the outflow from PV Ceph.

Our main results may be summarized as follows:

1) Giant HH flows entrain large quantities of mass and inject a vast amount of momentum and kinetic energy into their host molecular cloud. Our results show that the total mass of the HH 300 molecular redshifted outflow lobe is ~ 4 $M_\odot$, and for both lobes of the HH 315 molecular outflow the total mass is ~ 7 $M_\odot$. The momentum and kinetic energy of the redshifted outflow lobe of both outflows are ~ 10 $M_\odot$ km s^{-1}, and $\sim 10^{44}$ erg, respectively.

2) Giant HH flows are able to redistribute their surrounding medium-density gas, even at parsec-scale distances from the outflow source. Both of the giant HH flows we studied have been able to modify the density and velocity distribution of their parent clouds. The effects of these outflows on the surrounding $n \sim 10^3$ cm^{-3} medium are observed at distances as far as 1 to 1.5 pc from the source.

3) The energy input of giant HH flows into the surrounding ambient medium is comparable to the turbulent energy of the parent molecular cloud. Our detailed study of two giant outflows (HH 300 and HH 315) and their host clouds, combined with information about three other giant outflows and their parent clouds, indicate that giant molecular outflows have kinetic energies comparable to or larger than the turbulent energy of their respective host cloud. Although the amount of *kinetic* energy transferred from the molecular outflow to the cloud depends on an unknown coupling efficiency, outflows certainly have the potential to be a major source of turbulent energy in clouds. Further detailed numerical simulations of outflow-cloud interactions, which can estimate a coupling efficiency, are needed in order to understand the energy transfer between outflow and cloud.

4) Giant HH flows are a source of non-negligible power which may help drive the MHD turbulence in clouds. Using the small sample of 5 giant

outflows and their host clouds, described above (in summary # 3), we compared the outflows' power with the power needed to maintain the MHD turbulence in their respective host clouds —based on the results of published numerical studies. We find that in all five cases the outflow power is more than 25% the power needed to sustain MHD turbulence in the host cloud.

5) A single giant outflow has the potential to gravitationally perturb and disrupt a small cloud or clump with a radius of ~ 0.8 pc and mass of ~ 80 $M_\odot$. Using the small sample of 5 giant outflows and their host clouds, described above (in summary # 3), we compare the kinetic energy of each molecular outflow and its host cloud's gravitational binding energy. We also compare the outflow momentum with the cloud's mass and escape velocity in order to investigate what percentage of the cloud's mass could potentially be dispersed. We find that the kinetic energy of a giant molecular outflow is typically comparable to the binding energy of a cloud with mass of ~ 80 $M_\odot$. And, a giant outflow in such a cloud has enough momentum to potentially disperse about 20% of the cloud's mass. Larger clouds, as one might expect, are more massive and have much greater gravitational binding energy, and so a single molecular outflow does not have the energy and momentum to cause a major perturbation in the cloud.

6) The cumulative action of many giant outflows will certainly have a profound effect on a cloud's evolution and fate. Typically, clouds with mass greater than ~ 100 $M_\odot$ harbor more than one young star capable of producing a giant molecular outflow. So, in principle, a medium sized cloud with a mass ~ 100 $M_\odot$ could ultimately be dispersed by just a handful of outflows. Further detailed studies of star-forming clouds with many outflows, at different evolutionary stages, are needed in order to better understand the process of cloud dispersal by outflows.

7) Episodicity is a general characteristic of giant HH flows. We find tremendously strong evidence for the episodic nature of giant HH flows in their mass- and position-velocity relations and in their morphology. We explain how recent observational results disagree with the predictions of non-episodic outflow

models, and we offer simple explanations for the discrepancies. We discuss how an episodic stellar outflow can steepen the power-law slope of the mass-velocity relation in a molecular outflow. And, we illustrate how an episodic outflow can produce multiple "Hubble-wedges" in the position-velocity distribution of a molecular outflow. Further support for the episodic nature of outflows comes from the fact that the observed giant molecular outflows show a clumpy (spatially discrete) morphology, instead of a continuous smooth morphology. The outflow clumps are readily apparent in position-position-velocity space, exhibit different sizes and shapes, and some are spatially coincident with HH knots. In general, a local increase in the molecular outflow velocity (a Hubble-wedge) is observed at the position of these clumps.

8) A time-varying (wandering) outflow axis is a common characteristic among giant HH flows. Our millimeter observations of HH 300 and HH 315 (PV Ceph) both reveal a time-varying outflow axis. In addition, both sources show large- and small- scale axis wandering with different timescales. In both cases, pure precession of the outflow source due to tidal forces between binary components and a circumstellar disk may explain *only one* of the two axis wandering timescales. But, it is very hard to explain the coexistence of *more than one* time- and size-scale in axis angle variation by pure precession of a simple system composed of two stars and a circumstellar disk.

9) Jet bow shock entrainment by an episodic stellar wind, with a time-varying axis, produces most of the high-velocity molecular outflow observed in the two sources studied. In the case of HH 300, we draw this conclusion from the facts that the spatial distribution of the clumps, the velocity structure, and the momentum distribution of the outflow are all consistent with bow shock entrainment by an episodic jet. In the case of HH 315, using our high-resolution observations we are able to compare the temperature, momentum and velocity distributions, as well as the flow morphology, with those expected from different entrainment models. Our detailed comparison shows that bow shock entrainment best describes most (but not all, see below) of the properties of the molecular outflow gas in HH 315.

10) Our high resolution data of the outflow within 0.3 pc of PV Ceph, shows evidence for the coexistence of a wide-angle wind and a collimated (jet-like) wind. There are an increasing number of studies which suggest, that both a collimated (jet-like) component and a wide-angle (poorly collimated) component are needed to explain the observed outflow properties, similar to what we find in PV Ceph. Thus, a stellar wind model which allows for the coexistence of these two components (e.g., the X-wind model of Shu et al. 1995 or another similar model) is needed to explain the observed properties of outflows showing such characteristics.

7.2 Future Work

In this last section we discuss possible future work that could be done to widen our knowledge of the effects of giant HH flows on their surroundings:

• Expand the sample of observed giant molecular outflows and their parent clouds. Our results show that giant outflows have the *potential* to disrupt their host cloud, but more data are needed to statistically quantify how "good" this potential is. The observations should be carried out in ^{12}CO and ^{13}CO in order to properly correct for the velocity-dependent ^{12}CO opacity. Most of the outflow mass is found at low-velocities, where the opacity is greater. So, proper opacity correction is essential in order to obtain accurate outflow mass, momentum and energy estimates. Plenty of giant HH flows have been optically observed, it is now time to study their molecular surroundings.

• Study the effects that many outflows acting in concert have on their parent cloud. A very limited number of such studies exist. Different star-forming regions with different environments and at different evolutionary stages should be studied, in order to understand how outflows affect the evolution and lifetime of their parent cloud. This, of course, would take an enormous amount of observing time with the current technology. But there is hope; in the very near future mm-wave telescopes will be able to do on-the-fly mapping with focal plane array receivers,

while observing two (or more) spectral lines simultaneously.

• Investigate how, exactly, outflows disrupt their parent core. One of the goals of the study would be to produce an empirical model of core disruption at different evolutionary stages. It has been established that cores can be disrupted by outflows, but an exact picture of the outflow-core interaction at different evolutionary stages is lacking. Existing focal plane array receivers (e.g., SEQUOIA at the FCRAO 14 m) can be used to easily obtain a statistical sample of cores with outflows, at different evolutionary stages, observed in molecular lines tracing a variety of density regimes. This study could serve also as a path to understanding the disruption of *clouds* by outflows (see above), before the instrumentation for the study discussed in the previous paragraph becomes available. Studying the evolution of core disruption by outflows could shed important information on how the same process works on larger scales.

• Study the kinematics of giant HH flows. Although more than 30 giant HH flows have been discovered, the kinematics of only two giant HH flows have been thoroughly studied. Proper motion measurements of HH knots in combination with (optical) spectral line observations can be used to derive three-dimensional velocities for features in a giant HH flow. One can then use the inferred 3D velocity of the *molecular* gas associated with the HH knots to obtain accurate estimates of the molecular outflow momentum and kinetic energy. Measuring proper motions for a large ($\sim$ 10) sample of HH flows should not be hard. Images at different epochs of the same HH knot in a flow can be used to calculate its proper motion. Assuming a (typical) tangential velocity of 200 km s^{-1} and a distance to the HH flow of about 500 pc, the knot's proper motion should be about 0.08$''$ yr^{-1}. The majority of the currently known giant HH flows were observed about 5 years ago and lie within 500 pc of the Sun, so it will be relatively easy to measure their proper motions, even from ground-based optical telescopes —displacements of as low as 0.3" can be detected by ground-based observations. So, in principle, a new set of optical images for each flow studied, spectroscopic data for each knot, and patience reducing the data is all that is needed to carry out a kinematical study of giant HH flows.

• Investigate the effects of giant HH flows on the intercloud medium (ICM). Many giant HH flows contain HH knots found in regions of little or no CO emission, well outside their parent clouds and cores. Thus, it is evident that these HH flows have blown out of their host clouds, and are injecting some of their momentum and energy into the ICM. One way to investigate the effects of giant HH flows on the mostly neutral ICM, is by studying the high-velocity neutral hydrogen (HI) entrained by the HH flows. Trying to detect a low-level high-velocity wing of entrained HI is very difficult because of "contaminating" Galactic HI emission. The width of the spectral line (at its base) at any given position usually is about 80 to 100 km s^{-1}. So, in order to be able to detect the low-level emission from the neutral gas entrained by the HH flow: 1) the HI must have been accelerated to velocities high enough ($\gtrsim$ 40 km s^{-1}) so that the "HI outflow" emission is not lost under the Galactic HI emission; 2) even if the entrained HI attains extremely high velocities one needs to properly subtract the Galactic HI from the spectra, in order to cancel any (unknown) contaminating Galactic HI high-velocity feature which is not due to the HH flow; and 3) the observations need to be highly sensitive. It was our original plan to include a project, in this thesis, to study the effects of giant HH flows on the ICM. We were awarded observing time in Arecibo to conduct the study, but unfortunately, the baselines of our spectral observations were not stable enough to detect a low-level high-velocity wing. Although it is a difficult experiment, we believe that the atomic gas entrained by a giant HH flow, can be detected. The upgraded Arecibo telescope, the new GBT, and (in the near future) the expanded VLA will be all excellent instruments for this experiment.

• Study the outflow-circumstellar envelope interaction. The stellar outflow originates very close to the star, so it must interact with the mass envelope surrounding the YSO. The outflow-envelope interaction could play a crucial role in the YSO mass-assembling process, and in determining the final mass of the forming star. The common belief is that the stellar outflow cavity (near the source) widens with time, thereby halting infall and the accreting phase of the protostar. Yet, *strong* evidence for outflow cavity widening with time is only evident in the inner region of the B5-IRS1. Thus, additional observations are needed to confirm that

widening of outflow cavities holds in general. To perform the study, high-sensitivity millimeter-line interferometric observations of the circumstellar envelope of several outflows sources are needed. Instruments like the OVRO-MMA and CARMA are perfect for conducting this study.

• Expand the list of molecular outflows observed at high resolution. Additional high spatial resolution observations are always useful to further constrain the theoretical numerical entrainment models. Specifically, though, more observations are needed to determine whether the coexistence of a jet-like wind and a wide-angle is common, and whether the ratio of mass in one kind of wind to the other depends on physical conditions, or on time.

Appendix A

Estimating Excitation Temperature Using CO Line Ratios

In this Appendix, we discuss how to estimate the excitation temperature of the CO gas, using the ^{12}CO(2–1) to ^{12}CO(1–0) line ratio.

The radiative transfer equation, which gives the observed radiation temperature (T_R) of a molecular line emission at frequency ν, is given by:

$$T_R = [\eta_{mb_\nu} f_\nu]^{-1}[J_\nu(T_{ex}) - J_\nu(T_{bg})](1 - e^{-\tau_\nu}). \quad \text{(A.1)}$$

The first set of terms in the right hand size of Equation A.1 convert the apparent intensity (T_A^*) into the radiation temperature (T_R). Specifically, η_{mb_ν} is the main beam efficiency of the telescope (a known quantity, see Wild 1999 for the values of the IRAM 30 m telescope) and f_ν is the beam filling factor at frequency ν (see, e.g., Kutner & Ulich 1981; Rohlfs & Wilson 2000). Also,

$$J_\nu(T) = \frac{T_{o_\nu}}{e^{T_{o_\nu}/T_{ex}} - 1}, \quad \text{(A.2)}$$

where we define $T_{o_\nu} = h\nu/k$, T_{ex} is the excitation temperature, T_{bg} is the microwave background temperature (2.7 K), and τ_ν is the optical depth of the observed line

emission at the frequency ν. We define the ratio of brightness temperatures of the ^{12}CO(2–1) and ^{12}CO(1–0) lines as $R_{21/10}$ which, from Equation A.1, is given by:

$$R_{21/10} = \frac{[\eta_{mb_{12}}]^{-1}[J_{21}(T_{ex}) - J_{21}(T_{bg})](1 - e^{-\tau_{21}})}{[\eta_{mb_{10}}]^{-1}[J_{10}(T_{ex}) - J_{10}(T_{bg})](1 - e^{-\tau_{10}})}. \tag{A.3}$$

In Equation A.3 we assumed the excitation temperature of the $1 \rightarrow 0$ transition is the same as the T_{ex} of the $2 \rightarrow 1$ transition. In addition, since we are able to grid and smooth our ^{12}CO(2–1) and ^{12}CO(1–0) OTF maps to the same beam and pixel sizes, we can set $f_{10} = f_{21}$.

Consider also the equation which gives the value of the opacity τ_ν of a molecular line two-level transition from level u to level l, with frequency ν:

$$\tau_{ul} = \frac{c^3}{8\pi\nu^3} A_{ul} N_u (e^{T_{o_\nu}/T_{ex}} - 1), \tag{A.4}$$

where N_u is the column density of molecules in the upper level, and A_{ul} is the Einstein A coefficient for the CO line transition between u and l. Then, the ratio of optical depths of the $2 \rightarrow 1$ and $1 \rightarrow 0$ transitions is given by:

$$\frac{\tau_{21}}{\tau_{10}} = \frac{A_{21}}{A_{10}} \frac{N_2}{N_1} \frac{e^{T_{o21}/T_{ex}} - 1}{e^{T_{o10}/T_{ex}} - 1} \left(\frac{\nu_{10}}{\nu_{21}}\right)^3 \tag{A.5}$$

Assuming LTE, we may use Boltzmann's equation:

$$\frac{N_1}{N_2} = \frac{g_1}{g_2} e^{T_{o21}/T_{ex}}, \tag{A.6}$$

where g is the statistical weight of the given level. Then, Equation A.5 can be written as:

$$\frac{\tau_{21}}{\tau_{10}} = \frac{A_{21}}{A_{10}} \frac{g_2}{g_1} \frac{1 - e^{-T_{o21}/T_{ex}} - 1}{e^{T_{o10}/T_{ex}} - 1} \left(\frac{\nu_{10}}{\nu_{21}}\right)^3. \tag{A.7}$$

Using the values of ν, A, and g for the $2 \rightarrow 1$ and $1 \rightarrow 0$ transitions we obtain that the optical depth of the $2 \rightarrow 1$ transition can be expressed in terms of the $1 \rightarrow 0$ optical depth and the excitation temperature by:

$$\tau_{21} = 2\ \tau_{10}\ \frac{1 - e^{-11.06/T_{ex}}}{e^{5.53/T_{ex}} - 1}. \tag{A.8}$$

Thus, if available, one may use an estimate of the ^{12}CO(1–0) optical depth, the observed ^{12}CO(2–1) to ^{12}CO(1–0) line ratio, and Equations A.3 and A.8 to obtain an estimate of the excitation temperature.

In Figure A.1 we show the ^{12}CO(2–1) to ^{12}CO(1–0) line ratio as a function of excitation temperature for different values of the ^{12}CO(1–0) line opacity. As can be seen in Figure A.1 only in the optically thin limit is the line ratio reasonably sensitive to the excitation temperature. For higher ^{12}CO(1–0) optical depths the line ratio becomes less sensitive to T_{ex}, and so it is usually very unreliable to obtain an estimate of the excitation temperature for optically thick gas ($\tau > 1$).

If only optically thin gas is used, then one may use the optical thin case of Equation A.3 to obtain a simpler relation between $R_{21/10}$ and T_{ex}:

$$R_{21/10} = 4 \, \frac{\eta_{mb_{21}}}{\eta_{mb_{10}}} \, e^{-T_{o_{21}}/T_{ex}}, \tag{A.9}$$

where we assumed that the microwave background terms are negligible, as $J_\nu(T_{bg}) = 0.19$ K for ^{12}CO(2–1) and 0.82 K for ^{12}CO(1–0).

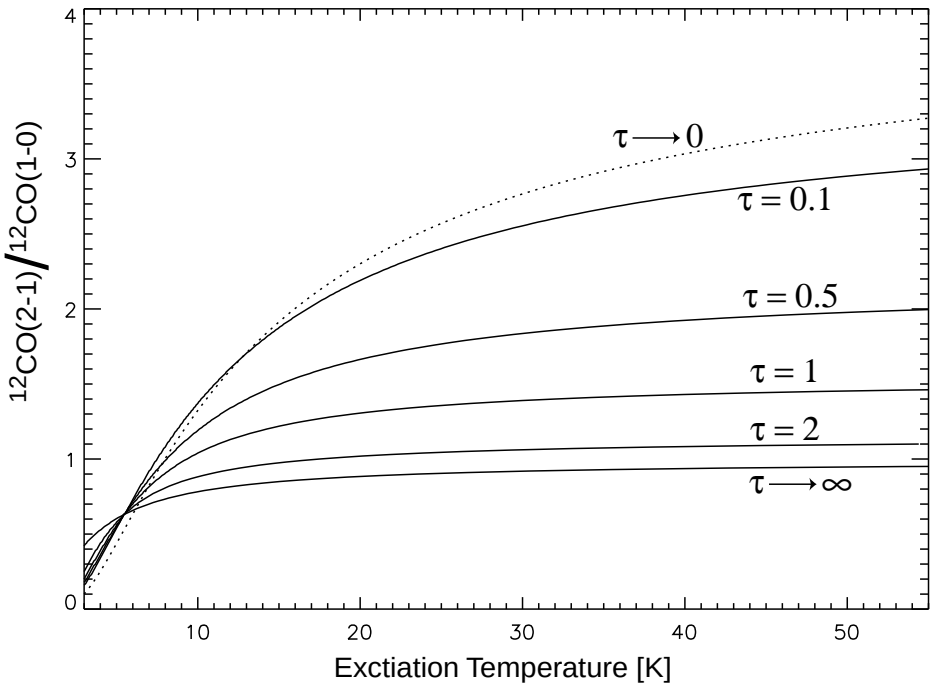

Fig. A.1.— ^{12}CO(2–1) to ^{12}CO(1–0) line ratio ($R_{21/10}$) as a function of excitation temperature (T_{ex}) for different values of the ^{12}CO(1–0) line opacity (τ).

Bibliography

Ambartsumian, V. A. 1954, Comm. Byurakan Obs. No. 13

Anglada, G., Estalella, R., Mauersberger, R., Torrelles, J. M., Rodríguez, L. F., Cantó, J., Ho, P. T. P., & D'Alessio, P. 1995, ApJ, 443, 682

Anglada, G., Sepúlveda, I., Gómez, J. F. 1997, A&AS, 121, 255

Arce, H. G., & Goodman, A. A. 2001a, ApJ, 551, L171

Arce, H. G., & Goodman, A. A. 2001b, ApJ, 554, 132

Armstrong, J. T., & Winnewisser, G. 1989, A&A, 210, 373

Aspin, C., & Reipurth, B. 2000, MNRAS, 311, 522

Bachiller, R. 1996, ARA&A, 34, 111

Bachiller, R., Cernicharo, J., Martín-Pintado, J., Tafalla, M., & Lazareff, B. 1990, A&A, 231, 174

Bachiller, R., & Codella, J. 1990, A&A, 239, 276

Bachiller, R., Gueth, F., Guilloteau, S., Tafalla, M., & Dutrey, A. 2000, A&A, 362, L33

Bachiller, R., Martín-Pintado, J., & Planesas, P. 1991, A&A, 251, 639

Bachiller, R., & Tafalla, M. 1999, in The Origin of Stars and Planetary Systems, ed. N. D. Kylafis & C. J. Lada (Dordrecht:Kluwer), 227

Bachiller, R., Tafalla, M., & Cernicharo, J. 1994, ApJ, 425, L93

Ballesteros-Paredes, J., Hartmann, L., & Vázquez-Samadeni, E. 1999, ApJ, 527, 285

Barral, J. F., & Cantó, J. 1981, Rev. Mex. Astron. Astrofis., 5, 101

Bally, J., Castets, A., & Duvert, G. 1994, ApJ, 423, 310

Bally, J., Devine, D., Fesen, R. A., & Lane, A. P. 1995, ApJ454, 345

Bally, J., & Lada, C. J. 1983, ApJ, 265, 824

Bally, J., Langer, W. D., Stark, A. A., & Wilson, R. W. 1987, ApJ, 312, L45

Bally, J., Reipurth, B., Lada, C. J., & Billawala, Y. 1999, AJ, 117, 410 (BRLB)

Bell, K. R., & Lin, D. N. C., 1994, ApJ, 427, 987

Bence, S. J., Padman, R., Isaak, K. G., Wiedner, M. C., & Wright, G. S. 1998, MNRAS, 299, 965

Bence, S. J., Richer, J. S., & Padman, R. 1996, MNRAS, 279, 866

Benson, P. J., Caselli, P., & Myers, P. C. 1998, ApJ, 506, 743

Blitz, L., & Thaddeus, P. 1980, ApJ, 241, 676

Blitz, L., & Shu, F. H. 1980, ApJ, 238, 148

Blitz, L., & Williams, J. P. 1999, in The Origin of Stars and Planetary Systems, ed. N. D. Kylafis & C. J. Lada (Dordrecht:Kluwer), 3

Boss, A. P. 1987, ApJ, 316, 721

Bourke, T. L., Garay, G., Lehtinen, K. K., Köhnenkamp, I., Launhardt, R., Nyman, L-Å., May, J., Robinson, G., & Hyland, A. R. 1997, ApJ, 476, 781

Cabrit, S., Goldsmith, P. F., & Snell, R. L. 1988, ApJ, 334, 196

Cabrit, S., Raga, A., & Gueth, F. 1997, in IAU Symp No. 182, Herbig-Haro Flows and the Birth of Low Mass Stars, ed. B. Reipurth, & C. Bertout (Dordrecht: Kluwer), 163

Campbell, B., Persson, S. E., & McGregor, P. J. 1986, ApJ, 305, 336

Cantó, J., & Raga, A. C. 1991, ApJ, 372, 646

Cantó, J., Raga, A. C., & D'Alessio, P. 2000, MNRAS, 313, 656

Cantó, J., Tenorio-Tagle, G. & Różyczka, M. 1988, A&A, 192, 287

Cassen, P., & Moosman, A. 1981, Icarus, 48, 353

Cernicharo, J., & Reipurth, B. 1996, ApJ, 460, L57

Chandler, C. J., & Richer, J. S. 2001, ApJ, 555, 139

Chernin, L. M., & Masson, C. R. 1995b, ApJ, 455, 182

Chernin, L. M., & Masson, C. R. 1995a, ApJ, 443, 181

Chernin, L. M., Masson, C. R., Gouveia Dal Pino, E., & Benz, W. 1994, ApJ, 426, 204

Cliffe, J. A., Frank, A., & Jones, T. W. 1996, MNRAS, 282, 1114

Cohen, M., Kuhi, L. V., Harlan, E. A., & Spinrad, H. 1981, ApJ, 245, 920

Cudworth, K. M., & Herbig, G. H. 1979, AJ, 84, 548

Dame, T. M., Elmegreen, B. G., Cohesn, R. S., & Thaddeus, P. 1986, ApJ, 305, 892

Davis, C. J., Mundt, R., Eislöffel, J., & Ray, T. P. 1995, AJ, 110, 766

Davis, C. J., Eislöffel, J., Ray, T. P., & Jenness, T. 1997, A&A, 324, 1013

Davis, C. J., Dent, W. R. F., Matthews, H. E., Coulson, I. M., & McCaughrean, M. J. 2000, MNRAS, 318, 952

Davis, C. J., Matthews, H. E., Ray, T. P., Dent, W. R. F, & Richer, J. S. 1999, MNRAS, 309, 141

Davis, C. J., Smith, M. D., & Moriarty-Schieven, G. H. 1998, MNRAS, 299, 825

Devine, D. 1997, Ph.D. Thesis, University of Colorado

Devine, D., Bally, J., Reipurth, B., & Heathcote, S. 1997, AJ, 114, 2095

Devine, Reipurth, B., D., Bally, J., & Balonek, T. J. 1999, AJ, 117, 2931

De Young, D. S. 1986, ApJ, 307, 62

Downes, T. P., & Ray, T. P. 1999, A&A, 345, 977

Draine, B. T., & McKee, C. F. 1993, ARA&A, 31, 73

Dyson, J. E., & Williams, D. A. 1997, The Physics of the Interstellar Medium (2nd ed.; London: Institute of Physics Publishing)

Eislöffel, J. 2000, A&A, 354, 236

Eislöffel, J. & Mundt, R. 1997, AJ, 114, 280

Elmegreen, B. G. 2000, ApJ, 530, 277

Erickson, N. R., Goldsmith P. F., Novak, G., Grosslein, R. M., Viscuso, P. J., Erickson, R. B., & Predmore, C. R. 1992, IEEE Transactions on Microwave Theory and Techniques, 40, 1

Estalella, R., & Anglada, G. 1997, Introducción a la Física del Medio Interestelar (1a ed.; Barcelona: Edicions Universitat de Barcelona)

Fuente, A., Martín-Pintado, J., Bachiller, R., Neri, R., & Palla, F. 1998a, A&A, 334, 253

Fuente, A., Martín-Pintado, J., Rodríguez-Franco, A., & Moriarty-Schieven, G. D. 1998b, A&A, 339, 575

Fuente, A., Neri, R., Martín-Pintado, J., Bachiller, R., Rodríguez-Franco, A., & Palla, F. 2001, A&A, 366, 873

Fukui, Y., Iwata, T., Mizuno, A., Bally, J., & Lane, A. 1993, in Protostars & Planets III, ed. E. H. Levy & J. I. Lunine (Tucson: Univ. Arizona Press), 603

Fukui, Y., Sugitani, K., Takaba, H., Iwata, T., Mizuno, A., Ogawa, H., & Kawabata, K. 1986, ApJ, 311, L85

Fuller, G. A., Lada, E. A., Masson, C. R., & Myers, P. C. 1995, ApJ, 453, 754

Frerking, M. A., Langer, W. D., & Wilson, R. W. 1982, ApJ, 262, 590

Gammie, C. F., & Ostriker, E. C. 1996, ApJ, 466, 814

Gibb, A. G., & Davis, C. J. 1998, MNRAS, 298, 644

Gledhill, T. M., Warren-Smith, R. F., & Scarrott, S. M. 1987, MNRAS, 229, 643

Goldreich, P. & Kwan, J. 1974, ApJ, 189, 441

Gómez, M., Kenyon, S., & Whitney, B. A. 1997, AJ, 114, 265 (GKW)

Goodman, A. A., & Arce, H. G. 2002, in preparation

Greene, T. P., & Lada, C. L. 1996, ApJ, 461, 345

Gueth, F., & Guilloteau, S. 1999, A&A, 343, 571

Gueth, F., Guilloteau, S., & Bachiller, R. 1996, A&A, 307, 891

Gueth, F., Guilloteau, S., & Bachiller, R. 1998, A&A, 333, 287

Hajjar, R., & Bastien, P. 2000, ApJ, 531, 494

Haro, G. 1952, ApJ, 115, 572

Hartigan, P., Bally, J., Reipurth, B., & Morse, J. A. 2000, in Protostars and Planets IV, ed. V. Mannings, A. P. Boss, & S. S. Russell (Tucson: University of Arizona Press), 867

Hartmann, L., Ballesteros-Paredes, J., Bergin, E. A. 2001, preprint (astro-ph/0108023)

Hartmann, L., Kenyon, S., & Hartigan, P. 1993, in Protostars & Planets III, ed. E. H. Levy & J. I. Lunine (Tucson: Univ. Arizona Press), 497

Hartmann, L., & MacGregor, K. B. 1982, ApJ, 259, 180, 192

Harvey, D. W. A., Wilner, D. J., Lada, C. L., Myers, P. C., Alves, J. F., & Chen, H. 2001, preprint (astro-ph/0108470)

Hatchell, J., Fuller, G. A., Ladd, E. F. 1999, A&A, 344, 687

Heathcote, S., Morse, J. A., Hartigan, P., Reipurth, B., Schwartz, R. D., Bally, J., & Stone, J. M. 1996, AJ, 112, 1141

Herbig, G. H. 1951, ApJ, 113, 697

Herbig, G. H. 1958, ApJ, 128, 259

Herbig, G. H., & Jones, B. F. 1981, AJ, 86, 1232

Heyer, M. H. 2000, in ASP Conf. Ser. 217, Imaging at Radio through Submillimeter Wavelenghts, ed. J. G. Mangum & S. J. E. Radford (San Francisco:ASP), 213

Heyer, M. H., Snell, R. L., Goldsmith, P. F., & Myers, P. C. 1987a, 321, 370

Heyer, M. H., Vrba, F. J., Snell, R. L., Schloerb, F. P., Strom, S. E., Goldsmith, P. F., & Strom, K. M. 1987b, ApJ, 321, 855

Hirose, S., Uchida, Y., Shibata, K., & Matsumoto, R. 1997, PASJ, 49, 193

Hodapp, K.-W. 1998, ApJ, 500, L183

Jijina, J., Myers, P. C., & Adams, F. C. 1999, ApJS, 125, 161

Kenyon, S. J., Dobrzycka, D., & Hartmann, L. 1994, AJ, 108, 1872

Königl, A. 1982, ApJ, 261, 115

Kudoh, T., & Shibata, K. 1995, ApJ, 452, L41

Knee, L. B. G., & Sandell, G. 2000, A&A, 361, 671

Kutner, M. L., & Ulich, B. L. 1981, ApJ, 250, 341

Kwan, J. & Scoville, N. 1976, ApJ, 210, L39

Lada, C., Dickinson, D. F., & Penfield, H. 1974, ApJ, 189, L35

Lada, C. J., & Fich, M. 1996, ApJ, 459, 638

Lada, C. J., Lada, E. A., Clemens, D. P., & Bally, J. 1994, ApJ, 429, 694

Langer, W. D., Castets, A., & Lefloch, B. 1996b, ApJ, 471, L111

Langer, W. D., & Penzias, A. A. 1993, ApJ, 408, 539

Langer, W. D., Velusamy, T., & Xie, T. 1996a, ApJ, 468, L41

Langer, W. D., Wilson, R. W., Goldsmith, P. G., & Beichman, C. A. 1989, ApJ, 337, 355

Lee, C.-F., Mundy, L. M., Reipurth, B., Ostriker, E. C., & Stone, J. M. 2000, ApJ, 542, 925

Lee, C.-F., Stone, J. M., Ostriker, E. C., & Mundy, L. G. 2001, ApJ, 557, 429

Lefloch, B., Castets, A., Cernicharo, J., Langer, W. D., & Zylka, R. 1998, A&A, 334, 269

Leinert, C., Richichi, A., & Hass M. 1997, A&A, 318, 472

Lery, T., Heyvaerts, J., Appl, S., & Norman, C. A. 1999, A&A, 347, 1055

Levreault, R. M. 1984, ApJ, 277, 634

Levreault, R. M. 1988, ApJS, 67, 283

Levreault, R. M., & Opal, C. B. 1987, AJ, 93, 669

Li, Z.-Y., & Shu, F. H. 1996, ApJ, 472, 211

Lichten, S. M. 1982, ApJ, 255, L119

Liseau, R., & Sandell, G. 1986, ApJ, 304, 459

Lizano, S., & Giovanardi, C. 1995, ApJ, 447, 742

Mac Low, M.-M. 1999, ApJ, 524, 169

Mader, S. L., Zealey, W. J., Parker, Q. A., & Masheder, M. R. W. 1999, MNRAS, 310, 331

Margulis, M., & Lada, C. J. 1985, ApJ, 299, 925

Martín-Pintado, J., & Cernicharo, J. 1987, A&A, 176, L27

Masson, C. R., & Chernin, M. L. 1993, ApJ, 414, 230

Mathieu, R. D., Benson, P., Fuller, G. A., Myers, P. C., & Schild, R. E. 1988, ApJ, 330, 385

Matzner, C. D., & McKee, C. F. 1999, ApJ, 526, L109

Matzner, C. D., & McKee, C. F. 2000, ApJ, 545, 364

Meyers-Rice, B. A., & Lada, C. J. 1991, ApJ, 368, 445

McKee, C. F., & Hollenbach, D. J. 1980, ARA&A, 18, 219

Miesch, M. S., & Bally, J. 1994, ApJ, 429, 645

Mizuno, A., Fukui, Y., Iwata, T., Nozama, S., & Takano, T. 1990, ApJ, 356, 184

Mizuno, A., Onishi, T., Yonekura, Y., Nagahama, T., Ogawa, H., Fukui, & Y. 1995, ApJ, 445, L161

Moriarty-Schieven, G. H., & Snell, R. L. 1988, ApJ, 332, 364

Moriarty-Schieven, G. H., Snell, R. L., Strom, S. E., & Grasdalen, G. L. 1987, ApJ, 317, L95

Moriarty-Schieven, G. H., Wannier, P. G., Tamura, M., & Keene, J. 1992, ApJ, 400, 260

Moro-Martín, A., Cernicahro, J., Noriega-Crespo, A., & Martín-Pintado, J. 1999, ApJ, 520, L111

Mundt, R., Bührke, T., Fried, J. W., Neckel, T., Sarcander, M., & Stocke, J. 1984, A&A, 140, 17

Mundt, R., & Fried, J. W. 1983, ApJ, 274, L83

Mundt, R., Ray, & T. P., & Raga, A. C. 1991, A&A, 252, 740

Myers, P. C., & Benson, P. J. 1983, ApJ, 266, 309

Myers, P. C., Fuller, G. A., Goodman, A. A., & Benson, P. J. 1991, ApJ, 376, 561

Myers, P. C., Fuller, G. A., Mathieu, R. D., Beichman, C. A., Benson, P. J., Schild, R. E., & Emerson, J. P. 1987, ApJ, 319, 340

Myers, P. C., Heyer, M., Snell, R. L., & Goldsmith, P. F. 1988, ApJ, 324, 907

Najita, J. R., & Shu, F. H. 1994, ApJ, 429, 808

Nakano, M., Sugitani, K., Sato, F., & Ogura, K. 1994, ApJ, 423, L147

Narayanan, G., & Walker, C. K. 1996, ApJ, 466, 844

Neckel, T., Staude, H. J., Sarcander, M., & Birkle, K. 1987, A&A, 175, 231

Norman, C., & Silk, J. 1980, ApJ, 238, 158

Olmi, L., Felli, M., & Cesaroni, R. 1997, A&A, 326, 373

Onishi, T., Mizuno, A., Kawamura, A., Ogawa, H., & Fukui, Y. 1996, ApJ, 465, 815

Ostriker, E. C., Lee, C.-F., Stone, J. M., & Mundy, L. G. 2001, ApJ, 557, 443

Ostriker, E. C., & Shu, F. H. 1995, ApJ, 447, 813

Ostriker, E. C., Stone, J. M., & Gammie, C. F. 2001, ApJ, 546, 980

Padoan, P., Nordlund, Å. 1999, ApJ, 526, 279

Papaloizou, J. C. B., & Terquem, C. 1995, MNRAS, 274, 987

Parker, N. D., Padman, R., & Scott, P. F. 1991, MNRAS, 252, 442

Raga, A., & Cabrit, S. 1993, A&A, 278, 267

Raga, A. C., Cantó, J., Binette, L., & Calvet, N. 1990, ApJ, 364, 601

Raga, A. C., Cantó, J., Calvet, N., Rodríguez, L. F., & Torrelles, J. M. 1993, A&A, 276, 539

Raga, A. C., Cantó, J., Steffen, & W. 1996, QJRAS, 37, 493

Raga, A. C., & Kofman, L. 1992, ApJ, 386, 222

Reipurth, B. 1989, Nature, 340, 42

Reipurth, B. 2000, AJ, 120, 3177

Reipurth, B., Bally, J., & Devine, D. 1997c, AJ, 114, 2708 (RBD)

Reipurth, B., Bally, J., Graham, J. A., Lane, A. P., & Zealey, W. J. 1986, A&A, 164, 51

Reipurth, B., Olberg, M., Gredel, R., & Booth, R. S. 1997c, A&A, 327, 1164

Reipurth, B., Hartigan, P., Heathcote, S., Morse, J. A., & Bally, J. 1997b, AJ, 114, 757

Reipurth, B., Raga, A. C., & Heathcote, S. 1992, ApJ, 392, 145

Reipurth, B., Yu, K. C., Heathcote, S., Bally, J., & Rodríguez, L. F. 2000, AJ, 120, 1449

Richer, J. S., Hills, R. E., & Padman, R. 1992, MNRAS, 254, 525

Richer, J. S., Shepherd, D. S., Cabrit, S., Bachiller, R., & Churchwell, E. 2000, in Protostars and Planets IV, ed. V. Mannings, A. P. Boss, & S. S. Russell (Tucson: University of Arizona Press), 867 (RSCBC)

Rodríguez, L. F., Ho, T. P. T, & Moran, J. M. 1980, ApJ, 240, L149

Rohlfs, K., & Wilson, T. L. 2000, Tools of Radio Astronomy (3rd ed.; New York: Springer)

Sandell, G., & Knee, L. B. G. 2001, ApJ, 546, L49

Sato, F., & Fukui, Y. 1989, ApJ, 343, 773

Scarrott, S. M., Rolph, C. D., & Tadhunter, C. N. 1991, MNRAS, 249, 131

Schwartz, R. D. 1975, ApJ, 195, 631

Snell, R. L., Loren, R. B., & Plambeck, R. L. 1980, ApJ, 239, L17

Snell, R. L., & Schloerb, P. 1985, ApJ, 295, 490

Shang, H., Shu, F. H., Glassgold, A. E. 1998, ApJ, 493, L91

Shepherd, D. S., Watson, A. M., Sargent, A. I., & Churchwell, E. 1998, ApJ, 507, 861

Shepherd, D. S., Yu, K. C., Bally, J., & Testi, L. 2000, ApJ, 535, 833

Shu, F. H., Adams, F. C., & Lizano, S. 1987, ARA&A, 25, 23

Shu, F. H., Ruden, S. P., Lada, C. J., & Lizano, S. 1991, ApJ, 370, L31

Shu, F. H., Najita, J., Ostriker, E. C., & Shang, H. 1995, ApJ, 455, L155

Shu, F. H., Najita, J., Ruden, S. P., & Lizano, S. 1994b, ApJ, 429, 797

Shu, F. H., Najita, J., Ostriker, E. C., Wilkin, F., Ruden, S. P., & Lizano, S. 1994a, ApJ, 429, 781

Shull, J. M., & Draine, B. T. 1987, in Interstellar Processes, eds. D. J. Hollenbach & H. A. Thronson, Jr. (Drodrecht: D. Reidel Publishing), 283

Stahler, S. W. 1994, ApJ, 422, 616

Stanke, Th., McCaughrean, M. J., & Zinnecker, H. 2000, A&A, 355, 639

Smith, M. D., Suttner, G., & Yorke, H. W. 1997, A&A, 323, 223

Stone, J. M., & Norman, M. L. 1993a, ApJ, 413, 198

Stone, J. M., & Norman, M. L. 1993b, ApJ, 413, 210

Stone, J. M., & Norman, M. L. 1994, ApJ, 420, 237

Stone, J. M., Ostriker, E. C., & Gammie, C. F. 1998, ApJ, 508, L99

Suttner, G., Smith, M. D., Yorke, H. W., & Zinnecker, H. 1997, A&A, 318, 595

Tafalla, M., Bachiller, R., Martín-Pintado, J., & Wright, M. C. H. 1993, ApJ, 415, L39

Tafalla, M., Bachiller, R., & Wright, M. C. H. 1994, ApJ, 432, L127

Tafalla, M., Bachiller, R., Wright, M. C. H., & Welch, W. J. 1997, ApJ, 474, 329

Tafalla, M., & Myers, P. C. 1997, ApJ, 491, 653

Terebey, S., Shu, F. H., & Cassen, P. 1984, ApJ, 286, 529

Terebey, S., Vogel, S. N., & Myers, P. C. 1989, ApJ, 340, 472

Terquem, C., Eislöffel, J., Papaploizou, J. C. B., & Nelson, R. P. 1999, ApJ, 512, L131

Torrelles, J. M., Ho, P. T. P., Rodríguez, L. F., Cantó, J., & Moran, J. M. 1987, 321, 884

Umemoto, T., Hirano, N., Kameya, O., Fukui, Y., Kuno, N., & Takakubo, K. 1991, ApJ, 377, 510

Velusamy, T., & Langer, W. D. 1998, Nature, 392, 685

Wang, H., Yang, J., Wang, M., Deng, L., Yan, J., & Chen, J. 2001, ApJ, 121, 1551

Warin, S., Castes, A., Langer, W. D., Wilson, R. W., & Pagani, L. 1996, A&A, 306, 935

White, G. J., & Fridlund, C. V. M. 1992, A&A, 266, 452

Wild, W. 1999, A Handbook for the IRAM 30m Telescope, Instituto de Radioastronomía Milimétrica

Wilken, F. P. 1996, ApJ, 459, L31

Wolf, G. A., Lada, C. J., & Bally, J. 1990, AJ, 100, 1892

Wood, D., Myers, P. C., & Daugherty D. A. 1994, ApJS, 95, 457

Wu, Y., Huang, M., & He, J. 1996, A&AS, 115, 283

Yorke, H. W., Bodenheimer, P., & Laughlin, G. 1993, ApJ, 411, 274

Yu, K. C., Billawala, Y., & Bally, J. 1999, AJ, 118, 2940 (YBB)

Yu, K. C., Billawala, Y., Smith, M. D., Bally, J., & Butner, H. 2000, AJ, 120, 1974 (YBSBB)

Zhang, Q., & Zheng, X. 1997, ApJ, 474, 719

Zuckerman, B., Kuiper, T. B. H., & Kuiper, E. N. R. 1976, ApJ, 209, L137